UNIVERSITEIT VAN PRETORIA
UNIVERSITY OF PRETORIA
YUNIBESITHI YA PRETORIA

Experimental Investigation of Film-Cooling Hole Performance

SUBMITTED IN PARTIAL FULFILMENT OF THE REQUIREMENTS FOR THE DEGREE OF

MASTER OF ENGINEERING

IN THE DEPARTMENT OF MECHANICAL AND AERONAUTICAL ENGINEERING

UNIVERSITY OF PRETORIA

BY

ZIMASE DLAMINI

June 2020

SUPERVISOR: DR G.I. MAHMOOD

Abstract

Film cooling has, over the years, allowed for the operation of modern gas turbines at temperatures far exceeding the limits of the material properties of the turbine components. This has resulted in increased power output and efficiency of the gas turbines. But over 40+ years of research has not culminated in the goal of achieving ideal cooling films, such as from two-dimensional (2D) continuous slots.

This study employed a curvature in the forward diffuser section of the film cooling hole; these holes are referred to as cases 1 to 4 in this study. This was expected to improve the performance of the hole. The performance parameters investigated and reported were the discharge coefficient of the holes, the flowfield downstream of the hole exit trailing edge, the temperature field downstream of the hole exit trailing edge and the effectiveness.

The effects of pressure ratio, mainstream crossflow, compound angle, hole geometry, manufacturing method, 3D print build orientation, and inclination angle, on the discharge coefficient were investigated.

The effects of blowing ratio, hole geometry, compound angle, turbulence intensity and downstream distance from hole exit trailing edge, on the flowfield, temperature field and effectiveness were also investigated.

The hole geometries had a diameter of 8 mm and length to diameter ratio equals to 7.5. The compound angle was varied between zero (0) to sixty (60) degrees. The inclination angles of the holes were either thirty (30) and forty (40) degrees.

The effect of the compound angle, manufacturing method and 3D print build orientation was found to be negligible for the discharge coefficient. But the above parameters had a significant effect on the adiabatic film cooling effectiveness.

Cases 1 to 4 holes showed higher discharge coefficient values as compared to the cylindrical and the laidback fan-shaped holes. This was a result of the development of the flow inside the hole and the resulting exit coolant jet velocity profile and its interaction with the mainstream crossflow.

From the flow structure and temperature field measurements it was determined that employing the curvature and the lateral expansion of the cases 1 to 4 holes decreases the height and trajectory of the jet on exit. The decreased height is due to the decreased vertical momentum content of the coolant jet. The decreased trajectory positions the longitudinal vortices closer to the wall which results in better lateral spread of the coolant.

From the effectiveness measurements it was found that increasing the compound angle decreases the lateral averaged effectiveness. And a decrease in the lateral averaged effectiveness was observed as the blowing ratio was increased.

The case 2 hole geometry resulted in low jet height when in the mainstream, which means that it was closer to the surface that requires cooling. It also resulted in a relatively good lateral spread of the coolant on the surface. And it resulted in the highest laterally averaged effectiveness at most of the compound angles and blowing ratios tested.

Acknowledgements

I would like to thank the people and institutions listed below for their help and support:

- Dr G.I. Mahmood for his supervision and sharing his knowledge.
- Mr C. Govinder, Mr D. Keetse and Mr E. Mohale for their assistance in the wind tunnel labs and mechanical workshop at UP.
- Undergraduate students, Ms A. Mutyaba, Mr L. Phiri, Mr T. Manyelo, Mr K. Gouwe and Mr N. Ndlovu, for their help building the testing facility.
- My family and friends for their continuous support.
- The National Research Foundation for the 'NRF Freestanding' funding.

Table of Contents

List of Figures

List of Tables

Nomenclature

BR : blowing ratio, $BR = \frac{\rho_c U_c}{\rho_m U_m}$

CA : compound angle or orientation angle relative to mainstream flow direction

$C_{d,orifice}$: discharge coefficient of orifice plate located in the compressor inlet pipe $= 0.596$

C_d : film cooling hole discharge coefficient with mainstream crossflow

$C_{d,o}$: film cooling hole discharge coefficient without mainstream crossflow

C_{py} : yaw pressure coefficient

C_{pp} : pitch pressure coefficient

C_{pt} : total pressure coefficient

C_{pts} : total minus static pressure coefficient

C_{ps} : static pressure coefficient

d : orifice diameter

D : diameter of the cylindrical portion of hole

$\dot{m}_{actual}$: actual mass flow rate through hole

MFR : momentum flux ratio, $MFR = \frac{\rho_c {U_c}^2}{\rho_m {U_m}^2}$

p_0 : differential pressure across orifice

P_{tc} : total coolant pressure in plenum box

P_{sm} : static mainstream pressure

PR : pressure ratio, $PR = \frac{P_{tc}}{P_{sm}}$

P_{atm} : atmospheric pressure

ΔP : gauge pressure reading from transducers

P_{tm} : total mainstream pressure

P_{sm} : static mainstream pressure

P_1 : central port pressure

$P_{2\,\&\,3}$: pressure ports on the yaw plane

$P_{4\,\&\,5}$: pressure ports on the pitch plane

$\overline{P} = \frac{P_2+P_3+P_4+P_5}{4}$: average pressure of the yaw and pitch

p : pitch angle

Q_v : volume flow rate

R : ideal gas constant

T_{aw} : adiabatic wall/surface temperature

T_{tc} : total temperature inside plenum

$T_{thermocouple}$: thermocouple temperature measurement inside plenum

T_{actual} : actual temperature inside plenum

T_{tm} : total mainstream temperature

T_{probe} : probe temperature

TG : mainstream flow with turbulence grid

U_c : average coolant velocity

U_m : freestream velocity

U_x : velocity in the $x-$direction (mainstream direction)

U_y : velocity in the $y-$direction

U_z : velocity in the $z-$direction

$\overline{U}_{WC}$: average coolant velocity with mainstream crossflow

$\overline{U}_{WOC}$: average coolant velocity without mainstream crossflow

V_{tc} : plenum transducer voltage response

$V_{offset,tc}$: plenum transducer offset voltage response

V_{sm} : mainstream static transducer voltage response

$V_{offset,sm}$: mainstream static transducer offset voltage response

WC : with crossflow

WOC : without crossflow

WOTG : mainstream flow without turbulence grid

W_x : vorticity in the $x-$direction

X : longitudinal flow direction

y : yaw angle

Y : lateral flow direction

ρ_c : density of coolant through film cooling hole

ρ_m : freestream density

ρ_{air_inlet} : density of air at the inlet of compressor

θ : non $-$ dimensionalized temperature

δ_{out} : outlet additive losses coefficient

η : adiabatic film cooling effectiveness

Subscripts

c：coolant

m：freestream/mainstream

tc : ′total coolant′ pressure/temperature/density in plenum box

tm : ′total mainstream′ pressure/temperature/density

sm : ′static mainstream′ pressure/temperature/density

WC：with crossflow

WOC：without crossflow

1.Introduction

1.1.Background

Increasing the temperature of the fluid at the entrance of gas turbines would result in an increase in the power output and the efficiency. However, the material properties of the gas turbine components limit the operating temperature. High operating temperatures degrade the structural materials of the gas turbine. Internal and external cooling methods have been employed in modern gas turbines which allows operation at temperatures far exceeding the material properties limit. These methods ensure that the temperatures in vulnerable areas remain well below the mainstream temperature. Cooling air is bled from the compressors and channelled through internal passages to the various components that require cooling (Hay *et al*. 1994; Hay & Lampard 1998).

Film cooling is an external cooling method whereby coolant is injected into the mainstream through holes along structural surfaces in the gas turbine with the purpose of providing a thin insulating protective layer (Hay *et al*. 1994; Hay & Lampard 1998) (Figure 1-1).

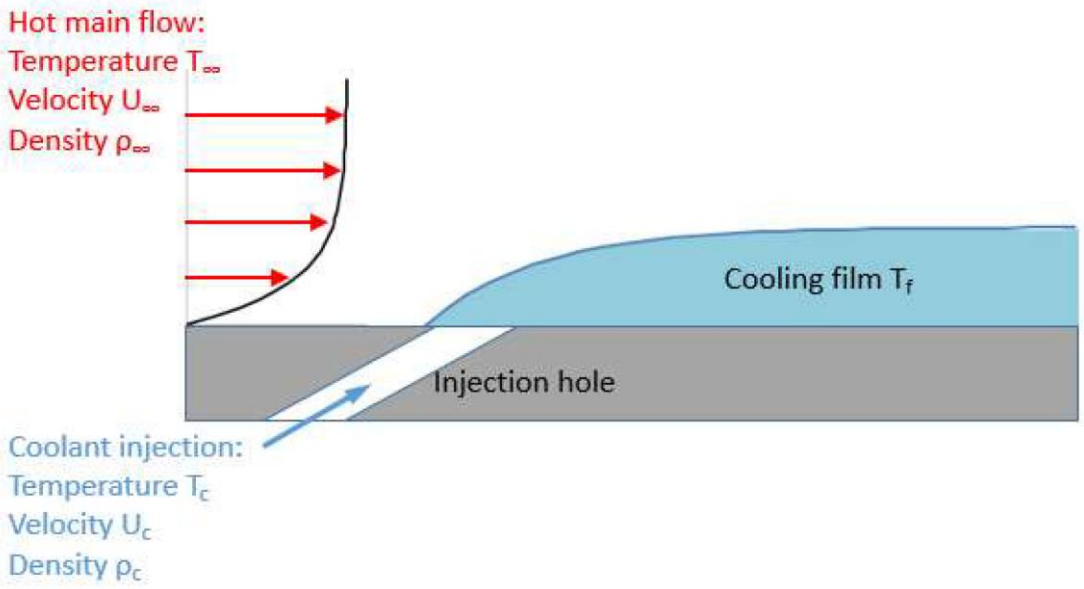

Figure 1-1: Film cooling illustration (Xue, S & Ng, WF 2018).

As stated above, cooling air is bled from the compressors. The coolant air does not get heated in the combustion chamber and bypasses one to two turbine stages, which implies less work. This results in a loss of output of approximately five (5) percent or more of the total flow. Therefore, the cooling air must be minimized to the amount that will achieve the required cooling. The amount of cooling air injected is dependent on the size and the number of cooling holes. So, parameters such as the discharge coefficient and the flow behaviour downstream of the film cooling hole for the variety of geometries and flow conditions that can arise need to be known by designers. This is crucial as coolant underfed or overfed can both result in the formation of hotspots on the surface, and consequently reduced component life (Hay *et al*. 1994; Hay & Lampard 1998).

1.2.Problem Statement

Over 40+ years of research into film cooling has led to a single improvement in this method being put into widespread use. This improvement has been the change from purely cylindrical holes to those with expanded hole exits, which resulted in lower momentum coolant jets with greater surface coverage (Bunker, RS 2005). However, the goal of achieving ideal film cooling,

such as that obtained from two-dimensional (2D) continuous slots has not been reached. The ideal film cooling hole geometry would provide a coolant film that is uniformly distributed over the surface that is to be insulated.

1.3.Motivation of the new design features

The increased design freedom of additive manufacturing, or 3D printing, has created the opportunity to test a wider range of film cooling hole geometries.

This study aims to employ a curvature in the forward diffuser section of the film cooling hole (Figure 1-2). This is expected to improve the performance of the hole.

Based on the literature reviewed of the cylindrical film hole, it was expected that this new hole geometry would minimise penetration of the jet into the mainstream flow on exit and minimise jet lift-off downstream of the hole exit. This is expected because the curvature allows the jet to remain close to the wall. This would lead to an increased range of blowing ratios usage with less of the detrimental effects caused by jet penetration and lift-off into mainstream flow. Jet lift-off and penetration into the mainstream flow adversely affects thermal performance because the coolant is no longer located on the surface of the component so as to insulate it from the hot mainstream gases.

Based on the literature reviewed of the holes with expanded exits, it was expected that the curvature in this new hole geometry would minimise flow separation in the diffused section of the hole. This would allow for higher blowing ratios to be used without the adverse effects of flow separation in the forward diffuser direction.

The advantage of being able to use higher blowing ratios is that the coolant has more momentum to reach and cool further downstream of the holes. This means that less holes need to be used which preserves the structural integrity of the components. Additionally, it means a less complicated design of the film-cooling scheme which results in less cost to manufacture.

Ultimately, the curvature is expected to help with the turning of the jet, gradually guiding the jet in the direction of the mainstream flow. This should result in less counterproductive interaction of the coolant jet and the mainstream flow at the hole exit, which in turn is expected to result in less coolant jet energy losses and loss of coolant into the boundary layer. Less coolant jet energy losses means that the jet has more momentum to reach and cool further downstream of the film cooling hole.

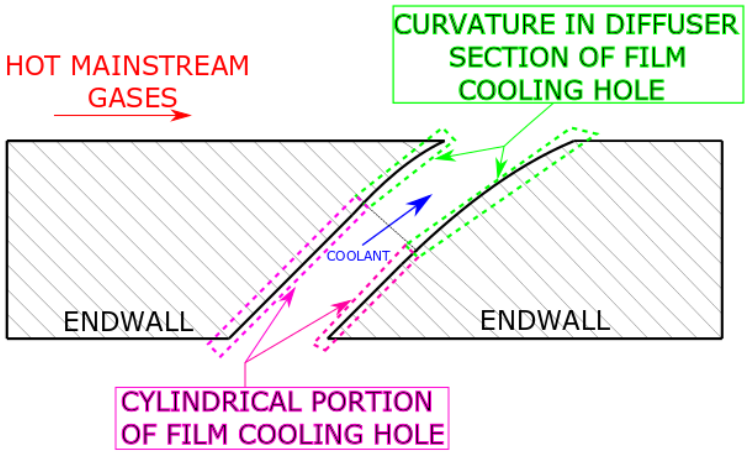

Figure 1-2: Film cooling hole with curvature.

1.4. Experimental Objectives

The main objective of this study is to experimentally investigate the aerothermal performance of the hole geometry with a curvature incorporated in the forward diffuser section (see Figure 1-2). This implies the comparison of aerothermal performance between the newly designed holes against the baseline cylindrical and laidback fan-shaped holes. The performance parameters investigated and reported are the discharge coefficient of the hole, the flow field and temperature field downstream of the hole and the film-cooling effectiveness on the end-wall.

Nine (9) film cooling holes were manufactured and tested:

a) cylindrical hole (machined);
b) cylindrical hole (3D printed; 60-degrees print orientation);
c) laidback fan-shaped hole (machined);
d) laidback fan-shaped (3D printed; 0-degrees print orientation);
e) laidback fan-shaped (3D printed; 67-degrees print orientation); and
f) cases 1 to 4; holes with curvature (3D printed; 0-degrees print orientation).

Further details of the film cooling hole geometries are given in section 3.3.

Meeting the main objective above is accomplished by:

- Investigating the effect of compound angle on the hole discharge coefficient, the flow structure and temperature field far downstream of the hole exit, and the adiabatic effectiveness. The orientation (compound angle) of the film cooling hole with respect to the mainstream flow will be varied for all the test pieces to determine the effect of compound angle. The purpose of testing the behaviour at different orientations is because situations occur where the film cooling hole cannot be aligned with the mainstream flow direction. Additionally, it has been reported in literature that offsetting the film cooling holes from the direction of the mainstream flow weakens the physical mechanisms that are detrimental to film cooling performance. This is elaborated in the literature review presented Chapter 2.
- Investigating the effect of the manufacturing method and 3D print build orientation on the hole discharge coefficient, the flow structure and temperature field far downstream of the hole exit, and the adiabatic effectiveness. The results of a) and b), and the results of c), d) and e) will be compared to determine the effect of manufacturing method and 3D print build orientation. The reason for this investigation is because Cases 1 to 4 (f) can only be 3D printed. Therefore, the effect of 3D printing on film cooling behaviour must be investigated. The manufacturing method followed is devised by Aghasi *et al*. (2017) and is shown in Appendix E.
- Investigating the effect of hole geometry on the hole discharge coefficient, the flow structure and temperature field far downstream of the hole exit, and the adiabatic effectiveness. Cases 1 to 4 , (f), form the basis of this study, which is to investigate the effect of employing a curvature as the forward diffuser section of the film cooling hole. Results from the b), d) and f) will be compared.
- Investigating the effect of inclination angle on the hole discharge coefficient, the flow structure and temperature field far downstream of the hole exit, and the adiabatic effectiveness. The purpose of testing the behaviour at different inclination angles is that situations occur where the film cooling hole must be inclined at a different angle.

Additionally, it has been reported in literature that varying the film cooling hole configuration is an efficient way to weaken the physical mechanisms that are detrimental to film cooling performance. This is elaborated in the literature review presented in Chapter 2.

1.5. Scope of Work

- Designing and building of testing facility for flat plate end-wall film cooling testing. Flat plate film cooling isolates the effects of film cooling hole geometry from other considerations such as wall curvature.
- Discharge coefficient, flow structure, temperature field and heat transfer (adiabatic wall effectiveness) testing.
- Reporting findings in the form of a dissertation.

1.6. Overview of dissertation

The dissertation is divided into the chapters shown below:

- Chapter 2 provides a detailed literature review on the discharge coefficient and the physical mechanisms that determine the behaviour observed. A general review of the flow structure, temperature field and effectiveness, when the coolant is downstream of the film cooling hole is also presented.
- Chapter 3 describes the experimental set-up, the film cooling hole geometries, flow parameters, data reduction methods, the experimental procedure followed, and reports the error expected from the measured values (uncertainty analysis).
- Chapter 4 presents and discusses the discharge coefficient results for the different film cooling hole geometries and configurations. An in-depth analysis into the physical mechanisms that govern the discharge coefficient behaviour observed is undertaken.
- Chapter 5 presents and discusses the flow structure results downstream of the hole exit.
- Chapter 6 presents and discusses the temperature field results downstream of the hole exit.
- Chapter 7 presents and discusses the adiabatic wall effectiveness results downstream of the hole exit.
- Chapter 1 concludes the results and provides recommendations for future works.

2.Literature Review

Figure 2-1 below shows a schematic of the cylindrical film cooling hole geometry. The student has included labels that are important in order to understand the work in the corresponding reference presented and the discussion of results. The upstream and downstream edge, for all the film cooling hole geometries, is the edge that is considered as upstream/downstream when the meridional cross-section of the film-cooling hole is aligned to the mainstream flow direction.

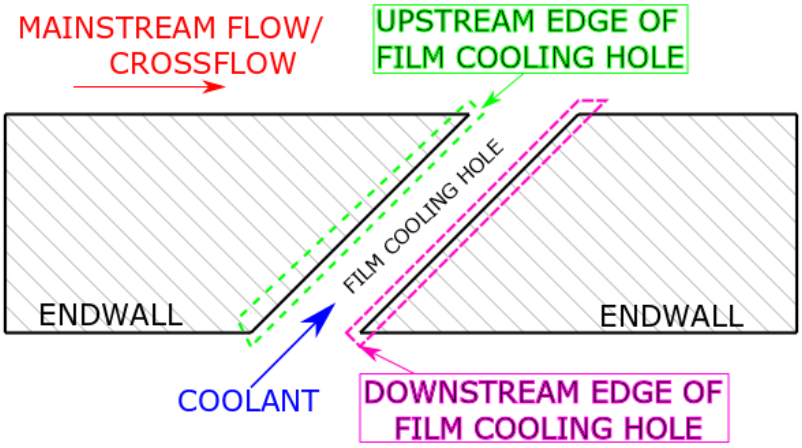

Figure 2-1: General schematic of cylindrical film cooling hole.

Figure 2-2 extends on the above by illustrating a uniform smooth parabolic velocity profile and a velocity profile that is skewed to the upstream edge of the film cooling hole. This will also be referred to extensively in the rest of the report.

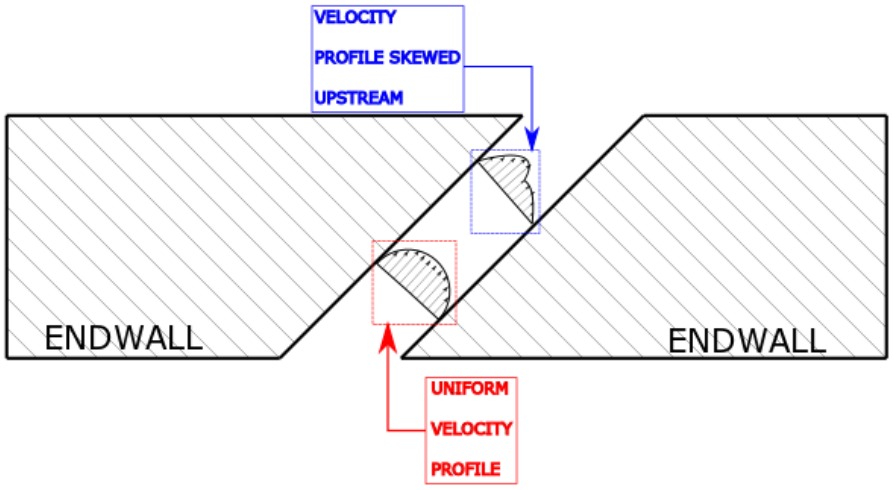

Figure 2-2: Illustration of velocity profiles.

2.1.Discharge Coefficient in film-cooling

The discharge coefficient quantifies the irrecoverable portion of energy that is lost in the conversion from static pressure energy to kinetic energy in a contraction. It is defined as the ratio of the actual mass flow rate to the ideal mass flow rate through the contraction (Beckwith *et* al. 2009). The definition of the discharge coefficient, C_d,is shown in Equation (1) below.

$$C_d = \frac{\dot{m}_{actual}}{\dot{m}_{ideal}} \quad (1)$$

Equation (2) below is obtained with the derivation of the ideal mass flow rate. The derivation of the ideal flow rate is shown in Appendix A.

$$C_d = \frac{\dot{m}_{actual}}{A_{hole}\sqrt{2 \times \rho_c \times (P_{tc} - P_{sm})}} \quad (2)$$

Equation (2) ignores compressibility effects of the coolant; the density of the coolant is assumed to be constant. It is shown in Appendix B that this is a valid assumption in the pressure ratio range tested in this study.

In film-cooling, the discharge coefficient is includes the flow losses through the coolant supply plenum, hole, and the coolant-freestream interaction zone. A separation region is expected at the inlet. The location and size of the separation zone at the inlet influences the coolant velocity distribution inside the hole (Thole *et al.* 1997). The coolant velocity distribution inside the hole determines the exit velocity profile which influences the interaction of the jet with the mainstream flow (Burd & Simon 1999). This chain of physical phenomena determines the discharge coefficient of the hole.

The geometric variables of the hole and the flow conditions influence the values of the discharge coefficient. The geometric parameters include: 1) the ratio of the length of the hole to the diameter of the hole; 2) the angle at which the hole is inclined; 3) the angle at which the hole is oriented relative to the mainstream flow direction; 4) the radiusing of the hole at inlet and/or outlet and the degree of radiusing; 5) the chamfering of the hole; and 6) the resultant geometry of the hole. The flow parameters include: 1) the ratio of the total pressure in the supply and the static pressure in the mainstream flow across the hole; 2) the hole Reynolds number; 3) the presence of crossflow at inlet and outlet; 4) the boundary layer thickness near the hole outlet; 5) the presence of swirl within the hole; and 6) rotation of the hole (Hay & Lampard 1998).

The above paragraph makes the reader aware that the discharge coefficient is strongly dependent on the geometry and flow parameters. Therefore, the literature presented includes a brief description of the experimental set-up used in the different studies. This makes it easier to understand the behaviours observed and allows for better comparisons to be made on the different behaviours.

Below, detail is presented regarding the individual components of losses. These are the losses due to entry, hole friction losses and outlet losses. Understanding the individual components of losses allows us to make sense of the discharge coefficient behaviour observed. Also reviewed are the flow structures observed in the locations where losses are expected. This is to help support the discharge coefficient behaviours observed.

2.1.1. Coolant supply plenum losses

These are also referred to as hole inlet losses. The film-cooling hole serves as a restriction in the path of the flowing fluid. As a fluid enters a contraction, according to the continuity of mass and conservation of energy, there is a trade-off between kinetic energy (signified by an increase in the velocity of the fluid) and the static energy (decrease in static pressure).

In the conversion from pressure to velocity, a certain portion of the pressure drop is irrecoverable, lost to the universe (entropy) owing to dissipation of kinetic energy. Basically, at the minimum area (minimum pressure) of the contraction the velocity does not attain a maximum value that is proportional to the minimum pressure value. This is evidenced by the

output energy values, in the expansion of the fluid, never returning to original input energy values (Beckwith *et* al. 2009).

A separation zone at the entrance of the hole has been reported to be the reason for the losses at entry. This separation zone decreases the cross-sectional area of flow. Hence, there is less than the ideal mass flow into the hole (Lichtarowicz *et* al. 1965; Pietrzyk *et* al. 1989; Leylek & Zerkle 1993; Thole *et al.* 1997).

According to Hay *et al*. (1983), the case of a plenum at the inlet of a 90 degrees hole and no mainstream flow at the outlet reduces to that of flow through a long orifice. For length to diameter ratios greater than 2, downstream of the entrance the coolant reattaches to the surface of the orifice and fills the cross-sectional area. The discharge coefficient is a result of pressure losses due to entry and frictional losses in the length of the orifice. For high Reynolds numbers, the discharge coefficient becomes constant at a value ranging between 074 - 0.8, depending on the length to diameter ratio.

- **Flow structure at the inlet of Hole**

In a study by Lichtarowicz *et al*. (1965), the flow through long orifices was investigated. The effect of the length-to-diameter ratio (= 1 to 10), the approach pipe diameter to orifice diameter ratio, and the Reynolds number (= 1 to more than 10^4) of the flow through the orifice, on the flow structure at the orifice entrance and the discharge coefficient were reported.

With orifices manufactured from Perspex and dye injected into the flow stream, the following flow patterns were observed at the entrance of orifices. At very low Reynolds numbers (creeping flow), the flow remained attached to the cylindrical wall at entry. As the Reynolds number was increased, firstly, laminar separation was observed at the entrance of the orifice bore. The flow then reattached at a well-defined point (reattachment is observed if the orifice is sufficiently long) and a laminar flow profile subsequently developed along the orifice.

Further increase of the Reynolds number then produces a condition in which the separated flow becomes turbulent, where this transition results in a reattachment being distributed over an area rather than being concentrated at a clearly defined point. This area is identified by a relatively steep rise in pressure. The transition to turbulence is accompanied by a significant change in the length of the separation zone.

A circulating flow is set-up in the separation region. As the length of the orifice is progressively reduced, the turbulent reattachment becomes less complete, at length-to-diameter ratio equals to 1, it is no longer certain to take place. When the flow does not reattach, it emerges as a jet, but recirculation of the fluid in the separated zone is still produced by jet mixing, with the result that fluid from the downstream side of the orifice is drawn upstream in an annulus surrounding the jet. A noticeable pressure recovery may thus be generated along the bore where further shortening of the orifice reduces these effects, until ultimately the sharp-edged orifice condition is reached.

In the experimental study by Rogers and Hersh (1975) the inlet and the outlet, of a 90 degrees (normal) short orifice were supplied by a crossflow. They performed water tunnel testing and wind tunnel testing. The flow structure, at the orifice entrance and exit, as well as the discharge coefficient were reported.

The following flow regimes were observed: 1) low inflow; and 2) high inflow. It was reported that a separated flow region was observed on the upstream lip of the orifice. This separated region initially extended through the full depth of the orifice and filled up almost the full cross-sectional area of the orifice at the exit. As the flow rate increased the cross-sectional area of

the separated region at the orifice inlet decreased, implying a decreasing in the necking/constriction of the orifice inflow.

In the experimental study by Pietrzyk *et al*. (1989), the experimental set-up was such that the 35 degrees inclined cylindrical hole was supplied by a stagnant plenum with the presence of mainstream crossflow at the hole exit. The length-to-diameter ratio of the hole was equals to 3.5. Laser doppler anemometry (LDA) was used to measure velocity components. Flow field measurements, performed at the hole exit, were reported for jet-to-mainstream velocity ratios of 0.25, 0.5 and 1.0, at a density ratio of 1, and velocity ratios of 0.5 and 1.0, at a density ratio equals to 2.

Pietrzyk *et al*. (1989) hypothesised that as the jet-to-mainstream velocity ratio increased, a separation region begins to form at the downstream side of the cooling hole. This causes the primary jet exit location to shift from the downstream side of the cooling hole at low blowing ratios, to the upstream side of the film-cooling hole. This separation region being on the downstream edge is due to the large turning angle undergone by the coolant on the downstream side of the hole (see Figure 2-3).

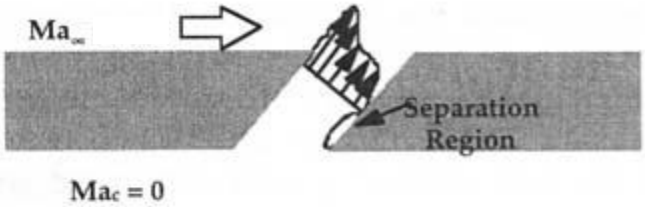

Figure 2-3: Coolant jet flow structure result at the entrance of film cooling hole due to supply plenum and sharp turning angle (Thole *et al.* 1997).

Pietrzyk *et al*. (1989) measured the turbulence intensity at the exit of the hole to confirm that the sharp entrance at the hole entrance caused a separation region on the downstream side of the hole, which becomes more severe for higher hole velocities. It was reported that an increase in the blowing ratio resulted in increased turbulence intensity inside the hole. The increased separation region at higher blowing ratios would account for the skewing of the jet inlet profiles toward the leading edge of the hole for large blowing ratios.

In a computational study by Leylek and Zerkle (1993), the model included a supply plenum, a cylindrical film cooling hole and the mainstream flow. It was shown that the jet inside the hole is pushed towards the upstream edge of the hole because of the separation region on the downstream edge at the hole entrance.

It was also reported that at large length-to-diameter ratios greater than 3, and high blowing ratios, greater than 1 or small length-to-diameter ratios, less than 3, and low blowing ratios, less than 1, the flow inside the cooling hole became more similar to a fully developed turbulent pipe flow.

In an experimental study by Thole *et al.* (1997) the experimental set-up was such that there was a crossflow at the inlet and the hole exit (mainstream flow), supplying cylindrical holes at an inclination angle of 30 degrees and length-to-diameter ratio equal to 6. Laser-Doppler velocimetry (LDV) was used to measure velocity components. Flow field measurements were performed at a velocity ratio of 1, with the mainstream Mach number kept constant at 0.25 and the crossflow Mach number in the coolant channel varied (= 0, 0.3 & 0.5). The velocity ratio is defined as the ratio of the velocity of the coolant jet and the mainstream flow.

Mean velocity field measurements inside the hole, for the case where the crossflow Mach number in the coolant channel was equal to zero (= 0, stagnant plenum case), confirming that

a large portion of the jet is pushed to the top portion of the film cooling hole. This proved that a separation zone exists at the downstream (relative to the mainstream) edge of the hole entrance. This region forms on the downstream edge because the downstream fluid has a large turning angle to overcome which causes the separation on the downstream side of the hole entrance.

In addition to a skewed jet profile, the separation region occurring at the hole inlet produces relatively high turbulence levels. This high turbulence levels increase the coolant diffusion. The jet will tend to mix with the 'hot' mainstream fluid more rapidly and not be as effective in cooling.

According to Thole *et al.* (1997) the flow separation at the hole entry is responsible for the losses when the flow enters the hole. The size of the separation region, which is primarily dependent on the crossflow conditions and the hole angles, determines the amount of losses and therefore, the discharge coefficient.

- **Key points from the student regarding the inlet losses**

Figure 2-4 shows some of the different inlet configurations of coolant holes and experimental setups employed in film-cooling investigations in the literatures. The student has included this section because each configuration has significance and the behaviour observed in different configurations are related to each other. The blue elliptical shapes are illustrations of the separation region at the inlet.

In Figure 2-4(a), the supply has approach flow momentum and the hole is normal to the supply at the entrance. In Figure 2-4(b), the hole is normal to the plenum at the entrance. In Figure 2-4(c), the hole is inclined to the plenum at the entrance.

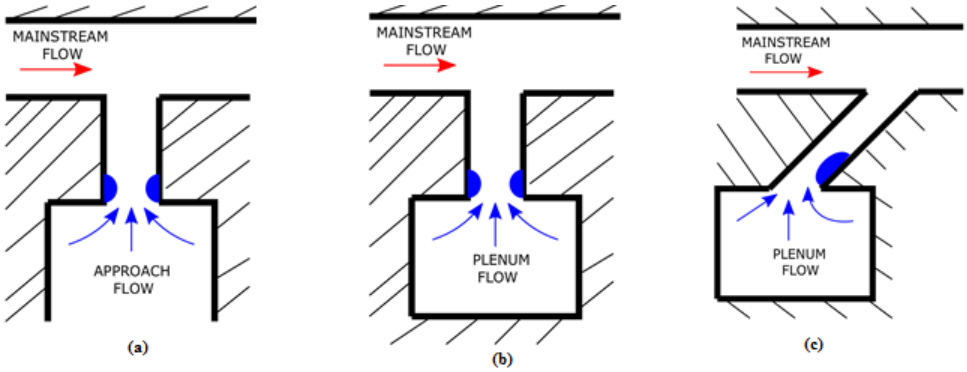

Figure 2-4: Illustration of the inlet physical mechanism for different inlet conditions reported in literature. a) plenum with approach flow momentum and normal film cooling hole, b) stagnant plenum with normal film cooling hole, c) stagnant plenum with inclined film cooling hole.

It is known that there are losses due to contraction when a fluid flows from a reservoir into a pipe. For the case of sharp-edged entrances, it was noted that a portion of these losses can be associated with a separation region that forms at the hole inlet.

In comparing the configurations of Figure 2-4(a) and Figure 2-4(b), the total pressure at the inlet in Figure 2-4(a) is the sum of the static component of pressure and the dynamic component of pressure, whereas the total pressure in Figure 2-4(b) is only a static pressure (stagnant plenum). The separation region in Figure 2-4(b) is expected to be larger than that of Figure 2-4(a), due to a form of contribution from the dynamic head of the coolant in Figure

2-4(a). The dynamic head decreases the size of the separation region, which allows for more coolant to flow through.

The take-home point in the comparison of the configurations in Figure 2-4(a) and Figure 2-4(b) is that there is less losses if the coolant has dynamic head when entering the hole.

In comparing the configuration of Figure 2-4(b) and Figure 2-4(c), in the configuration of Figure 2-4(c) the separation region is reported, in literature, to be on the downstream edge at the hole inlet. It is reported that this is due to the coolant having to take a larger turning angle for it to enter the hole; The turning of the fluid causes the separation region to shift primarily to the downstream edge of the hole. This additional turning of the fluid possibly presents itself in the form of a larger separation region at the downstream edge of the hole inlet, as compared to what can be seen in Figure 2-4(b).

The conclusion in the comparison of the configurations in Figure 2-4(b) and Figure 2-4(c) is that the additional turning of the fluid when entering the hole causes a larger separation region on the downstream edge, which forces the coolant to the upstream edge. This affects the flow structure of the coolant at entry, which may influence the coolant-mainstream interaction at the hole outlet.

From the above it can be seen that there are losses due to contraction, and additional losses due to turning and lack of dynamic head of the coolant.

The purpose of the above discussion was to show that each configuration has significance, and that the behaviour observed in each can be related to the other. The significance of this is that the configuration chosen isolates certain effects. If normalised adequately, the behaviour observed from either configuration can be used to deduce the expected behaviour in the other configurations. The importance of being able to relate behaviour from alternate configurations is so that good comparisons can be made with the literature available.

2.1.2.Hole losses

These losses are due to friction and mixing of the fluid as the fluid flows through the hole. Regarding friction losses, it is well known that there are kinetic energy losses in flow due to the viscosity of fluids. Additionally, downstream of the separation zone that is at the hole inlet, there are mixing losses as the fluid expands to the cross-sectional area of the film-cooling hole.

An experimental investigation by Hay *et al*. (1983) reported the discharge coefficient for a range of inclination angles (= 30, 60, and 90 degrees) and for a range length to diameter ratios (= 2 to 10) and crossflow. Tests were done on cylindrical holes. It was found that for length-to-diameter ratios greater than 2, the effect on the discharge coefficient is very weak.

In an experimental study by Burd and Simon (1999) the experimental set-up had crossflow at the outlet of the cylindrical holes and the holes were inclined at 35 degrees. Measurements of hole exit velocity profile, discharge coefficients and outlet additive losses were reported as the coolant supply method (Sink-flow/plenum, Counter-Flow & Co-Flow) at the inlet of holes was varied, and the length to diameter ratio (= 2.3, 4.6, 6.6 and 7) and angle of orientation (=0 & 90 degrees) of the holes were varied.

When the discharge coefficient was measured without mainstream flow, it was found that the variation in length to diameter ratio had very little effect on the discharge coefficient. In the case of ‘without mainstream flow’, the discharge coefficient is a function of entry losses and hole losses. The losses due to entry are expected to be the same as the inlet of the four (4) length-to-diameter ratios is the same. For this reason, since the discharge coefficient was

nominally the same for the four (4) cases, it is expected that the friction losses for the four (4) cases be the same. The data suggests that the friction losses are negligible, which agrees with findings by Lichtarowicz *et al.* (1965), Andrews and Mkpadi (1984), and Hay and Lampard (1998).

From the above it is concluded that, for length-to-diameter ratio greater than 2 for the cylindrical holes, the effect of varying the length-to-diameter ratio has very little effect on the losses as compared to the inlet losses. The inlet losses determine the discharge coefficient.

2.1.3.Coolant jet-mainstream flow interaction zone losses

These are also referred to as hole outlet losses and have been referred to as outlet additive losses in many studies. The jet-crossflow interaction zone is also referred to as the near-field interaction zone. It is the region immediately around the hole exit plane, including the hole exit plane area. In this region, the upstream flow conditions (mainstream flow conditions) and the jet exit conditions dominate in determining the discharge coefficient.

To get a better sense of the outlet losses the three flow regimes that were observed by Rogers and Hersh (1975): 1) Net zero outflow; 2) low outflow; and 3) high outflow, will be used (see Figure 2-5).

The net zero flow regime, Figure 2-5(a), occurs when there is no coolant that flows into the mainstream. There is basically a balance of static pressure (normal forces) between the mainstream and the plenum. A 'lid' model was proposed by Rogers and Hersh (1975) as aid to understanding the effect, on the discharge coefficient, of the presence of the mainstream flow at the exit of the film cooling hole. We are told to imagine the interface between the coolant flow and mainstream flow as a lid that is hinged at the upstream edge of the film cooling hole and covers the whole cross-sectional area of the hole, in the case of net zero flow.

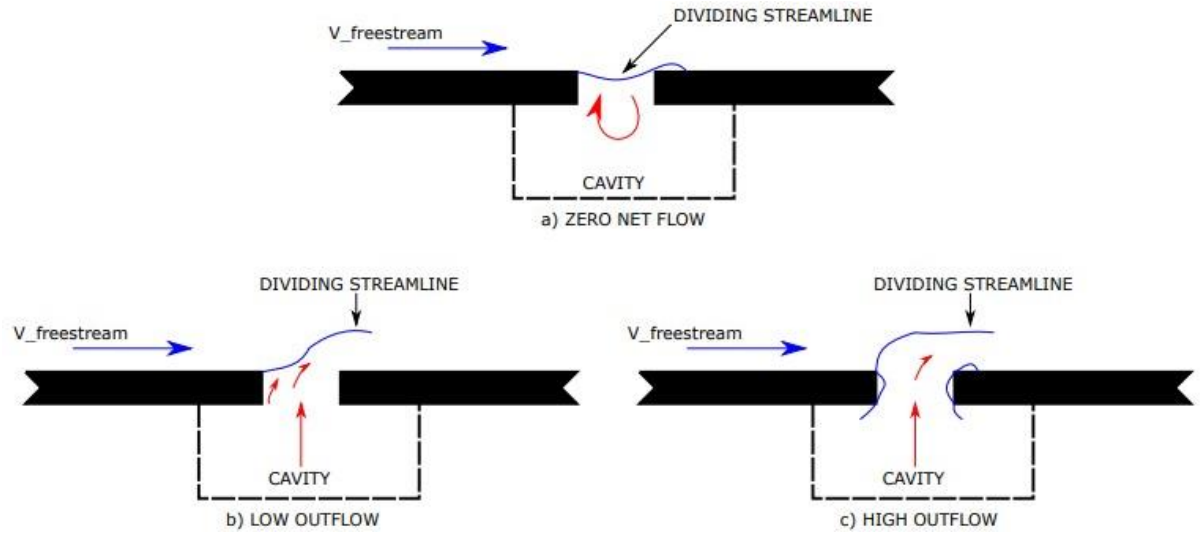

Figure 2-5: Outflow regimes observed in water tunnel (redrawn from Rogers & Hersh 1975).

When the pressure in the plenum is increased above the static pressure of the mainstream, there is then an imbalance of normal forces between the two streams (mainstream and jet/coolant stream) and the lid is raised from the exit of the hole (low outflow regime; Figure 2-5(b)). This allows coolant mass to flow through. The coolant is deflected downstream by the mainstream flow upon exiting, due to the stagnation pressure exerted by the mainstream flow. Hence, the 'lid' is hinged at the upstream edge. Mixing and shearing with the freestream along the jet periphery causes the flow in the outer regions of the jet to lose momentum and, thus, to deflect (Burd & Simon, 1999).

The interaction between the mainstream and the coolant jet, upon exiting, affects the amount that the 'lid' is deflected from the exit. The amount that the lid is deflected from the exit determines the amount of coolant flow allowed into the mainstream. This blockage/resistance to flow by the mainstream flow is what adds to the losses of the hole (decreases discharge coefficient) and is what is called outlet additive losses.

In the high outflow regime depicted in, Figure 2-5(c), the 'lid' is completely opened at the hole outlet, hence, there is no blockage by the mainstream flow. The discharge coefficient is determined more by the inlet conditions than by the effects of the mainstream crossflow. At this point, the mainstream crossflow serves only to turn the coolant jet in the direction of the mainstream crossflow.

According to Hay *et al*. (1983), the issuing jet is 'pinched' by the crossflow, leading to a reduction in the effective cross section and the noted decrease in discharge coefficient values.

The experimental set-up by Andreopoulus and Rodi (1984) was normal (90 degrees) circular holes into a mainstream flow. Three sensor hot-wire probes were used to measure the mean and fluctuating velocity components at the hole exit for jet-to-mainstream flow velocity ratios equal to 0.5, 1.0 and 2.0.

It was reported that both the jet and mainstream flow deflect. The jet is bent over by the mainstream flow, while the mainstream flow is deflected as if it were blocked by a rigid obstacle, the difference being that the jet interacts with the deflected flow and entrains fluid from it. In the case of the small velocity ratio (= 0.5), the flow behaves as if a partial, inclined 'cover' were put over the front part of the exit hole, causing the jet streamlines to start bending while still in the discharge tube and also to lift up the oncoming flow over the bent-over jet. In the case of the higher velocity ratio (= 2.0) the jet is only weakly affected near the exit and penetrates the mainstream flow before it is deflected in the direction of the mainstream flow.

In a study by Hay and Lampard (1995), with cylindrical hole data obtained from the study by Benmansour (1981), a slight decrease was observed in the discharge coefficient when a mainstream flow was added for the cylindrical hole. Results for the diffused hole showed an increase in the discharge coefficient with the addition of mainstream crossflow. From these results it was seen that the effect of the mainstream flow is more pronounced at lower pressure ratios.

In a study by Hay and Lampard (1995) for holes inclined 30 degrees, with cylindrical hole data obtained from study by Bromley (1994), the cylindrical hole results showed that a decrease was observed in the discharge coefficient when a mainstream flow is added, and the effect of the mainstream flow is more pronounced at lower pressure ratios. Little to no effect was observed for the diffused holes with the addition of mainstream crossflow.

In a study by Gritsch *et al*. (1998) it was reported that high mainstream crossflow Mach numbers at the hole exit lead to significantly reduced discharge coefficients, particularly at low pressure ratios for all geometries tested.

In a study by Burd and Simon (1999) it was noted that the free-stream flow causes a reduction in the discharge coefficient values at each pressure ratio, significant at low pressure ratios and reducing to near zero at high pressure ratios.

In a study by Gritsch *et al.* (2001) it was noted that at low momentum flux ratios, the normalised discharge coefficient values were less than one. This indicated additional losses due to the external crossflow. At high momentum flux ratios, the discharge coefficient was not affected by the mainstream crossflow.

2.1.3.1. Flow structure at the outlet of Hole

Mean velocity component measurements, from a study by Pietrzyk *et al*. (1989) taken nearest the exit of the hole showed relatively flat velocity profiles as the jet exited the hole. The magnitudes of the velocity vectors just past the jet exit were larger than might be expected for the respective blowing ratios because of an acceleration as the jets were diverted downstream by the crossflow. The velocity profile was relatively uniform for blowing ratio equals to 0.5, but slightly skewed downstream for blowing ratio equal to 0.25, and slightly skewed upstream for blowing ratio equals to 1.

Turbulence intensity measurements at the exit of the hole confirmed that the sharp entrance at the hole entrance caused a separation region on the downstream side of the hole, which becomes more severe for higher hole velocities. It was reported that an increase in the blowing ratio resulted in increased turbulence intensity inside the hole. The increased separation region at higher blowing ratios would account for the skewing of the jet inlet profiles toward the leading edge of the hole for large blowing ratios.

Mean velocity field measurements at the hole exit, in a study by Thole *et al.* (1997), showed that a large portion of the jet is in the upstream side of the cooling hole. The skewing of the jet profile would be such that the jet flow is able to counteract the mainstream flow at the jet exit. In fact, the jet exit location begins near the upstream side of the cooling hole. The skewing of the jet as it exits the cooling hole causes a higher penetration into the crossflow at the exit of the hole. Very high turbulence levels were observed.

In a study by Burd and Simon (1999), hole exit mean velocity distributions were measured along the hole centrelines at a velocity ratio equal to 1. It was found that the velocity distributions over the hole exit plane vary significantly, with changes in hole length to diameter ratio. The short length holes allow shorter distances over which the separation zone effect at the inlet can attenuate. Therefore, the velocity distribution of the coolant jet at the exit of the hole is such that it has increasingly higher momentum at the upstream side of the hole as the hole length to diameter ratios are reduced. It was reported that the significance of the velocity distribution at the exit is in that it influences the discharge coefficient values. This effect is related to the interaction of the mainstream flow and coolant at the hole exit. This effect was quantified using an outlet additive losses parameter as discussed further in section 2.3.

In this study flow structures will not be measured at the inlet, inside the hole, and the coolant jet–mainstream flow interaction will not be measured at the outlet. Rather, the effect of the above will be quantified in terms of the discharge coefficient and outlet additive losses. The study uses results from previous studies that investigated these flow structures to substantiate the discharge coefficient behaviour observed in this study. The flowfield tests done and presented here are downstream of the coolant jet-mainstream flow interaction zone; far-field behaviour.

2.2. Discharge coefficient curve

Shown in Figure 2-6 is the general trend, reported in literature, of the discharge coefficient as a function of the pressure ratio. The discharge coefficient curve is a sum of all the losses (inlet, hole and outlet losses) of the hole in the film-cooling process. On the graph, the student has shown the different flow regimes that have been reported, in the literature that was available to the student. The importance of being able to determine which flow regime the experiment captures will allow the student to determine the flow structure and the losses that are significant on the discharge coefficient.

Examining Figure 2-6, it is apparent that as the pressure ratio increases, the performance of the hole (discharge coefficient) increases. This implies a decrease in the losses of the coolant.

An asymptote is then approached, where the performance of the hole (discharge coefficient) is constant.

The different regions shown in the graph, 1) low outflow region, 2) high outflow region, are based on observations by Rogers and Hersh (1975) and, 5) low pressure region, and 6) high pressure region.

Low outflow region (A to B) and high outflow region (B to D) are defined based on the blockage created by the mainstream crossflow at the hole outlet. According to Rogers and Hersh (1975), the low outflow region, is characterised by the lifting of the dividing surface by the mainstream flow and then the emerging of the coolant flow as the flow rate is increased. Andreopoulus and Rodi (1984) made similar observations but chose to classify it as low and high velocity ratios. But the ranges were not quantified. This is possibly because film cooling behaviour has been observed to be very sensitive to flow and geometric conditions.

In the low outflow regime, an increase in the discharge coefficient is observed, as the jet flow rate is increased. Available literature suggests that the increase in the discharge coefficient as the flow rate is increased is determined by a decrease in the cross-section of the separation region at the inlet and the reduction in the blockage of the mainstream at the hole exit.

In the regime of high outflow, the discharge coefficient is determined more by the inlet conditions than by the effects of the mainstream crossflow. There is no longer a blockage ('lid' is removed) at the hole outlet due to the mainstream crossflow. Hence, the losses are a function of the inlet conditions. At this point, the mainstream crossflow serves only to turn the coolant jet in the direction of the mainstream crossflow. The literature available to the student suggests that the increase in the discharge coefficient in this regime is due to a decrease in the cross-section of the separation region as the flow rate increases.

The distinction between the low-pressure region (A to C) and the high-pressure region (C to D) is the point at which the discharge coefficient is a weak function of the pressure ratio. This point was found to be strongly dependent of the coolant geometric and flow parameters.

At low pressure ratios, the discharge coefficient is a strong function of the pressure ratio, increasing with it. In the study by Gritsch *et al*. (2001) it was reported that, for all cases investigated, increasing the pressure ratio resulted in higher discharge coefficients.

At high pressure ratios the flow is choked, and the mass flow is determined by the hole diameter and the upstream stagnation conditions (Hay & Lampard 1995). Previous studies have reported this plateau at pressure ratios greater than 1.4 (Hay *et al*. 1983; Hay & Lampard 1995). From the results of the study by Burd and Simon (1999), it was seen that the plateau was reached at much smaller pressure ratios; approximately equal to 1.001. The discharge coefficient value obtained is strongly dependent on the coolant geometric and flow parameters. In a study by Hay and Lampard (1995), and Burd and Simon (1999), the discharge coefficient assumes values of approximately equals to 0.83.

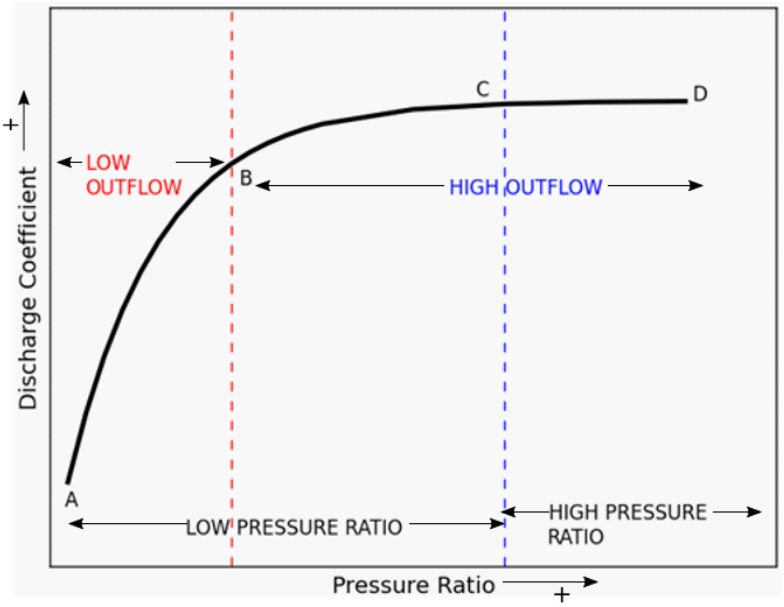

Figure 2-6: Graph illustrating the gross discharge coefficient behaviour reported in literature.

In summary, region A to B is low pressure ratio and low outflow. The discharge coefficient is a strong function of the pressure ratio and the discharge coefficient values are determined by the sum of losses at the inlet of the hole and at the outlet of the hole. Region B to C is a low-pressure ratio and high outflow region. The discharge coefficient is still a function of the pressure ratio, but the discharge coefficient values are determined more by the losses at the inlet only. Region C to D is high pressure ratio and high outflow. The discharge coefficient weakly depends on the pressure ratio because the flow is choked.

2.3.Outlet Losses curve

As stated above, the losses in the holes are a sum of losses at the inlet (flow contraction at the inlet), friction and mixing, and the interaction between the outer flow and the ejective flow at the exit of the hole. To isolate the effects of outlet losses, Sasaki *et al.* (1975) defined an outlet additive losses coefficient. These are losses associated with the external freestream. This loss relates the difference between measured pressures, with and without the external freestream, to the film cooling velocity head. This is shown in equation (3) below:

$$\delta_{out} = \frac{\left[(P_{tc} - P_{sm})_{U_\infty \neq 0} - (P_{tc} - P_{sm})_{U_\infty = 0}\right]}{{}^{1}/_{2}\,(U_{hole})^2} \tag{3}$$

This expression can be simplified in terms of discharge coefficients with, C_d, and without, $C_{d,o}$, the freestream, in Equation (4):

$$\delta_{out} = \frac{1}{(C_d)^2} - \frac{1}{(C_{d,o})^2} \tag{4}$$

According to Burd and Simon (1999), when the bulk mean velocity, density, and thus, momentum flux of the coolant are matched, the net loss introduced exclusively by the external freestream flow can be quantified. This means that a comparison between the case of with and without crossflow can only lead to the conclusion that 'the net loss calculated is only due to external freestream', in such case where comparison is made at points where the velocities in the two cases are the same. In Appendix D the student shows how the velocities were matched between the two cases.

Figure 2-7 represents the general trend, as reported in literature, of the outlet additive losses coefficient as a function of the momentum flux ratio. As the momentum flux ratio increases the outlet losses decrease due to the mainstream crossflow deflecting from the exit of the hole and allowing more coolant to flow through. An asymptote is then approached, where the outlet additive losses are zero.

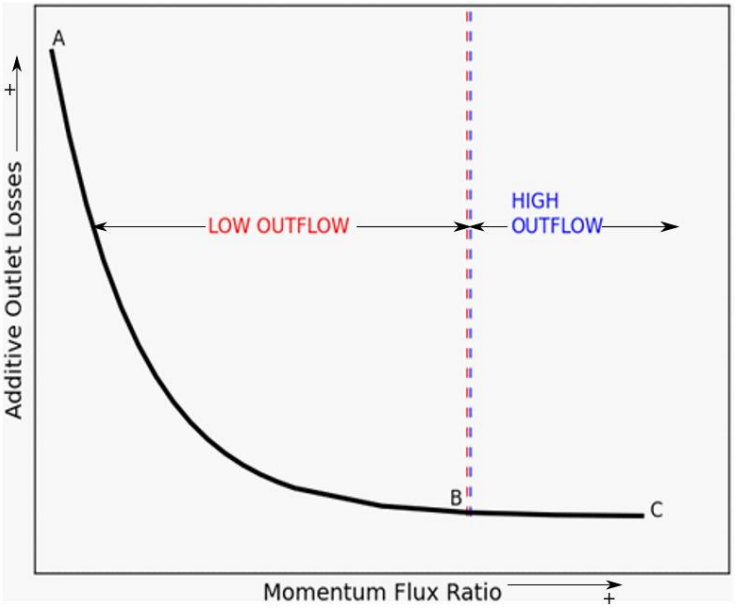

Figure 2-7: Graph illustrating the general outlet additive losses behaviour reported in literature.

The low outflow region (A to B) and high outflow region (B to C) are defined based on the blockage/resistance created by the mainstream crossflow at the hole outlet. According to Rogers and Hersh (1975), in the low outflow region, the decrease in the outlet losses is due to the reduction in the blockage of the coolant jet by the mainstream crossflow, as the jet flow rate is increased. In the regime of high outflow, there is no longer a blockage ('lid' is removed) at the hole outlet due to the mainstream crossflow. Hence, the outlet additive losses are zero.

In a study by Burd and Simon (1999), results showed a decrease in the outlet additive losses at low momentum flux ratios approaching an asymptote of zero (0) at high momentum flux ratios. The outlet additive losses being greater than zero (0) implies that the freestream restricts the emerging coolant flow.

It was also seen in the results that the geometries with which coolant was distributed in the upstream portion of the hole, the outlet additional losses were reduced. For such cases, this is due to the interaction with the mainstream being more active at the upstream edge location. This results in higher pressures at the upstream location, which results in reduced pressures over much of the hole exit plane. The low downstream pressure increases the mass flux at the downstream portion of the hole exit.

Geometries with more coolant distributed on the downstream portion of the hole exit have higher outlet additive losses. With less coolant momentum on the upstream edge, the high-pressure zone is shifted further downstream across the hole exit. This results in a smaller low-pressure region in the downstream portion of the hole exit plane and higher effective static pressures at the hole exit.

Results at low momentum flux ratios, in the study by Gritsch *et al*. (2001), showed an increase in the normalised discharge coefficient values as the momentum flux ratio was increased. This implied a decrease in the losses due to the mainstream crossflow. At momentum flux ratios

approximately exceeding 2, the discharge coefficient was not affected by the mainstream crossflow.

2.4.Effect of Compound angle

2.4.1.Discharge Coefficients of Holes Angled to the Flow Direction (Hay *et al.* 1994)

In the experimental study by Hay *et al*. (1994) the experimental set-up was such that there is a crossflow at the inlet of the holes and a plenum chamber (no flow) at the outlet. The holes were inclined at 30 degrees with a length to diameter ratio equals to 6. The discharge coefficient is reported as the orientation (= 0 to 180 degrees) of the holes is varied, relative to the inlet crossflow. This isolates the effect of orientation at the inlet on the discharge coefficient. Results are given for nominal crossflow Mach numbers of 0, 0.15 and 0.3.

It is reported that for coolant crossflow Mach number equal zero (0) (no crossflow, a stagnant plenum, at the inlet of hole) the orientation is not a variable. The effect of orientation is more pronounced the higher the value of coolant crossflow Mach. For coolant crossflow Mach number equal to 0.3 an increase in the angle of orientation led to a decrease in the discharge coefficient, a result to be expected as the flow has to turn more and more as the angle of orientation increases (the loss coefficient due to turning increases).

2.4.2.Measurements of Discharge Coefficients in Film Cooling (Burd & Simon 1999)

In the experimental study by Burd and Simon (1999) the experimental set-up had crossflow at the outlet of the hole and the holes were inclined at 35 degrees. Measurements of discharge coefficients and outlet additive losses are reported as the coolant supply method (Sink-flow/plenum, Counter-Flow & Co-Flow) at the inlet of holes is varied, and the length to diameter ratio and angle of orientation (=0 & 90 degrees) of the holes are varied. The length to diameter ratio is varied between two (2) and seven (7).

Results showed that without free-stream flow the discharge coefficient values for lateral injection (orientation angle = 90 degrees) resemble those of the stream-wise (orientation angle = 0 degrees) injection case, as anticipated, since both have the same length to diameter ratio equals to 2.3 and both eject into the same ambient. With the addition of free-stream flow, the discharge coefficient values for lateral injection drop more rapidly at low pressure ratios than for the stream-wise injection case. The opposite is true at high pressure ratios.

The lateral injection had higher outlet additive losses for momentum flux ratio less than or equal to 0.4. For momentum flux ratio greater than 0.4, they were lower than the stream-wise injection case, even assuming negative values. It is reported in this paper that similar behaviour was described by Khaldi (1987) for large momentum flux ratios. This is also consistent with the model of Rowbury *et al*. (1997), which contends that negative losses are more common and significant for film cooling holes with greater angles of orientation.

2.4.3.Effect of Crossflows on the Discharge Coefficient of Film Cooling Holes With Varying Angles of Inclination and Orientation (Gritsch *et al.* 2001)

In an experimental study by Gritsch *et al.* (2001), the experimental set-up was such that there is a crossflow at the inlet (internal) and outlet (external) of the hole. The discharge coefficient is reported for cylindrical holes as the inclination angle (= 30, 45 & 90 degrees) and the angle the orientation (= 0, 45 & 90 degrees) of the holes is varied. The tests were carried out in a pressure ratio range (= 1 to 2.25), internal Mach number range (= 0 to 0.6) and external Mach number range (=0 to 1.2). The holes had a length to diameter ratio equals to 6.

It was reported that the effect of the compound angle on the normalized discharge coefficient is determined more by crossflow at the inlet than by mainstream crossflow. A decrease in the normalised discharge coefficient was observed as the compound angle was varied. The decrease in the discharge coefficient is due to the increasing turning angle, which requires that the coolant turn more when entering the hole. This additional loss due to turning possibly presents itself as a larger separation region at the inlet, which causes a decrease in the discharge coefficient values.

2.5.Effect of Inclination angle

2.5.1.Effect of Crossflows on the discharge coefficient of film cooling holes with varying Angles of Inclination and Orientation (Gritsch *et al*. 2001)

In an experimental study by Gritsch *et al.* (2001) the experimental set-up was such that there is a crossflow at the inlet (internal) and outlet (external) of the hole. The discharge coefficient is reported for cylindrical holes as the inclination angle (= 30, 45 & 90 degrees) and the angle the orientation (= 0, 45 & 90 degrees) of the holes is varied. The tests were carried out in a pressure ratio range (= 1 to 2.25), internal Mach number range (= 0 to 0.6) and external Mach number range (=0 to 1.2). The holes had a length to diameter ratio equals to 6.

It was reported that the effect of the inclination angle on the normalized discharge coefficient is determined more by crossflow at the inlet than by mainstream crossflow. A decrease in the normalised discharge coefficient was observed as the inclination angle was varied. The decrease in the discharge coefficient is due to the increasing turning angle, which requires that the coolant turn more when entering the hole. This additional loss due to turning possibly presents itself as a larger separation region at the inlet, which causes a decrease in the discharge coefficient values.

2.6.Effect of Hole Geometry

The definition of the discharge coefficient for the shaped holes is based on the ideal flow through a cylindrical hole having the same diameter as the inlet section, rather than on the ideal flow through the actual geometry (see Equation (5)). This ensures that comparison of the shaped geometries and the cylindrical geometry yields an immediate indication of the effect on the discharge coefficient, of the incorporation of the different shapes (Hay & Lampard 1995).

$$C_d = \frac{\text{actual mass flow rate through shaped hole}}{\text{ideal mass flow rate through a cylindrical hole}} \quad (5)$$

2.6.1.The discharge coefficient of flared film cooling holes (Hay & Lampard 1995)

In an experimental study by Hay and Lampard (1995) the experimental set-up was such that a crossflow could be imposed at the inlet (internal) and the outlet (external) of the hole. Discharge coefficients were measured for normal (90 degrees) and for 30 degrees inclined holes over the pressure ratio range of 1.1 to 1.8. The holes tested either had only a lateral-spread or had a lateral-spread and a layback. Tests were done with no crossflow on either side and with crossflows at inlet and exit of 0.15 and 0.3 Mach numbers.

In the study by Hay and Lampard (1995), with cylindrical hole data taken from the study by Benmansour (1981), enhanced discharge coefficient values for the diffused holes as compared to the cylindrical holes were observed. It is said that this is due to jet pressure recovery in the diffused section.

The same behaviour was observed for 30 degrees inclined holes. The cylindrical hole data was taken from the study by Bromley (1994). It was also reported that the addition of the layback had little effect on the discharge coefficient.

It was additionally reported that the performance of the diffuser is strongly dependent upon the inlet flow conditions, where the flow within the diffuser is very sensitive to upstream flow history. The entry length reflects the entry flow behaviour. Increased distortion at the inlet results in increased distortion at the outlet, which affects pressure recovery within the diffused section (Klein 1981).

2.6.2. Discharge coefficient measurements of Film-Cooling Holes with expanded exits (Gritsch *et al.* 1998)

In an experimental study by Gritsch *et al.* (1998) the experimental set-up was such that there is a crossflow at the inlet (internal) and outlet (external) of the hole. Flow conditions for testing were hole entrance side crossflow Mach number in the range 0 - 0.6, hole exit side crossflow Mach number in the range 0 - 1.2, and pressure ratio range 1 - 2. Discharge coefficients were measured for a cylindrical hole, a fan-shaped hole and a laidback fan-shaped hole.

The results showed that the discharge coefficients of the expanded holes are higher than that of the cylindrical hole, with the same flow conditions applied. It is said that this is due to pressure recovery in taking place in the diffuser section of the hole.

It was additionally reported that the diffused holes operate best in the low-pressure ratio range, resulting in a high-pressure recovery and, thus, high discharge coefficients. At elevated pressure ratios, the rate of increase of the discharge coefficient values for the cylindrical holes is higher than that of the expanded holes. Therefore, the discharge coefficient values of the cylindrical holes quickly approach those of the expanded holes. This tells us that the effect of the pressure recovery decreases; at elevated pressure ratios the pressure recovery is reduced. This is due to the flow entering the diffuser section separating from the diffuser walls and reducing the pressure recovery and the discharge coefficients. It is also seen that the addition of the layback has a weak effect on the discharge coefficient.

2.7. Effect of Manufacturing Method & Build orientation

2.7.1. Effects of coolant feed direction on additively manufactured film cooling holes (Stimpson *et al.* 2018)

In an experimental study by Stimpson *et al.* (2018) the experimental set-up allowed for a crossflow at the inlet and outlet of the hole. Tests were done in the crossflow Mach number range, less than 0.1 at the inlet and less than or equals to 0.3 at the outlet. The film cooling hole geometry used is the 7-7-7 laidback fan-shaped hole by Schroeder and Thole (2014).

Flow and pressure drop measurements across the holes were collected to determine the discharge coefficient from the film cooling holes. Five (5) film cooling geometries were investigated. One (1) film cooling hole was machined (EDM) and had a hole diameter of 0.38 mm. Two (2) film cooling holes were additively manufactured with a hole diameter of 0.38 mm, but the build direction was varied. The last two (2) film cooling holes were additively manufactured with a hole diameter of 0.76 mm with the build direction varied.

The hole roughness was reported in terms of a relative roughness parameter, which was defined as the roughness divided by the hole diameter.

From their results it was determined that the discharge coefficient values of the additively manufactured holes are less than those of the machined holes. It is also noted that the

discharge coefficient is a strong function of the relative roughness in the hole. A decrease in the relative roughness results in an increase in the discharge coefficient values.

A detailed characterisation of the 0.38 mm holes by Stimpson *et al.* (2017) showed that the large roughness of the angled build direction holes significantly blocked the flow area which contributed to low discharge coefficient values.

2.8.Scaling Parameters

The scaling parameters that will be used in this study are defined below. A good scaling parameter captures, and places significance on, effects that primarily govern the gross behaviour observed in the system. This allows for data obtained at conditions unrepresentative of the gas turbine engine to be correctly interpreted in order to predict behaviour in the actual engine.

2.8.1.Pressure Ratio

Based on the results from the studies reviewed above, and countless others, the discharge coefficient scales best with the total coolant-to-static mainstream pressure ratio (see Equation (6)). Additionally, it is better to work with pressures because they are easier to measure.

$$PR = \frac{P_{tc}}{P_{sm}} \tag{6}$$

2.8.2.Blowing Ratio

The blowing ratio (BR) is a ratio of the mass flux of the coolant to that of the mainstream flow (see Equation (7)). This parameter is commonly used in film cooling to characterize the coolant flow rate and quantifies the heat capacity of the coolant (Anderson *et al.* 2015).

$$BR = \frac{\rho_c U_c}{\rho_m U_m} \tag{7}$$

2.8.3.Momentum Flux Ratio

The momentum flux ratio (MFR) is the ratio of the momentum flux of the coolant and the mainstream gas, equation (8). It quantifies the ability of the mainstream to turn the coolant jet towards the wall (Anderson *et al.* 2015).

$$MFR = \frac{\rho_c {U_c}^2}{\rho_m {U_m}^2} \tag{8}$$

2.9.Flow Structure, temperature field and adiabatic effectiveness downstream of the hole exit

The literature presented below focuses on four (4) studies. These are predominately numerical studies but, as their titles suggest, they provide an in-depth analysis of the flow physics in film cooling. Additionally, the results from these studies agree well with experimental results.

In a study by Leylek and Zerkle (1993) it was found that the flow immediately upstream of the hole exit plane and the flow inside the film cooling hole have a considerable effect on the coolant jet exit conditions. The jet exit conditions were found to subsequently influence the downstream behaviour and the overall film-cooling performance.

Therefore, in the literature presented below, the student will briefly touch on the flow physics at the hole inlet, inside the film cooling hole and in the immediate vicinity of the jet exit in order to give a well-rounded picture that shows the progression of events that leads to the observed behaviour downstream of the hole exit.

2.9.1.A detailed analysis of film cooling physics: Part 1 - Streamwise injection with cylindrical hole (Walters & Leylek 1997)

The model comprised of a plenum as the supply to cylindrical film cooling holes aligned to the freestream direction. Tests were done on two (2) film cooling hole with length to diameter ratios equal to 1.75 and 3.5, and three (3) blowing ratios in the range 0.5 to 2. The density ratio equalled two (2) and the injection angle of the holes was 35 degrees. This computational study is representative of the experimental study by Pietrzyk *et al*. (1989b).

As the flow turns into the film hole cooling hole, separation and flow turning at the inlet result in a jetting region along the upstream wall, as well as counter-rotating secondary flow within the film hole. An increase in the blowing ratio results in an increase in the strength of the jetting and the secondary flow, which influences the jet exit conditions.

Two (2) primary mechanisms influence the jet exit conditions, namely: 1) the relative strength of the jetting and the counter-rotating flow; and 2) the interaction of the of the exiting jet with the crossflow. The coolant jet exiting the film hole blocks the crossflow resulting in a high pressure region upstream of the hole upstream edge. The bending and turning of the jet, in the direction of the crossflow, results in a low pressure region downstream of the hole downstream edge.

The jet-crossflow interaction, in the immediate vicinity of the hole exit, is reported to result in the formation of separate flow regions, secondary flows and turbulence production. Special attention is given to the secondary flows in this literature review, as a means of locating the coolant jet in the flow and understanding the flow behaviour downstream because, firstly, the secondary flows are measured in this study and, secondly, the secondary flows are reported to be the most dominant mechanism in determining the film cooling performance. As a result, the effect of these secondary flows on the flow structure, downstream of the hole exit, is of interest.

The streamwise counter-rotating vortex structure, downstream of hole exit, is made up of the vorticity emanating from the film hole (film hole boundary layer vorticity) and the shearing between the jet crossflow due to the mismatch in streamwise momentum. It was reported that the vorticity from the film hole boundary layer controls the strength of the longitudinal vortices, is more significant, for the case of streamwise oriented holes.

These secondary flows are reported to significantly aid in the degradation of film cooling performance. The streamwise counterrotating vortices suck crossflow fluid beneath the coolant jet, causing upward lift (induction lift), which hinders thermal performance because the coolant is no longer on the surface to provide insulation. Additionally, these vortices oppose lateral spread of the coolant jet by convection toward the centreline.

In the near field, at lower blowing ratios, because of the small vertical momentum of the coolant jet at the exit, the coolant jet remains close to the wall. At higher blowing ratios, the increased vertical momentum of the jet positions it farther from the wall. This is significant because the wall is reported to have a destructive effect on the streamwise vorticity, which is sought-after.

As the coolant jet moves downstream the counter-rotating vortices grow larger and become less strong downstream of injection. At lower blowing ratios, the vortices degrade rapidly because the locations of maximum vorticity, which corresponds to the centre of the vortices, are closer to the wall. At higher blowing ratios, the coolant jet is lifted away from the surface by the counter-rotating vortices. Since the location of maximum vorticity is farther from the wall the streamwise counter-rotating vorticity is dissipated less rapidly and is apparent farther downstream.

Presented below are the results of the flowfield downstream of the hole exit. It is important to note that the location of the coolant core, which varies with blowing ratio, is also highly sensitive to the jet-crossflow near-field interaction, as discussed above. Shown in Figure 2-8 are the well-known counterrotating vortices for a blowing ratio equals to one (1) measured five (5) diameters downstream of hole exit.

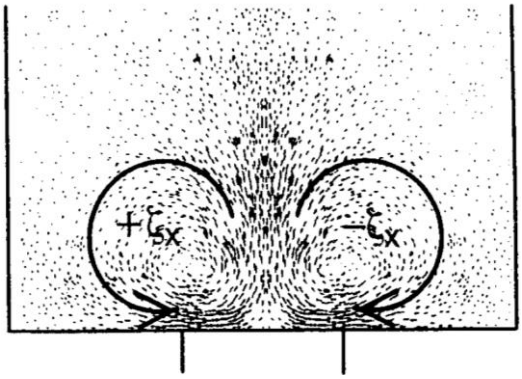

Figure 2-8: Velocity vectors showing counter-rotating vortices (Walters & Leylek 1997).

Figure 2-9 shows the flowfield results downstream of the jet-crossflow interaction region for blowing ratios equal to 0.5 and 1. It is reported that at around five (5) diameters downstream, the secondary flows are negligible/weak. The flow takes the appearance of a wake-like structure with a momentum deficit due to the exiting coolant. It also reported that the momentum, thermal energy, and turbulent energy are diffused in all directions. As the flow moves farther downstream it diffuses and takes on the shape of the boundary layer.

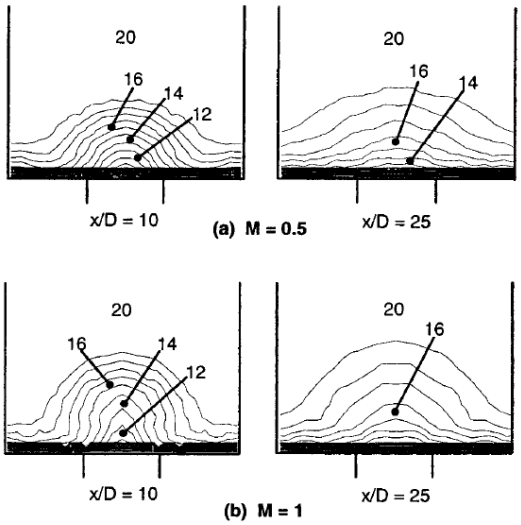

Figure 2-9: Velocity contours downstream of near-field interaction zone (Walters & Leylek 1997).

Figure 2-10 shows temperature contours closer to near-field inetraction zone. It is reported that at lower blowing ratios the coolant remains close to the wall at both downstream locations. This is due to relatively low upward lift. Additionally, the coolant diffuses outwards as it moves downstream because of lateral diffusion is opposed by weak secondary flow. At higher blowing ratios the coolant is seen to be lifted from the wall downstream because movement of crossflow fluid towards the centreline by relatively strong counterrotating vortices.

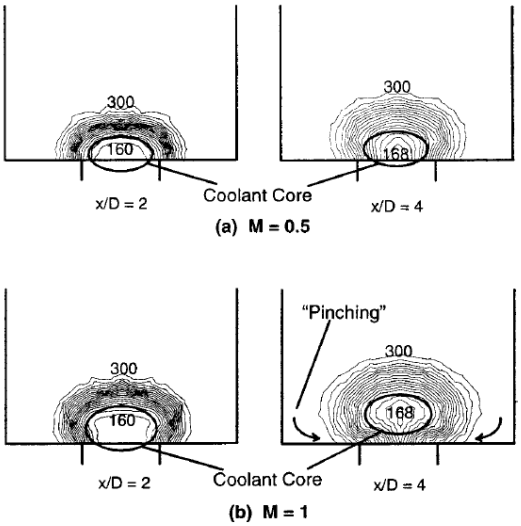

Figure 2-10: Temperature contours downstream of hole exit trailing edge (Walters & Leylek 1997).

Further downstream of the near field interaction zone it is reported that the coolant diffuses further as it moves downstream. It is also reported that it is important to note that the downstream behaviour is highly sensitive to the near-field interaction, which serves to locate the coolant at a certain position away from the surface.

2.9.2. A detailed analysis of film cooling physics: Part 2 - Compound angle injection with cylindrical hole (McGovern & Leylek 2000)

The model comprised of a plenum as the supply to cylindrical film cooling holes, whose compound angles were varied from 0 degrees to 45, 60 and 90 degrees to the freestream direction. Tests were done on a film cooling hole with length to diameter ratios equal to four (4), and two (2) blowing ratios of 1.25 and 1.88. The density ratio was equal to 1.6 and the injection angle of the holes was 35 degrees.

The variation in compound angle does not change the physical mechanisms at the entrance of the film hole. These physical mechanisms are reported in section 2.9.1. The relative strength of the mechanisms mentioned below increases with increasing blowing ratio.

Differences are observed at the exit, as compared to the streamwise case, because of significant changes in the pressure distribution at the hole exit. The changes in the way the pressure is distributed results in higher blockage at the hole exit. This leads to deviations of the coolant trajectory after it leaves the film hole.

In compound angle injection, as compared to streamwise injection, the vorticity generated at the interface plays a significant role in the vortex structure downstream of hole exit. The vortex structure downstream of the hole exit, in compound angle injection, is strongly dependent on the compound angle. As the compound angle is increased, the originally symmetric counter-rotating vortex structure becomes increasingly asymmetric because of a weakening of one (1) of the vortices in the pair and the strengthening of the other. The weakening of the one (1) vortex in the pair is caused by crossflow blockage of the film hole boundary layer that comes into initial contact with the crossflow. The strengthening of the other vortex in the pair is due to shear between the crossflow and the jet.

In the far-field, the asymmetric vortex structure eventually collapses into a single rotating vortex with significant lateral motion of the coolant near the wall. The coolant core is convected and diffused towards the surface more quickly which results in better lateral spread of the coolant. The vortex losses strength with downstream distance (see Figure 2-11).

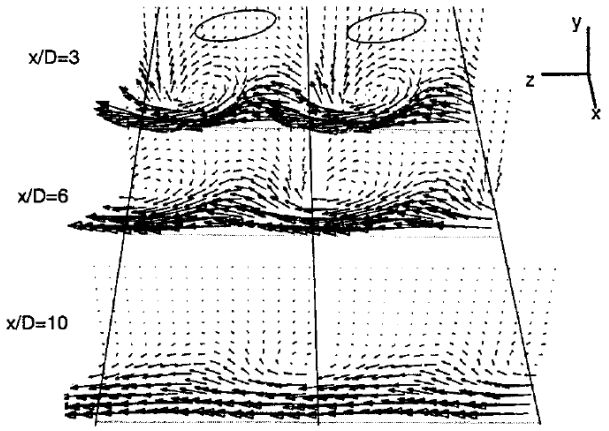

Figure 2-11: Strength velocity vectors with increasing downstream distance for compound angle equals to 60 degrees and blowing ratio equals to 1.25 (McGovern & Leylek 2000).

Non-dimensional temperature contours results supported the above stated observations. From these results it was seen that the single vortex structure convectively mixes the coolant and the mainstream flow which leads to a relatively uniform lateral distribution of temperature as the coolant moves further downstream.

From laterally averaged adiabatic effectiveness results, as the blowing ratio and compound angle is varied, it was noted that the were lower adiabatic effectiveness values in the near field. It is reported that these are due to a narrower attached region as the compound angle is increased.

Further downstream it was seen that increasing the compound angle resulted in an increase in the adiabatic effectiveness. It was reported that this is due to the coolant core being convected and diffused towards the surface more quickly as the compound angle is varied.

2.9.3.A detailed analysis of film cooling physics: Part 3 - Streamwise injection with shaped holes (Hyams & Leylek 2000)

The model comprised of a plenum as the supply to shaped film cooling holes oriented in the freestream direction. The shapes tested were cylindrical, forward diffused, laterally diffused, inlet-shaped and cusp shaped. This literature review will only focus on the behaviour reported for the first three (3) shapes. Tests were done on a film cooling hole with length to diameter ratios equals to four (4), and two (2) blowing ratios of 1.25 and 1.88. The density ratio was equals to 1.6 and the injection angle of the holes was 35 degrees.

At the entrance to the film hole, it was observed that for the forward diffused and laterally diffused holes, the same mechanisms exist as for the cylindrical shaped hole. These are reported in section 2.9.1. Additionally, differences in flow behaviour between the three (3) geometries only started at the diffusing sections of the holes, for the holes with expanded exits.

As was stated in section 2.9.1. the longitudinal vortices are the most dominant in determining film cooling performance and the vorticity from the film hole boundary layer controls the strength of these vortices in the case of streamwise aligned holes. Therefore, the effect of the different geometries on these vortices is reported.

Results for the forward diffused geometry show that the forward expansion decreases the effective velocity of the coolant jet on exit. Further to this, the interaction with the crossflow, due to less of a pressure gradient across the hole exit (caused by the decrease in effective exit velocity), results in a decrease in the flow exit angle of the jet. This leads to two (2) findings

that significantly affect the strength of the longitudinal vortices and hence the downstream behaviour of the coolant jet.

Firstly, the decreased y-momentum content of the jet results in less penetration into the crossflow which positions the coolant jet, on exit, closer to the wall. As stated in section 2.9.1., the wall is destructive to streamwise vorticity. Secondly, it decreases a component of the vorticity in the film hole boundary layer. This decrease is due to the relaxed velocity gradients near the sidewalls afforded by the area expansion. This results in a decrease in the streamwise vorticity strength.

The decreased strength of the streamwise vorticity results in weak longitudinal vortices/secondary flows. This results in minimised induction lift, as compared to the cylindrical case. This allows the coolant, as it moves downstream, to remain firmly attached to the surface. However, it was observed that, for the forward diffused hole, the difference in lateral spread was negligible, as compared to the cylindrical case.

Similar mechanisms, as for the forward diffused shape, determine the weakened strength of the film hole boundary layer vortices for the laterally diffused geometry, as compared to the cylindrical hole.

The increased performance of the laterally diffused geometry, as compared to the forward diffused shape, is due to the vortices emanating from the film hole boundary layer (streamwise aligned vortices) being located farther apart from each other as they exit the hole. This is due to the lateral expansion. This results in decreased strength of the longitudinal vortices which reduces the induction lift and the convective strength of the secondary flow at the centreline.

Regarding turbulence levels, for the shaped geometries, turbulence generation becomes a dominant film cooling mechanism, downstream of the jet-crossflow interaction zone. This difference in behaviour, as compared to the cylindrical hole, is due to the large mismatch in exit velocity created by the shaped geometries. The turbulence contributes significantly to the dissipation of the coolant in the far-field.

It is reported that as the coolant moves downstream significant amounts of turbulence are generated throughout the film for the shaped geometries, as compared to the cylindrical geometry. This is due to strong mixing at the film-crossflow interface and mixing throughout the film itself.

Shown in Figure 2-12(a) is the temperature footprint of the film cooling hole configurations reported and in Figure 2-12(b) are the laterally averaged adiabatic effectiveness results.

It is reported that the cylindrical hole performs the least in terms of effectiveness and lateral spread, as compared to the forward diffused and the laterally diffused film cooling geometries. The forward diffused geometry performs very well along the centreline as compared to the cylindrical geometry. The laterally diffused geometry outperforms the other hole geometries with very high effectiveness values along the centreline, and impressive lateral spread and overall coverage of the test surface.

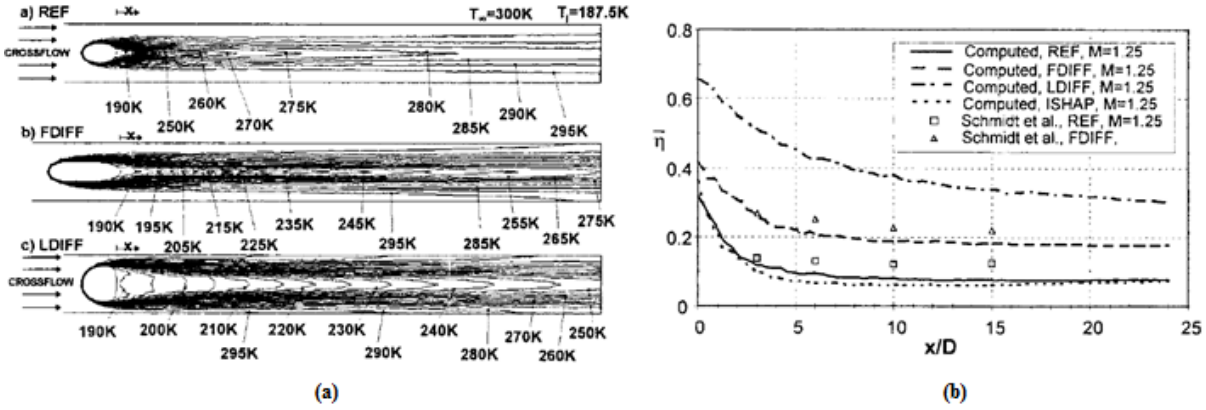

Figure 2-12: Effectiveness results downstream of hole exit. a) temperature footprint, b) laterally averaged adiabatic effectiveness (Hayms & Leylek 2000).

It is reported that the good performance of the laterally diffused hole geometry is partly due to its low trajectory and wide breadth. The low trajectory results in the coolant being effectively injected into the mainstream flow boundary layer and remaining in the boundary layer until dissipated by diffusion mechanisms downstream. The wide breadth results in the vortex cores being spread apart in the lateral direction, which weakens induction lift.

2.9.4.A detailed analysis of film cooling physics: Part 4 - Compound angle injection with shaped holes (Brittingham & Leylek 2000)

The model comprised of a plenum as the supply to cylindrical, forward and laterally diffused film cooling geometries. The cylindrical hole compound angle was in the direction of the freestream. The compound angles of the laterally diffused and forward diffused holes was 45 and 60 degrees to the freestream direction, respectively. Tests were done on a film cooling hole with length to diameter ratios equals to four (4), and two (2) blowing ratios of 1.25 and 1.88. The density ratio was equals to 1.55 and the injection angle of the holes was 35 degrees.

The variation in compound angle does not change the physical mechanisms at the entrance of the film holes. These are discussed in section 2.9.1. The relative strength of the physical mechanisms discussed below is strongly dependent on the blowing ratio increasing with it.

Slight differences at the diffused sections of the expanded holes are observed, but they are reported to have little effect on the jet exit conditions. As with the cylindrical holes, differences are observed at the exit, as compared to the streamwise case, because of significant changes in the pressure distribution at the hole exit. The changes in the way the pressure is distributed results in higher blockage at the hole exit. This leads to deviations of the coolant trajectory after it leaves the film hole.

As with the cylindrical geometries, in compound angle injection for the shaped geometries, as compared to streamwise injection, the vorticity generated at the interface plays a significant role in the vortex structure downstream of hole exit. The vortex structure downstream of the hole exit, in compound angle injection, is strongly dependent on the compound angle. As the compound angle is increased, the originally symmetric counter-rotating vortex structure becomes increasingly asymmetric because of a weakening of one (1) of the vortices in the pair and the strengthening of the other. The weakening of the one (1) vortex in the pair is caused by crossflow blockage of the film hole boundary layer that comes into initial contact with the crossflow. The strengthening of the other vortex in the pair is due to shear between the crossflow and the jet.

The differences in the vorticity for the different shapes and compound angles is due to the differences in the strength of the vorticity emanating from the film hole boundary layer (was determined to be a strong function of shape) and the differences in strength of the vortices generated by jet-crossflow shearing (was determined to be a strong function of compound angle). The combined effects of the hole geometry and compound angle determines the strength of the longitudinal vorticity which determines the film cooling performance downstream of the hole exit. But it is reported that the behaviour cannot be predicted using the superposition principles.

3.Experimental set-up, method and data reduction

3.1.Introduction

The purpose of this chapter is to describe the experimental facility used to measure the discharge coefficient, the coolant jet flow distribution and temperature field as the coolant jet interacts with the mainstream, and the adiabatic film-cooling effectiveness on the endwall characteristics of the different film cooling hole geometries. Included are also the film cooling hole geometries, the instrumentation used for measurement and data capturing and an experimental uncertainty analysis.

3.2.Experimental set-up

Discharge coefficient, flowfield, temperature field and effectiveness measurements were acquired in a low speed open loop wind tunnel shown in Figure 3-1.The facility has two major systems, namely the mainstream and the coolant supply systems.

The mainstream flow was driven by a 2.2 kW axial fan. Atmospheric air was drawn into the tunnel through a flow straightener. The flow contracts (cross-sectional area contraction ratio equals to 3.33:1) to supply velocities up to 16 m/s in the test section; a pitot static probe placed in the freestream was used to determine the velocity. The cross-sectional area at the test section was 375 mm x 700 mm.

After the contraction, the boundary layer was bled (1500 mm from the upstream edge of the cooling holes) into a suction plenum, so that a new boundary layer could develop along the flat wall. Turbulence was induced into the flow 600 mm from the upstream edge of the cooling holes. The design of the turbulence grid was based on study by Roach (1987). Based on the study by Roach (1987) the theoretical freestream turbulence intensity induced should be 4.9 percent at the location of hole exit. The grid was constructed with 12 mm diameter rods with rectangular grid size 37.5 mm x 50 mm. Details of the design of the turbulence grid are given in Appendix C.

Approximately 500 mm after the test section the flow is diffused in a two (2) dimensional diffuser (area diffusion ratio equals to 1.23:1) and then flows into a large mainstream plenum (volume equals to 1000 mm x 1000 mm x 1000 mmm). The axial fan is mounted to the plenum box and drives the flow in the tunnel.

The coolant flow was supplied by an experimental FM 42 multistage centrifugal compressor manufactured by Armfield Ltd. The laboratory atmospheric air is compressed in the compressor. On exiting the compressor, the flow expands into a 152 mm internal diameter pipe, flows through a heat exchanger and then into the large coolant plenum-box located at the inlet side of the film-cooling hole. The purpose of the plenum box is to get an even distribution of coolant into the film cooling holes.

The coolant plenum box is trapezoidal in shape with a volume approximately equals to 257 mm x 473 mm x 696 mm. A baffle divides the plenum into two sections, inlet and outlet. The inlet being the coolant from the compressor and the outlet being the entrance to the cooling holes. The baffle helps guide the flow and reduce the effects of flow speed at the coolant hole entrance.

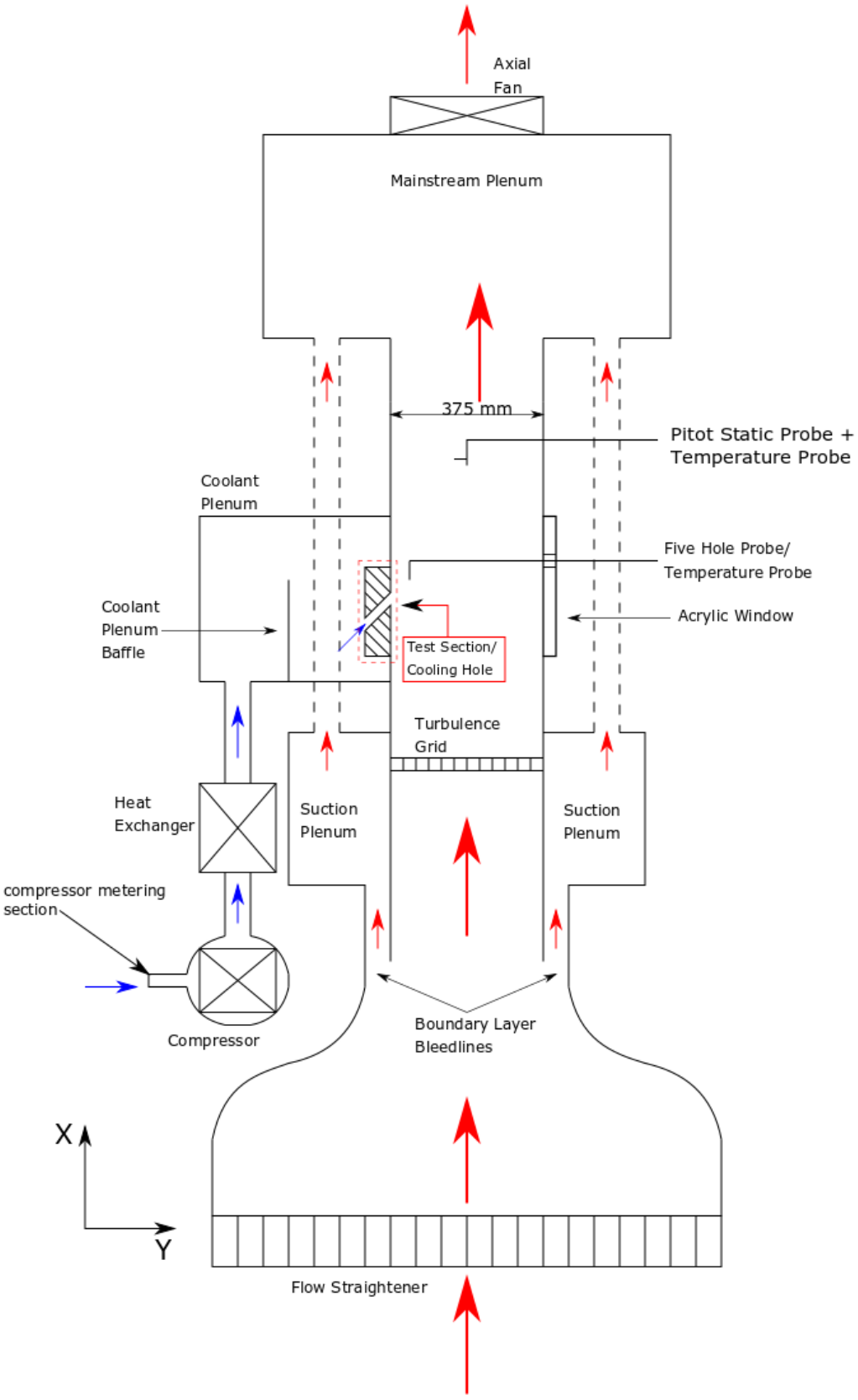

Figure 3-1: Schematic of flat plate end-wall film cooling testing facility.

3.3. Film-cooling hole geometries

Shown in Figure 3-2 are the film cooling hole geometries investigated in this study. They were designed in the CAD software SolidWorks™, and then they were either machined or 3D printed in a commercial three-dimensional printer. All the holes were sharp edged at the inlet and the outlet. A picture of a 3D printed hole is shown in Appendix I.

Figure 3-2(a) and Figure 3-2(b) are the cylindrical and the laidback fan-shaped holes. The aerothermal performances from these geometries have been tested and reported in extant literature, including in Hay and Lampard (1995), Gritsch *et al.* (1998), and Thole *et al.* (1998). These two (2) types of holes serve as the baseline cases for comparison with the other holes. This is of importance because the pressure ratio range tested in this study is not reported in literature. The baseline cases will also be used for comparison against the new shapes investigated in this study.

The hole shapes shown in Figure 3-2 (c-d) were printed in the three-dimensional printer at zero (0) percent porosity and at zero (0) degrees build orientation. To investigate the effects of printing angle on the aerothermal performance, the cylindrical and the laidback fan-shaped holes in Figure 3-2 (a, b) were machined in the CNC milling machine as well as printed in the three-dimensional printer with zero (0) percent porosity. All the printings used the standard ABS plastic filament. Further details of each hole geometry are given below.

The hole geometry in Figure 3-2(a) is a cylindrical hole with a diameter of 8 mm and length to diameter ratio equals 7.5. A length to diameter ratio greater than two (2) ensures that the coolant jet, after the separation at the inlet, reattaches to the walls before ejecting into the mainstream (Lichtarowicz *et al.* 1965; Hay & Lampard 1995). The inclination angle of the hole is 30 degrees relative to the endwall surface. A machined piece and a 3D printed piece were manufactured and tested. The purpose being to determine the effect of manufacturing method. The 3D printing build orientation for the cylindrical hole was such that the cross-sectional area plane of the cylinder was parallel to the printer bed. This is discussed in more detail in Appendix E. In the rest of the report it will be called ‘60 degrees print orientation’. The relative surface roughness of the machined and 3D printed hole was 0.003 and 0.0165, respectively.

The design of the laidback fan-shaped hole in Figure 3-2(b) is based on that by Schroeder and Thole (2014); the 7-7-7 shaped hole. It has a lateral expansion, on both sides, of seven (7) degrees and a forward expansion angle of seven (7) degrees. In the rest of the report the student will either refer to this hole geometry as laidback fan-shaped hole or diffused hole. The diameter of the cylindrical portion of the hole is 8 mm and the length to diameter ratio of the cylindrical portion (metering section) is 3.75 (half the length to diameter of the whole hole). The inclination angle of the holes is 30 degrees. One (1) machined piece and two (2) 3D printed piece were manufactured and tested. The build orientation of the first 3D printed piece was such that the cylindrical portion of the hole was 30 degrees to the printer bed. In the rest of the report it will be called ‘0 degrees print orientation’. The build orientation of the second 3D printed piece was such that the diffused section was perpendicular to the printer bed. This is discussed in more detail in Appendix E. In the rest of the report it will be referred to as ‘67 degrees print orientation’. The relative surface roughness of the first and second 3D printed hole was 0.0165 and 0.00525, respectively.

It was determined in this study that the build orientation had little effect on the discharge coefficient behaviour. The discharge coefficient results for the cylindrical and the laidback fan-shaped holes are provided in the next chapter for illustration. It was then decided that the remainder of the holes be 3D printed at a zero (0) degrees print/build orientation.

The hole geometry in Figure 3-2(c) has a lateral expansion, on both sides, of 3.46 degrees and a forward expansion angle of seven (7) degrees. A curvature has been employed on the upstream edge of the hole, in diffused section, and on the downstream edge of the hole, in the forward expansion direction. The radius of the arc is 193.88 mm. The diameter of the cylindrical portion of the hole is 8 mm and the length to diameter ratio of the cylindrical portion (metering section) is 3.75; half the length to diameter of the entire hole. This piece could not be machined, was only 3D printed, because of the arcs. In the rest of the report the student will refer to this hole geometry as ‘Case 1’.

The hole geometry of Figure 3-2(d) is similar to that of Figure 3-2(c), the difference being that the curvature on the upstream edge of the hole, in the diffused section, has been replaced with a straight edge. It has a lateral expansion on both sides of 8.21 degrees and a forward expansion angle of seven (7) degrees. A curvature has been employed on the downstream edge of the hole, in the forward expansion direction. The radius of the arc is 193.88 mm. The diameter of the cylindrical portion of the hole is 8 mm and the length to diameter ratio of the cylindrical portion (metering section) is 3.75; half the length to diameter of the entire hole. This piece could not be machined, was only 3D printed, because of the arcs. In the rest of the report the student will refer to this hole geometry as ‘Case 2’.

The hole geometry of Figure 3-2(e) has an inclination angle of 40 degrees, which changed the length to diameter ratio of the hole to approximately 5.83. The diameter of the cylindrical portion of the hole is 8 mm. It has a lateral expansion, on both sides, of 4.63 degrees and a forward expansion angle of seven (7) degrees. A curvature has been employed on the upstream edge of the hole, in diffused section, and on the downstream edge of the hole, in the forward expansion direction. The radius of the arc is 136.01 mm. This piece could not be machined, was only 3D printed, because of the arcs. The purpose of this hole is to determine the effect of inclination angle. In the rest of the report the student will refer to this hole geometry as ‘Case 3’.

The hole geometry of Figure 3-2(f) has an inclination angle of 40 degrees and a length to diameter ratio of approximately 5.83. The diameter of the cylindrical portion of the hole is 8 mm. It has a lateral expansion, on both sides, of 10.21 degrees. A curvature has been employed on the upstream edge of the hole, in diffused section, and on the downstream edge of the hole, in the forward expansion direction. The radius of the arc on the upstream edge is 136.01 mm. The forward expansion arc was extended beyond the seven (7) degrees angle used in the geometry of Figure 3-2(e) to a distance of 52.80 mm. This piece could not be machined, was only 3D printed, because of the arcs. In the rest of the report the student will refer to this hole geometry as ‘Case 4’.

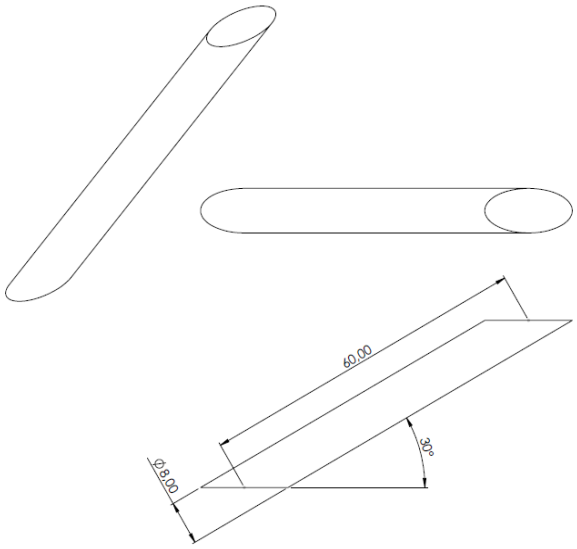

(a)

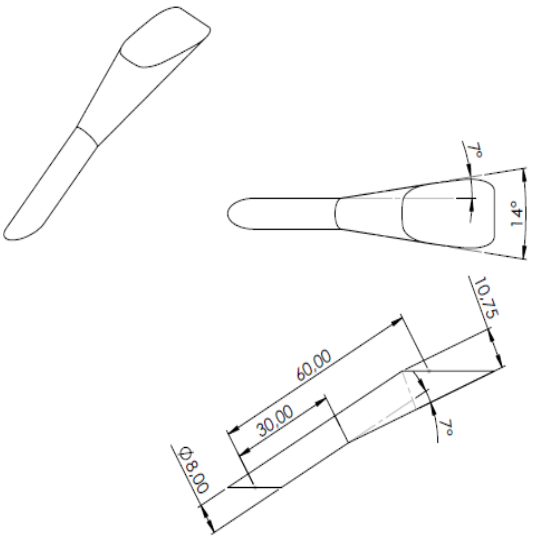

(b)

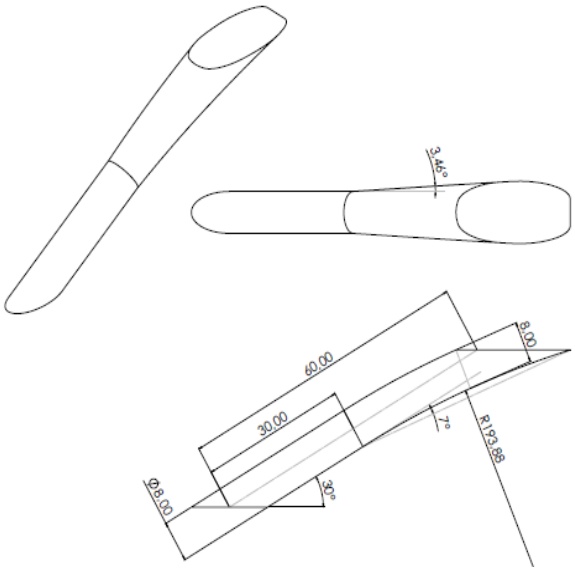

(c)

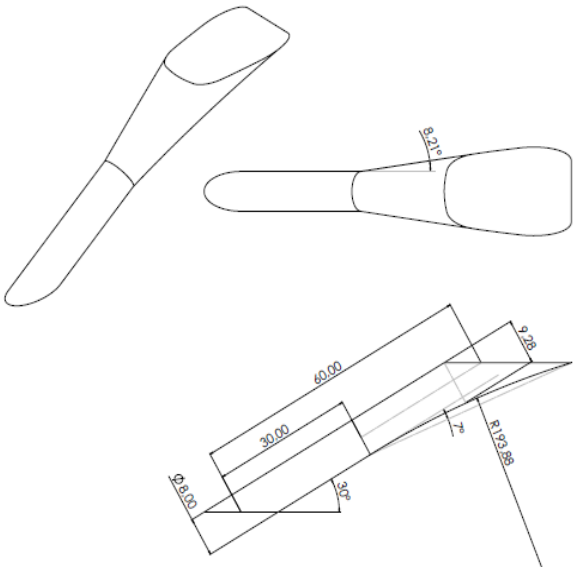

(d)

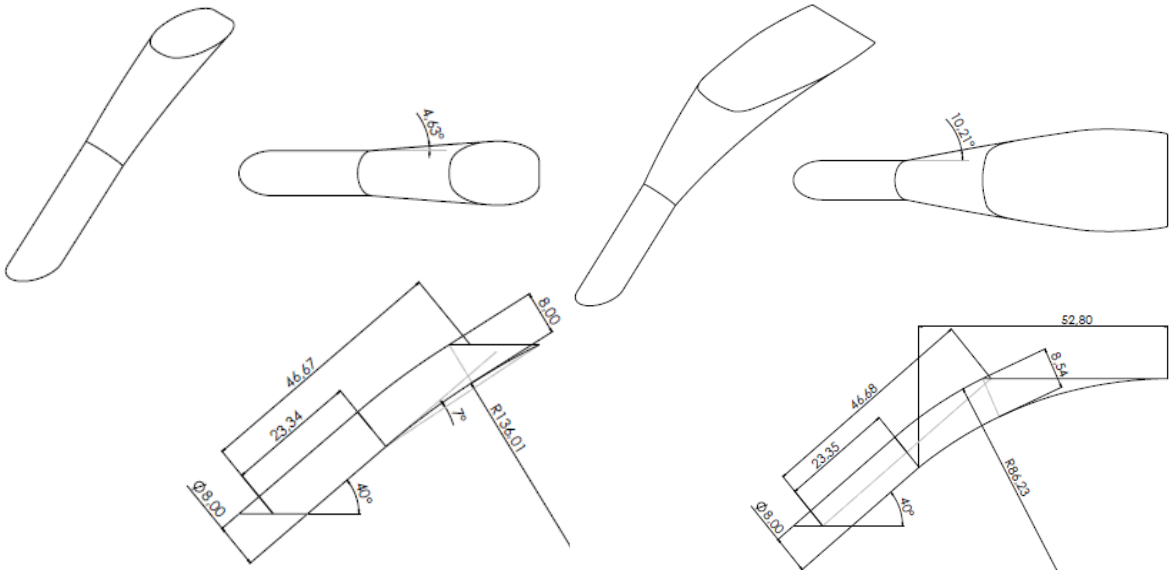

(e) (f)

Figure 3-2: Film cooling hole geometries investigated in this study. a) cylindrical hole, b) laidback fan-shaped hole, c) case 1 hole, d) case 2 hole, e) case 3 hole, f) case 4 hole. Dimensions are in millimetres.

Table 3-1 summarises the geometric parameters stated above.

Table 3-1: Hole geometric parameters (refer to Figure 3-2).

	Cylindrical Hole	**Laidback fan-shaped/ diffused hole**	**Case 1**	**Case 2**	**Case 3**	**Case 4**
Inclination angle	30 degrees	30 degrees	30 degrees	30 degrees	40 degrees	40 degrees
Metering length-to-diameter ratio	N/A	3.75	3.75	3.75	2.92	2.92
Length-to-diameter ratio	7.5	7.5	7.5	7.5	5.83	5.83
Forward expansion angle	N/A	7 degrees	N/A (curvature radius 193.88)	N/A (curvature radius 193.88)	N/A (curvature radius 136.01)	N/A (curvature radius 86.23)
Lateral expansion	N/A	7 degrees	3.46 degrees	8.21 degrees	4.63 degrees	10.21 degrees
Radius of Upstream	N/A	N/A	193.88 mm	N/A	136.01 mm	86.23 mm

edge curvature						
Radius of downstream edge curvature	N/A	N/A	193.88 mm	193.88 mm	136.01 mm	N/A

Table 3-2 summarises the relative surface roughness of the holes. The surface roughness was measured using 'Testex replica tape' and a micrometric dial thickness gage.

Table 3-2: Relative surface roughness of hole geometries.

	Machined	**3D Printed (0 degrees print orientation)**	**3D Printed (60 degrees print orientation)**	**3D Printed (67 degrees print orientation)**
Relative Surface Roughness	0.003	0.0165	0.00525	0.00525

Table 3-3 shows is a matrix of the holes that are investigated in this study.

Table 3-3: Hole geometries investigated in this study.

	Machined	**3D Printed (0 degrees print orientation)**	**3D Printed (60 degrees print orientation)**	**3D Printed (67 degrees print orientation)**
Cylindrical Hole	X		X	
Laidback fan-shaped/ diffused hole	X	X		X
Case 1		X		
Case 2		X		
Case 3		X		
Case 4		X		

In the study by Timko (1984) a full scale turbine was used for testing. The diameter of the smallest film cooling hole used in the study was 0.36 mm. The diameter of the film cooling holes used in this study was 8 mm. This implies a scaling-up of the dimensions in this study of approximately 22.22. The reason an 8 mm diameter film cooling hole was used in this study is so that the flow structure could be visualized with a probe that has a tip diameter of 2.54 mm.

3.4. End-wall test section

Figure 3-3 shows the top view of the end-wall test section. The area of the test section allowed for two (2) holes to be used for each test. The pitch to diameter ratio between the holes was kept at five (5) diameters, 5D, for all tests. According to Schroeder and Thole (2014) this falls within the range commonly tested in literature.

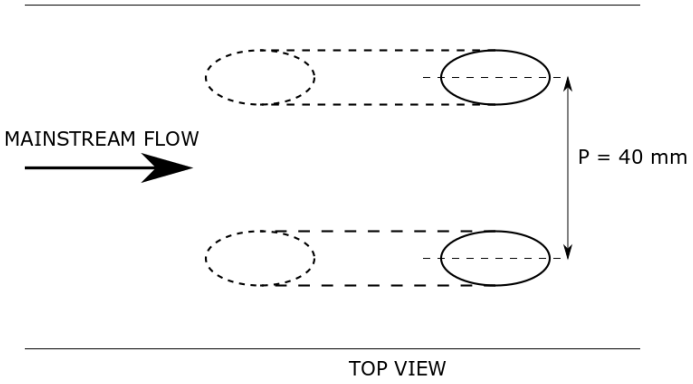

Figure 3-3: Top view of end-wall test section.

Figure 3-4 shows the top view of the test section with the orientation/ compound angle (CA) varied. In this study the compound angle was varied between the range 0–60 degrees, in increments of 10 degrees, to investigate the effect of compound angle. This was done for all film cooling hole geometries. The base plate that facilitates the change in compound angle is shown in Appendix I.

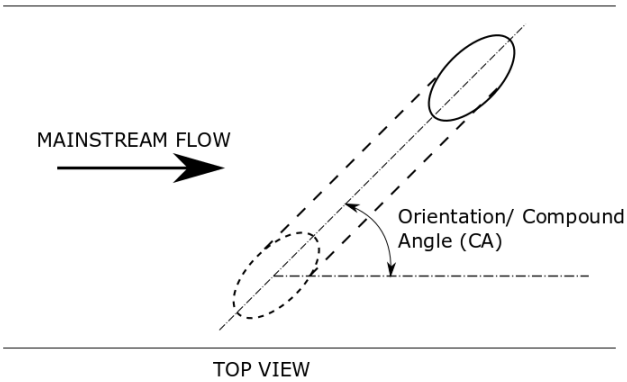

Figure 3-4: Top view of end-wall test section showing varying compound angle.

Figure 3-5 is the side view of the test section with the inclination angle varied. In this study, two (2) inclination angles, 30 & 40 degrees, were used to investigate the effect of inclination angle.

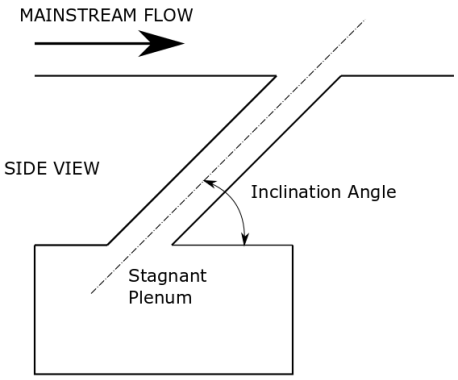

Figure 3-5: Side view of test section showing varying inclination angle.

3.5.Flow parameters

The axial blower generated air velocity up to 16 m/s in the wind tunnel; Mach number approximately equals to 0.047. A pitot static tube and a thermocouple placed in the centre of the tunnel was used to measure the freestream velocity and temperature. The pressure ratio (the ratio of the total pressure inside the plenum box to the static pressure in the mainstream flow) range tested was between 1.004 to 1.014. This limited the flow to the incompressible flow regime; Appendix B. Coolant to mainstream momentum flux ratios less than six (6) were tested. The temperature in the wind tunnel and in the plenum box was around room temperature, 299 K, for the discharge coefficient and flow field measurements. So the density ratio, the ratio of the density of the coolant to that of the freestream, was approximately equals to one (1).

The above flow parameters applied for all configurations tested in this study; unless stated otherwise. These parameters are summarised in Table 3-4.

Table 3-4: Summary of flow parameters in this study.

Parameter	Value
Freestream average velocity	16 m/s
Freestream Mach number	0.047
Pressure ratio range	1.004 – 1.014
Momentum flux ratio	0.5 – 6
Temperature in wind tunnel	299 K
Temperature in plenum box	299 K
Density ratio	1
Induced turbulence (calculated)	4.89%
Velocity boundary layer thickness	4.53

3.6.Instrumentation

3.6.1.Pressure transducers

The Omega PX277-05D5V differential pressure transducer was used to measure the pressure inside the coolant plenum box. The reference pressure for the pressure transducer was

atmospheric conditions. Four (4) pressure tap locations, around the plenum box on the inside surface, were connected to the positive end of the transducer in-order to get an average pressure inside the box. The locations were one (1) pressure tap at the centre of each side of the four (4) walls of the box. This was far enough from the inlet and outlet of the box such that no dynamic components of pressure would be measured. Therefore, this static pressure measurement is equal to the total pressure inside the plenum.

A Pitot-Static probe was used to measure the total and static pressure components inside the tunnel. The probe was located 150 mm downstream of the film cooling holes (see Figure 3-6), with the probe tip positioned in the centre of the tunnel, far from the walls. This was to ensure that only the freestream conditions, which are used as reference in most of the scaling parameters in film cooling studies, are measured.

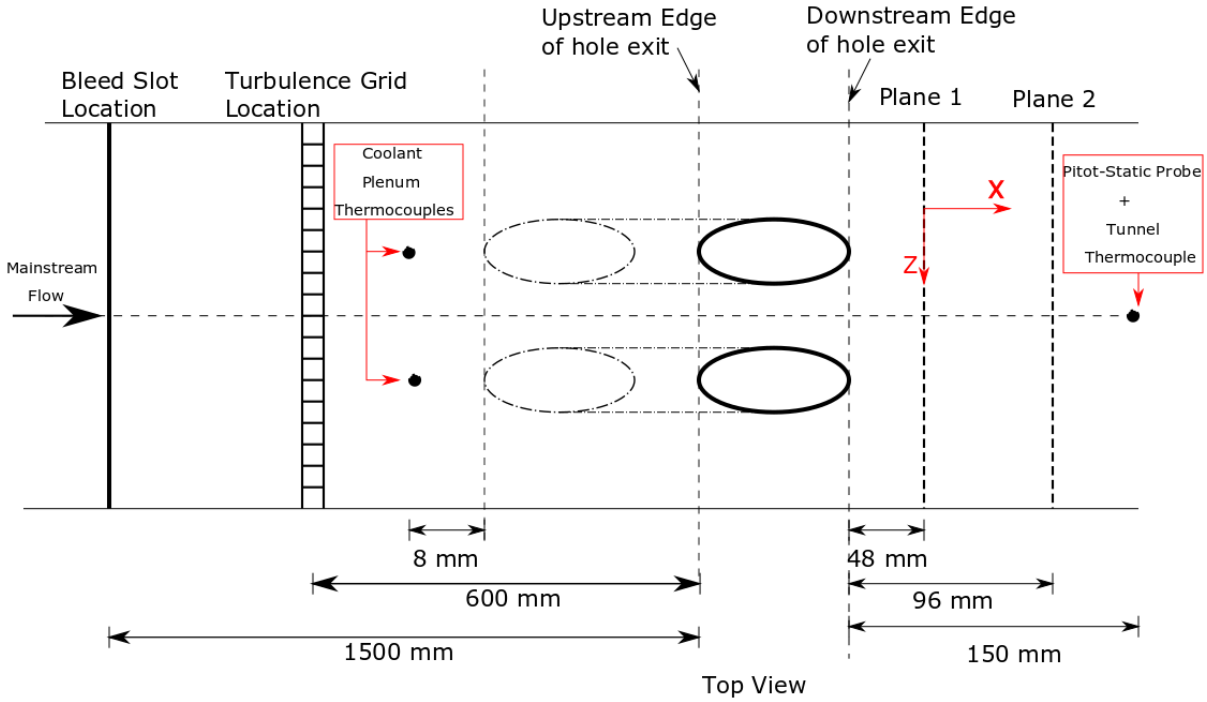

Figure 3-6: End-wall test section showing locations where measurements were taken.

The probe was connected to two (2) Omega PX277-01D5V differential pressure transducers. The reference pressure for the pressure transducers was atmospheric conditions. The connections were on the negative end of the transducers because the pressure measurements inside the tunnel were expected to be less than atmospheric conditions.

A 'five hole probe' with a tip diameter of 2.4 mm was used to measure the three (3) dimensional flow structure in the wind tunnel. Each of the five (5) ports of the probe was connected to an individual Omega PX277-01D5V differential pressure transducer, on the negative end because the reference pressure for the pressure transducers was atmospheric conditions. The pressure inside the tunnel was below atmospheric as the airflow was generated with the suction of the blower. The voltage signals from each of the transducers were recorded at 20 Hz for 3 seconds through the National Instruments™ data acquisition system and time averaged.

A two (2) dimensional motor-controlled traversing system was used to position the probe. The probe started all its runs 2 mm from the wall. This was to minimise the effects of blockage, between the wall and the probe tip, on the pressure measurements. The probe moved an area of 81 mm x 42 mm, in 3 mm increments, to cover both film cooling holes. It stopped at each

position for 30 seconds to record data (this was enough time for the flow to settle after movement). For each parameter, a single data point was recorded at each position. The flow structure was measured in two (2) planes; 48 mm and 96 mm downstream of the film cooling holes (shown as plane 1 and 2 in Figure 3-6). The probe was inserted through a cut-out slot in the top wall on the opposite side of the end-wall test section. Two (2) slots in the top wall were employed at the locations of plane-1 and plane-2 to traverse the probe along the planes. The open part of a slot is covered with the tape liner during measurement.

Details of the calibration process of the transducers are given in Appendix F.

3.6.2. Thermocouples

Two (2) T-type thermocouples were used to measure the temperature of the coolant inside the plenum. As was stated above, two (2) film cooling holes, per test, were used in this study. Therefore, it was one (1) thermocouple for each hole. The thermocouples were positioned 8 mm away from the hole inlet, far enough from the hole inlets to minimise temperature differences caused by the movement of the coolant as it enters the holes (see Figure 3-6).

One (1) T-type thermocouple was placed inside the wind tunnel to measure the temperature of the mainstream. It was positioned along the stem of the Pitot-Static probe, 150 mm downstream of film cooling holes (see Figure 3-6), with the tip far enough into the freestream to minimise effects from the probe stem.

The temperature probe that traversed plane 1 (see Figure 3-6) for the temperature field measurements employed a K-type calibrated thermocouple. The probe started all its runs 0.5 mm from the wall. The probe scanned an area of 36 mm by 24 mm, in 1 mm increments, to cover one (1) film cooling hole. It transmitted the temperature signals to the National Instruments™ data acquisition system. The signals were digitized at 100 Hz for 10 seconds and time averaged. A single Labview™ program was employed to record the temperature data and control the motion of the traverse to move the probe in the measureAment plane.

The probe was built in-house. The construction of the probe has a long metal stem with two needle prongs attached on one end. The two (2) prongs hold the thermocouple tip in the middle space between the prongs. The size of the probe tip is 10 mm. Thermocouple wires run through the hole of the hollow stem and comes out on the other side. Shote (2020) provides further detail on the temperature probe construction.

Thirty-seven (37) T-type thermocouples were used to measure the temperature of the end-wall surface area downstream of the holes. The temperatures from the thermocouples were used for the in-situ calibration of the infra-red thermal image obtained with a FLIR™ thermal camera. Details of the infrared camera calibration process are given in Appendix F.

The positions of the thermocouple tips on the end-wall surface are shown in Figure 3-7. The tips were inserted through drilled holes in the wall and positioned on the flow side in the tunnel. Thermal paste was used to fill-in gaps between the thermocouples and the hole in the wall.

Details of the calibration process of the thermocouples are given in Appendix F.

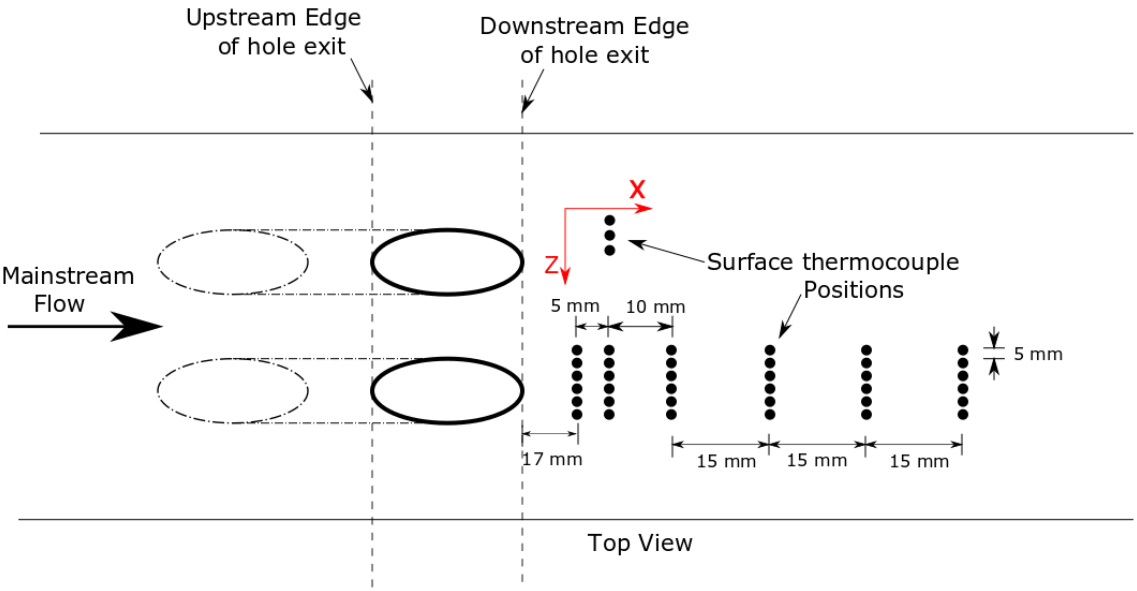

Figure 3-7: End-wall/surface thermocouple positions.

3.6.3.Coolant flow Compressor

As was stated in the experimental set-up the FM42 centrifugal compressor by Armfield™ Ltd was used to supply the coolant line. The compressor is equipped with a calibrated flow metering device (orifice plate) at the inlet, and pressure and temperature sensors.

The quantity of interest from the compressor is the actual mass flow rate, in kilogrammes per second, delivered to the film cooling holes. The manufacturer of the compressor provided a computer program and the interface devices to control the compressor speed and measure and record the pressure ratio, temperature ratio, and flow rate across the compressor.

The software outputs a calculated volume flow rate. The volume flow rate is measured by using the pressure difference across the orifice plate at the inlet; the reference pressure being atmospheric conditions. It is then calculated using the equation (9):

$$Q_v = \frac{C_{d,orifice} \times \pi \times d^2 \times \sqrt{2 \times \rho_{air\_inlet} \times p_0}}{\rho} \quad (9)$$

To convert the volume flow rate to a mass flow rate it is multiplied with the density of the air at the inlet; equation (10):

$$\dot{m}_{actual} = Q_v \times \rho_{air\_inlet} \quad (10)$$

3.6.4.Infrared (IR) Camera

The FLIR™ AX5 infrared camera was used for surface temperature measurements.

3.6.5.Control and data logging

The pressure transducers, thermocouples and the probe traversing system were connected to a personal computer and the software, National Instruments™ Labview, was used for all control and data logging. The compressor is separately controlled with software that comes with the unit. The compressor motor speed is controlled, which allows for control of the flow rate. The software also allows for data logging.

The IR camera software called FLIR™ ResearchIR allowed for control of the camera settings and data logging of infrared images. National Instruments™ Labview was used for data logging of thermocouple surface temperatures.

3.7.Data Reduction

Below the student introduces the parameters/variables used in this study and shows how they are calculated. A more detailed data reduction process is presented in Appendix D.

3.7.1.Discharge coefficient

The discharge coefficient is defined as shown in Equation (11):

$$C_d = \frac{\dot{m}_{actual}}{\dot{m}_{ideal}} \tag{11}$$

The actual mass flow rate is calculated as shown in Equation (12):

$$\dot{m}_{actual} = \left(\frac{Q_v}{2} \times 0.001\right) \times \rho_{air\_inlet} \tag{12}$$

The volume flow rate and the density of air at the inlet are acquired from the compressor software. The volume flow rate is divided by two (2) because the compressor supplies two (2) film cooling holes. It is multiplied by 0.001 to convert the units from litres to cubic meters. The student takes a sample of 10 data points for each calculation. The average of this sample is used in the calculation of the mass flow rate.

The ideal mass flow is defined as shown in equation (13):

$$\dot{m}_{ideal} = A_{hole}\sqrt{2 \times \rho_c \times (P_{tc} - P_{sm})} \tag{13}$$

Substitution of the equations (12) and (13), into equation (11), leads to equation (14):

$$C_d = \frac{Q_v \times \rho_{air\_inlet}}{A_{hole}\sqrt{2 \times \rho_c \times (P_{tc} - P_{sm})}} \tag{14}$$

The coolant density is calculated using the ideal gas law, using state conditions inside the plenum box (see equation (15)):

$$\rho_c = \frac{P_{tc}}{R \times T_{tc}} \tag{15}$$

3.7.2.Outlet Additive Losses Coefficient

The outlet additive losses coefficient is defined by Sasaki *et al.* (1975) as shown in Equation (16):

$$\delta_{out} = \frac{1}{(C_d)^2} - \frac{1}{(C_{d,o})^2} \tag{16}$$

The outlet losses are calculated at data points where the velocities between both cases, with and without mainstream crossflow, match. The student manually matches the velocities. This isolates the losses to those caused by the presence of the mainstream crossflow. Shown in Appendix D is a sample of the process of manually matching velocities.

3.7.3.Pressure Ratio

The pressure ratio (PR) is defined as shown in Equation (17):

$$PR = \frac{P_{tc}}{P_{sm}} \tag{17}$$

3.7.4.Blowing Ratio

The blowing ratio (BR) is defined as shown in Equation (18):

$$BR = \frac{\rho_c \times U_c}{\rho_m \times U_m} \quad (18)$$

The product $\rho_c \times U_c$ is determined using Equation (19):

$$\rho_c \times U_c = \frac{\dot{m}_{actual}}{A_{hole}} \quad (19)$$

The freestream velocity is calculated using Equation (20):

$$U_m = \sqrt{\frac{2(P_{tm} - P_{sm})}{\rho_m}} \quad (20)$$

The freestream density is calculated using Equation (21):

$$\rho_m = \frac{P_{tm}}{R \times T_{tm}} \quad (21)$$

3.7.5.Momentum Flux Ratio

The momentum flux ratio (MFR) is calculated using Equation (22):

$$MFR = \frac{\rho_c \times {U_c}^2}{\rho_m \times {U_m}^2} \quad (22)$$

The momentum flux of the coolant flow is calculated using Equation (23):

$$\rho_c {U_c}^2 = \frac{\left(\frac{\dot{m}_{actual}}{A_{hole}}\right)^2}{\rho_c} \quad (23)$$

3.7.6.Flow structure

The method by Ligrani, Singer and Baun (1989) was used to calibrate the five hole probe and then to decompose the three mean velocity components (Ux, Uy and Uz) and the streamwise vorticity from the actual measurements. The corrections due to the probe spatial dimensions and streamline curvature near the probe body are applied on the measured data following Ligani *et al.* (1989b).

A more detailed description of the five hole probe calibration process and data reduction procedure is given in Appendix F and D, respectively.

3.7.7.Temperature field

A non-dimensionalised temperature parameter was used to present the results. The measured temperature from the probe is normalized using the temperature of the freestream and that of the coolant inside the plenum box. The effectiveness of this parameter is in removing the effects of different temperatures in the freestream and in the plenum box, for comparison purposes. It is calculated as shown in Equation (24):

$$\theta = \frac{T_{probe} - T_c}{T_{tm} - T_c} \quad (25)$$

3.7.8.Adiabatic wall effectiveness

The in-situ method by Sargent, Hedlund and Ligrani (1998) was used for the wall temperature measurements. Using this in-situ procedure the infrared images from the IR camera are calibrated at the same time as measurements are taken by using thermocouples positioned at discrete locations on the surface, which measure the surface temperature. A second or third

order polynomial where surface temperature is a function of grey scale value is then determined for every infrared image. A sample of the calibration curves is shown in Figure 3-8 and the rest are shown in Appendix F. The calibration curves are used to spatially resolve the surface temperature over the entire test surface.

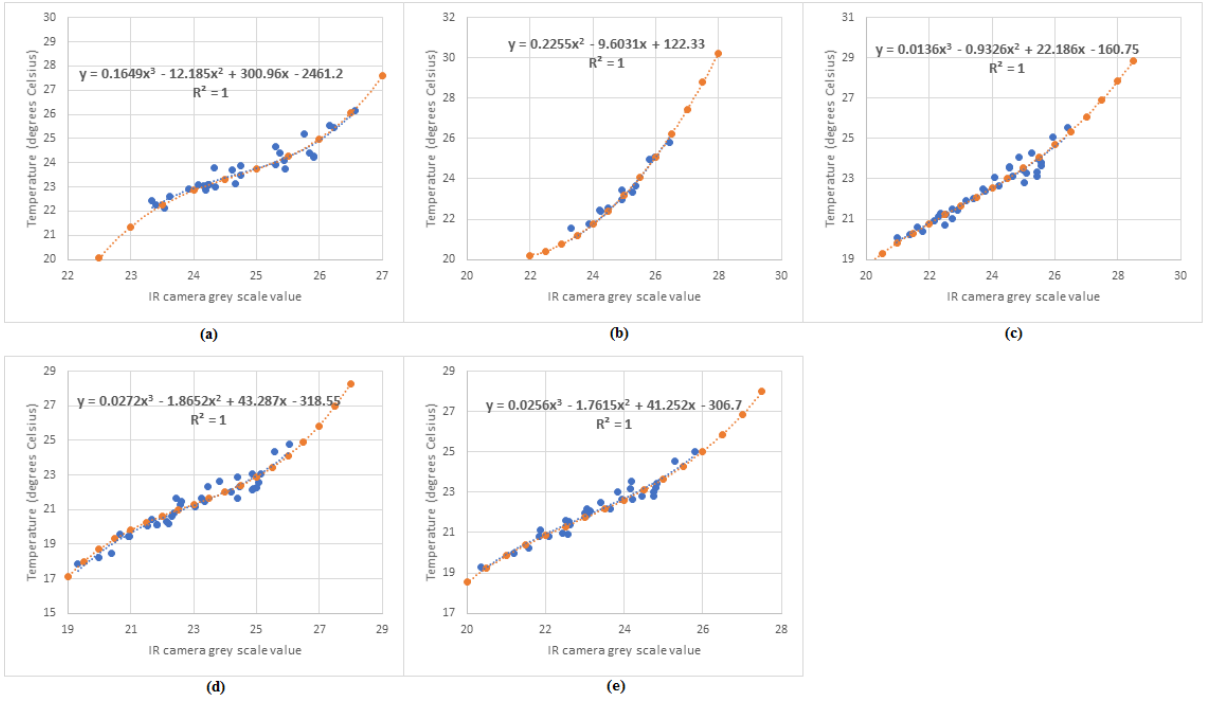

Figure 3-8: IR camera calibration curves for the configuration blowing ratio equals to 0.9 and compound angle equals to zero (0) degrees, without a turbulence grid. a) cylindrical machined hole, b) cylindrical 3D 60 degrees printed hole, c) laidback fan-shaped machined hole, d) laidback fan-shaped 3D zero (0) degrees printed hole, e) laidback fan-shaped 3D 67 degrees printed hole.

The dimensionless parameter, adiabatic film-cooling effectiveness, was used to present the adiabatic wall temperatures. The effectiveness is used to quantify the cooling ability of the different film cooling hole geometries. It is calculated as shown in Equation (26):

$$\eta = \frac{T_{aw} - T_{tm}}{T_c - T_{tm}} \tag{26}$$

The low thermal conductivity of the acrylic test plate minimises heat flux, which creates a nearly adiabatic surface boundary condition (Sargent, Hedlund & Ligrani 1998).

3.8. Experimental Procedure

3.8.1. Discharge Coefficient

The compressor speed was increased until the compressor pressure overcomes the system resistance. This was noted as the point when a relatively steady flow rate reading was observed.

The tunnel was run for a few minutes, until the flow rate, pressure and temperature readings relatively settled, before measurements were recorded. One (1) hundred pressure and temperature samples and ten (10) flow rate and density samples were recorded in ten (10) seconds. The average of these sample was used in the calculation of the parameters mentioned above.

To get the discharge coefficient behaviour with an increase in flow rate, the pressure ratio was increased by increasing the compressor speed by one (1) percent increments.

3.8.2.Flow field Measurements

Flow structure measurements were taken on two (2) planes (see Figure 3-1 and Figure 3-6). Plane 1 was six (6) diameters downstream of the hole exit downstream edge and Plane 2 was twelve (12) diameters downstream of the hole exit downstream edge. This helps determine how the coolant flow develops as it travels further downstream from the film cooling hole exit.

The Omega PX277-05D5V differential pressure transducer was used to measure the pressure inside the coolant plenum box. The reference pressure for the pressure transducer was atmospheric conditions. Four (4) pressure tap locations, around the plenum box on the inside surface, were connected to the positive end of the transducer in-order to get an average pressure inside the box. The locations were one (1) pressure tap at the centre of each side of the four (4) walls of the box. This was far enough from the inlet and outlet of the box such that no dynamic components of pressure would be measured. Therefore, this static pressure measurement is equals to the total pressure inside the plenum.

A Pitot-Static probe was used to measure the total and static pressure components inside the tunnel. The probe was located 150 mm downstream of the film cooling holes (see Figure 3-1 and Figure 3-6), with the probe tip positioned in the centre of the tunnel, far from the walls. This was to ensure that only the freestream conditions, which are used as reference in most of the scaling parameters in film cooling studies, are measured.

The probe was connected to two (2) Omega PX277-01D5V differential pressure transducers. The reference pressure for the pressure transducers was atmospheric conditions. The connections were on the negative end of the transducers because the pressure measurements inside the tunnel were expected to be less than atmospheric conditions.

A ‘five hole probe’ was used to measure the three (3) dimensional flow structure in the wind tunnel. Each of the five (5) ports of the probe was connected to an individual Omega PX277-01D5V differential pressure transducer, on the negative end because the reference pressure for the pressure transducers was atmospheric conditions.

A two (2) dimensional motor-controlled traversing system was used to position the probe. The probe started all its runs 2 mm from the wall. This was to minimise the effects of blockage, between the wall and the probe tip, on the pressure measurements. The probe moved an area of 81 mm x 42 mm, in 3 mm increments, to cover both film cooling holes. It stopped at each position for 30 seconds to record data (this was enough time for the flow to settle after movement). For each parameter, a single data point was recorded at each position.

Two (2) blowing ratios, 0.9 and 1.3, and two (2) compound angles, 0 degrees and 20 degrees, with and without a turbulence grid were investigated. The two (2) blowing ratios are classified as low and high blowing ratios.

Tests were only done on the 3D printed film cooling holes. This is because it was determined, from the discharge coefficient results (see Chapter 4), that the manufacturing method and 3D print build orientation have a negligible effect.

The data was processed on the software called Tecplot™.

3.8.3.Temperature field Measurements

Temperature field measurements were taken on one (1) plane (see Figure 3-1 and Figure 3-6). Plane 1 was six (6) diameters downstream of the hole exit downstream edge. Two (2) blowing ratios, 0.9 and 1.1, and two (2) compound angles, 0 degrees and 20 degrees, with and without a turbulence grid were investigated. The two (2) blowing ratios are classified as low and high blowing ratios. This agrees with extant literature. Tests were only done on the

3D printed film cooling holes. This is because it was determined, from the discharge coefficient results (see Chapter 4), that the manufacturing method and 3D print build orientation have a negligible effect.

A heat exchanger, connected to the coolant line (see Figure 3-1), was used to drop the temperature of the coolant in the plenum box to an average of 18 degrees Celsius. This resulted in a density ratio of approximately 1.05; the density ratio defined as the density of the coolant in the plenum box to the density of air in the freestream.

Two (2) T-type thermocouples were used to measure the temperature of the coolant inside the plenum. As was stated above, two (2) film cooling holes, per test, were used in this study. Therefore, it was one (1) thermocouple for each hole. The thermocouples were positioned 8 mm away from the hole inlet, far enough from the hole inlets to minimise temperature differences caused by the movement of the coolant as it enters the holes (see Figure 3-6).

One (1) T-type thermocouple was placed inside the wind tunnel to measure the temperature of the mainstream. It was positioned along the stem of the Pitot-Static probe, 150 mm downstream of film cooling holes (see Figure 3-6), with the tip far enough into the freestream to minimise effects from the probe stem.

The temperature probe that traversed the tunnel for the temperature field measurements was a K-type thermocouple. The probe started all its runs 0.5 mm from the wall. The probe moved an area of 36 mm x 24 mm, in 1 mm increments, to cover one (1) film cooling hole. It stopped at each position for 10 seconds to record data. For each parameter, a single data point was recorded at each position.

The data was processed on the software called Tecplot™.

3.8.4. Adiabatic film-cooling effectiveness measurements

Adiabatic film cooling effectiveness measurements were taken at three (3) blowing ratios, 0.6, 0.9 and 1.1, and three (3) compound angles, zero (0), 20 and 40 degrees, with and without a turbulence grid.

Tests were initially done on all film cooling holes to determine whether the manufacturing method and the build orientation influenced the effectiveness.

A heat exchanger, connected to the coolant line (see Figure 3-1), was used to drop the temperature of the coolant in the plenum box to an average of 18 degrees Celsius. This resulted in a density ratio of approximately 1.05; the density ratio defined as the density of the coolant in the plenum box to the density of air in the freestream.

The FLIR™ AX5 infrared camera was used to measure the wall temperature of the entire test section. Downstream of the film cooling holes, on the test section, the acrylic plate was painted with black paint in order to increase the emissivity of the surface. The camera views each test section through a zinc—selenide window.

For each test the flow was allowed 10 minutes to settle and then measurements were taken. The flow was deemed settled when changes in surface temperature were less than 0.1 degrees Celsius. Surface temperatures at discrete locations (see Figure 3-7) were then recorded using the National Instruments™ Labview program and infrared images of the entire test surface were recorded using the FLIR™ ResearchIR program.

The data was plotted on the software called Tecplot™.

Laterally averaged effectiveness values were obtained by averaging the effectiveness values across the bottom hole. The average was calculated using the bottom hole because it was

determined that the coolant ejects at a lower temperature from the bottom hole. This is shown in chapter 7.

3.9. Summary of tests done

Table 3-5 summarizes all the tests done in this study.

Table 3-5: Summary of tests done.

Test Case No.	Test conditions										Measurement obtained
	Film cooling geometry	Compound angle	Coolant flowrate, l/s		Compressor flowrate, l/s		Temperature coolant	Blowing ratio	Ratio of coolant temperature and mainstream temperature	%turbulence intensity based on Roach	
N/A	Cylindrical Machined	0 to 60 degrees	Without turbulence grid:	With turbulence grid:	Without turbulence grid:	With turbulence grid:	= 28 degrees Celsius without heat exchanger,	0.6,	= 1 without heat exchanger,	4.87%with turbulence grid	Discharge coefficient, velocity and streamwise vorticity, non-dimensional temperature field and adiabatic effectiveness
			0.45,	0.33,	0.905,	0.66,	= 18 degrees Celsius with heat exchanger	0.7,	= 0.97 with heat exchanger		
			0.53,	0.39,	106,	0.774,		0.9,			
			0.76,	0.5,	151	0.995,		1			
			0.68,	0.56,	13572,	111,		11,			
			0.83,	0.61,	1659,	122,		13			
			0.98	0.72	196	144					
N/A	Cylindrical 3D 60 degrees print	0 to 60 degrees	Without turbulence grid:	With turbulence grid:	Without turbulence grid:	With turbulence grid:	= 28 degrees Celsius without heat exchanger,	0.6,	= 1 without heat exchanger,	4.87%with turbulence grid	Discharge coefficient, velocity and streamwise vorticity, non-dimensional temperature field and adiabatic effectiveness
			0.45,	0.33,	0.905,	0.66,	= 18 degrees Celsius with heat exchanger	0.7,	= 0.97 with heat exchanger		
			0.53,	0.39,	106,	0.774,		0.9,			
			0.76,	0.5,	151	0.995,		1			
			0.68,	0.56,	13572,	111,		11,			
			0.83,	0.61,	1659,	122,		13			
			0.98	0.72	196	144					
N/A	Laidback fan-shaped machined	0 to 60 degrees	Without turbulence grid:	With turbulence grid:	Without turbulence grid:	With turbulence grid:	= 28 degrees Celsius without heat exchanger,	0.6,	= 1 without heat exchanger,	4.87%with turbulence grid	Discharge coefficient, velocity and streamwise vorticity, non-dimensional temperature field and adiabatic effectiveness
			0.45,	0.33,	0.905,	0.66,	= 18 degrees Celsius with heat exchanger	0.7,	= 0.97 with heat exchanger		
			0.53,	0.39,	106,	0.774,		0.9,			
			0.76,	0.5,	151	0.995,		1			
			0.68,	0.56,	13572,	111,		11,			
			0.83,	0.61,	1659,	122,		13,			
			0.98,	0.72,	196,	144,		18			
			136	0.995	2.71	199					
N/A	Laidback fan-shaped 3D 0 degrees print	0 to 60 degrees	Without turbulence grid:	With turbulence grid:	Without turbulence grid:	With turbulence grid:	= 28 degrees Celsius without heat exchanger,	0.6,	= 1 without heat exchanger,	4.87%with turbulence grid	Discharge coefficient, velocity and streamwise vorticity, non-dimensional temperature field and adiabatic effectiveness
			0.45,	0.33,	0.905,	0.66,	= 18 degrees Celsius with heat exchanger	0.7,	= 0.97 with heat exchanger		
			0.53,	0.39,	106,	0.774,		0.9,			
			0.76,	0.5,	151	0.995,		1			
			0.68,	0.56,	13572,	111,		11,			
			0.83,	0.61	1659,	122,		13,			
			0.98,	0.72,	196,	144,		18			
			136	0.995	2.71	199					
N/A	Laidback fan-shaped 3D 67 degrees print	0 to 60 degrees	Without turbulence grid:	With turbulence grid:	Without turbulence grid:	With turbulence grid:	= 28 degrees Celsius without heat exchanger,	0.6,	= 1 without heat exchanger,	4.87%with turbulence grid	Discharge coefficient, velocity and streamwise vorticity, non-dimensional temperature field and adiabatic effectiveness
			0.45,	0.33,	0.905,	0.66,	= 18 degrees Celsius with heat exchanger	0.7,	= 0.97 with heat exchanger		
			0.53,	0.39,	106,	0.774,		0.9,			
			0.76,	0.5,	151	0.995,		1			
			0.68,	0.56,	13572,	111,		11,			
			0.83,	0.61	1659,	122,		13,			
			0.98,	0.72,	196,	144,		18			
			136	0.995	2.71	199					
1	1	0 to 60 degrees	Without turbulence grid:	With turbulence grid:	Without turbulence grid:	With turbulence grid:	= 28 degrees Celsius without heat exchanger,	0.6,	= 1 without heat exchanger,	4.87%with turbulence grid	Discharge coefficient, velocity and streamwise vorticity, non-dimensional temperature field and adiabatic effectiveness
			0.45,	0.33,	0.905,	0.66,	= 18 degrees Celsius with heat exchanger	0.9,	= 0.97 with heat exchanger		
			0.68,	0.5,	13572,	0.995,		11,			
			0.83	0.61	1659	122					
2	2	0 to 60 degrees	Without turbulence grid:	With turbulence grid:	Without turbulence grid:	With turbulence grid:	= 28 degrees Celsius without heat exchanger,	0.6,	= 1 without heat exchanger,	4.87%with turbulence grid	Discharge coefficient, velocity and streamwise vorticity, non-dimensional temperature field and adiabatic effectiveness
			0.45,	0.33,	0.905,	0.66,	= 18 degrees Celsius with heat exchanger	0.9,	= 0.97 with heat exchanger		
			0.68,	0.5,	13572,	0.995,		11			
			0.83	0.61	1659	122					
3	3	0 to 60 degrees	Without turbulence grid:	With turbulence grid:	Without turbulence grid:	With turbulence grid:	= 28 degrees Celsius without heat exchanger,	0.6,	= 1 without heat exchanger,	4.87%with turbulence grid	Discharge coefficient, velocity and streamwise vorticity, non-dimensional temperature field and adiabatic effectiveness
			0.45,	0.33,	0.905,	0.66,	= 18 degrees Celsius with heat exchanger	0.9,	= 0.97 with heat exchanger		
			0.68,	0.5,	13572,	0.995,		11			
			0.83	0.61	1659	122					
4	4	0 to 60 degrees	Without turbulence grid:	With turbulence grid:	Without turbulence grid:	With turbulence grid:	= 28 degrees Celsius without heat exchanger,	0.6,	= 1 without heat exchanger,	4.87%with turbulence grid	Discharge coefficient, velocity and streamwise vorticity, non-dimensional temperature field and adiabatic effectiveness
			0.45,	0.33,	0.905,	0.66,	= 18 degrees Celsius with heat exchanger	0.9,	= 0.97 with heat exchanger		
			0.68,	0.5,	13572,	0.995,		11			
			0.83	0.61	1659	122					

3.10.Uncertainty

An uncertainty/error analysis is performed because the true values of measured variables is seldom known, and experiments inherently have errors. These errors are due to instrumentation, data acquisition and reduction limitations, and facility and environmental effects (Stern *et al.* 1999).

The uncertainty analysis was performed on the cylindrical machined holes at a compound angle of zero (0) degrees. The analysis is performed on the discharge coefficient, pressure ratio, blowing ratio and momentum flux ratio. The analysis is detailed in Appendix G.

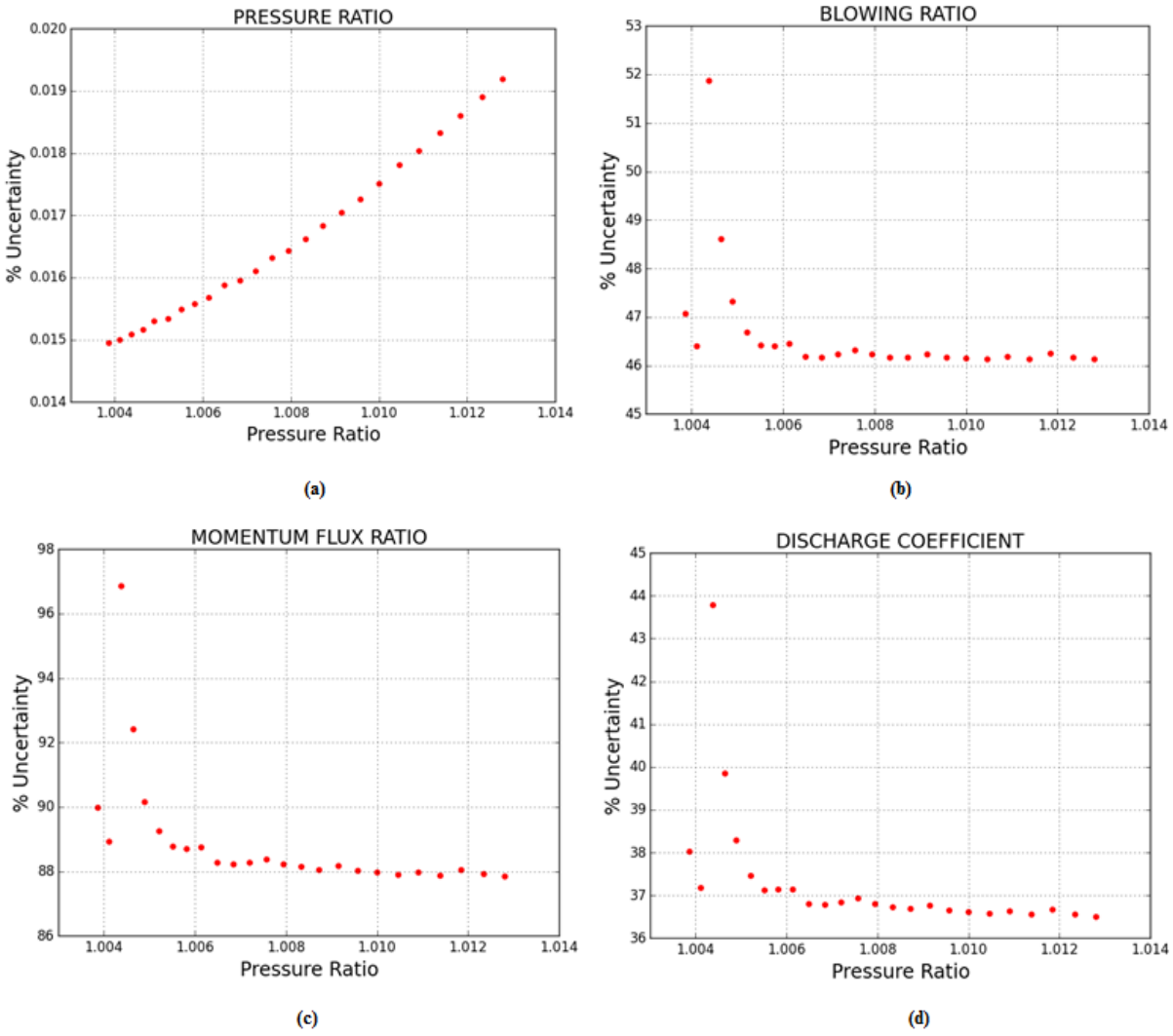

Figure 3-9: Percentage total uncertainty of a) Pressure ratio, b) Blowing ratio, c) Momentum flux ratio, d) Discharge coefficient.

It is seen in Figure 3-9 that the percentage total uncertainty of the pressure ratio is small but increases almost linearly. The total uncertainty is small because the pressure ratio equation is not a function of many variables. This results in less sources of possible errors.

The percentage total uncertainty of the blowing ratio, momentum flux ratio and the discharge coefficient is relatively large. It is, on average, 46%, 88% and 37%, respectively. The contributor to this large uncertainty is the bias error. Therefore, the large total uncertainty is due to the multiple sources of possible errors and their associated large bias/systematic errors. These multiple sources of errors are the pressure transducers and thermocouples. The bias errors of the individual variables propagate in the data reduction equations.

Of importance in this study is the precision uncertainty of the discharge coefficient. The precision error quantifies the scatter of the data. From the precision error we learn the possible range in which the measured variable may lie. It will helps determine whether certain effects can be considered significant or negligible.

Figure 3-10 shows the discharge coefficient as the pressure ratio is increased, with the uncertainty (error bars) on the values. This helps us see how the scatter of the data changes as the pressure ratio is increased. It is seen that the randomness decreases as the pressure ratio increases. The average percentage precision error in the whole pressure ratio range is 5% of the average of the measured variable.

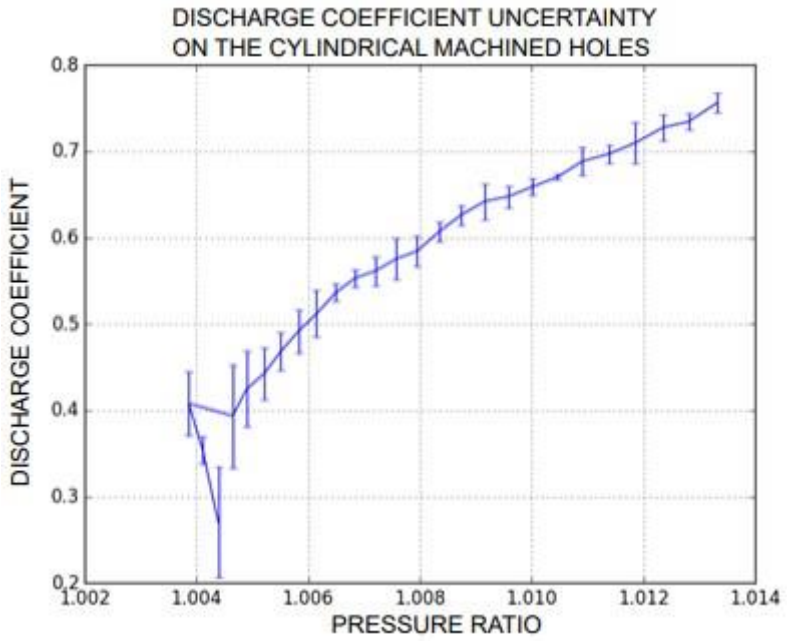

Figure 3-10: Discharge coefficient uncertainty on the cylindrical machined holes.

The average percentage precision error of the discharge coefficient, in the pressure ratio range tested, is 5%.

The uncertainty estimate of the velocity and vorticity, is 8% and 11%, respectively (Shote *et al.* 2020).

The percentage total uncertainty of the non-dimensional temperature parameter is 36.94% and the percentage precision uncertainty is 4.15%. A detailed analysis of the error is shown in Appendix G.

The uncertainty estimate of the adiabatic wall effectiveness is 10% (Shote *et al.* n.d.; Mahmood *et al.* n.d.).

4.Discharge coefficient results and discussion

4.1.Introduction

Results are presented below and discussed in terms of the effects of pressure ratio, mainstream crossflow, compound angle, hole geometry, manufacturing method, 3D print build orientation, and inclination angle on the discharge coefficient. Uncertainty bars were not included in the results presented below because it would be clustered. The uncertainty in the results has been presented in Figure 3-10, and is also discussed in the text for each set of results presented below.

The student systematically evaluates the discharge coefficient behaviour by first analysing the discharge coefficient without mainstream crossflow. By removing the effects of the mainstream flow we isolate the effects of other variables that determine the discharge coefficient behaviour.

Discharge coefficient results with the presence of mainstream flow are then presented and discussed in conjunction with the results without mainstream crossflow. Outlet additive losses coefficient results are then presented and flow structure results (acquired from literature) are included in the discussions to substantiate the discharge coefficient behaviour observed.

The cylindrical and laidback fan-shaped machined holes will be used for model validation and also serve as baseline cases to compare with the new shapes investigated in this study. The pressure ratio range tested in this study has not been reported in previous literature. Therefore, the model is validated by supporting the discharge coefficient behaviours observed with literature that reports the physical mechanisms (flow structure measurements) that govern discharge coefficient behaviour in film cooling.

It should be noted that the laidback fan-shaped hole will, in some cases in the report, be referred to simply as diffused hole. The hole geometries that have curvatures employed will simply be referred to using their case numbers, i.e. Case 1, Case 2, etc. The case numbers for each hole geometry are shown in section 3.3.

It should also be noted that the solid lines used to join the points in all graphs are to help the reader follow the pattern observed. They do not represent a linear relationship between the points that are joined.

4.2.Model Validation & Effect of Compound angle

4.2.1.Cylindrical Machined Film Cooling Holes

Figure 4-2 shows the discharge coefficient results, without mainstream crossflow, as the compound angle is varied, for the cylindrical machined holes. The purpose of testing without mainstream flow is to remove the effects of the mainstream crossflow on the discharge coefficient. This means that we isolate the effects of the other variables on the discharge coefficient.

In this study, for the case of ‘without mainstream crossflow’, the hole outlet was to ambient conditions. The outlet being to ambient conditions, for all compound angles, implies that there is no blockage due to the mainstream flow (no outlet additive losses). Therefore, based on the classification by Rogers and Hersh (1975), it is a high outflow case. This tells us that the discharge coefficient behaviour is determined more by inlet conditions and frictional losses (Rogers & Hersh 1975; Hay, Lampard & Benmansour 1983).

The supply at the inlet is a stagnant plenum. The inclination angle of the holes (30 degrees) causes a large turning angle for the coolant on the downstream edge as it enters the hole. Due to this large turning angle and the sharp edge at the inlet a flow separation region is

expected on the downstream edge at hole entry and is responsible for the losses when the flow enters the hole (Lichtarowicz *et al.* 1965; Pietrzyk *et al.* 1989; Leylek & Zerkle 1993; Thole *et al*. 1997).

Pietrzyk *et al.* (1989) reported that an increase in the blowing ratio resulted in increased turbulence intensity values inside the hole. This confirmed the existence and increase in severity of a separation region at the downstream edge of the hole inlet. The computational study by Leylek and Zerkle (1993) showed that the jet inside the hole is pushed towards the upstream edge of the hole because of the separation region on the downstream edge at the hole entrance. Laser-Doppler velocimeter (LDV) results by Thole *et al.* (1997) proved that a separation zone exists at the downstream edge of the hole entrance and said that the cause is the large turning angle of the coolant on the downstream edge as it enters the hole. This caused the jet to skew to the upstream wall of the hole. Additionally, it was shown that the separation region occurring at the hole inlet produced relatively high turbulence levels.

To clarify the above, the student reminds the reader that, a separation region is expected at the entrance of the film cooling, regardless of the inclination angle (see Figure 4-1(a)). The sharp edge at the inlet together with the inclination angle causes the separation region to shift primarily to the downstream edge of the film cooling hole (see Figure 4-1(b)).

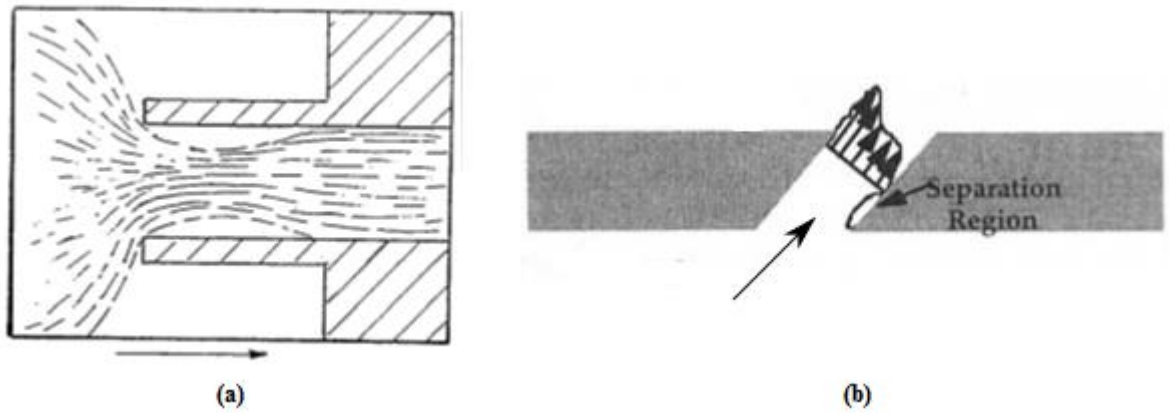

Figure 4-1: a) flow separation in long sharp-edged orifice (based on JSME 1988), b) flow separation in inclined film cooling hole (Thole *et al.* 1997).

Figure 4-2 shows that, for all compound angles, the discharge coefficient is a strong function of the pressure ratio and increases with it. Firstly, this tells us that the same physical mechanisms occur for all compound angles. Secondly, the experiments are being carried out in the low-pressure ratio regime (see Figure 2-6). This agrees with studies by Hay *et al.* (1983), Gritsch *et al.* (1998), and Gritsch *et al.* (2001).

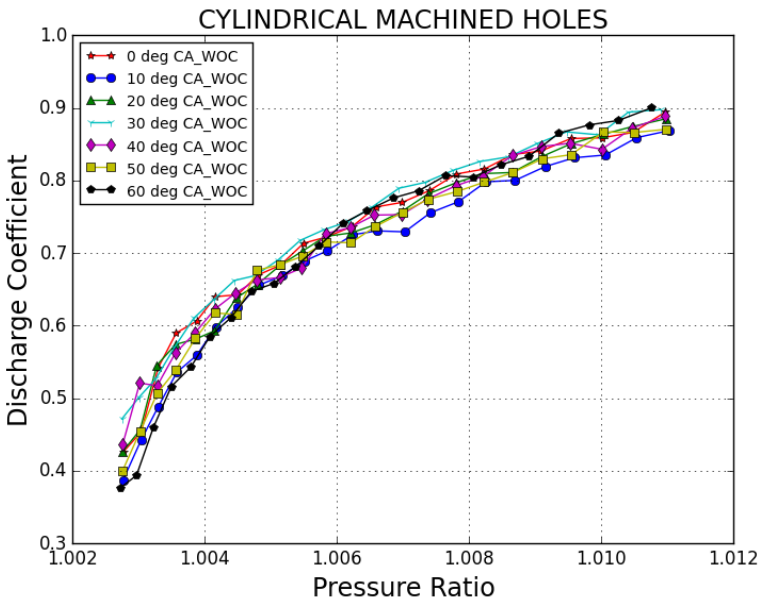

Figure 4-2: Without Mainstream Crossflow (WOC), effect of Pressure Ratio & Compound angle on the Discharge Coefficient of Cylindrical Machined Holes.

Studies by Burd and Simon (1999), Lichtarowicz *et al.* (1965), Andrews and Mkpadi (1984), and Hay and Lampard (1998) showed that the frictional losses inside the hole negligible.

Based on the above it is plausible to conclude that the losses are determined more by inlet conditions. More specifically, the presence of a separation region on the downstream edge of the hole inlet.

The observed increase in the discharge coefficient suggests a decrease in the size of the separation zone at the inlet as the flow rate is increased. This agrees with Rogers and Hersh (1975), where it was reported that the cross-sectional area of the separation decreased as the inflow rate was increased. However, in a study by Rogers and Hersh (1975), the inlet was supplied by a crossflow which resulted in the separation region on the upstream edge of the hole. A study by Rogers and Hersh (1975) is used in this discussion because it is the only study that clearly reported the behaviour of the separation region at the inlet as the flow rate through the hole was increased. In a study by Pietrzyk *et al.* (1989), as the blowing ratio increased, increased turbulence intensity levels were used to confirm an increase in the severity of the separation region.

The results of the studies by Rogers and Hersh (1975), and Pietrzyk *et al.* (1989) appear contradictory. To answer this, it had to be determined ‘what influences the severity of the separation region?’. In a study by Lichtarowicz *et al.* (1965), it was reported that the length of the separation region changes as the Reynolds number is increased. From this the student concluded that the severity of the separation region is influenced by the length of the separation region (the distance between separation and reattachment of the jet to the walls).

In the current study the length to diameter ratio is greater than two (2) for all film cooling test pieces. Consequently, reattachment of the jet is expected (Lichtarowicz *et al.* 1965; Hay *et al.* 1983).

Based on the above the student concludes that the increase in the discharge coefficient, as the flow rate increases, is due to a decrease in the cross-sectional area of the separation region. Thus, the pressure increase in the plenum results in the jet minimum area, inside the hole, opening more and allowing more flow to pass through. This decrease in cross-sectional

area of the separation region is accompanied by an increase in the length of the separation region. The increasing length of the separation region implies that the jet remains in an unstable state for longer periods before reattaching to the walls. This would explain the higher turbulence intensity values reported by Pietrzyk *et al.* (1989). The increased length of the separation region also means that the jet then has a shorter distance, after reattachment, to stabilise before exiting the hole. It is also assumed by the student that the increased length of the separation region causes a delay in the pressure recovery (after the separation region) of the jet which ought to adversely affect the discharge coefficient.

Regarding the effect of the compound angle on the discharge coefficient, it is seen that the discharge coefficient values are, on average, the same (there is little to no effect on the discharge coefficient as the orientation is varied). It is important to remember that in the case of 'without' mainstream flow, it was determined that any effect on the discharge coefficient was only due to the inlet conditions.

In the study by Hay *et al.* (1994) it was reported that for coolant channel Mach number equal to zero (no coolant crossflow, a stagnant plenum, at the inlet of hole) the orientation is not a variable. The effect of orientation is more pronounced the higher the value of coolant crossflow Mach number. For coolant crossflow Mach number equal to 0.3, an increase in the angle of orientation led to a decrease in the discharge coefficient; a result to be expected as the flow must turn more and more as the angle of orientation increases (the loss coefficient due to turning increases).

Results by Burd and Simon (1999) showed that without free-stream flow, the discharge coefficient values for lateral injection (orientation angle = 90 degrees) resemble those of the stream-wise (orientation angle = 0 degrees) injection case, as anticipated, since both have the same length to diameter ratio equal to 2.3 and both eject into the same ambient.

According to Gritsch *et al.* (2001), increasing the angle of orientation results in increased losses at the hole entry and thus, decreased discharge coefficients. The decrease in the discharge coefficient is due to the increasing turning angle which requires that the coolant turn more when entering the hole. This additional loss due to turning possibly presents itself as a larger separation region at the inlet which causes the decrease in the discharge coefficient values.

As stated above, in this study, for the case of 'without mainstream crossflow', a plenum is used as supply in the inlet. For the case of a supply plenum, the stream tube of the coolant entering the hole is always in the direction of the hole, no matter the orientation of the hole (Hay *et al.* 1983). For this reason, it is expected that the losses at the inlet remain the same as the compound angle is varied. It is plausible to conclude that the slight differences in the discharge coefficient values are due to measurement uncertainty.

Figure 4-3 shows the discharge coefficient results, with mainstream crossflow, as the compound angle is varied. In the case of 'with' mainstream crossflow the discharge coefficient ought to be the sum of the losses at the inlet of the hole, inside the hole and the outlet of the hole. According to Burd and Simon (1991), Lichtarowicz *et al.* (1965), Andrews and Mkpadi (1984), and Hay and Lampard (1998), friction losses are negligible. Therefore, the discharge coefficient should be a sum of only the losses in the inlet and the outlet of the hole.

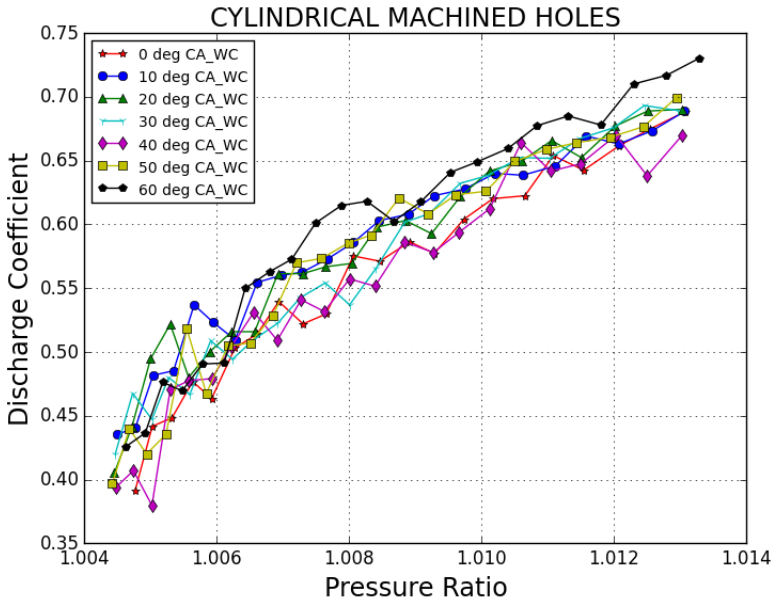

Figure 4-3: With Mainstream Crossflow (WC), effect of Pressure Ratio & Compound Angle on the Discharge Coefficient of Cylindrical Machined Holes.

As for the case of without mainstream crossflow, it is seen that, for all compound angles, the discharge coefficient is a strong function of the pressure ratio, increasing with it. This implies that the losses decrease as the flow rate increases. The losses should be due to hole entry and the presence of the mainstream crossflow.

It was determined, for the case of without mainstream crossflow, that the increase in the discharge coefficient was due to a decrease in the separation region at the inlet. So, the question that results is 'what is the effect of the crossflow on the discharge coefficient?'

It is expected that the effect of the inclusion of the mainstream crossflow would be to decrease the discharge coefficient. Therefore, the discharge coefficient values for the case of with mainstream crossflow would be lower than those without mainstream crossflow. It should be noted that the inverse has also been reported in literature and was termed the 'cross-over effect' (Hay *et al.* 1994; Rowbury *et al.* 1997; Gritsch *et al.* 1998; Burd & Simon, 1999; Rowbury *et al.* 2001; Gritsch *et al.* 2001).

Rogers and Hersh (1975) used a 'lid' model as aid to explain the blockage effect caused by the mainstream crossflow on the coolant jet. Hay *et al.* (1983) described this as 'the issuing jet being 'pinched' by the crossflow, leading to a reduction in the effective cross section and the noted decrease in discharge coefficient values'. Andreopoulus and Rodi (1984) reported that the flow behaves as if a partial, inclined 'cover' were put over the front part of the exit hole, causing the jet streamlines to start bending while still in the discharge tube and also to lift up the oncoming flow over the bent-over jet. Burd and Simon (1999) note that the free-stream flow causes a reduction in the discharge coefficient values at each pressure ratio; significant at low pressure ratios, reducing to near zero at high pressure ratios. Gritsch *et al.* (1998) reported that the effect of the mainstream crossflow is to decrease the discharge coefficient. In the results by Gritsch *et al.* (2001) at low momentum flux ratios the normalised discharge coefficient values were less than one. This indicates additional losses due to the external crossflow. At high momentum flux ratios the discharge coefficient is not affected by the mainstream crossflow.

Figure 4-4 shows the discharge coefficient results for both cases, with and without mainstream crossflow. This is to determine the effect of the mainstream crossflow on the discharge

coefficient. It should be noted that the points that are plotted have been selected where the velocities between the two (2) cases (with & without mainstream flow) match; hence, the discharge coefficient values have been plotted against the momentum flux ratio in Figure 4-3. As stated by Burd and Simon (1999), when the bulk mean velocity, density, and thus, momentum flux ratios of the coolant are matched, the net loss introduced exclusively by the external freestream flow can be quantified.

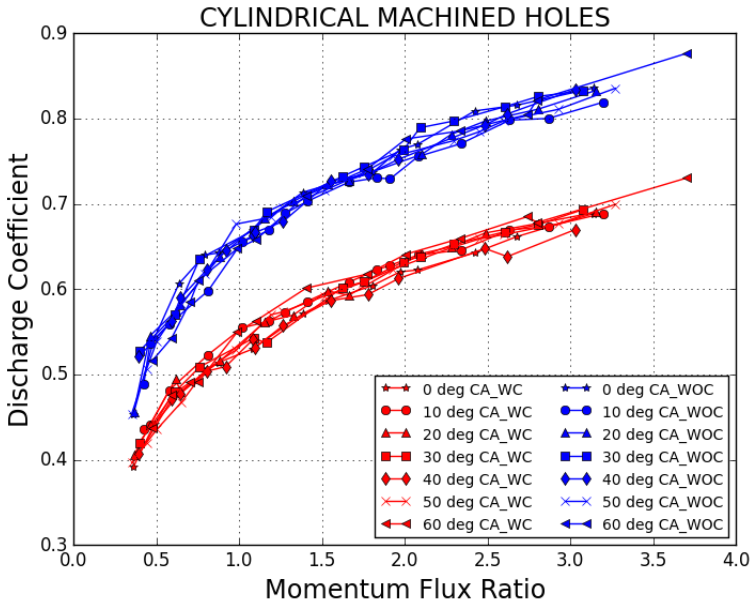

Figure 4-4: With (WC) & Without (WOC) Mainstream Crossflow Discharge Coefficient values for different Momentum Flux Ratios and Compound Angles of Cylindrical Machined Holes.

Figure 4-4 shows that the discharge coefficient values 'without mainstream crossflow' are higher than those 'with mainstream crossflow'. This is expected, because, as stated above, the mainstream flow has a blockage effect on the coolant flow (it adds losses). This agrees with Rogers and Hersh (1975), Benmansour (1981), Hay *et al.* (1983), Andreopoulus and Rodi (1984), Bromley (1994), Gritsch *et al.* (1998), Burd and Simon (1999), and Gritsch *et al.* (2001).

Results by Benmansour (1981) for cylindrical, normal (90 degrees inclination angle), holes, showed a slight decrease in the discharge coefficient when a mainstream flow (Mach number = 0.3) was added. Results from the study by Bromley (1994) for cylindrical holes inclined 30 degrees, also showed a decrease in the discharge coefficient with the addition of mainstream crossflow. From these results, it was also notable that the effect of the mainstream flow is more pronounced at lower pressure ratios. It can be assumed that at even smaller pressure ratios, like those in this study, the effect becomes more pronounced as is observed in the results of this study (see Figure 4-4). This effect is more pronounced as the pressure ratio decreases. The student reminds the reader that the effect of the mainstream flow gets less pronounced at higher pressure ratios because the blockage due to the mainstream flow decreases. The blockage decreases because the jet gains more momentum.

It can be concluded that, for the range tested in this study, the mainstream crossflow influences the discharge coefficient values. The mainstream crossflow adds blockage/resistance to the coolant jet flow at the hole outlet thereby decreasing the discharge coefficient values.

The question that is asked now is 'what is the effect on the mainstream crossflow blockage as the flow rate is increased?' In Figure 4-5 the additive outlet losses have been plotted against

the momentum flux ratio to determine the effect of increasing the flow rate. The purpose is to determine the net loss introduced exclusively by the mainstream crossflow.

To remind the reader what was stated in the literature, section 2.3., the outlet additive losses coefficient is a parameter that was defined to quantify the amount of blockage introduced by the external mainstream flow with the reference being the specific hole geometry when there is no mainstream crossflow (the outlet is fully open/ no resistance/ without mainstream crossflow).

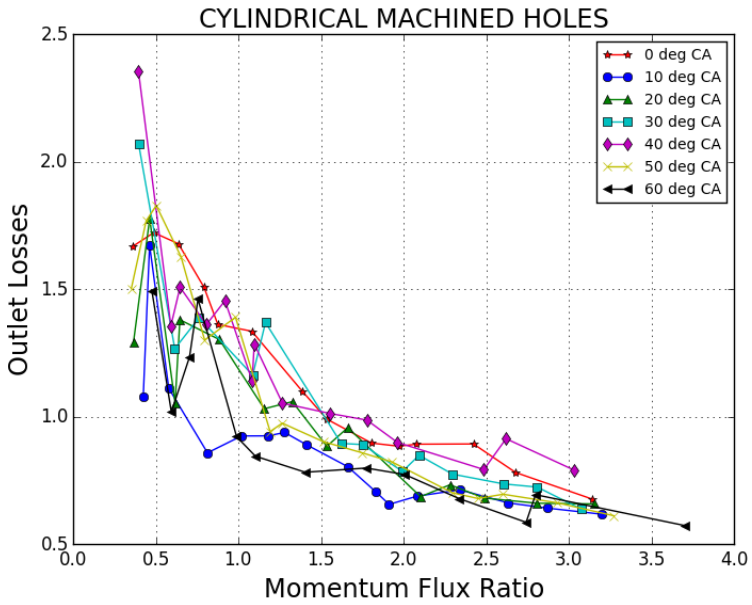

Figure 4-5: Outlet Additive Losses as the Flow Rate is increased for different Compound Angles of Cylindrical Machined Holes.

As can be seen in Figure 4-5, the general trend for all compound angles, is a decrease in the outlet losses as the momentum flux ratio increases, where the decrease is seen to approach a discharge coefficient value of 0.5. This tells us that the region is the low outflow regime, where at high outflow the outlet additive losses are zero (0) as there is no blockage due to mainstream crossflow at the hole outlet.

It was stated previously that the discharge coefficient is a strong function of the pressure ratio, therefore, the region is the low-pressure ratio regime. On this basis we can conclude that the experiments are being carried out in the low-pressure ratio, low outflow regime.

According to Rogers and Hersh (1975), in the low outflow region, the decrease in the outlet losses is due to the reduction in the blockage of the coolant jet by the mainstream crossflow, as the jet flow rate is increased. In a study by Burd and Simon (1999), all results showed a decrease in the outlet additive losses at low momentum flux ratios. All results in the study by Gritsch *et al.* (2001), at low momentum flux ratios, showed an increase in the normalised discharge coefficient values. This implies a decrease in the losses due to the mainstream crossflow.

Based on the above we can conclude that the blockage/resistance due to the mainstream crossflow, at the hole outlet, decreases as the flow rate increases. This is due to the coolant jet having more momentum to displace the mainstream crossflow at the hole exit.

What cannot be determined from the literature available to the student is a relationship between the separation region and the blockage due to the mainstream flow. What has been

reported in literature is that the effects of the inlet and outlet can be modelled separately to determine the discharge coefficient of the hole (Hay & Lampard 1998).

Therefore, the student can only conclude that the increase in the discharge coefficient is determined by a combination of a decrease in the cross-sectional area of the separation region at the inlet and a decrease in the blockage due to the mainstream at the outlet, as the flow rate is increased. In the range tested, both the inlet and outlet losses are significant in determining the discharge coefficient.

Regarding the effect of orientation (compound angle), Figure 4-3 shows that there is no clear pattern as to the effect of the orientation of the film cooling holes on the discharge coefficient in the pressure range tested. At pressure ratios greater than approximately 1.006 the 60-degrees compound angle shows slightly higher discharge coefficient values in most of that region.

It is important to remember that, in the case 'without' mainstream flow, it was determined that the losses at the inlet remain the same as the compound angle is varied. It was also determined, based on literature, that friction losses are negligible. Therefore, any effect on the discharge coefficient would be due to the outlet conditions.

It was expected, by the student, that the mainstream flow causes an effect on the discharge coefficient as the compound angle is varied (a decrease in the discharge coefficient as the compound angle is varied). Examining Figure 4-6 it is notable that the amount of mainstream flow that is in contact with the coolant flow, on exit, increases as the compound angle is increased. Basically, the contact cross-sectional area of the mainstream flow with the coolant flow should increase based on the increase from 8.00 mm to 14.42 mm, shown in Figure 4-6. This increase was expected to result in higher mainstream flow blockage at the hole exit, which would result to lower discharge coefficients.

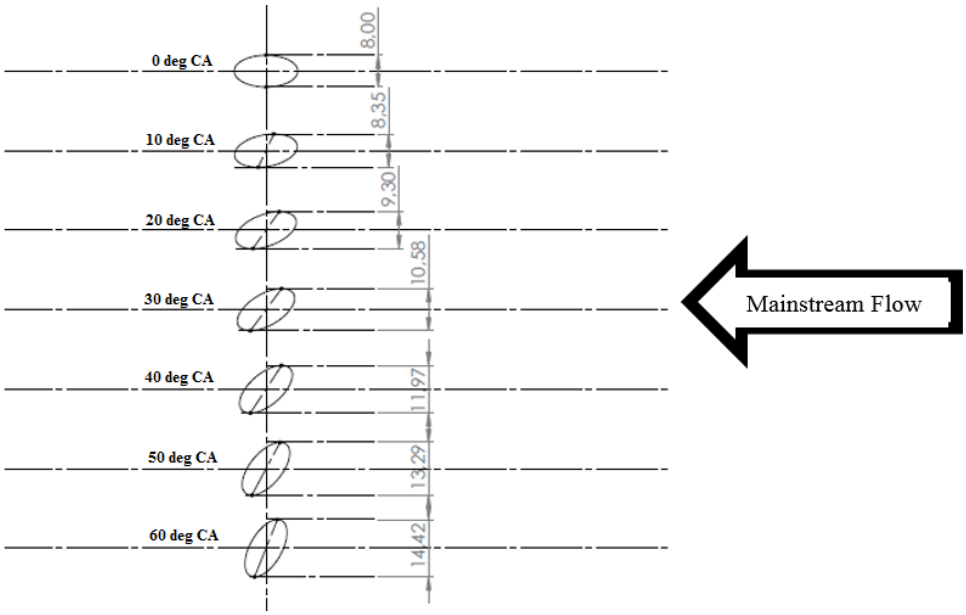

Figure 4-6: Increase in Mainstream Crossflow Contact Region as the Compound Angle is varied for Cylindrical Machined Holes.

In a study by Burd and Simon (1999) the discharge coefficient values for lateral injection (orientation angle = 90 degrees) were reported to be lower than for the stream-wise injection case (orientation angle = 0 degrees), at low pressure ratios. For momentum flux ratio less than

or equal to 0.4, lateral injection had higher outlet additive losses. In the study, the length-to-diameter ratio of the holes was equal to 2.3.

In the study by Gritsch *et al.* (2001) all the data nearly collapsed on a single curve. This tells us that the effect of orientation, on the mainstream crossflow side, is negligible. According to M. Gritsch *et al.* (2001), on the hole exit side, increasing the orientation angles only slightly affects the discharge coefficient. In the study, the length-to-diameter ratio of the holes was equal to 6.

The student assumes that the discrepancy between the findings of Burd and Simon (1999), and Gritsch *et al.* (2001) is due to the difference in the length-to-diameter ratio of the holes in both studies.

For the short holes in the study by Burd and Simon (1999), the jet has higher momentum flux on the upstream edge of the hole (the jet profile, on exit, is skewed; nonuniform). This is due to the separation region at the hole inlet. As stated in the study, the interaction with the mainstream at the higher momentum flux location results in higher pressures observed at that location. The higher pressures are a result of the higher momentum flux coolant jet actively trying to stop the mainstream flow from blocking much more of the hole exit. This results in less blockage which implies lower outlet losses.

For the lateral injection configuration, the jet on exit has a portion of higher momentum flux fluid initially contacting the mainstream flow and another portion of lower momentum flux fluid initially contacting with the mainstream flow (see Figure 4-7). On the side of lower momentum flux jet, it is expected that the mainstream flow causes higher blockage effects. In the case of streamwise injection the mainstream flow initially contacts only the high momentum flux jet. This could explain the higher outlet losses observed for the lateral configuration as compared to the streamwise configuration.

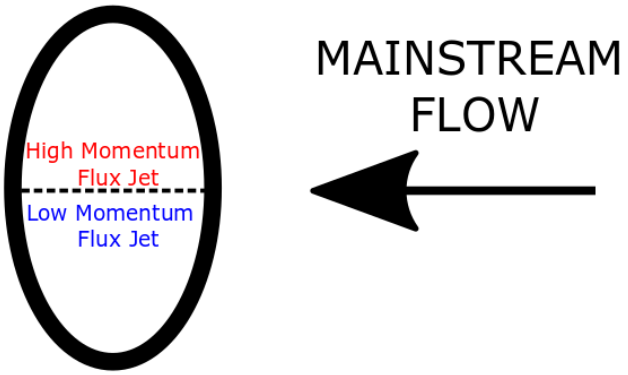

Figure 4-7: Lateral Configuration. Top View of Jet Momentum Distribution at Cylindrical Hole Exit.

For the long holes in the study by Gritsch *et al.* (2001) the exiting jet profile is expected to be relatively uniform because the length, after separation at the inlet, allows for the jet to approach fully developed flow. This implies that regardless of the orientation of the holes the mainstream flow initially contacts a uniform profile across the hole.

It was also reported in the computational study by Leylek and Zerkle (1993) that at large length-to-diameter ratios greater than 3, and high blowing ratios, greater than 1 or small length-to-diameter ratios, less than 3, and low blowing ratios, less than 1, the flow inside the cooling hole became more similar to a fully developed turbulent pipe flow.

The student concludes that the difference in observations in the studies by Burd and Simon (1999), and Gritsch *et al.* (2001) is caused by the difference in the length-to-diameter ratio. It

is important to note that this difference in length-to-diameter ratio results in different jet profiles at the exit, which results in different interactions with the mainstream crossflow. Just for clarity, it is not friction losses that the make difference, but flow development after the separation region at the inlet.

In the present study, the length-to-diameter ratio of the holes is 7.5; this is generally classified as a long hole. Therefore, the results of this study should agree with those of Gritsch *et al.* (2001).

Above, the student stated that it was expected that the discharge coefficient would decrease as the compound angle is increased. The reason given by the student is that the amount of mainstream flow that is in contact with the coolant flow, on exit, increases as the compound angle is increased (see Figure 4-6). Therefore, the student expected that this would result in higher mainstream flow blockage. The results in Figure 4-3, and the results of Gritsch *et al.* (2001), lead to the conclusion that the increase in the amount of mainstream flow contact has a negligible effect on the discharge coefficient.

Based on the above it is plausible to conclude that for the case where a plenum is used as supply, the effect of the compound angle, on the discharge coefficient, is determined more by the length-to-diameter ratio of the hole, which determines the exiting velocity profile of the jet.

Therefore, in this study, the effect of the compound angle is negligible. This is due to the length-to-diameter ratio of the holes being sufficiently long for the jet to fully reattach to the walls and approach full development after the separation region.

In the case where a crossflow is present at the inlet (not a stagnant plenum), the effect of the compound angle, on the discharge coefficient, is determined more by the inlet conditions. The effect is due to the additional turning of the coolant when entering the hole. This results in additional losses which causes the decrease in the discharge coefficient (Hay *et al.* 1983; Hay *et al.* 1994; Gritsch *et al.* 2001).

The above discussion shows that the model is valid because the discharge coefficient and outlet additive losses behaviour, the general trend of the curves, is similar to that observed in other studies and the behaviour can be explained by the physical mechanisms that govern discharge coefficient behaviour in film cooling.

These general trends are that:

- at low pressure ratios the discharge coefficient is a strong function of the pressure ratio, increasing with it.
- the mainstream crossflow influences the discharge coefficient by decreasing the discharge coefficient values.
- the outlet additive losses decrease as the momentum flux increases.

As stated above the pressure ratio range tested in this study has not been reported in literature in as much detail as it is in this study. Therefore, the student had to validate the model by substantiating the discharge coefficient behaviours observed with literature that reports the physical mechanisms (flow structure measurements) that govern discharge coefficient behaviour in film cooling.

4.2.2.Laidback fan-shaped Machined Film Cooling Holes

Figure 4-8 shows the results for the laidback fan-shaped machined holes. The student uses the same procedure as for the cylindrical machined holes above, to analyse the effect of pressure ratio, mainstream crossflow and compound angle on the discharge coefficient.

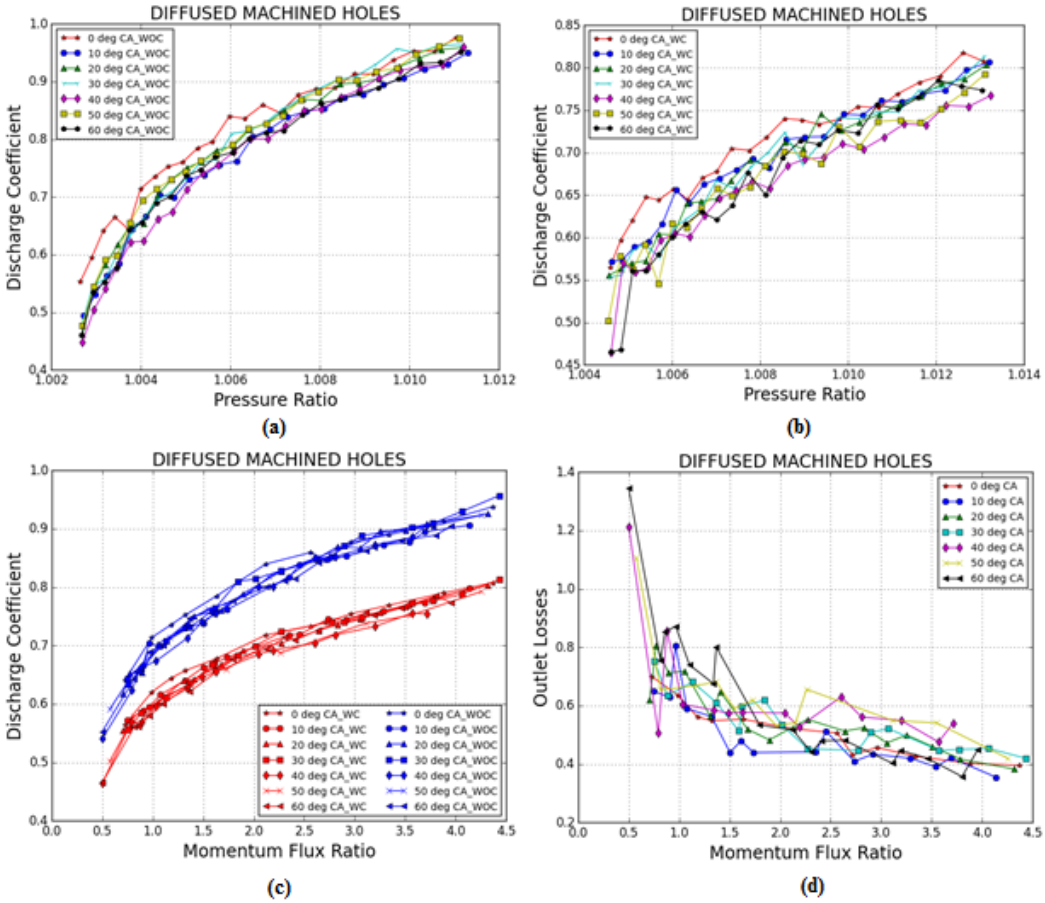

Figure 4-8: Effect of Pressure Ratio & Compound Angle of Diffused Machined Holes. (a) Without Mainstream Crossflow (WOC), (b) With Mainstream Crossflow (WC), (c) With (WC) & Without (WOC) Mainstream Crossflow, (d) Outlet Additive Losses.

It can be clearly seen that the trends are like those observed for the cylindrical machined holes. These trends are:

- at low pressure ratios the discharge coefficient is a strong function of the pressure ratio, increasing with it. Therefore, the testing range is the low-pressure ratio region (see Figure 4-8(a) and Figure 4-8(b));
- the mainstream crossflow influences the discharge coefficient by decreasing the discharge coefficient values (see Figure 4-8(c));
- the blockage/resistance due to the mainstream crossflow, at the hole outlet, decreases as the flow rate increases. This is due to the coolant jet having more momentum to displace the mainstream crossflow at the hole exit (see Figure 4-8(d));
- the outlet additive losses approach but do not reach a value of zero (0). Therefore, the testing range is the low outflow region; and
- the effect of the compound angle on the discharge coefficient is negligible (see Figure 4-8(a) to Figure 4-8(d)).

Therefore, it is plausible to assume that:

- the physical mechanisms, at the inlet, that determine the discharge coefficient, as the pressure ratio is varied, for the cylindrical machined holes, are also responsible for the behaviour observed for the laidback fan-shaped holes as in Hayms and Leylek (2000);

- similar physical mechanisms, as the cylindrical machined holes, determine the effect of the compound angle on the discharge coefficient; and
- similar physical mechanisms, as the cylindrical machined holes, determine the effect of the mainstream crossflow on the discharge coefficient.

Regarding the flow structure, as was the case with the cylindrical machined holes, a separation region is expected to be present at the hole inlet which decreases in cross-sectional area as the plenum pressure is increased. This separation region forces the coolant jet to the upstream edge of the wall. Since the length to diameter ratio of the holes is greater than 2, the jet is expected to reattach to the walls. The jet profile is expected to be skewed towards the upstream wall after reattachment.

Due to the expansion of the hole at the metering length to diameter ratio of 3.75, it is assumed that the coolant enters the diffused section skewed to the upstream edge. It is reported in the study by Hay and Lampard (1995) that the flow within the diffuser is very sensitive to upstream flow history. In a study by Klein (1981), it is reported that distortion of the outlet profile increases with that of the inlet profile. Therefore, it is expected that the velocity profile of the coolant at the hole exit remains skewed towards the upstream edge because of the expansion of the hole at length to diameter ratio equals to 3.75.

From the results of studies by Burd and Simon (1999), and Gritsch *et al.* (2001), on cylindrical holes, the student determined that the skewness of the velocity profile on exit causes an effect on the discharge coefficient as the compound angle is varied, when a mainstream crossflow is present.

But it is seen from the results of Figure 4-8(b) and Figure 4-8(d) that there is little to no effect on the discharge coefficient as the compound angle is varied. Therefore, the student concludes that the skewness of the coolant jet at the hole exit is not significant enough for an effect on the discharge coefficient to be observed as the compound angle is varied.

So, the severity of the skewness of the exiting jet profile is a factor in the discharge coefficient behaviour. This agrees with the results of the Burd and Simon (1999) where it was observed that the outlet losses of the short cylindrical holes were higher than that of the long holes because of the severity in skewness of the velocity profiles at the hole exit; the short holes had higher momentum flux on the upstream edge, as compared to the long holes because of the skewed velocity profile of the coolant jet after the separation region at the inlet.

Additionally, because of the sudden expansion of the hole, higher turbulence levels are expected at the hole exit, as compared to the cylindrical machined holes. This agrees with the results of the study by Thole *et al*. (1998). As was stated previously, ideally, the coolant jet should have relatively low turbulent mixing to avoid dilution of the jet by the hot mainstream fluid (Thole *et al*. 1998).

4.3. Effect of Compound angle: All Hole Geometries

Shown in Figure 4-9 are all the discharge coefficient results for the hole geometries investigated in this study, as the compound angle and the pressure ratio is varied. All results are with the presence of the mainstream crossflow.

From the results it is seen that the different hole geometries generally follow the same trends that were observed in the sections above. Therefore, it is not far-fetched to assume that similar physical mechanisms, as those for the cylindrical and the laidback fan-shaped machined holes, determine the discharge coefficient behaviour observed.

Close inspection of the results of the 3D printed holes shows that they are noisier and slightly more scattered as compared to the results of the machined holes. The results of Figure 4-9, (e) and (i), warrant discussion.

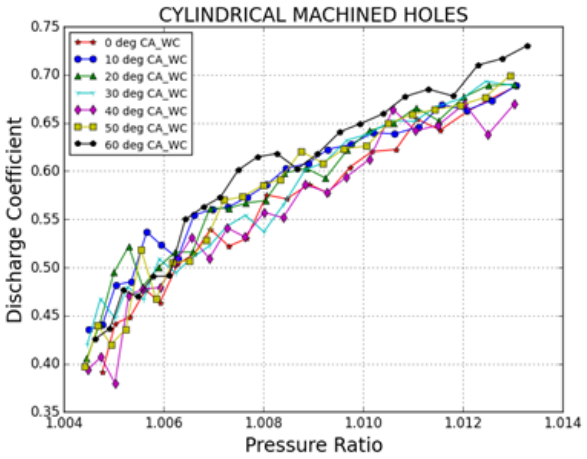

(a)

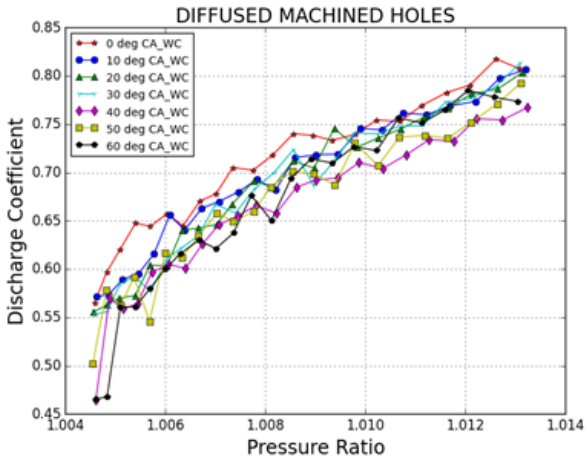

(b)

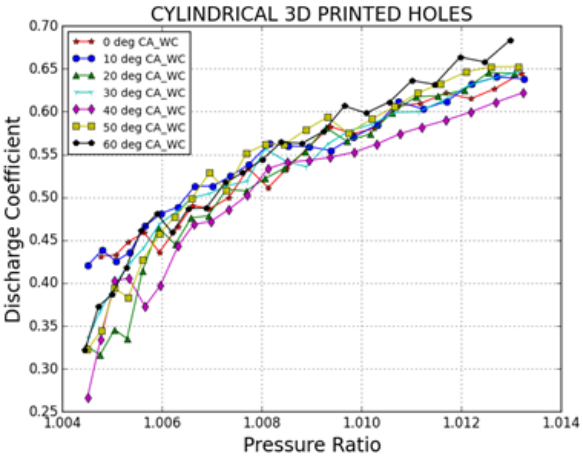

(c)

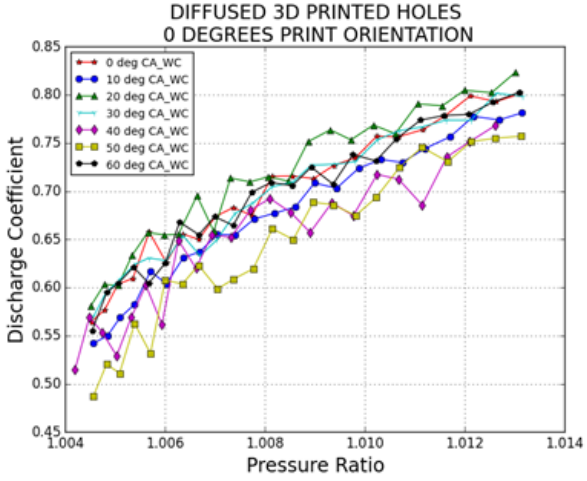

(d)

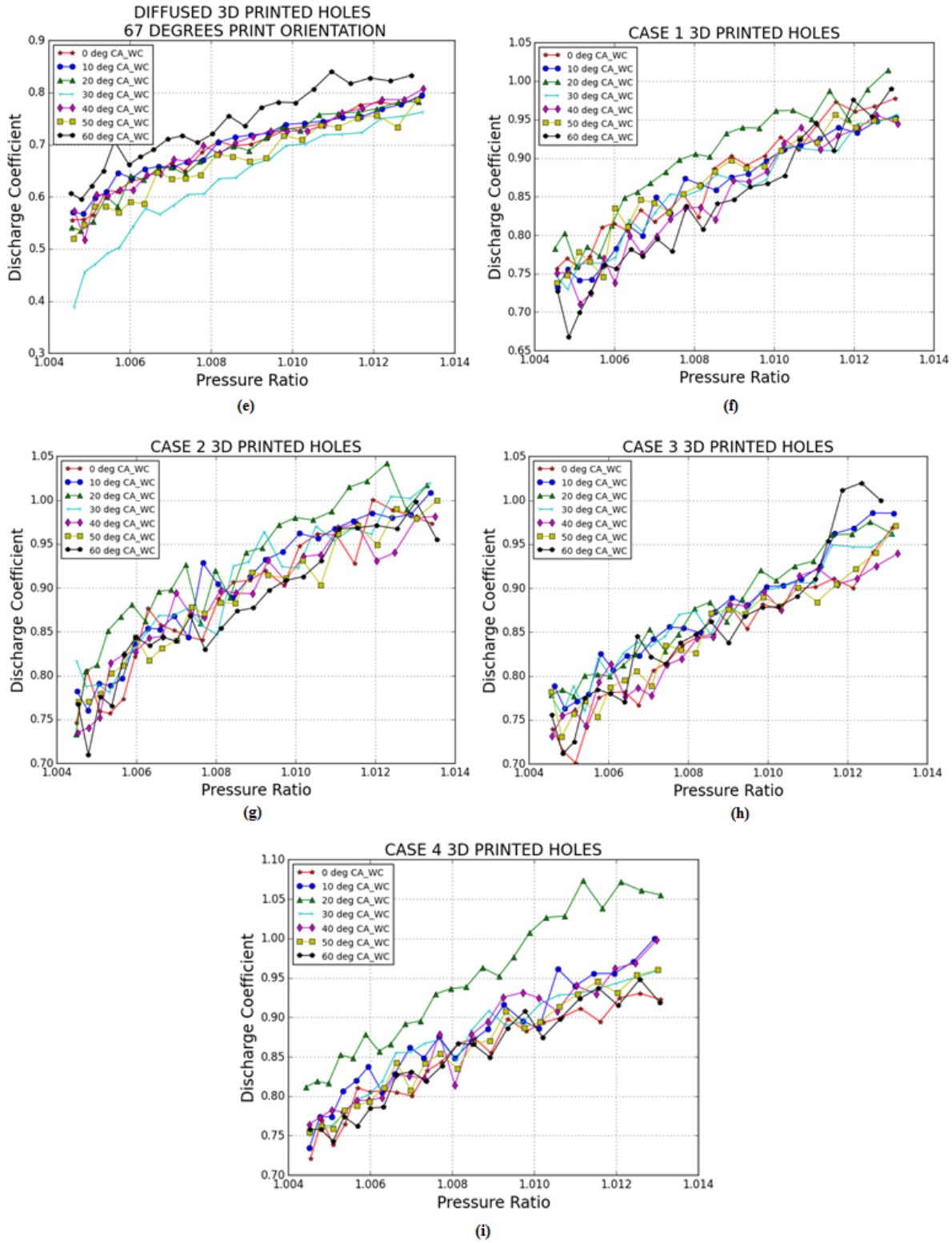

Figure 4-9: Effect of the Compound Angle and the Pressure Ratio on the Discharge Coefficient for the Hole Geometries investigated in this study, a) cylindrical machined holes, b) laidback fan-shaped holes, c) cylindrical 3D 60 degrees print holes, d) laidback fan-shaped 3D 0 degrees print holes, e) laidback fan-shaped 3D print 67 degrees print holes, f) case 1, g) case 2, h) case 3, i) case 4.

In Figure 4-9(e) it is seen that the is no pattern as the compound angle is varied. However, the compound angle of 30 degrees has the lowest discharge coefficient in the whole pressure

ratio range tested, and the compound angle of 60 degrees has the highest discharge coefficient for the whole pressure ratio range tested. In Figure 4-9(i) the compound angle of 20 degrees has the highest discharge coefficient for the whole pressure ratio tested. It is notable that Figure 4-9(d), (f) and (g) also show higher discharge coefficient values for the compound angle 20 degrees, in a large pressure ratio range.

Based on the literature reviewed, the discussion presented above regarding the cylindrical and laidback fan-shaped machined holes, and after much thought and deliberation of the possible physical mechanisms that could result in a difference in discharge coefficient values as the compound angle is varied for Figure 4-9(d), (e), (f), (g) and (i), where the student concludes that they should not be an effect on the discharge coefficient as the compound angle varies. The differences observed are due to measurement uncertainty.

Repetition of the tests would have allowed for clarity on the conclusion of measurement uncertainty. Unfortunately, due to time constraints the student could not repeat the tests.

Therefore, it is concluded that regardless of hole geometry, manufacturing method, print/build orientation of the 3D printed pieces and inclination angle, the effect of the compound angle on the discharge coefficient is negligible.

Regarding the flow structure for the 3D printed cylindrical and laidback fan-shaped holes, it is expected that the flow structures be the same as those for the machined pieces. This is investigated further in section 4.4. where the effect of manufacturing method, on the discharge coefficient, is discussed.

Regarding the flow structure of cases 1 to 4, it is expected that since the forward diffusion is a smooth curvature, instead of a sudden sharp expansion, as is the case for the laidback fan-shaped hole, this is expected to result in a more uniform exit velocity profile. As determined in the sections above, the uniformity of the exit velocity profile influences the interaction with the mainstream flow, which affects the discharge coefficient.

A more uniform coolant velocity profile at the hole exit would support the conclusion that the compound angle does not influence the discharge coefficient. This was determined in the discussion above of the cylindrical machined holes and is also supported by the results of the study by Gritsch *et al.* (2001). This is investigated further in section 4.4., where the effect of hole geometry, on the discharge coefficient, is discussed.

Additionally, because of the smooth gradual expansion of the hole, lower turbulence levels are expected at the hole exit, as compared to the laidback fan-shaped holes. High turbulence levels promote dissipation of the coolant jet when it exits into the mainstream. This is not ideal for film cooling thermal performance (Thole *et al*. 1998).

4.4. Effect of Hole Geometry, manufacturing method, 3D print build orientation & Inclination angle

4.4.1. Model Validation & Effect of Hole Geometry: Cylindrical & Laidback fan-shaped Machined Holes

The analysis of the effect of hole geometry is first carried out on the baseline cases (machined holes). The behaviour of the baseline cases has been investigated and is reported in literature. Therefore, this serves as a model validation process. Additionally, this analysis is done in order to set a reference of the additional factors that govern the discharge coefficient behaviour observed in the ranges tested.

Section 4.2 covered the physical mechanisms that govern the discharge coefficient behaviour of the hole geometries investigated in this study. The reader is encouraged to consult this

section. The flow structure of the cylindrical machined holes was covered in depth because of the vast literature available and because it is less complex as compared to other hole geometries. This section, which compares the cylindrical and laidback fan-shaped machined holes, allows for a better analysis and understanding of the discharge coefficient behaviour when an expansion/diffusion has been incorporated in the hole.

Figure 4-10 shows the discharge coefficient results, without mainstream crossflow, for the cylindrical and laidback fan-shaped holes as the pressure ratio is varied. The holes are oriented 0 degrees compound angle, relative to the mainstream flow direction. As stated earlier, the purpose of testing without mainstream flow is to remove the effects of the mainstream crossflow on the discharge coefficient. This means that we isolate the effects of the other variables on the discharge coefficient. The variable we are interested in isolating, in this specific comparison, is the effect of adding the expansion to the hole.

It is seen that, for both hole geometries, the discharge coefficient is a strong function of the pressure ratio and increases with it. Firstly, this tells us that the losses decrease as the flow rate increases. Secondly, the experiments are being carried out in the low-pressure ratio regime (see Figure 2-6). This agrees with studies by Hay *et al.* (1983), Gritsch *et al.* (1998) and Gritsch *et al.* (2001).

The supply at the inlet is a stagnant plenum. The inclination angle of the holes (30 degrees) causes a large turning angle for the coolant on the downstream edge as it enters the hole. Therefore, for both geometries, a flow separation region is expected on the downstream edge at hole entry and is responsible for the losses when the flow enters the hole (Lichtarowicz *et al.* 1965; Pietrzyk *et al.* 1989; Leylek & Zerkle 1993; Thole *et al.* 1997). The presence of a separation region on the downstream edge at the inlet was proved in the study by Thole *et al.* (1997).

Studies by Burd and Simon (1999), Lichtarowicz *et al.* (1965), Andrews and Mkpadi (1984), and Hay and Lampard (1998) showed that the frictional losses inside the hole negligible. The length to diameter ratio for both hole geometries is the same. Therefore, the frictional losses are not significant for both hole geometries.

According to Gritsch *et al.* (1998), at low pressure ratios, jet separation in the diffuser section is avoided. Above, it was determined that the experiments are being carried out in the low-pressure ratio regime because the results show that the discharge coefficient is a strong function of the pressure ratio. In the study by Schroeder and Thole (2014) it was stated that expansion angles of seven (7) degrees help ensure that the is no jet separation inside the hole. It is said that this agreed with studies by Thole *et al.* (1998), Saumweber and Schulz (2012), and Gritsch *et al.* (1998b).

Therefore, it can be assumed with relative confidence that no separation region is expected in the diffuser section of the expanded hole in the range tested, in the lateral and forward direction.

Based on the above it is plausible to conclude that the losses, for both hole geometries, are determined more by inlet conditions. As stated in the sections above, the increase in the discharge coefficient, as the flow rate increases, is due to a decrease in the cross-sectional area of the separation region at the inlet.

It is also seen in Figure 4-10, that the discharge coefficient values of the diffused holes are higher than those of the cylindrical holes, in the whole range tested. Referring to Equation (27), this tells us that at the same pressure ratio, there is more mass that flows through the hole for the laidback fan-shaped holes as compared to the cylindrical holes. From this we can

conclude that the separation zone at the inlet is smaller for the laidback fan-shaped holes as compared to the cylindrical holes.

$$C_d = \frac{\dot{m}_{actual}}{A_{hole}\sqrt{2 \times \rho_c \times (P_{tc} - P_{sm})}} \quad (27)$$

The question now is 'why does more mass flow through the hole for the laidback fan-shaped holes as compared to the cylindrical holes?

In the studies by Hay and Lampard (1995), and Gritsch *et al.* (1998), it was reported that discharge coefficients for expanded holes are higher than for the cylindrical holes with the same flow conditions. It was also reported that the effect was more pronounced at low pressure ratios, decreasing at elevated pressure ratios. The reason given for the higher discharge coefficient values is pressure recovery in the diffuser section of the hole.

The increase in cross sectional area in the diffuser section leads to an increase in the static pressure of the coolant (pressure recovery). Based on conservation of mass and energy this should be accompanied by a reduction in the dynamic/kinetic component of pressure. This increase in the static pressure of the coolant implies that there is now a smaller difference between the static pressure of the coolant and the static pressure of the mainstream (the reader is reminded that the coolant must expand to the mainstream static pressure at the exit; see Appendix A). Therefore, the diffuser assists, gradually, in this expansion of the coolant. This results in a smaller pressure drop required across the hole, for the laidback fan-shaped holes as compared to the cylindrical holes, to drive the same amount of mass through the hole. Referring to Equation (27), it is also seen that a smaller pressure difference results in higher discharge coefficients.

Based on the above it is concluded that, at the same flow conditions, the discharge coefficient values of the laidback fan-shaped holes are higher as compared to those of the cylindrical holes. The reason being pressure recovery in the expanded section of the laidback fan-shaped holes.

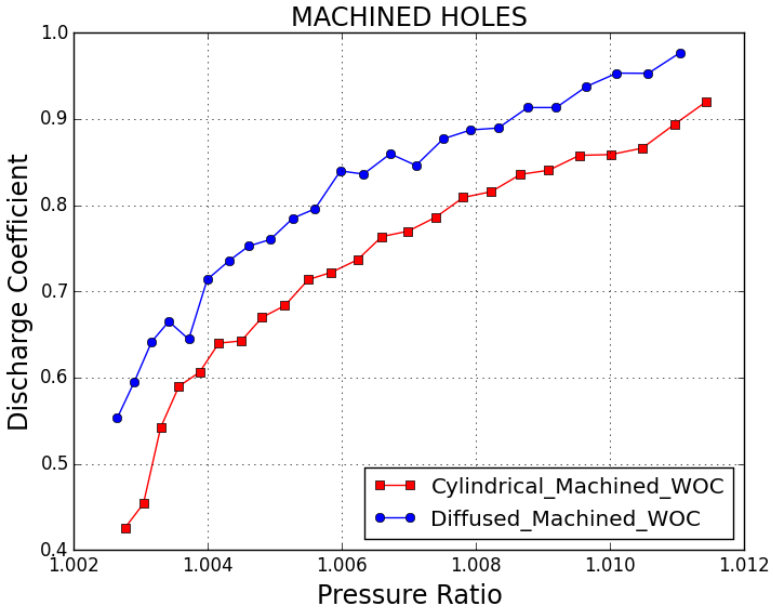

Figure 4-10: Without mainstream flow, discharge coefficient behaviour of cylindrical & laidback fan-shaped machined holes.

Figure 4-11 shows the discharge coefficient results, with mainstream crossflow, for the cylindrical and laidback fan-shaped holes as the pressure ratio is varied. From the results it is seen that similar trends exist for the case of 'without' mainstream crossflow. The most significant trend being that the discharge coefficient values of the laidback fan-shaped holes are higher than those of the cylindrical holes. As stated above this is due to pressure recovery in the expanded section of the hole.

In the sections above it has already been shown that the inclusion of mainstream crossflow results in a decrease in the discharge coefficient values. The mainstream crossflow adds blockage/resistance to the coolant jet flow at the hole outlet thereby decreasing the discharge coefficient values.

Based on the discussions in the sections above it was determined that the increase in the discharge coefficient is determined by a combination of a decrease in the cross-sectional area of the separation region at the inlet and a decrease in the blockage due to the mainstream at the outlet, as the flow rate is increased.

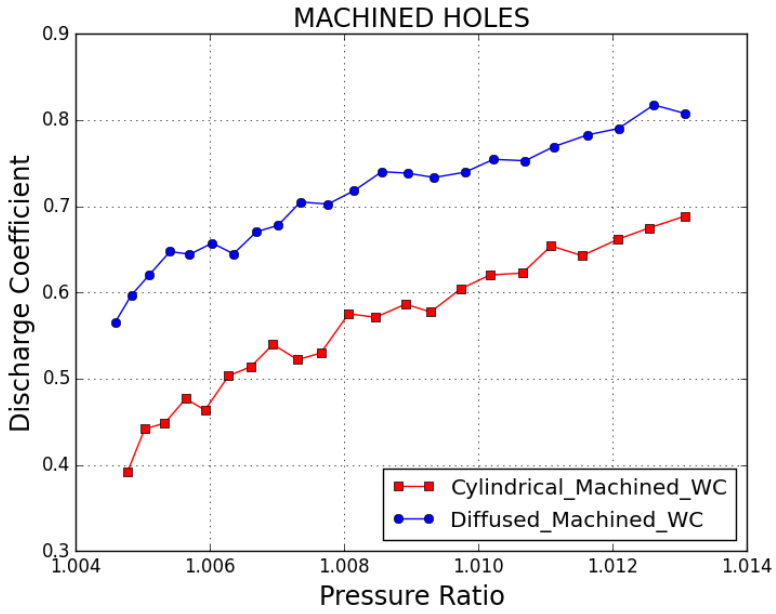

Figure 4-11: With mainstream flow, discharge coefficient behaviour of cylindrical & laidback fan-shaped machined holes.

The question that is asked at this stage is 'what is the effect on the blockage due to the mainstream crossflow as the flow rate is increased?' In Figure 4-12 the additive outlet losses have been plotted against the momentum flux ratio to determine the effect of increasing the flow rate. The purpose is to determine the net loss introduced exclusively by the mainstream crossflow.

On close inspection of the curves in Figure 4-12 it is seen that the range of the momentum flux ratio between the two (2) cases is not the same. This is because the pressure ratio range tested for both cases was kept constant. As stated in the discussion above, more mass is driven through the hole for the laidback fan-shaped hole when compared to the cylindrical hole. The reasons were given in the discussion above. This will also be seen in Figure 4-15. It is recommended for future studies, that the full range of momentum flux ratio be tested to verify that the behaviour observed at this constant pressure ratio range persists.

It is also important to mention to the reader that in calculation of the momentum flux ratio, the momentum flux of the coolant is based on the cylindrical portion cross-sectional area; equation

(28). This just ensures standardisation between different hole geometries in different studies. Therefore, it is expected that the momentum flux ratio, of the holes with expanded exits, is lower than that of the cylindrical holes at the exit of the holes (Thole *et al*. 1998).

$$\rho_c {U_c}^2 = \frac{\left(\frac{\dot{m}_{actual}}{A_{hole}}\right)^2}{\rho_c} \tag{28}$$

It is seen that, for both hole geometries, the outlet losses decrease as the momentum flux ratio increases. Firstly, this proves that the mainstream crossflow creates a resistance at the hole exit. Secondly, this tells us that the blockage due to the mainstream crossflow decreases as the flow rate of both hole geometries increases, where the mainstream crossflow deflects from the exit of the hole allowing more coolant to flow through. This agrees with studies by Rogers and Hersh (1975), Burd and Simon (1999), and Gritsch *et al.* (2001).

In the range tested the outlet losses do not reach a value of zero (0). This tells us that the region tested is the low outflow regime; at high outflow the outlet additive losses are zero (0) as there is no blockage due to mainstream crossflow at the hole outlet.

It is also seen that the cylindrical holes have higher outlet additive losses as compared to the laidback fan-shaped holes in the range tested. This means that the mainstream flow causes higher blockage effects for the cylindrical holes as compared to the laidback fan-shaped holes. The reader is reminded that the outlet losses coefficient isolates the losses due to the addition of a crossflow. Therefore, the higher outlet losses for the cylindrical hole, as compared to the laidback fan-shaped hole, should be due to the interaction of the jet with the mainstream flow. This implies a difference in the exit velocity profiles of the jet for the two (2) hole geometries.

It was determined previously that the velocity profile of the cylindrical holes is expected to be uniform at the hole exit because the coolant, after reattachment, has enough length to approach fully developed.

For the laidback fan-shaped holes, it was assumed that the expansion at a length to diameter ratio of 3.5 results in a relatively non-uniform velocity profile at the exit of the hole. This means that the coolant has higher momentum flux on the upstream edge of the hole. This implies that the jet at that location has more momentum to counter the blockage effects of the mainstream crossflow. This agrees with Burd and Simon (1999). This would explain the lower blockage effects for the laidback fan-shaped holes.

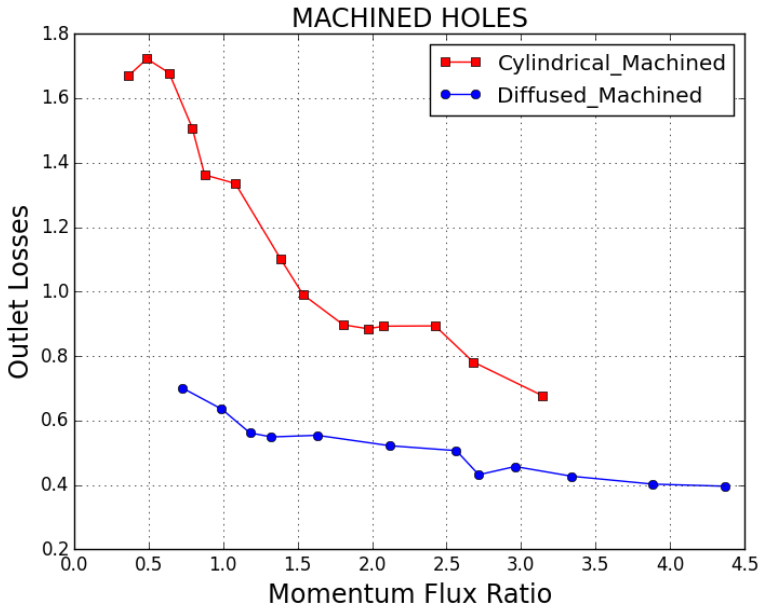

Figure 4-12: Outlet additive losses for cylindrical & laidback fan-shaped holes.

The above discussion shows that the model is valid because, as is reported in literature, the discharge coefficient behaviour of the laidback fan-shaped machined hole is higher than that of the cylindrical machined hole because of pressure recovery in the expanded section.

4.4.2. Effect of Hole Geometry, Manufacturing Method, 3D print orientation & Inclination Angle

Figure 4-13 shows the discharge coefficient results, without mainstream crossflow, for all the hole geometries investigated in this study, as the pressure ratio is varied. The holes are oriented zero (0) degrees compound angle, relative to the mainstream flow direction. As stated earlier, the purpose of testing without mainstream flow is to remove the effects of the mainstream crossflow on the discharge coefficient. In doing so we isolate the effects of hole geometry, manufacturing method, 3D print orientation and inclination angle on the discharge coefficient.

Firstly, it is clearly seen that the trends, without crossflow, are like those reported in sections above. This tells us that, for all the geometries, similar physical mechanisms govern the behaviour of the discharge coefficient observed.

From the results it is seen that the discharge coefficient values of the hole geometries with expanded sections are higher than those of the cylindrical holes. As stated in the sections above this is due to pressure recovery in the expanded section of the diffused holes.

It is also seen that the manufacturing method and 3D print orientation, regardless of the hole geometry, has a negligible effect on the discharge coefficient. The differences observed fall within experimental uncertainty. In the study by Stimpson *et al.* (2018) the results showed that the discharge coefficient values of the additively manufactured holes are lower than those of the machined holes. It was also seen that the discharge coefficient is a strong function of the relative roughness in the hole with a decrease in the relative roughness resulting in an increase in the discharge coefficient values.

The relative roughness is seen to be a good parameter because in the study by Stimpson *et al.* (2017) it was shown that the discharge coefficient was affected because of the flow area blockage caused by the roughness.

In the current study the relative roughness of the machined holes is equals to 0.003 and that of the 3D printed holes is in the range 0.00525 - 0.0165. Inspection of the results in the study by Stimpson *et al.* (2018), of the hole whose roughness is closest to those in this study, it is seen that at low pressure ratios the discharge coefficient behaviour of the additively manufactured holes approaches that of the machined holes. Therefore, the student concludes that the slight differences observed in Figure 4-13, in comparing the manufacturing method, are due to measurement uncertainty. The effect of manufacturing method and 3D print orientation being negligible is better seen in Figure 4-14.

In previous discussions it was assumed that the flow structure of the 3D printed holes should be like that of the machined holes, and it was said that this section would be used to investigate it further. Based on the negligible difference in the discharge coefficient results, when comparing the 3D printed and machined holes, it is plausible to conclude that the flow structure between these cases is the same.

In comparing the discharge coefficient behaviour of the diffused holes and the new hole geometries (cases 1 to 4) it is seen that the is little to no difference in the discharge coefficient values. It was reported in the study by Hay and Lampard (1995) that the was little effect in the discharge coefficient values for the hole geometries that only had a lateral-spread and to those that had a lateral-spread and a layback. In a study by Gritsch *et al.* (1998), it was reported that the addition of the layback has a weak effect on the discharge coefficient.

The results in Figure 4-13 agree with the results of the studies by Hay and Lampard (1995), and Gritsch *et al.* (1998). This tells us that the pressure recovery in the diffused section is weakly dependent on the geometry of the expansion.

Regarding the effect of inclination angle, on the discharge coefficient, which is observed by comparing the behaviour of cases 1 and 2 (30 degrees inclination angle) to that of cases 3 and 4 (40 degrees inclination angle), it is seen that the effect of inclination angle is negligible. This agrees with the study by Gritsch *et al.* (2001), where it was seen that the normalised discharge coefficient results collapsed onto a single curve.

From the results and discussion of Gritsch *et al.* (2001, it was also seen and said that the effect of the inclination angle is determined more by crossflow at the inlet. The decrease in the discharge coefficient, as the inclination angle increases, is due to the increasing turning angle which requires that the coolant turn more when entering the hole. This additional loss due to turning possibly presents itself as a larger separation region at the inlet which causes the decrease in the discharge coefficient values. The effect of inclination angle being negligible is better seen in Figure 4-14.

From this, the student can also conclude that, when the supply is a stagnant plenum, the separation region at the inlet may shift in location as the inclination angle is changed, but its effect on the discharge coefficient is negligible. It could also be said that the size of the separation region does not change as the inclination angle is varied.

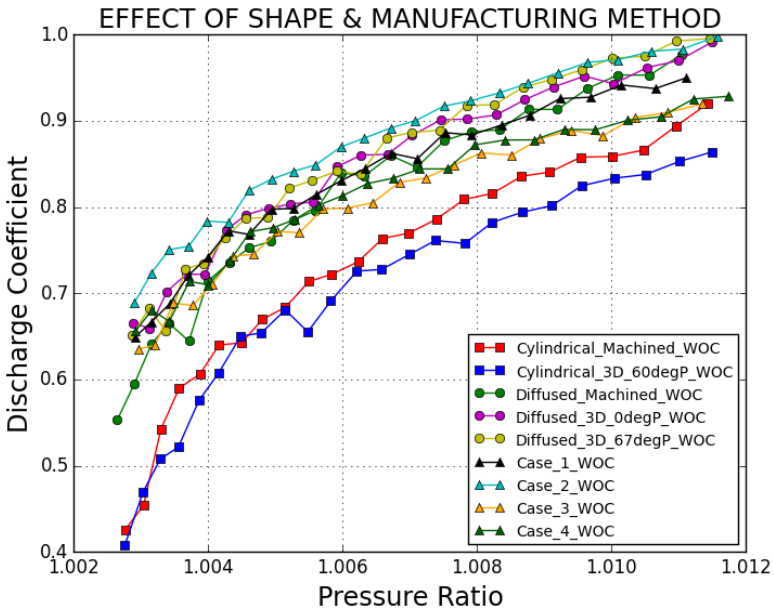

Figure 4-13: Without mainstream flow, effect of hole geometry, manufacturing method, 3D print orientation & inclination angle on the discharge coefficient.

Figure 4-14 shows the discharge coefficient results, with mainstream crossflow, for all the hole geometries investigated in this study, as the pressure ratio is varied. The holes are oriented zero (0) degrees compound angle, relative to the mainstream flow direction.

Firstly, it is clearly seen that the trends are like those reported in the sections above. This tells us that similar physical mechanisms govern the behaviour of the discharge coefficient observed.

It is also seen that the discharge coefficient values of cases 1 to 4 are higher than those of the laidback fan-shaped holes. Without the presence of a mainstream crossflow, Figure 4-13, the was little to no difference between the discharge coefficients of cases 1 to 4 and the laidback fan-shaped holes. Therefore, the difference is due to the interaction between the exit velocity profile of the hole geometries and the mainstream flow. The student investigates this further by reporting the outlet additive losses (see Figure 4-15).

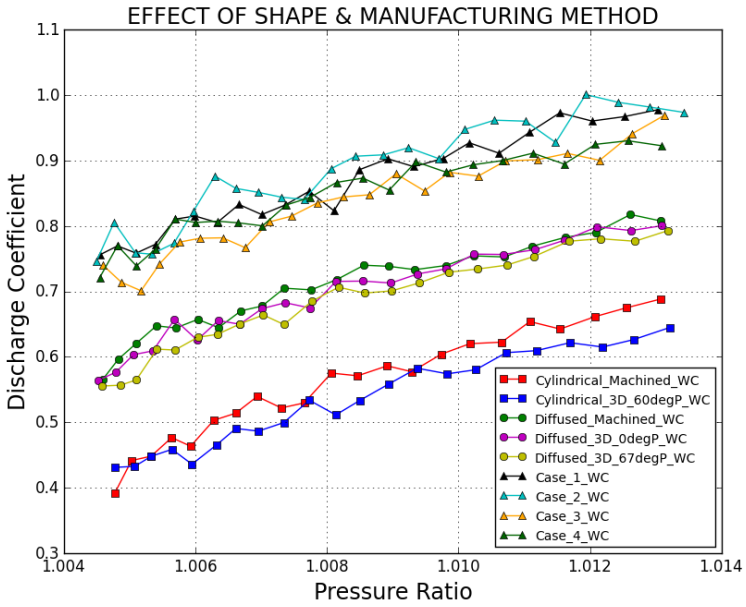

Figure 4-14: With mainstream flow, effect of hole geometry, manufacturing method, 3D print orientation & inclination angle on the discharge coefficient.

Figure 4-15 shows the outlet losses for all the hole geometries investigated in this study. It is seen that cases 1 to 4 have the least losses of all the hole geometries investigated. It is also seen that the outlet losses for cases 1 to 4 are very close to zero (0). This tells us that the mainstream flow creates negligible blockage of the coolant jet in the pressure range tested. In other words, the coolant has enough momentum flux, on the upstream edge, to block the mainstream crossflow from covering the hole exit. This agrees with Burd and Simon (1999) and explains the lower blockage.

Regarding the effect of inclination angle, on the discharge coefficient, which is observed by comparing the behaviour of cases 1 and 2 (30 degrees inclination angle) to that of cases 3 and 4 (40 degrees inclination angle), it is seen again that the effect of inclination angle is negligible. In changing the inclination angle, from 30 degrees to 40 degrees, the length to diameter ratio decreased because the thickness of the test piece was kept constant at 30 mm. It was expected that an effect on the discharge coefficient would have been due to the interaction of the coolant jet and the mainstream crossflow because of a difference in velocity profile at the exit of the hole. The outlet losses results of Figure 4-15 lead us to the conclusion that the change in the length to diameter ratio, as the inclination angle was changed, did not significantly alter the coolant exit velocity profile.

The results and discussion of the effect of compound angle, for cases 1 to 4, led the student to the conclusion that the smooth gradual expansion should result in a more uniform velocity profile at the hole exit, as compared to that of the laidback fan-shaped holes.

Regarding the flow distribution of cases 1 to 4, based on the results and discussion of the effect of compound angle on the discharge coefficient, it was determined that if the is skewness in the exit velocity profile, it is not significant enough to cause an effect on the discharge coefficient as the compound angle is varied. However, the coolant jet exit profile is expected to be more skew than that of the cylindrical holes because of the expansion. The lower outlet losses of cases 1 to 4, as compared to the cylindrical holes, also leads to the conclusion that there should be a skewness in the coolant jet exit velocity profile. This tells us that cases 1 to 4 has a higher momentum flux at the upstream edge of the hole, enough to stop the mainstream crossflow from blocking the hole exit. The skewness of the coolant jet

velocity profile of cases 1 to 4 is expected to be less than that of the laidback fan-shaped hole because of the smooth gradual expansion as compared to the sudden sharp expansion.

Additionally, because of the smooth gradual expansion of the hole, lower turbulence levels are expected at the hole exit, as compared to the laidback fan-shaped holes. High turbulence levels promote dissipation of the coolant jet when it exits into the mainstream. This is not ideal for film cooling thermal performance (Thole *et al*. 1998).

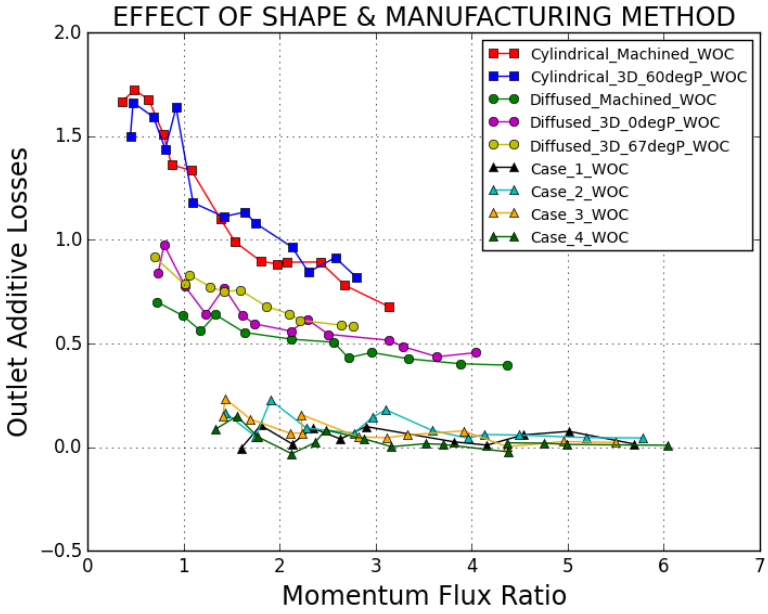

Figure 4-15: Effect of hole geometry & manufacturing method on the outlet additive losses.

The analysis above, of the effect of hole geometry, manufacturing method, 3D print build orientation, and inclination angle was done only at a compound angle of zero (0) degrees relative to the mainstream flow direction. Shown in Figure 4-16 are the discharge coefficient results for the different compound angles investigated in this study, with mainstream flow.

Comparing the case 2 hole and the cylindrical hole, the difference in discharge coefficient values in Figure 4-16(a) is approximately 0.31 (34%). In Figure 4-16(b) the difference is approximately 0.38 (40%). In Figure 4-16(c) the difference is approximately 0.4 (40.8%). In Figure 4-16(d) the difference is approximately 0.34 (37%). In Figure 4-16(e) the difference is approximately 0.35 (39%). In Figure 4-16(f) the difference is approximately 0.33 (36.3%). In Figure 4-16(g) the difference is approximately 0.3 (33.3%).

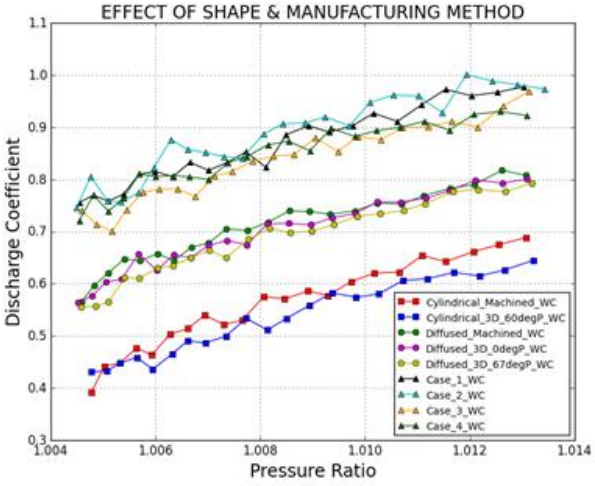

(a)

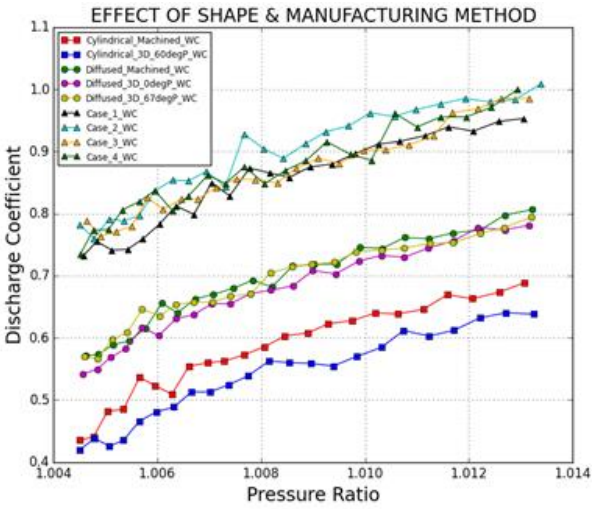

(b)

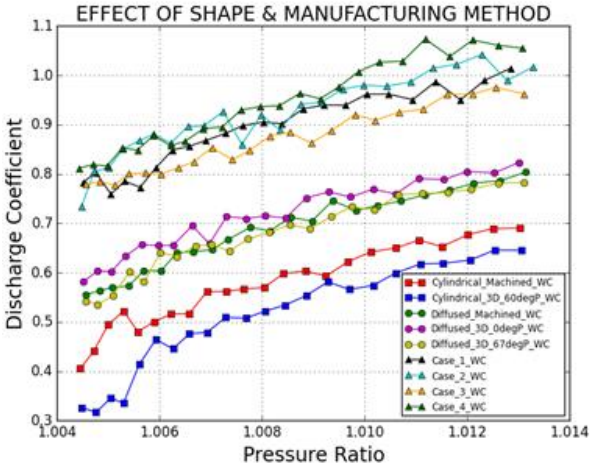

(c)

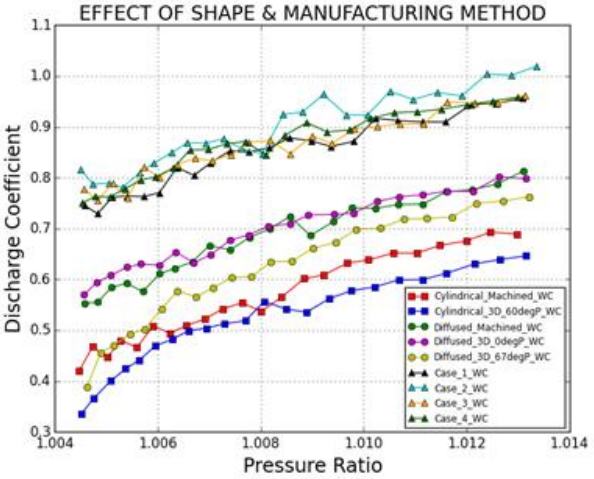

(d)

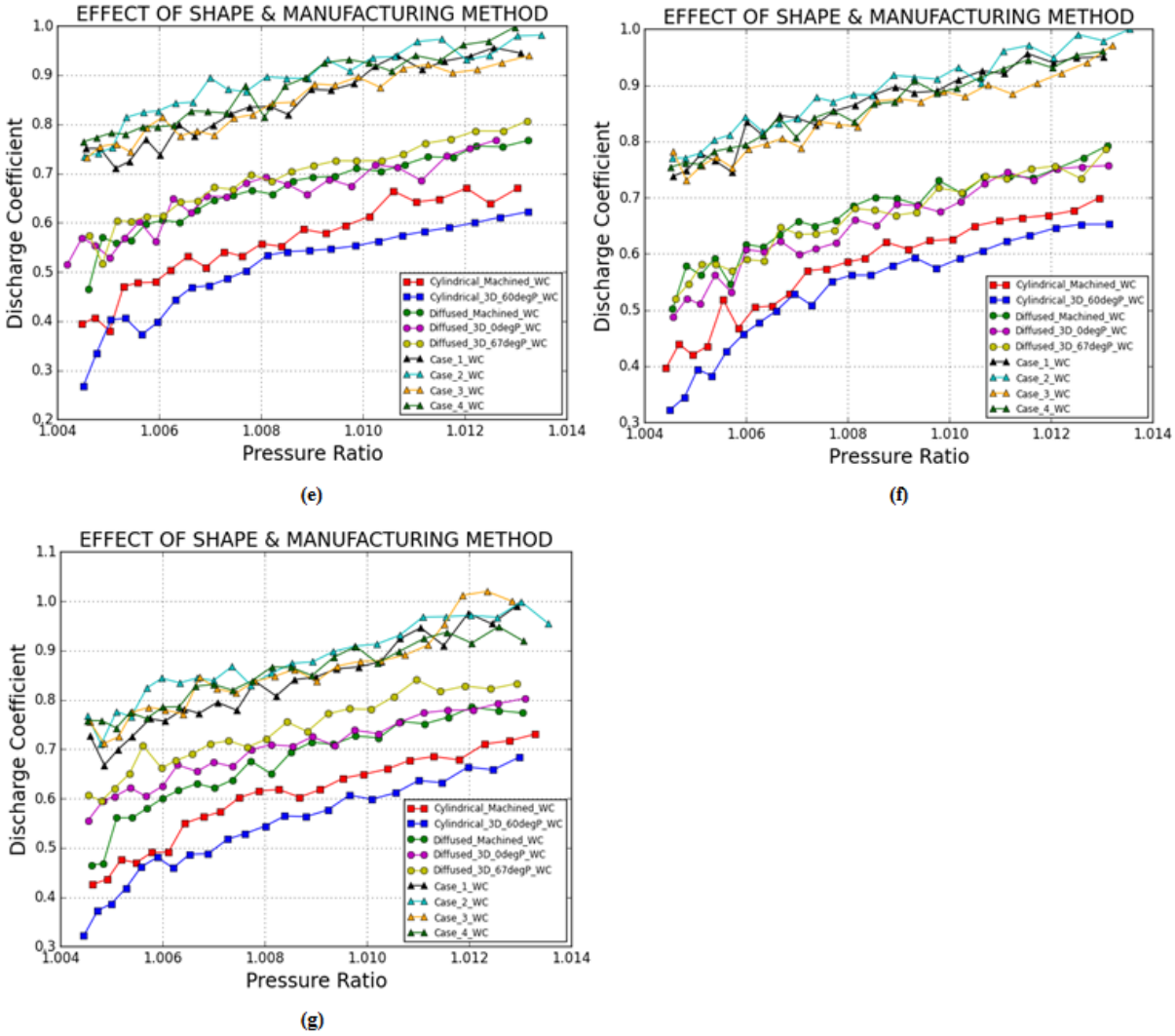

Figure 4-16: With mainstream flow, effect of hole geometry & manufacturing method, at different compound angles (CA). a) 0 degrees CA, b) 10 degrees CA, c) 20 degrees CA, d) 30 degrees CA, e) 40 degrees CA, f) 50 degrees CA, g) 60 degrees CA.

It is seen that, at the different compound angles, the trends do not significantly change from those reported above (at compound angle equals to zero (0) degrees). This is expected because it has been determined and reported previously, in this study, that the effect, on the discharge coefficient, of varying the compound angle is negligible. The slight deviations from the expected are assumed to be due to measurement uncertainty.

4.5.Conclusion

Based on the results and discussions above, it is concluded that:

- at low pressure ratios the discharge coefficient is a strong function of the pressure ratio, increasing with it, for all film cooling holes investigated;
- in the pressure ratio range tested, the mainstream crossflow only had a significant effect on the cylindrical and laidback fan-shaped holes. The effect of the mainstream crossflow was negligible for the cases where an arc was employed as the forward diffusion. This was due to the development of the flow inside the hole and the resulting exit coolant jet velocity profile and its interaction with the mainstream crossflow;
- the effect of the compound angle was found to be negligible for all film cooling hole geometries. This was a result of the development of the flow inside the hole and the

resulting exit coolant jet velocity profile and its interaction with the mainstream crossflow;

- higher discharge coefficient values are observed for the holes with expanded exits as compared to those of the cylindrical holes. The reason being pressure recovery in the expanded sections of the diffused holes;
- cases 1 to 4 showed higher discharge coefficient values as compared to the laidback fan-shaped holes. This was a result of the development of the flow inside the hole and the resulting exit coolant jet velocity profile and its interaction with the mainstream crossflow;
- the manufacturing method and 3D print orientation, regardless of the hole geometry, has a negligible effect on the discharge coefficient. This is due to the small relative roughness of the holes. This is more evident at low pressure ratios; and
- the inclination angle has a negligible effect on the discharge coefficient.

5.Flow field results and discussion

Presented in this chapter are the flowfield results downstream of the hole exit. The flowfield results presented are the normalized velocities and the secondary flow, normalized streamwise vorticity (Wx*D/U0). The normalized streamwise component of velocity, Ux/U0, is shown as contours and the normalized perpendicular components, Uy/U0 and Uz/U0, are plotted as vectors on the same plot.

The measurements are taken in two (2) planes, six (6) diameters and twelve (12) diameters downstream of the hole exit trailing edge, at two (2) blowing ratios, 0.9 and 1.3. These blowing ratios are characterised as low and high blowing ratios, respectively. Only two (2) compound angles, 0 and 20 degrees, are measured. Only the 3D printed hole geometries are investigated. This is because it was determined from the discharge coefficient results that the effect of manufacturing method and 3D print build orientation is negligible.

Normalized velocity results, with the inclusion of the turbulence grid, are also presented and discussed.

Shown in Figure 5-1 is the velocity boundary layer thickness of the approaching mainstream flow, with and without the inclusion of the turbulence grid. The boundary layer thickness is approximated at 99% of the mainstream flow velocity. It is at position approximately 4.53 in the flow without a turbulence grid. It seen that the flow with a turbulence grid is not as what is expected in channel flow. The boundary layer thickness helps determine whether the coolant jet is within the velocity boundary layer downstream of the film cooling holes.

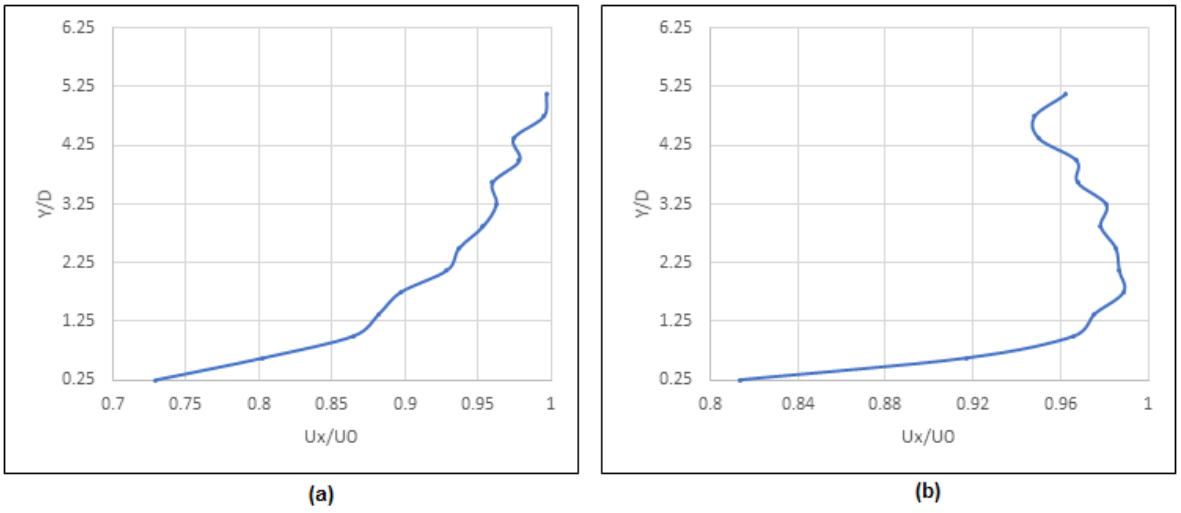

Figure 5-1: Velocity boundary layer thickness, a) flow without turbulence grid, b) flow with inclusion of turbulence grid.

The results also show that the flow has taken the appearance of a wake-like structure and it diffuses and takes on the shape of the boundary layer as it moves downstream. Additionally, it is also seen that the secondary flow is relatively weak. This agrees with the study by Walters and Leylek (1997), where it was reported that as close as five (5) diameters downstream, the secondary flows are negligible/weak; what is meant is that the effects of the secondary flow are weak. The effects of the secondary flow, downstream of the hole exit, include lifting the coolant jet from the surface and inhibiting lateral spread of the coolant on the surface by convecting coolant to the centreline. So, the coolant jet doesn't continue rising further from the

surface as it moves downstream. This is elaborated further in the discussions that follow below.

Looking at the velocity vector results in this chapter, and in Appendix H, for all the configurations investigated, it is seen that the shape is not like that commonly reported in literature. In literature, (Walters & Leylek 1997; Hayms & Leylek 2000), the velocity vectors around the jet core clearly show the presence of secondary motion, where circulatory motion in the regions of the coolant jet is clear. The student is uncertain of the cause. It was assumed that the discrepancy is due to resolution (the reader is reminded that measurements were taken at 3 mm increments).

The results show that the z-component of velocity is very small and the y-component of velocity dominates. Hence, the vectors are all mostly directed in the y-direction.

Consequently, the superimposed velocity vectors will be used as means to only locate the jet core and determine the range of its influence in the flow. The coolant jet core will be located in the area where a clear distortion in these vectors is seen. This distortion of the velocity vectors around the jet core is better seen in the results in Appendix H. These results have been included in the appendix for this purpose.

In the discussions below, coolant height refers to the height of the coolant jet core in the Y/D direction. Coolant lateral spread refers to the distribution of the coolant jet core in the Z/D direction.

5.1. Flow structure six (6) diameters downstream of hole exit (slot 1)

5.1.1. Blowing ratio of 0.9 and compound angle of zero (0) degrees

Figure 5-2 and show the flowfield results six (6) diameters downstream of the hole exit downstream edge at a compound angle of zero (0) degrees. Figure 5-2(a) is without coolant injection into the mainstream. Figure 5-2('b' to 'g') are the different hole geometries injecting coolant at a blowing ratio of 0.9. By comparing Figure 5-2(a) to Figure 5-2('b' to 'g'), there is clearly a distortion of the flowfield close to the wall, at y = 0 mm; the reader is reminded that the probe was two (2) mm from the wall at start position.

From the results it can be assumed, for all hole geometries, that the coolant jet core is relatively close to the wall. It is seen from the results that the distance of the coolant jet core from the wall cannot be determined. From this, it is determined that the 2 mm starting point distance from the wall, of the five hole probe, is not sufficient (too far), at low blowing ratios, to capture the location of the coolant jet core relative to the wall for the different hole geometries. Reasons why it was not possible to get close enough to the wall are given in section 3.8.2.

The location of the coolant jet (relative to the wall) far downstream of the hole exit is determined by two (2) primary mechanisms: 1) the strength of the vertical momentum content of the jet as it exits the hole; and 2) the strength of the longitudinal vortices as the jet moves downstream. The strength of both mechanisms is strongly dependent on the blowing ratio (Walters & Leylek 1997). This is discussed in more detail in section 5.1.2, where the effect of blowing ratio is investigated.

In the study by Walters and Leylek (1997) it was reported that, firstly, at low blowing ratios (= 0.5), because of the small vertical momentum of the coolant jet at the exit, the coolant jet remains close to the wall. Secondly, it was reported that at low blowing ratios the vortices degrade rapidly as the flow moves downstream because the locations of maximum vorticity, which corresponds to the centre of the vortices, are closer to the wall (Walters & Leylek 1997). Looking at it can be seen that the secondary flow is negligible for all hole geometries at a blowing ratio of 0.9.

One of the reasons for wanting the coolant jet, and hence, the counterrotating vortices to be closer to the surface is because of the destructive nature of the wall on the vortices. The vortices degrade film cooling performance because: 1) the longitudinal vortices continuously lift the coolant away from the surface, as the coolant jet moves downstream (the jet keeps rising from the surface the further it moves downstream – induction lift); and 2) the vortices inhibit lateral spread of the coolant on the surface by convecting coolant towards the centreline (Walters & Leylek 1997).

From close inspection of the velocity vector results and the streamwise vorticity results it is seen that the presence of the coolant, even at small blowing ratios, has a slight effect on the flow far from the wall. The difference between the measurements taken without coolant ejected into mainstream and the measurements taken with coolant ejected into mainstream highlight this observation.

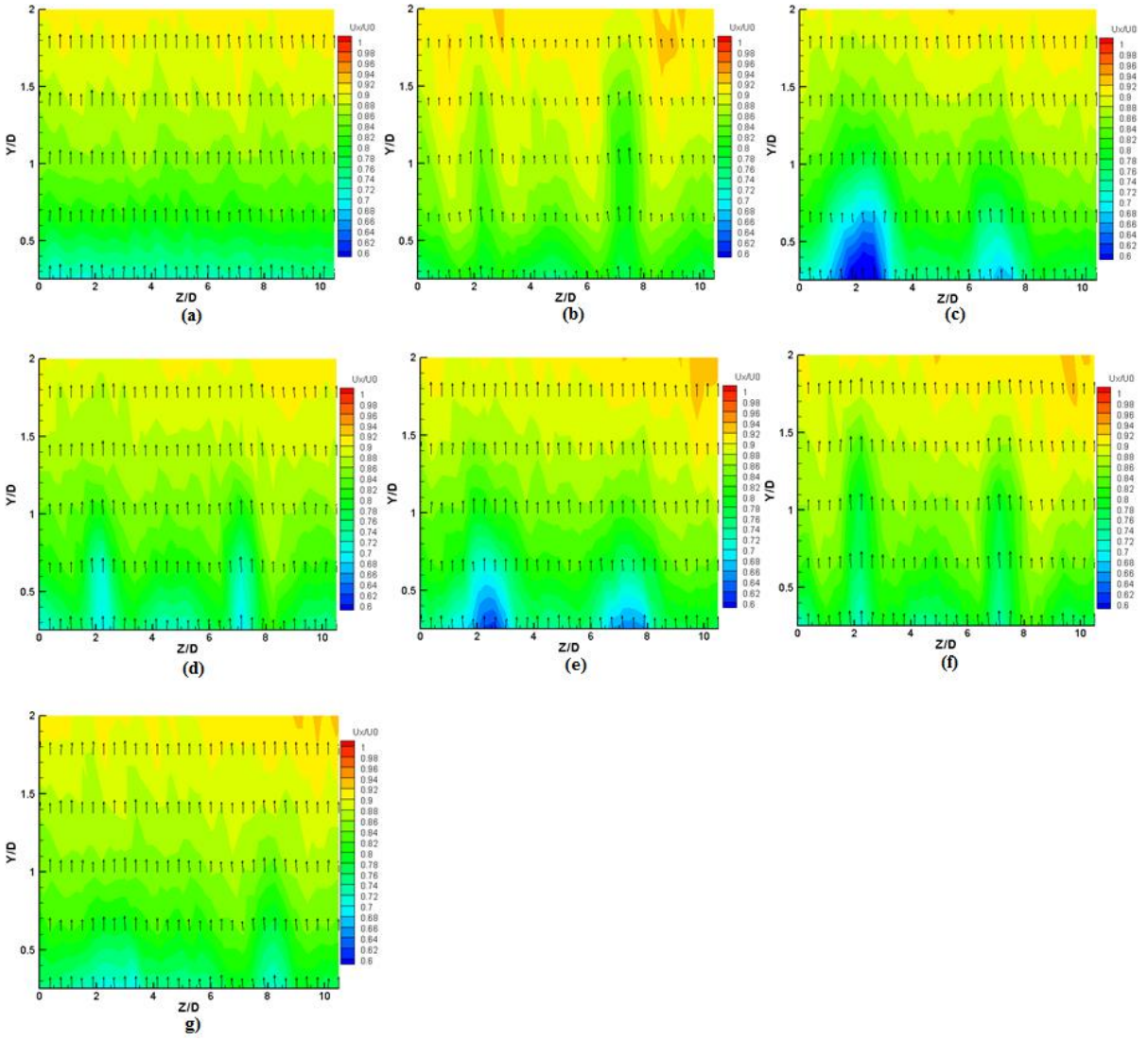

Figure 5-2: Flowfield measurements six (6) diameters downstream of hole exit trailing edge at blowing ratio of 0.9 and compound angle of zero (0) degrees. a) No coolant injection, b) cylindrical hole injection, c) laidback fan-shaped hole injection, d) case 1 hole injection, e) case 2 hole injection, f) case 3 hole injection, g) case 4 hole injection.

Regarding the effects of shape, because the flow structure results do not give detail closer to the wall, the student will initially compare the behaviour of the cylindrical hole and the laidback fan-shaped and support the discussions using literature.

In the studies by Sinha *et al.* (1991), Walters and Leylek (2000), and Bernsdorf *et al.* (2006), for streamwise aligned cylindrical holes, inclined 30 degrees, it was reported that the coolant jet begins to lift-off from the surface when the blowing ratio approaches 0.5. In the studies by Hayms and Leylek (2000), Bunker (2005), Bunker (2010), and Ekkad and Han (2013), it is reported that the shaped holes weaken the lift-off.

Based on the above, it can be stated with relative confidence that the cylindrical hole coolant jet core is not attached to the wall. Additionally, it is expected that the coolant jet core location of the cylindrical hole is farther from the wall, as compared to that of the laidback fan-shaped hole.

From the results of this study it is seen that the cylindrical hole has alittle more height (distance in the Y/D direction) as compared to the laidback fanshaped hole. But the laidback fan-shaped hole has more lateral spread (coolant jet coverage in the Z/D direction) as compared to the cylindrical hole.

The area expansion of the laidback fan-shaped hole should result in decreased effective velocity and vertical momentum content of the coolant jet on exit, which results in decreased penetration into the boundary layer of the crossflow. The area expansion should also result in relaxed velocity gradients on the side walls which decreases the strength of the streamwise film hole boundary layer vortices emanating from the hole. This decreases the strength of the counterrotating vortices. Additionally, the lateral spread of the laidback fan-shaped hole should locate the longitudinal vortices farther apart from each other such that the convective strength of the secondary flow at the centreline is reduced (Hayms & Leylek 2000). This would explain the higher height of the cylindrical holes and the increased lateral spread of the laidback fan-shaped holes.

Looking at the velocity contour results for the laidback fan-shaped hole it is seen that the flow structure from the coolant from the two (2) holes is not similar. This hints to an uneven distribution of coolant mass flow rates to the holes from the supply plenum. But if this were true, then similar behaviour would be observed for all the geometries tested. At the time of compiling this thesis there was still uncertainty towards the cause of this difference.

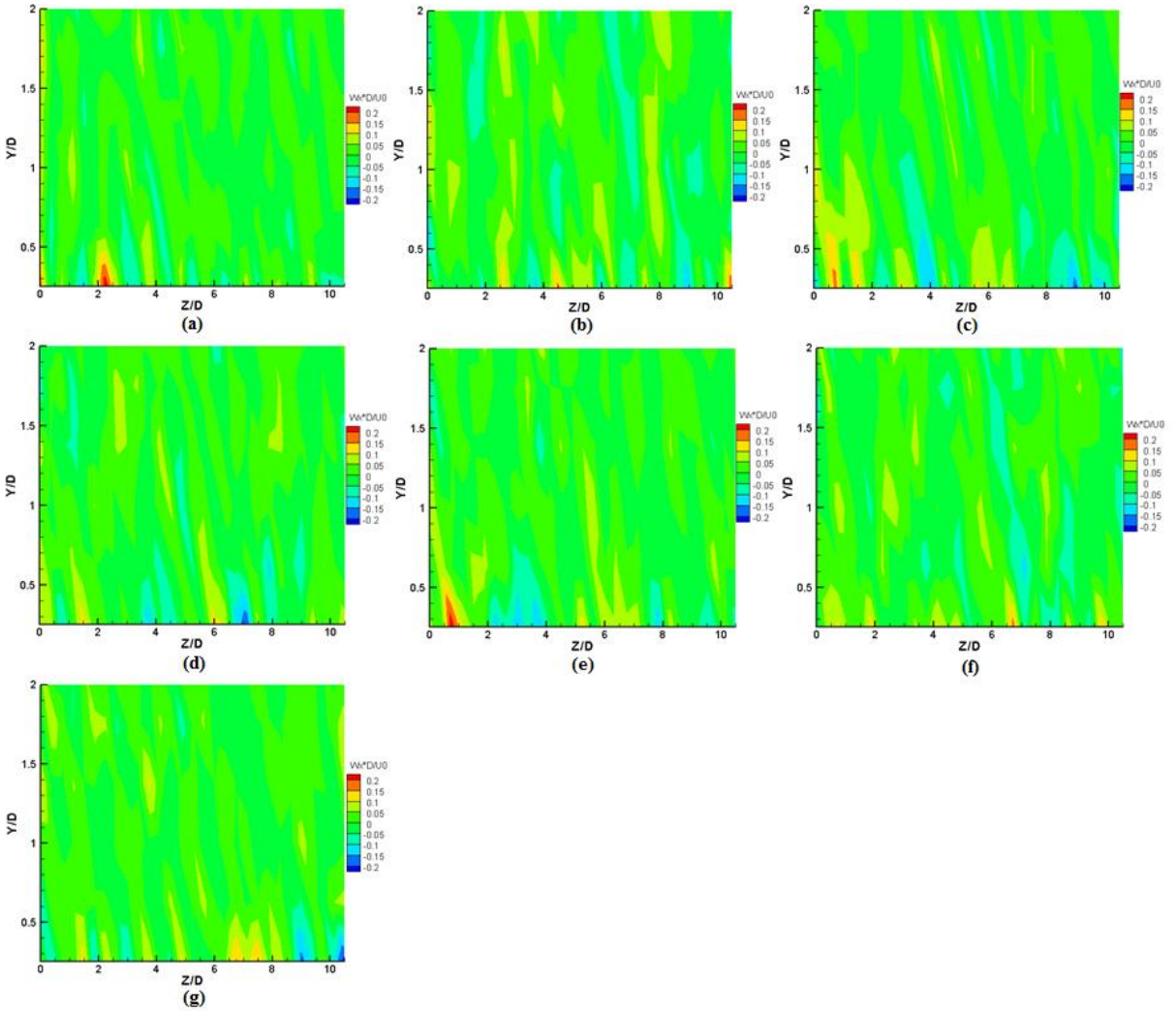

Figure 5-3: Streamwise vorticity measurements six (6) downstream of hole exit trailing edge at blowing ratio of 0.9 and compound angle of zero (0) degrees. a) no coolant injection, b) cylindrical hole injection, c) laidback fan-shaped hole injection, d) case 1 hole injection, e) case 2 hole injection, f) case 3 hole injection, g) case 4 hole injection.

Below, the student compares the behaviour of the baseline shapes, cylindrical and laidback fan-shaped, to the new shapes, cases 1 to 4, investigated in this study. Then, a comparison is made between the new shapes.

Comparing cases 1 to 4 to the cylindrical hole it is seen that the new shapes have better lateral spread and the cylindrical hole has more height. This is due to the area expansion in the new geometries.

As was explained previously, the area expansion decreases the effective velocity and the vertical momentum content of the coolant jet on exit, which decreases the penetration into the boundary layer of the crossflow (Hayms & Leylek 2000). This explains the higher height of the cylindrical hole.

Additionally, the area expansion relaxes the velocity gradients on the side walls which decreases the strength of the streamwise film hole boundary layer vortices emanating from the hole. This decreases the strength of the counterrotating vortices. Moreover, the lateral diffusion of the hole locates the longitudinal vortices farther apart from each other such that the convective strength of the secondary flow at the centreline is reduced (Hayms & Leylek 2000). This explains the better spread of the new shaped holes.

Regarding the effects of shape, comparing cases 1 and 3 to the laidback fan-shaped hole it is seen that the lateral spread of the laidback fan-shaped hole is superior, and the case 1 and 3 holes have higher height. The larger area expansion of the laidback fan-shaped hole due to the forward and lateral diffusion should significantly decrease the vertical momentum content of the coolant jet (Hayms & Leylek 2000). This would explain the higher height for the case 1 and 3 holes.

The smaller lateral spread of the case 1 and 3 holes is due to the smaller lateral expansion, 3.46 and 4.63 degrees respectively, as compared to the seven (7) degrees lateral expansion, on either side, for the laidback fanshaped hole. As explained previously, the increased lateral expansion locates the longitudinal vortices farther apart from each other such that the convective strength of the secondary flow at the centreline is reduced (Hayms & Leylek 2000).

Regarding the effects of shape, comparing case 2 and 4 to the laidback fan-shaped hole it can be said that slightly better lateral spread is observed for cases 2 and 4; case 4 spreading even better than case 2. The added lateral expansions of case 2 and 4 results in the better lateral spread observed.

Differences in coolant height between the configurations are not immediately obvious. But the student believes that the case 2 and case 4 holes should have lower height because they should have a lower vertical momentum content. The reason for this is that they have larger lateral expansions and the employed curvature should decrease the trajectory of the jet on exit.

Additionally, the decreased trajectory should position the longitudinal vortices even closer to the wall; the walls destructive effects on the streamwise vortices has been explained previously. This results in decreased upwards lift (Walters & Leylek 1997). This also reinforces the point of better lateral spread observed for case 2 and 4.

Comparing the new shapes against each other, it is seen that cases 2 and 4 have better lateral spread and cases 1 and 3 have better height. This is due to the increased lateral expansion of the holes in cases 2 and 4. As explained above, the added lateral expansion decreases the effective velocity and the y-momentum content of the coolant jet on exit, which decreases the penetration into the boundary layer of the crossflow. In addition, the added lateral expansion relaxes the velocity gradients on the side walls which decreases the strength of the streamwise film hole boundary layer vortices emanating from the hole. This decreases the strength of the counterrotating vortices. Additionally, the increased lateral expansion of the holes locates the longitudinal vortices farther apart from each other such that the convective strength of the secondary flow at the centreline is reduced (Hayms & Leylek 2000).

5.1.2. Blowing ratio of 1.3 and compound angle of zero (0) degrees

Shown in Figure 5-4 and are the flowfield results at a blowing ratio of 1.3. Comparing the velocity results, Figure 5-4, to those at a blowing ratio of 0.9, it is immediately seen that for the cylindrical hole, case 1 and case 3 holes, the coolant jet is not on the surface. For the laidback fanshaped hole, case 2 and case 4 holes, the coolant is still relatively close to the surface. It is evident that a significant difference between the configurations where the coolant has significantly lifted-off the wall and where it has remained relatively closer to the surface is the degree of lateral expansion. This is explained further in the discussions below.

Looking at the secondary flow results in , and comparing them to those at a blowing ratio of 0.9, it is seen that the counterrotating vortex structures are more pronounced and are positioned farther from the wall for the cylindrical hole, the Case 1 hole and the Case 3 hole. For the laidback fan-shaped hole, the Case 2 hole and the Case 4 hole, the velocity vectors,

Figure 5-4, are slightly more distorted as compared to the measurements taken at a blowing ratio of 0.9 but the secondary flow measurements show a negligible difference.

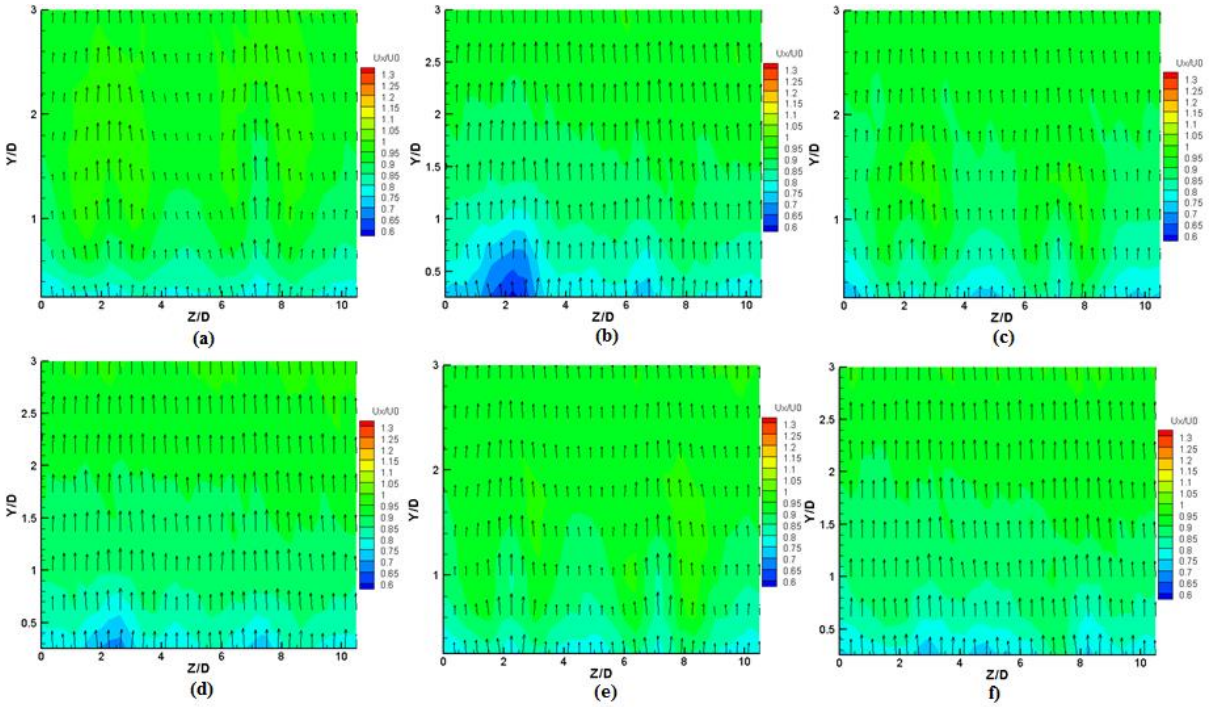

Figure 5-4: Flowfield measurements six (6) diameters downstream of hole exit trailing edge at blowing ratio of 1.3 and compound angle of zero (0) degrees. a) cylindrical hole injection, b) laidback fan-shaped hole injection, c) case 1 hole injection, d) case 2 hole injection, e) case 3 hole injection, f) case 4 hole injection.

Regarding the effects of blowing ratio (blowing ratio = 0.9 vs blowing ratio = 1.3), the behaviour observed for the cylindrical hole, the Case 1 hole and the Case 3 hole, is due to the initial positioning, in the near-field, of the coolant jet as it exits the hole coupled with the increased strength of the counterrotating vortices (due to the increased blowing ratio) as the coolant jet moves downstream. The strength of the counterrotating vortices, which is related to the upward lift (induction lift) generated by the counterrotating vortices downstream of the hole exit, is strongly dependent on the blowing ratio (Walters & Leylek 1997).

It is reported in literature that, at higher blowing ratios (=1 in the study by Walters and Leylek 1997), the increased vertical momentum of the jet positions it farther from the wall as it exits the film cooling hole. This is not ideal because the destructive effects of the wall on the vortices is not utilised. This results in further increased strength of the longitudinal vortices (Walters & Leylek 1997).

As the coolant jet moves downstream, it is lifted further away from the surface by the counter-rotating vortices. Since the location of maximum vorticity is farther from the wall the streamwise counter-rotating vorticity is dissipated less rapidly and is apparent farther downstream (Walters & Leylek 1997).

Regarding the effects of blowing ratio for the Case 2 hole, Case 4 hole and the laidback fan-shaped hole it is seen that the increased blowing ratio had very little impact on the observed behaviour; the height and lateral spread of the coolant looks relatively the same. This tells us that, for these geometries, the increased blowing ratio did not significantly strengthen the

mechanisms that result in poor film cooling performance in other geometries. These mechanisms include the strengthening of the longitudinal vortices which results in, 1) coolant upwards lift from the surface and 2) the inability of the coolant to properly laterally spread because of the strengthened coolant convection towards the centreline.

Comparing the behaviour of the cylindrical hole, the Case 1 hole and the Case 3 hole to the laidback fan-shaped hole, the Case 2 hole and the Case 4 hole, the student isolates the degree of lateral expansion as the key player in the observed behaviour. The added lateral expansion significantly reduces the vertical momentum content of coolant jet which positions it close to the wall on exit. Additionally, it locates the longitudinal vortices farther apart from each other which reduces the induction lift and convective strength (Hayms & Leylek 2000).

Regarding the effects of shape, comparing Case 1 and 3 to the cylindrical hole, it is seen that the coolant jet core is located slightly farther from the wall for the cylindrical hole. The streamwise vorticity results show that the is increased strength in the counterrotating vortices for the cylindrical hole.

This is due to the area expansion in cases 1 and 3. As explained previously, the area expansion decreases the effective velocity and the vertical momentum content of the coolant jet on exit, which decreases the penetration into the boundary layer of the crossflow. And the area expansion relaxes the velocity gradients on the side walls which decreases the strength of the streamwise film hole boundary layer vortices emanating from the hole. This decreases the strength of the counterrotating vortices. Additionally, the lateral expansion of the holes locates the longitudinal vortices farther apart from each other such that the convective strength of the secondary flow at the centreline is reduced (Hayms & Leylek 2000).

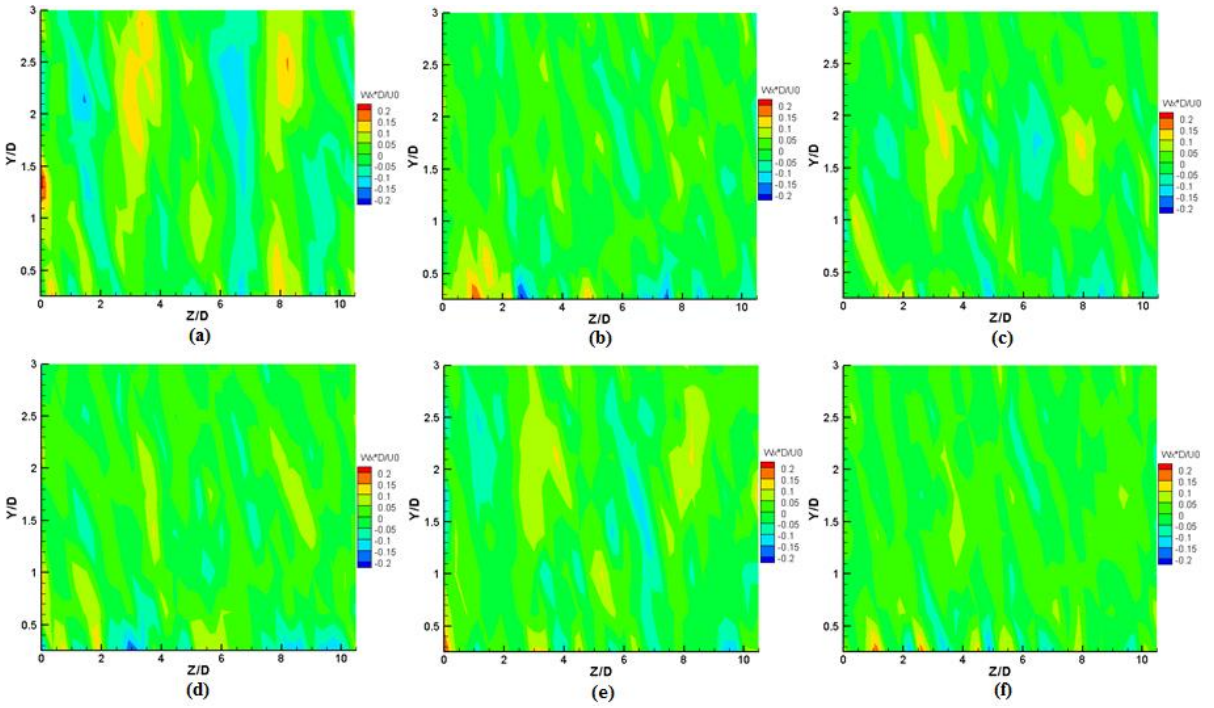

Figure 5-5: Streamwise vorticity measurements six (6) diameters downstream of hole exit trailing edge at blowing ratio of 1.3 and compound angle of zero (0) degrees. a) cylindrical hole injection, b) laidback fan-shaped hole injection, c) case 1 hole injection, d) case 2 hole injection, e) case 3 hole injection, f) case 4 hole injection.

Regarding the effects of shape, in comparing case 2 and 4 to the laidback fan-shaped hole similar patterns, as those at a blowing ratio of 0.9, are observed. Therefore, similar physical mechanisms must dictate the patterns observed. The reader is encouraged to consult the

discussions at a blowing ratio of 0.9. This tells us that increasing the blowing ratio did not significantly change the effect of these mechanisms on the flow behaviour.

5.1.3.Blowing ratio of 0.9 and compound angle of 20 degrees

Shown in Figure 5-6 and Figure 5-7 are the flowfield results at a blowing ratio of 0.9 with the holes oriented 20 degrees to the mainstream flow direction. From the velocity results it is seen, for all hole geometries, that the coolant is still relatively close to the wall. Similar behaviour was observed when the compound angle was zero (0) degrees to the mainstream flow direction. The reasons given for the behaviour observed at zero (0) degrees compound angle stand for the configuration when the holes are oriented 20 degrees to the mainstream flow direction.

Comparing the velocity results with those at a compound angle of zero (0) degrees, it is immediately seen that the coolant jet is skewed to the right. It could also be argued that better lateral spread is achieved. The reason for the skewness that comes to mind first is that more coolant is exiting from the high momentum flux region or upstream of the film hole. Due to the higher blockage caused by the mainstream flow on the downstream of film cooling hole more coolant is forced to exit on the upstream. This would agree with results from the study by Burd and Simon (1999) and, McGovern and Leylek (2000).

In a study by McGovern and Leylek (2000) it was reported that differences are observed at the exit, as compared to the streamwise case, due to significant changes in the pressure field at the exit. These changes in the pressure field cause higher blockage at the exit, which leads to deviations of the coolant trajectory after it leaves the film hole.

The reader is reminded that the length to diameter ratio of the holes in the by Burd and Simon (1999) and the study by McGovern and Leylek (2000) was 3.5 and 4, respectively. These are classified as short holes. For inclined short holes, when a stagnant plenum is supply, it has been reported that the velocity profile at the hole exit is expected to be skewed to the upstream edge of the hole because of the separation region at the inlet and the short distance to the hole exit (Leylek & Zerkle 1993; Burd & Simon 1999). Therefore, the higher blockage of the coolant jet at the downstream edge is due to its skewness of the coolant jet at the hole exit.

In the current study, the length to diameter ratio of the holes is 7.5, which is classified as a long hole. The reader is reminded that it was determined, in the discharge coefficient results and discussion, that the exiting jet profile is expected to be relatively uniform because the length, after separation at the inlet, allows for the jet to approach fully developed flow. This implies that regardless of the orientation of the holes the mainstream flow initially contacts a relatively uniform profile across the hole. This is especially true for the cylindrical holes. For the geometries with expanded exits it was determined that slight upstream skewness of the coolant jet at the hole exit should exist.

Therefore, the skewness of the coolant jet downstream of the hole exit cannot be primarily due to higher blockage at the hole exit.

Looking at the velocity vector results it is seen that close to the wall the velocity vectors predominantly point to the right direction.

It has been reported that in compound angle injection, as compared to streamwise injection, the vorticity generated at the interface plays a significant role in the vortex structure downstream of hole exit. The vortex structure downstream of the hole exit, in compound angle injection, is strongly dependent on the compound angle. As the compound angle is increased, the originally symmetric counter-rotating vortex structure becomes increasingly asymmetric due to a weakening of one (1) of the vortices in the pair and the strengthening of the other.

The weakening of the one (1) vortex in the pair is caused by crossflow blockage of the film hole boundary layer that comes into initial contact with the crossflow. The strengthening of the other vortex in the pair is due to the shearing between the crossflow and the jet increasing the strength of the vortex in the pair (McGovern and Leylek 2000).

In the far-field, the asymmetric vortex structure eventually collapses into a single rotating vortex with significant lateral motion of the coolant near the wall. The coolant core is convected and diffused towards the surface more quickly which results in better lateral spread of the coolant. The vortex losses strength with downstream distance (McGovern and Leylek 2000).

Based on the above the student concludes that the skewness to the right of the coolant jet downstream is primarily due to the significant lateral motion imposed by the asymmetric vortex structure. Unfortunately, looking at the streamwise vorticity results, the asymmetry of the vortex structure is not immediately apparent.

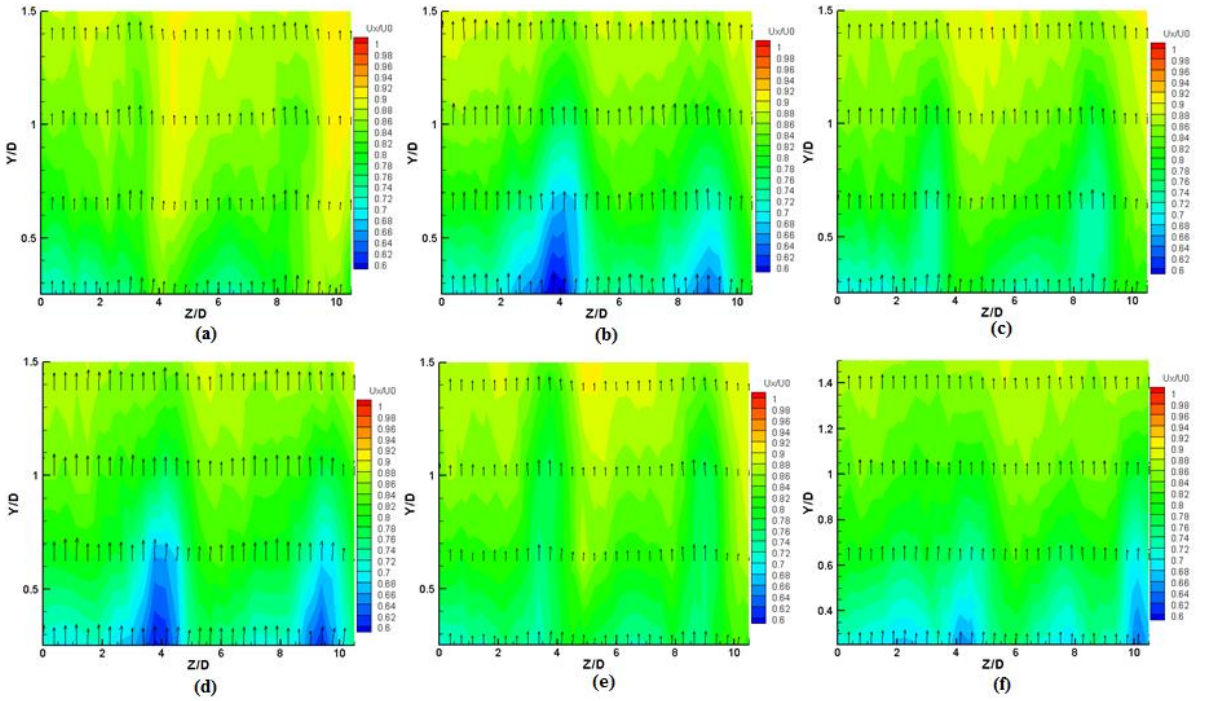

Figure 5-6: Flowfield measurements six (6) diameters downstream of hole exit trailing edge at blowing ratio of 0.9 and compound angle of 20 degrees. a) cylindrical hole injection, b) laidback fan-shaped hole injection, c) case 1 hole injection, d) case 2 hole injection, e) case 3 hole injection, f) case 4 hole injection.

Regarding the effects of shape, it is reported by Brittingham and Leylek (2000), that the differences in the vorticity for the different shapes and compound angles is due to the differences in the strength of the vorticity emanating from the film hole boundary layer (it was determined to be a strong function of shape) and the differences in strength of the vortices generated by jet-crossflow shearing (it was determined to be a strong function of compound angle). Basically, the combined effects of the hole geometry and compound angle determines the strength of the longitudinal vorticity which determines the film cooling performance downstream of the hole exit.

Comparing the laidback fan-shaped hole to the cylindrical hole, it is seen that the coolant jet from the cylindrical hole has more height and the coolant jet from the laidback fan-shaped hole has a more uniform distribution close to the wall.

The increased height of the coolant from the cylindrical hole is due to the increased vertical momentum content as the jet exits the hole. This allows for increased penetration into the

mainstream boundary layer and it positions the coolant farther from the wall on exit (Hayms & Leylek 2000).

The more uniform distribution of the coolant from the laidback fan-shaped hole is due to the decreased strength of the longitudinal vortices which results in reduced convective strength. This is as a result of the area expansion. This allows the coolant jet to diffuse better/more uniformly (Hayms & Leylek 2000).

Similar mechanisms, as those discussed above, are seen to dictate the behaviour observed in the other geometries when the different geometries are categorized in terms of those with significant lateral expansion (laidback fan-shaped hole, Case 2 hole and Case 4 hole) and those with less lateral expansion (cylindrical hole, Case 1 hole and Case 3 hole).

Regarding the effects of shape, in comparing Case 1 and Case 3 to the cylindrical hole it is seen that the Case 1 and 3 holes show heights that are comparable to the cylindrical hole. Increased lateral spread is expected for the Case 1 and Case 3 holes because of the lateral expansions. It is also seen that the coolant jet presence in the mainstream flow is more pronounced for Case 1 and 3.

As discussed above, the better lateral spread is due to the area expansion which decreases the strength of the longitudinal vortices. This results in reduced convective strength and allows the coolant jet to diffuse better/more uniformly (Hayms & Leylek 2000).

The better presence of the coolant jet in the mainstream flow tells us that employing the curvature results in less counterproductive interaction with the mainstream on exit. Hence, the coolant jet has more momentum in the streamwise direction.

Increased momentum in the streamwise direction would result in the coolant jet reaching further downstream for cooling purposes. This means that less holes can be used to achieve the required cooling downstream. Drilling less holes saves on cost and the structural integrity of the component.

Regarding the effects of shape, in comparing Case 2 and Case 4 to the laidback fan-shaped hole similar patterns, as those for the streamwise oriented hole at a blowing ratio of 0.9, are observed. This tells us that, for these geometries, even though the mechanisms that dictate the downstream flow structure differ, between the streamwise and the 20 degrees oriented, their effect produces the same pattern of behaviour downstream. The student suspects that this is largely determined by the lateral expansion of the holes.

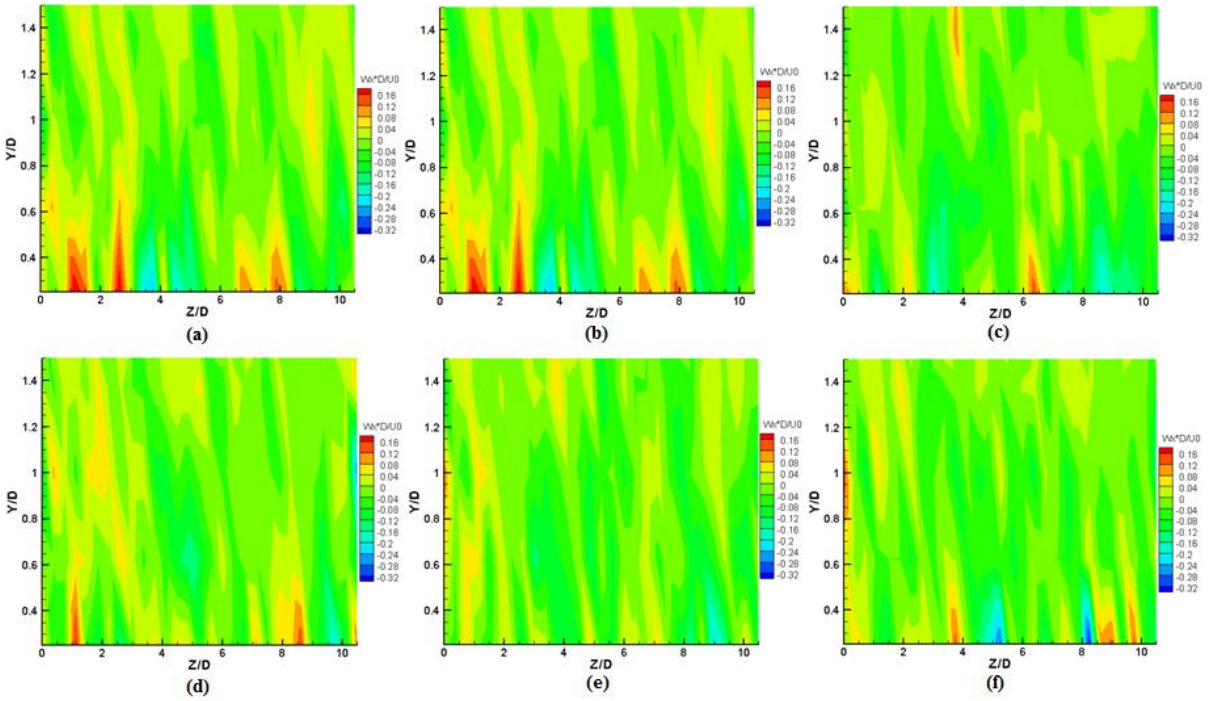

Figure 5-7: Streamwise vorticity measurements six (6) diameters downstream of hole exit trailing edge at blowing ratio of 0.9 and compound angle of 20 degrees. a) cylindrical hole injection, b) laidback fan-shaped hole injection, c) case 1 hole injection, d) case 2 hole injection, e) case 3 hole injection, f) case 4 hole injection.

5.1.4.Blowing ratio of 1.3 and compound angle of 20 degrees

and are the flowfield results at a blowing ratio of 1.3 with the holes oriented 20 degrees to the mainstream flow direction. Comparing the velocity results to those at a compound angle of 20 degrees and a blowing ratio of 0.9, it is immediately seen that for the cylindrical hole, case 1 and case 3, the coolant jet is significantly lifted from the surface.

Looking at the secondary flow results and comparing them to the results at a compound angle 20 degrees and blowing ratio 0.9, it is seen that the vortex structures are more pronounced and are positioned relatively far from the wall. Additionally, the asymmetry of the longitudinal vortices is more pronounced.

As stated previously, the behaviour observed for the cylindrical hole, the Case 1 hole and the Case 3 hole, is due to the initial positioning, in the near-field, of the coolant jet as it exits the hole coupled with the increased strength of the counterrotating vortices as the coolant jet moves downstream. The strength of the counterrotating vortices, which is related to the upward lift (induction lift) generated by the counterrotating vortices downstream of the hole exit, is strongly dependent on the blowing ratio (Walters & Leylek 1997).

It is reported in literature that, at higher blowing ratios, the increased vertical momentum of the jet positions it farther from the wall as it exits the film cooling hole. This is not ideal because the destructive properties of the wall on vortices is not utilised. This results in further increased strength of the longitudinal vortices (Walters & Leylek 1997).

As the coolant jet moves downstream, the coolant jet is lifted away from the surface by the counter-rotating vortices. Since the location of maximum vorticity is farther from the wall the streamwise counter-rotating vorticity is dissipated less rapidly and is apparent farther downstream (Walters & Leylek 1997).

For the laidback fan-shaped hole, Case 2 and Case 4 hole, comparing the velocity results, to those at a compound angle of 20 degrees and a blowing ratio of 0.9, it is seen that the coolant

is still closer to the wall. But the coolant jet is slightly more pronounced in the mainstream flow. This is expected because an increased amount of coolant is being injected into the flow.

The velocity vectors are slightly more distorted as compared to the measurements taken at a blowing ratio of 0.9 and a compound angle of 20 degrees, but the secondary flow measurements show a negligible difference.

This tells us that, for these geometries, even at a compound angle of 20 degrees the increased blowing ratio did not significantly strengthen the mechanisms that result in decreased film cooling performance in other geometries.

It is suspected that the lateral expansion is a key player in determining what is discussed in the paragraph above. This is supported by the fact that upwards lift is observed for the Case 1 and Case 3 hole, where, in these geometries the lateral expansion is relatively small.

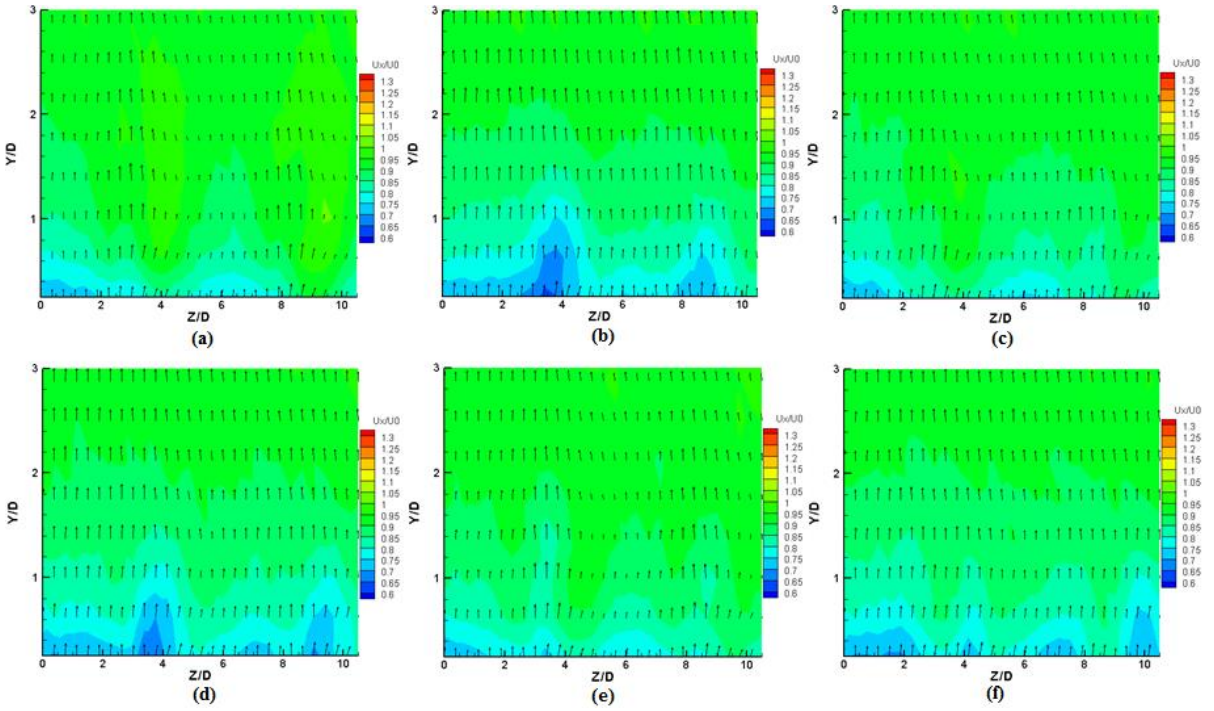

Figure 5-8: Flowfield measurements six (6) diameters downstream of hole exit trailing edge at blowing ratio of 1.3 and compound angle of 20 degrees. a) cylindrical hole injection, b) laidback fan-shaped hole injection, c) case 1 hole injection, d) case 2 hole injection, e) case 3 hole injection, f) case 4 hole injection.

Regarding the effect of shape, comparing the Case 1 and 3 hole to the cylindrical hole it is seen that the velocity results are not helpful; the location of the jet is not distinguishable for the Case 1 and Case 3 hole. From the streamwise vorticity results, increased strength in the counterrotating vortices for the cylindrical hole leads the student to conclude that the coolant jet core is located further from the wall, as compared to the case 1 and 3 hole.

This is due to the area expansion in Cases 1 and 3. As was explained previously, the area expansion decreases the effective velocity and the vertical momentum content of the coolant jet on exit, which decreases the penetration into the boundary layer of the crossflow. And, the area expansion relaxes the velocity gradients on the side walls which decreases the strength of the streamwise film hole boundary layer vortices emanating from the hole. This decreases the strength of the counterrotating vortices which results in upward lift from the surface (Hayms & Leylek 2000).

Regarding the effect of shape, comparing the Case 2 hole, Case 4 hole and the laidback fan-shaped hole, it is seen that the coolant jet from the Case 2 and the laidback fanshaped hole has higher height than the Case 4 hole. This is because the curvatures, on the upstream and downstream edge of the Case 4 hole, forces the coolant jet to be closer to the wall; the jet has less vertical momentum content. This coupled with the larger lateral expansion results in better lateral spread for the case 4 geometry.

Comparing the behaviour of the Case 2 geometry to the laidback fan-shaped hole it is seen that the Case 2 geometry has slightly less height because the curvature allows the coolant jet to be closer to the wall on exit; the destructive nature of the wall on the longitudinal has already been mentioned several times previously. This coupled with the slightly larger expansion angle, which locates the longitudinal vortices farther apart, results in better lateral spread. As stated previously, the vortices positioned farther apart diminishes induction lift on the coolant jet.

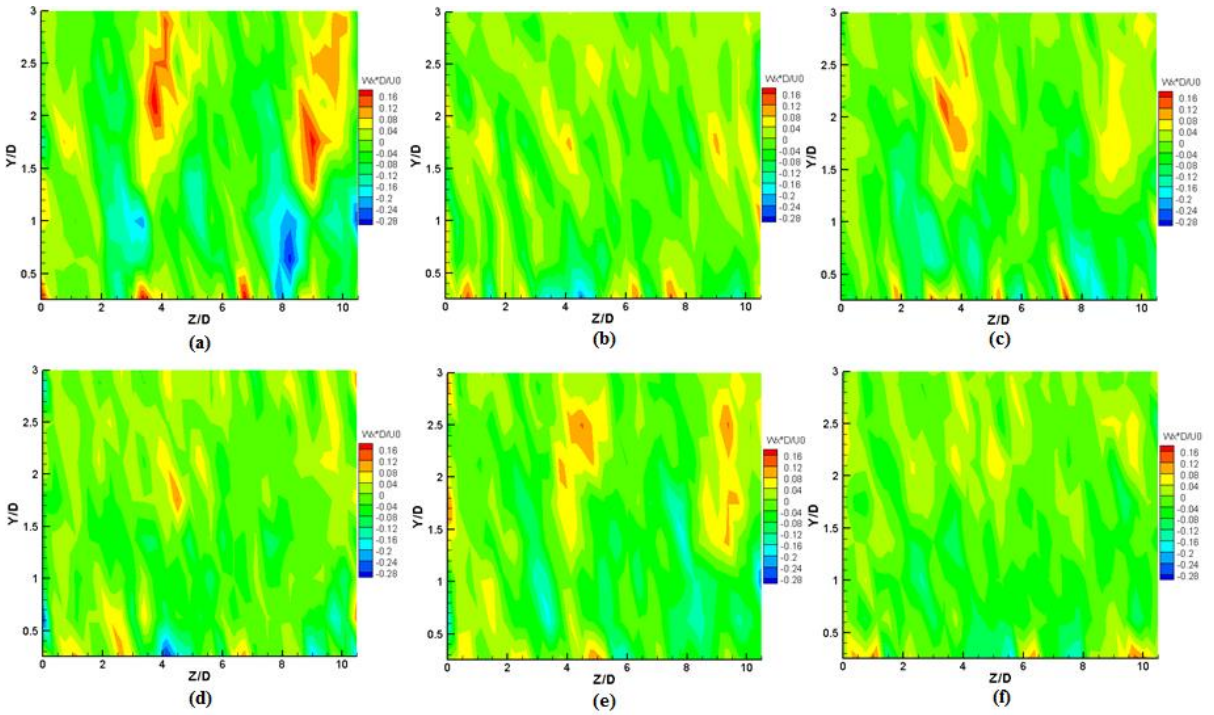

Figure 5-9: Streamwise vorticity measurements six (6) diameters downstream of hole exit trailing edge at blowing ratio of 1.3 and compound angle of 20 degrees. a) cylindrical hole injection, b) laidback fan-shaped hole injection, c) case 1 hole injection, d) case 2 hole injection, e) case 3 hole injection, f) case 4 hole injection.

Comparing the velocity results to those at a compound angle of zero (0) degrees, it is immediately seen, for all the geometries, that the motion of the coolant jet is skewed to the right. This is seen from the velocity vectors. According to McGovern and Leylek (2000) and, Brittingham and Leylek (2000) this is due to the lateral motion imposed by the asymmetric vortex structure.

In extant literature it has been reported that in compound angle injection, as compared to streamwise injection, the vorticity generated at the interface plays a significant role in the vortex structure downstream of hole exit. The vortex structure downstream of the hole exit, in compound angle injection, is strongly dependent on the compound angle. As the compound angle is increased, the originally symmetric counter-rotating vortex structure becomes increasingly asymmetric because of a weakening of one (1) of the vortices in the pair and the strengthening of the other. The weakening of the one (1) vortex in the pair is caused by

crossflow blockage of the film hole boundary layer that comes into initial contact with the crossflow. The strengthening of the other vortex in the pair is due to the shearing between the crossflow and the jet increasing the strength of the vortex in the pair (McGovern & Leylek 2000).

In the far-field, the asymmetric vortex structure eventually collapses into a single rotating vortex with significant lateral motion of the coolant near the wall. The coolant core is convected and diffused towards the surface more quickly which results in better lateral spread of the coolant. The vortex losses strength with downstream distance (McGovern & Leylek 2000).

5.1.5.Effect of turbulence grid

Below, the student presents the flow strucure measurements six (6) diameters downstream of the hole exit with the turbulence grid. The turbulence grid was positioned 600 mm from the upstream edge of the cooling holes. Because of the turbulence grid, the freestream velocity dropped from approximately 16 m/s to 12 m/s. The calculated freetsream turbulence intensity was 4.89 percent. This is a theoretically based approximation by Roach (1987). Unfortunately the turbulence intensity could not be measured. The coolant mass flow rate was adjusted accordingly to provide the required blowing ratios of 0.9 and 1.3.

The flowfield results presented are the streamwise components of velocities, Ux, are shown as contours and the perpendicular components, Uy and Uz, are plotted as vectors in the same plot. The streamwise vorticity results have been presented in Appendix H.

Comparing all the results presented below to those without a turbulence grid, it is immediately evident that the behaviour of the coolant jet in the mainstream flow is nominally the same. This tells us that the physical mechanisms that determine the flow behaviour downstream in the case ‘without a turbulence grid’ are still dominant in the case ‘with a turbulence grid’; the turbulence grid had little effect on the behaviour.

It was expected by the student that the added turbulence, induced by the turbulence grid, would aid in the process of diffusing the coolant on the surface. Diffusing the coolant on the surface is ideal because a uniform distribution of the coolant on the surface is sought after. This results in even insulation/protection of the surface from the mainstream gases.

It is reported in the study conducted Roach (1987) that the formation and growth of the turbulence eddies is strongly inhibited by the duct walls if the grid dimensions are large relative to the duct dimensions. Roach (1987) recommended that the grid mesh be much less than 10 percent of the minimum side length of the duct.

In the current study the ratio of the largest side in the grid mesh to the smallest side length of the duct is greater than 10 percent (see equation (29)). Therefore, it is expected that the measured freestream turbulence is less than the theoretically based calculated freestream turbulence. This explains the negligible effect of the incorporation of the turbulence grid on the flow structure.

$$\frac{\mathrm{M}}{\mathrm{W}} = \frac{50}{375} \times 100 = 13.3\% \qquad (29)$$

where ‘M’ is the mesh length and ‘W’ is the tunnel width.

Figure 5-10 shows that at the blowing ratio of 0.9, for all geometries, the coolant jet is relatively close to the surface. It is also seen that the geometries with less expansion areas (cylindrical, Case 1 and Case 3 hole) have more height, as compared to the geometries with larger expansion areas (laidback fan-shaped, Case 2 and Case 4 hole). The geometries with larger

lateral expansions show better spread of the coolant downstream of the hole exit. The mechanisms that determine the behaviours observed have been discussed in detail in the sections above.

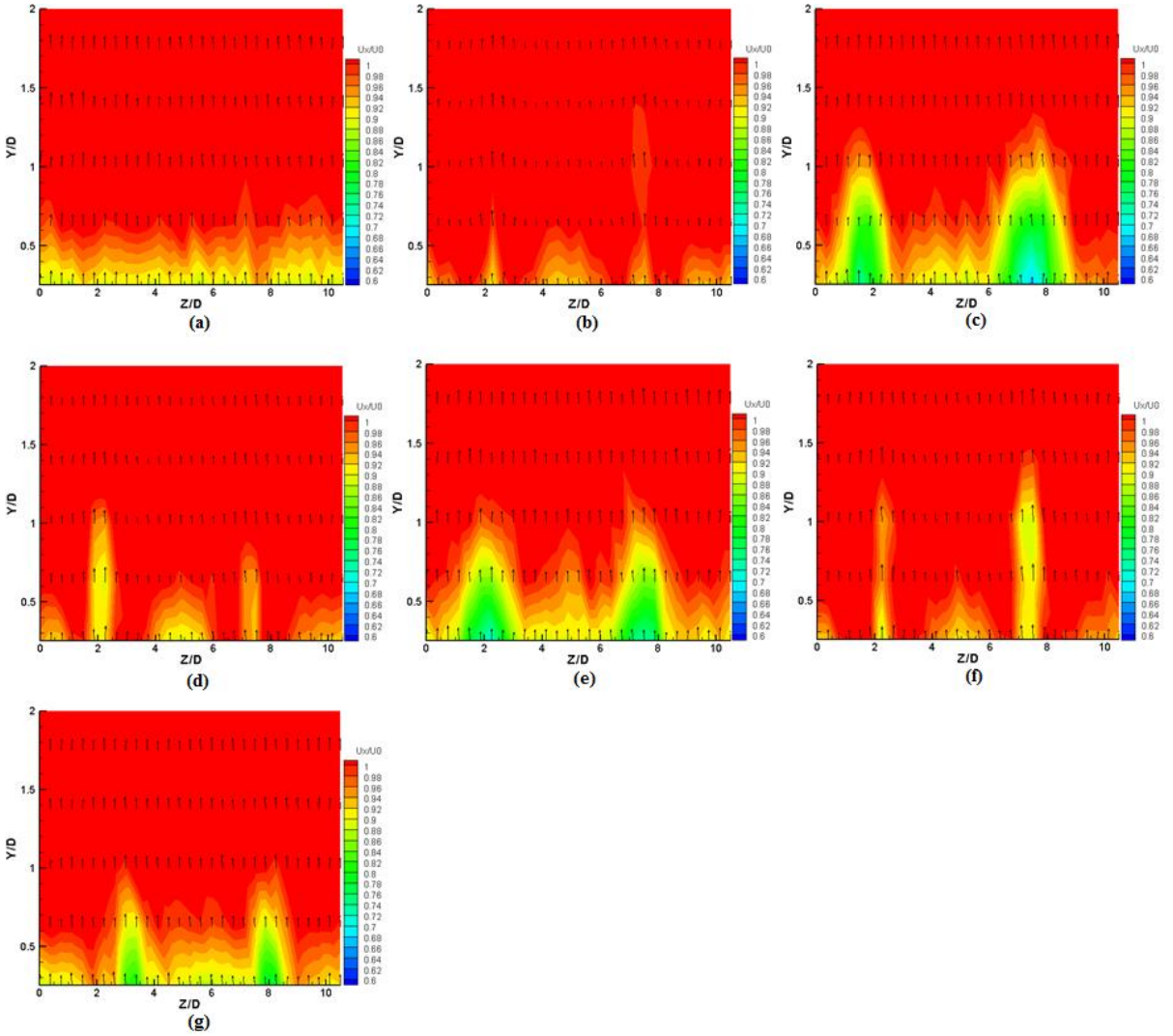

Figure 5-10: With turbulence grid flowfield measurements six (6) diameters downstream of hole exit trailing edge at blowing ratio of 0.9 and compound angle of zero (0) degrees. a) No coolant injection, b) cylindrical hole injection, c) laidback fan-shaped hole injection, d) case 1 hole injection, e) case 2 hole injection, f) case 3 hole injection, g) case 4 hole injection.

Figure 5-11 shows the results at a blowing ratio of 1.3. Comparing the results to those at a blowing ratio of 0.9 it is immediately seen that for the cylindrical hole, Case 1 and Case 3 holes, the coolant jet is significantly further from the surface. For the laidback fanshaped hole, Case 2 and Case 4 holes, the coolant is still close to the surface. As determined in the sections above this is significantly determined by the differences in lateral expansion between the geometries.

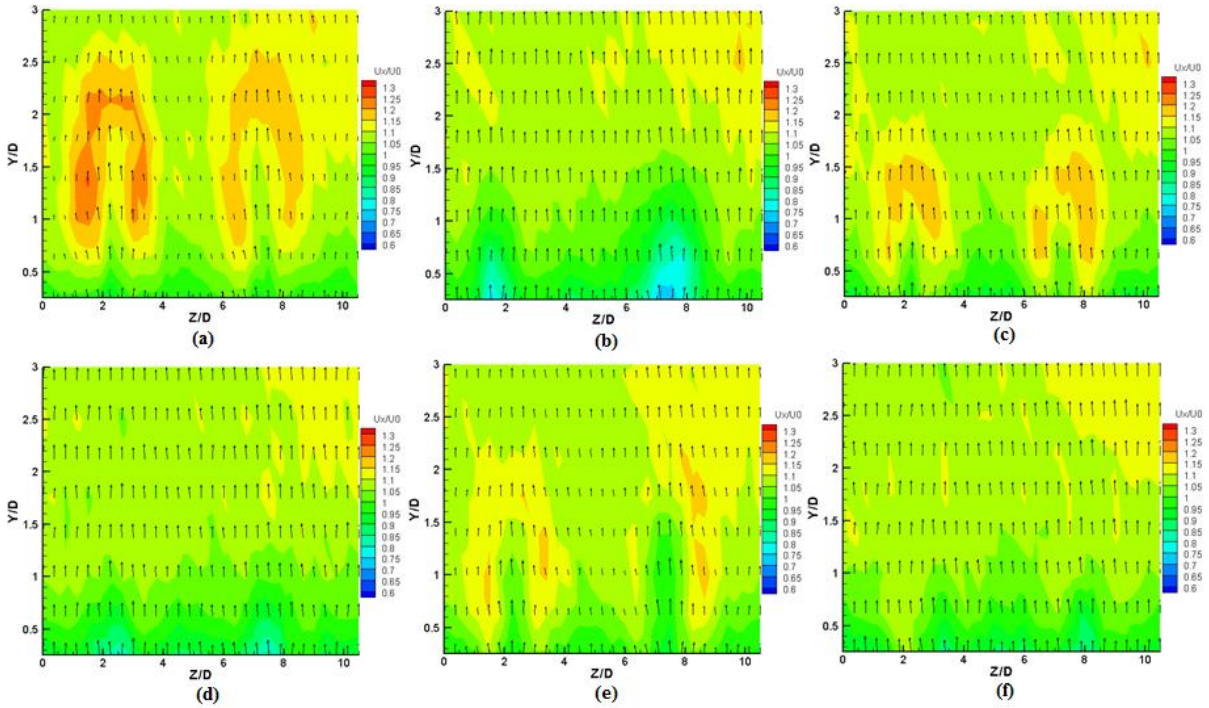

Figure 5-11: With turbulence grid flowfield measurements six (6) diameters downstream of hole exit trailing edge at blowing ratio of 1.3 and compound angle of zero (0) degrees. a) cylindrical hole injection, b) laidback fan-shaped hole injection, c) case 1 hole injection, d) case 2 hole injection, e) case 3 hole injection, f) case 4 hole injection.

Figure 5-12 are the flowfield results at a blowing ratio of 0.9 with the holes oriented 20 degrees to the mainstream flow direction. From the results it is seen, for all hole geometries, that the coolant is close to the wall and the coolant jet is skewed to the right and arguably better lateral spread is achieved, as compared to the streamwise oriented (zero (0) degrees compound angle) film cooling holes.

It was determined in the sections above that the skewness to the right of the coolant jet downstream is primarily due to the significant lateral motion imposed by the asymmetric vortex structure.

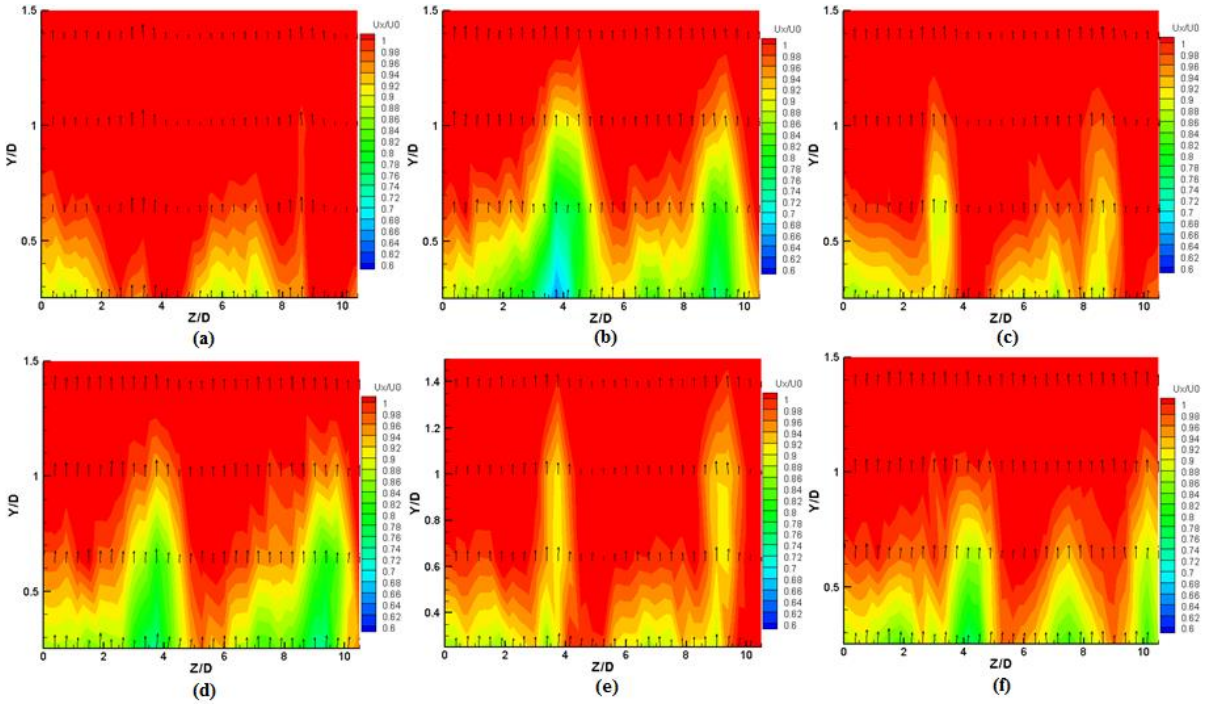

Figure 5-12: With turbulence grid flowfield measurements six (6) diameters downstream of hole exit trailing edge at blowing ratio of 0.9 and compound angle of 20 degrees. a) cylindrical hole injection, b) laidback fan-shaped hole injection, c) case 1 hole injection, d) case 2 hole injection, e) case 3 hole injection, f) case 4 hole injection.

Figure 5-13 are the flowfield results at a blowing ratio of 1.3 with the holes oriented 20 degrees to the mainstream flow direction. Comparing the results, to those at a compound angle of 20 degrees and a blowing ratio of 0.9, it is immediately seen that for the cylindrical hole, Case 1 and Case 3, the coolant jet is significantly lifted from the surface and the motion of the coolant jet is skewed to the right.

For the laidback fan-shaped hole, Case 2 and Case 4 hole, comparing the velocity results, to those at a compound angle of 20 degrees and a blowing ratio of 0.9, it is seen that the coolant is still close to the surface and the motion of the coolant jet is skewed to the right. But the coolant jet is slightly more pronounced in the mainstream flow. This is expected because an increased amount of coolant is being injected into the flow.

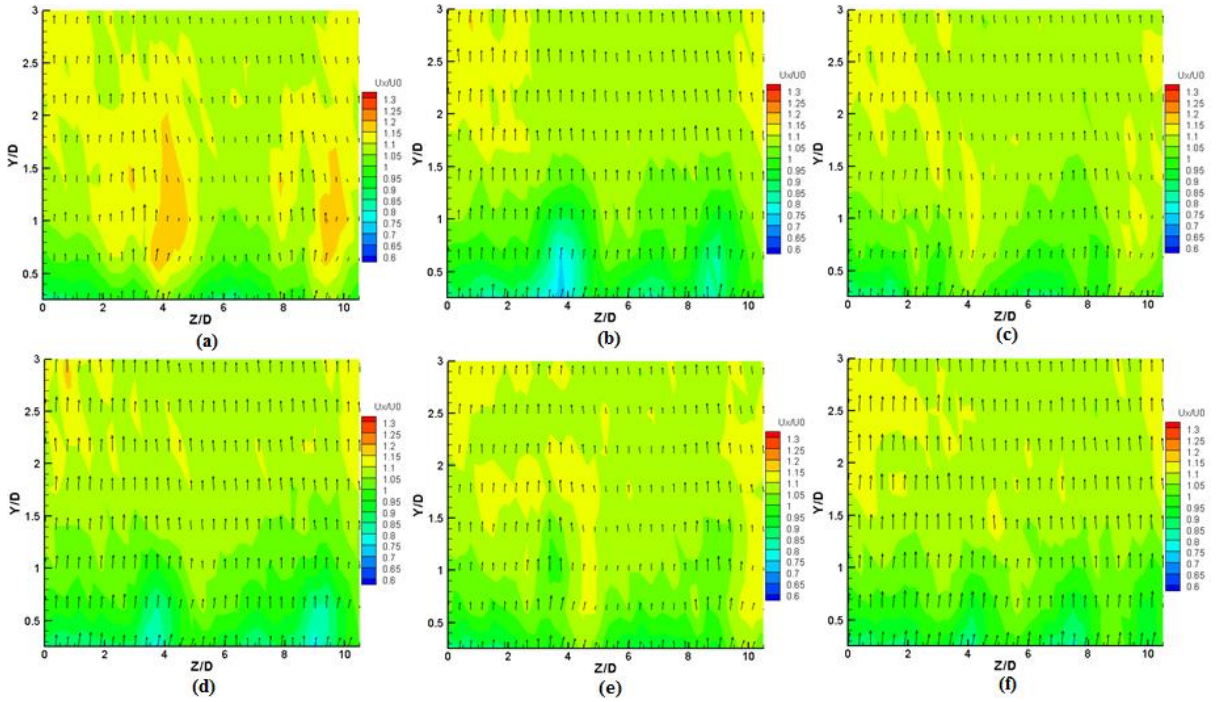

Figure 5-13: With turbulence grid flowfield measurements six (6) diameters downstream of hole exit trailing edge at blowing ratio of 1.3 and compound angle of zero (0) degrees. a) cylindrical hole injection, b) laidback fan-shaped hole injection, c) case 1 hole injection, d) case 2 hole injection, e) case 3 hole injection, f) case 4 hole injection.

Based on the above results and discussion the student concludes that the added turbulence intensity of approximately 4.9 percent, by the turbulence grid, was not significant enough to result in an appreciable effect on the flow structure downstream of the hole exit. The wanted effect being to aid in spreading the coolant jet on the surface.

5.2.Flow structure twelve (12) diameters downstream of hole exit (slot 2)

Figure 5-14 and Figure 5-15 are the flowfield results downstream of the hole exit. A comparison of the results six (6) diameters downstream and twelve (12) diameters downstream is made to determine how the flow develops as it moves further downstream. The results presented are for the cylindrical and laidback fan-shaped 3D printed holes at a compound angle of zero (0) degrees, a blowing ratio of 1.3 and without the presence of a turbulence grid.

Results for the other geometries investigated in this study, at different blowing ratios (= 0.7, 1 & 1.8) and different compound angles (= 20 & 30 degrees), have been presented in Appendix H.

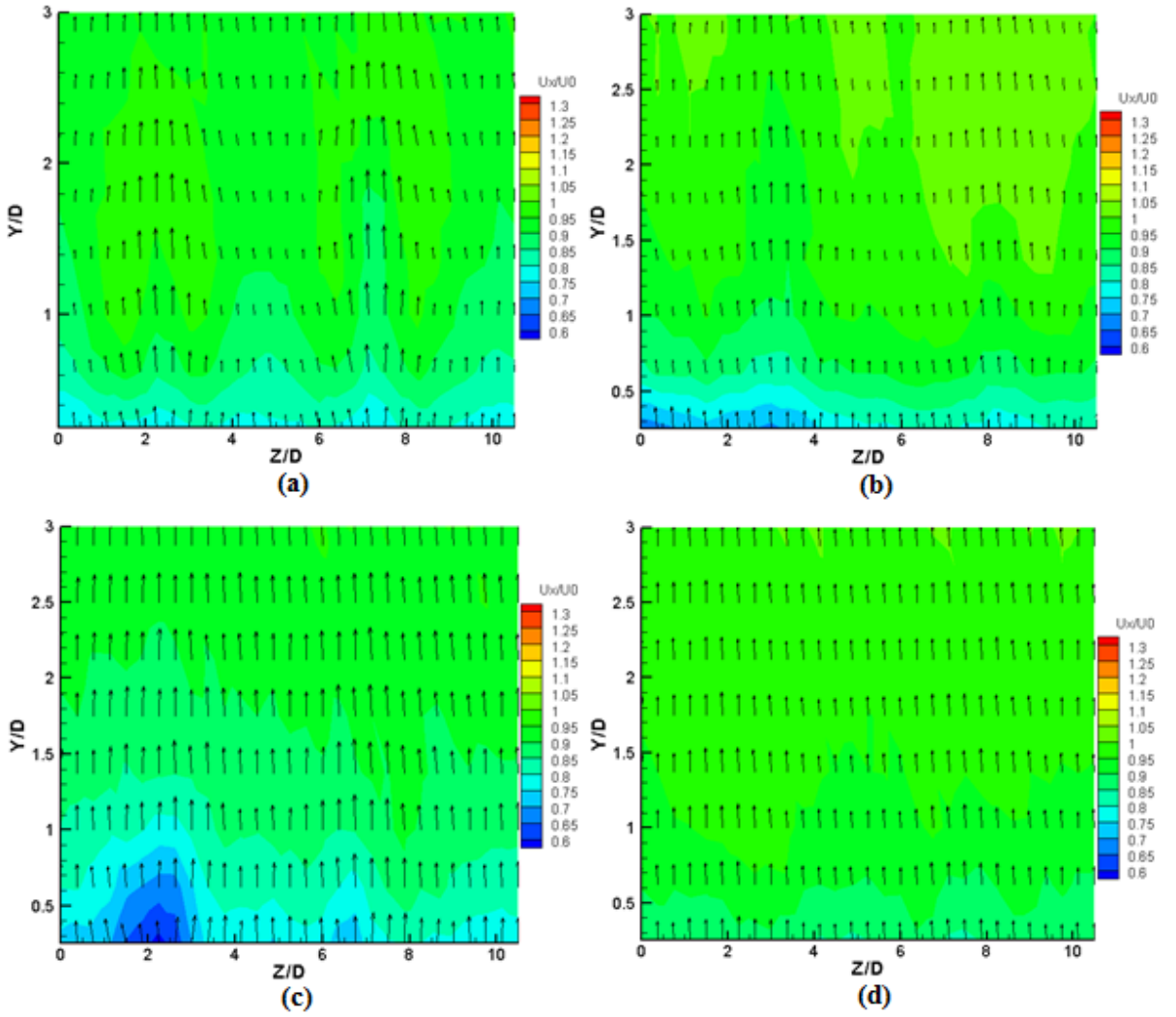

Figure 5-14: Flowfield measurements downstream of hole exit edge at a blowing ratio of 1.3 and a compound angle of zero (0) degrees. a) cylindrical hole injection six (6) diameters downstream, b) cylindrical hole twelve (12) diameters downstream, c) laidback fan-shaped hole six (6) diameters downstream, d) laidback fan-shaped hole twelve (12) diameters downstream.

It is seen from the velocity results that for both geometries, cylindrical and laidback fan-shaped, the coolant jet is barely noticeable in the mainstream flow twelve (12) diameters downstream of the hole exit trailing edge; it has dissipated even more for the laidback fan-shaped hole. From the vorticity results it is seen that the longitudinal vortices are weaker further downstream.

The above behaviour agrees with the study by Walters and Leylek (1997), where it is reported that as the flow moves further downstream the effects of the secondary flow are negligible and the coolant jet diffuses and takes on the shape of the boundary layer.

It is additionally reported in the study by Hayms and Leylek (2000) that turbulence generation becomes a dominant film cooling mechanism, further downstream of the jet-crossflow interaction zone. This difference in behaviour, as compared to the cylindrical hole, is due to the large mismatch in exit velocity created by the shaped geometries. The turbulence contributes significantly to the dissipation of the coolant in the far-field.

It is reported that as the coolant moves downstream, significant amounts of turbulence are generated throughout the film for the shaped geometries, as compared to the cylindrical

geometry. This is due to strong mixing at the film-crossflow interface and mixing throughout the film itself.

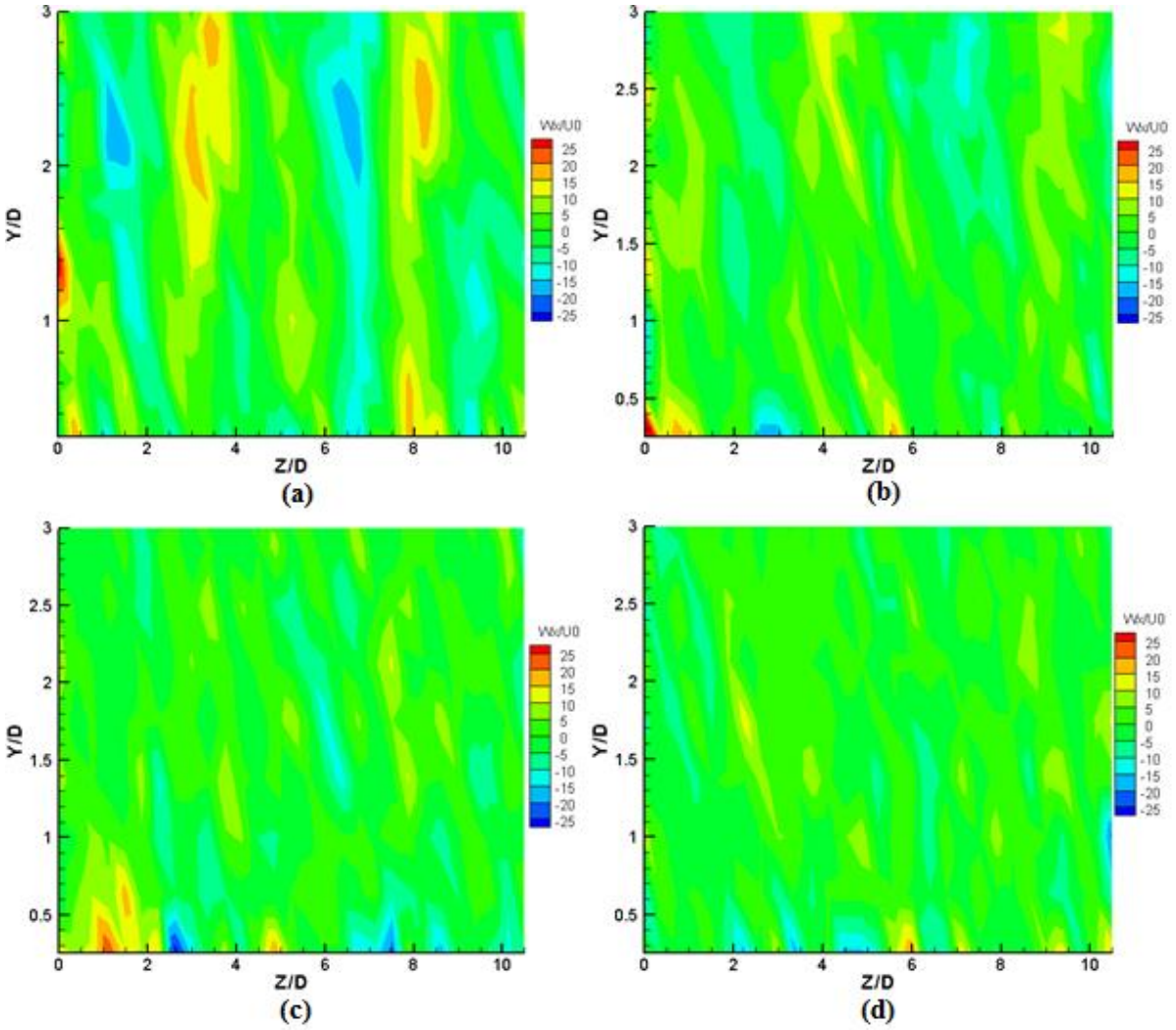

Figure 5-15: Streamwise vorticity measurements downstream of hole exit edge. a) cylindrical hole injection six (6) diameters downstream, b) cylindrical hole twelve (12) diameters downstream, c) laidback fan-shaped hole six (6) diameters downstream, d) laidback fan-shaped hole twelve (12) diameters downstream.

5.3.Conclusion

Above, the flowfield results were presented for six (6) film cooling hole geometries, with measurements taken at two (2) planes, six (6) and twelve (12) diameters downstream of hole exit trailing edge, for two (2) blowing ratios, 0.9 and 1.3, two (2) compound angles, 0 and 20 degrees, and with and without the presence of a turbulence grid.

It was found that at a blowing ratio of 0.9 and compound angle equals to zero (0) degrees, for all geometries, the coolant jet was relatively close to the surface. This is because of the small vertical momentum of the coolant jet at the exit. Additionally, because the jet is close to wall, the counterrotating vortices responsible for upward lift are rapidly diminished.

It was also found that the geometries with less expansion areas (cylindrical, Case 1 and Case 3 hole) have more height, as compared to the geometries with larger expansion areas (laidback fan-shaped, Case 2 and Case 4 hole). The geometries with larger lateral expansions showed better spread of the coolant downstream of the hole exit.

The higher height is due to the area expansion, which decreases the effective velocity and the vertical momentum content of the coolant jet on exit and decreases the penetration into the boundary layer of the crossflow. Additionally, the area expansion relaxes the velocity gradients on the side walls which decreases the strength of the streamwise film hole boundary layer vortices emanating from the hole. This decreases the strength of the counterrotating vortices. The better lateral spread is due to the lateral diffusion of the hole which locates the longitudinal vortices farther apart from each other such that the convective strength of the secondary flow at the centreline is reduced.

At a blowing ratio of 1.3 and compound angle equals to zero (0) degrees it was determined that for the cylindrical hole, case 1 and case 3 holes, the coolant jet is lifted from the wall. For the laidback fanshaped hole, case 2 and case 4 holes, the coolant is still close to the surface. It was determined that differences in behaviour were significantly due to the differences in lateral expansion between the geometries.

The coolant jet significantly lifting-off for the cylindrical hole, where the Case 1 hole and the Case 3 hole, is due to the initial positioning, in the near-field, of the coolant jet as it exits the hole coupled with the increased strength of the counterrotating vortices as the coolant jet moves downstream. The strength of the counterrotating vortices, related to the upward lift (induction lift) generated by the counterrotating vortices downstream of the hole exit, is strongly dependent on the blowing ratio.

The increased vertical momentum of the jet positions it farther from the wall as it exits the film cooling hole. The coolant jet exiting the hole further from the wall results in further increased strength of the longitudinal vortices. As the coolant jet moves downstream, it is lifted away from the surface by the counter-rotating vortices. Since the location of maximum vorticity is farther from the wall the streamwise counter-rotating vorticity is dissipated less rapidly and is apparent farther downstream.

For the Case 2 hole, Case 4 hole and the laidback fan-shaped hole it was determined that the increased blowing ratio did not significantly strengthen the mechanisms that result in poor film cooling performance in other geometries. These mechanisms include the strengthening of the longitudinal vortices which results in; 1) coolant upwards lift from the surface; and 2) the inability of the coolant to properly laterally spread because of the strengthened coolant convection towards the centreline.

At a blowing ratio of 0.9 and compound angle equals to 20 degrees it was determined, for all hole geometries, that the coolant is close to the wall and the coolant jet is skewed to the right and arguably better lateral spread is achieved. The skewness to the right of the coolant jet downstream is primarily due to the significant lateral motion imposed by the asymmetric vortex structure.

At a blowing ratio of 1.3 and compound angle equals to 20 degrees it was determined that for the cylindrical hole, case 1 and case 3, the coolant jet was significantly lifted from the surface and the motion of the coolant jet is skewed to the right.

For the laidback fan-shaped hole, Case 2 and Case 4 hole, comparing the velocity results, to those at a compound angle of 20 degrees and a blowing ratio of 0.9, it was seen that the coolant was still close to the wall and the motion of the coolant jet was skewed to the right. However, the coolant jet was slightly more pronounced in the mainstream flow. This was expected because an increased amount of coolant was being injected into the flow.

It was additionally determined that employing the curvature decreases the height and trajectory of the jet on exit. The decreased height is due to the decreased vertical momentum

content of the coolant jet. The decreased trajectory positions the longitudinal vortices closer to the wall which results in better lateral spread of the coolant. This could not be concluded with certainty because of the variation in the lateral expansion of the film cooling geometries, case 1 to 4 and also because the five hole probe could not get close enough to the wall.

With a turbulence grid included in the flow it was determined that the behaviour of the coolant jet in the mainstream flow is nominally the same. From this it was concluded that the physical mechanisms that determine the flow behaviour downstream in the case ‘without a turbulence grid’ are still dominant in the case ‘with a turbulence grid’; the turbulence grid had little effect on the behaviour. The added turbulence intensity of approximately 4.89%, by the turbulence grid, was not significant enough to result in an appreciable effect on the flow structure downstream of the hole exit. The desired effect is to aid in spreading the coolant jet on the surface.

Further downstream of the hole exit trailing edge, twelve (12) diameters downstream, the coolant jet is barely noticeable in the mainstream flow. The effects of the secondary flow are negligible, and the coolant jet diffuses and takes on the shape of the boundary layer.

Based on the results presented above the case 2 hole geometry is recommended for further investigation. The case 2 hole geometry resulted in low jet height when in the mainstream, which means that it was closer to the surface that requires cooling. It also resulted in a relatively good lateral spread of the coolant on the surface.

6.Temperature field results and discussion

The velocity and vorticity results presented in chapter 5 did not have sufficient information to allow the student to appropriately analyse and report on the behaviour of the different film cooling hole geometries. Hence, assumptions based on literature and educated guesses were made where needed.

Because the temperature probe could get closer to the wall (starting point of the temperature probe was 0.5 mm away from the wall) the temperature results presented below allow for a better analysis of the coolant jet behaviour closer to the wall.

The non-dimensionalised temperature results are presented below. The measurements are taken six (6) diameters downstream of the hole exit trailing edge and at one (1) blowing ratio of 0.9. Only two (2) compound angles, 0 and 20 degrees, and only the 3D printed hole geometries are investigated. This is because it was determined from the discharge coefficient results that the effect of manufacturing method and 3D print build orientation is negligible.

Additional tests were done at a blowing ratio of 1.1, without a turbulence grid, for selected geometries. These have been included in Appendix H.

In the results below, the coolant jet core corresponds to the lowest dimensionless temperature contour region in each figure. In the discussions below, coolant height refers to the height of the coolant jet core in the Y/D direction. Coolant lateral spread refers to the distribution of the coolant jet core in the Z/D direction.

6.1.Blowing ratio 0.9 without turbulence grid

The student first compares and discusses the behaviour of the baseline shapes; the cylindrical hole and the laidback fan-shaped hole. Figure 6-1 shows that the coolant jet core is lifted from the surface for the cylindrical hole to approximately Y/D = 1.5. For the laidback fan-shaped hole, it is seen that the coolant jet core is much closer to the surface, with a height of approximately Y/D = 0.3. Based on the spread of the coolant core at Y/D = 0 (0.5 mm from surface) from the surface, it can be assumed that the coolant core is attached to the surface for the laidback fan-shaped hole.

The behaviour of the cylindrical hole is expected because it has been reported literature. In the studies by Sinha *et al.* (1991), Walters and Leylek (2000), and Bernsdorf *et al.* (2006), for streamwise aligned cylindrical holes, inclined 30 degrees, it was reported that the coolant jet begins to lift-off from the surface when the blowing ratio approaches 0.5.

It is seen that the coolant from the cylindrical hole has more height than the laidback fan-shaped hole; the difference in height being approximately 1.2 (80%). The coolant from the laidback fan-shaped hole has more spread as compared to the cylindrical hole; the difference being approximately 0.25 (56%).

Additionally, it is seen that the coolant jet core of the cylindrical hole has a lower non-dimensionalised temperature than that of the laidback fan-shaped hole; the difference being approximately 0.1 (20%).

The lower non-dimensional temperature of the cylindrical hole is possibly due to the fact that the coolant is lifted farther from the surface and is surrounded by the hotter tunnel airflow all around. This possibly implies that a larger surface area is in contact with the hotter tunnel airflow which results in increased temperature (energy) gain.

Comparing Cases 1 to 4 with the cylindrical hole it is seen that the new shapes have better lateral spread and the cylindrical hole has more height.

The difference in height between the cylindrical hole and the case 1 hole is approximately 0.6 (40%). The difference in lateral spread is approximately 0.2 (44%).

The difference in height between the cylindrical hole and the case 2 hole is approximately 0.9 (60%). The difference in lateral spread is approximately 0.55 (73%).

The difference in height between the cylindrical hole and the case 3 hole is approximately 0.6 (40%). The difference in lateral spread is aprroximately 0.05 (20%).

The difference in height between the cylindrical hole and the case 4 hole is approximately 1.1 (74%). The difference in lateral spread is aprroximately 0.5 (67%).

Comparing Cases 1 and 3 to the laidback fan-shaped hole, it is seen that the lateral spread of the laidback fan-shaped hole is superior, and the case 1 and 3 holes have higher height. It is also seen that the coolant jet core of the case 3 hole has a lower non-dimensional temperature. This is possibly due to the fact that the 40 degrees inclination angle positioned the hole exit trailing edge further from the temperature probe measurement plane. When the coolant jet gets to the measurement location it has gained more heat.

Comparing case 2 and 4 to the laidback fan-shaped hole it is seen that better lateral spread of the coolant jet core is observed for cases 2 and 4. The difference in lateral spread between the case 2 hole and the laidback fan-shaped hole being approximately 0.25 (36%).

It is also seen that the coolant jet core of the case 4 hole has a lower non-dimensional temperature; the difference being approximately 0.1 (22%). This is possibly due to the fact that the 40 degrees inclination angle positioned the hole exit trailing edge further from the temperature probe measurement plane. When the coolant jet gets to the measurement location it has gained more heat.

Comparing the new shapes against each other, it is seen that the coolant jet core of cases 2 and 4 has better lateral spread and cases 1 and 3 have more height.

The physical mechanisms responsible for the above mentioned behaviours for the different geometries have been discussed in detail in Chapter 5.

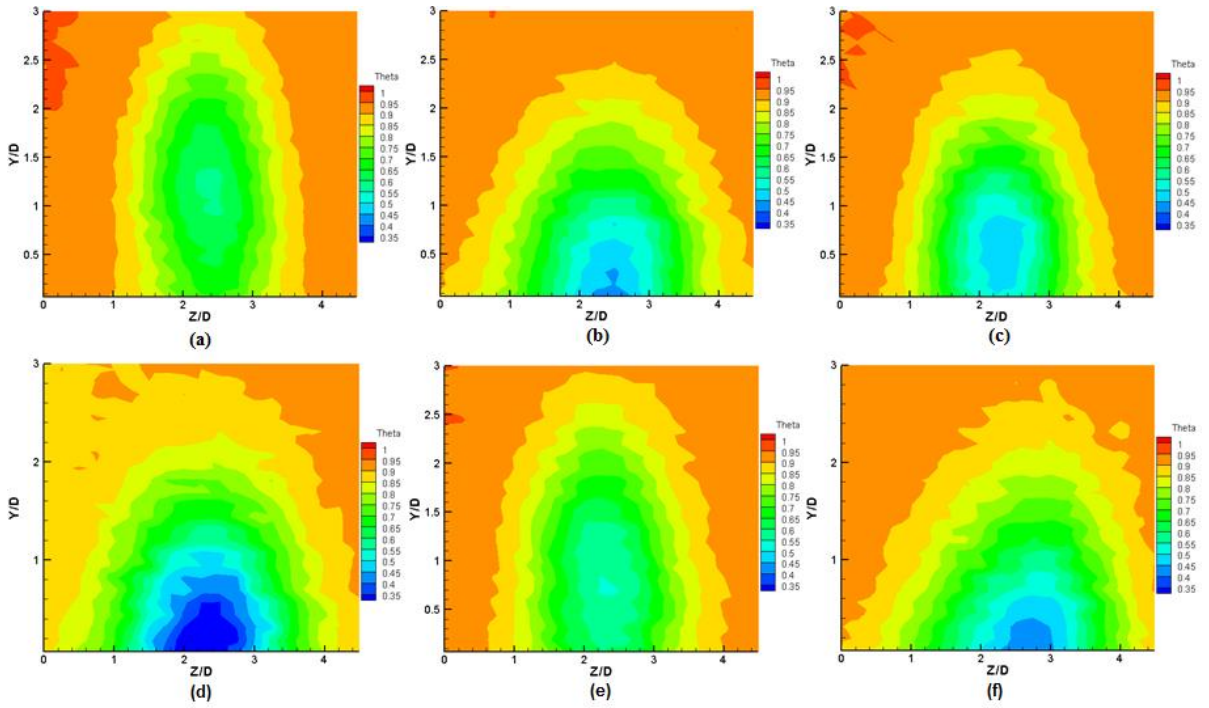

Figure 6-1: Temperature field measurements six (6) diameters downstream of hole exit trailing edge at blowing ratio of 0.9 and compound angle of 0 degrees. a) cylindrical hole injection, b) laidback fan-shaped hole injection, c) case 1 hole injection, d) case 2 hole injection, e) case 3 hole injection, f) case 4 hole injection.

At a 20 degrees compound angle, Figure 6-2, it is seen that the coolant jet core for the cylindrical hole, the case 1 hole and the case 3 hole is still lifted from the surface; more for the cylindrical hole. The coolant jet core of the laidback fan-shaped hole, the case 2 hole and the case 4 hole is closer to the wall. Based on the spread of the coolant core at 0.5 mm (Y/D = 0) from the surface, it can be assumed that the coolant core is attached to the surface for the laidback fan-shaped hole, the case 2 hole and the case 4 hole.

Comparing the results at 20 degrees to those at zero (0) degrees compound angle, it is seen that the coolant is skewed to the right. Increased lateral spread is also observed. As discussed in chapter 5, this is due to the significant lateral motion caused by the asymmetric longitudinal vortices that eventually collapse into a single unidirectional vortex. The physical mechanisms responsible for the observed behaviour have been discussed in detail in chapter 5.

Comparing the cylindrical hole geometries at the different compound angles, it is seen that an increased non-dimensional temperature at the jet core is observed at 20 degrees compound angle. The difference is approximately 0.05 (9%).

Comparing the laidback fan-shaped hole geometries at the different compound angles, it is seen that an increased non-dimensional temperature at the jet core is observed at 20 degrees compound angle. The difference is approximately 0.05 (13%).

Comparing the case 1 hole geometries at the different compound angles, it is seen that an increased non-dimensional temperature at the jet core is observed at 20 degrees compound angle. The difference is approximately 0.1 (22%).

Comparing the case 2 hole geometries at the different compound angles, it is seen that similar non-dimensional temperature values at the jet core are observed.

Comparing the case 3 geometries at the different compound angles, it is seen that an increased non-dimensional temperature is observed at 20 degrees compound angle. The difference is approximately 0.1 (20%).

Comparing the case 4 hole geometries at the different compound angles, it is seen that similar non-dimensional temperature values at the jet core are observed.

Regarding the effects of shape, similar patterns as those for the streamwise oriented holes at a blowing ratio of 0.9, are observed. This tells us that even though the mechanisms that dictate the downstream flow structure differ, between the streamwise and the 20 degrees oriented, their effect produces the same pattern of behaviour downstream. The student suspects that this is largely determined by the lateral expansion of the holes.

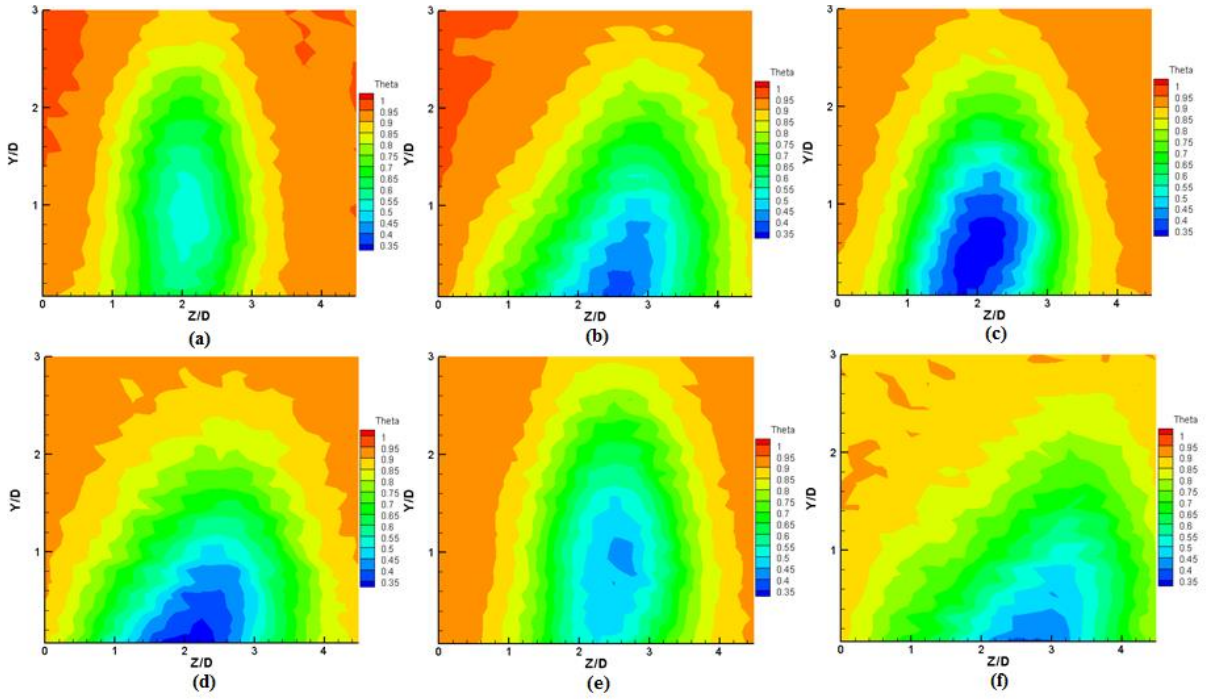

Figure 6-2: Temperature field measurements six (6) diameters downstream of hole exit trailing edge at blowing ratio of 0.9 and compound angle of 20 degrees. a) cylindrical hole injection, b) laidback fan-shaped hole injection, c) case 1 hole injection, d) case 2 hole injection, e) case 3 hole injection, f) case 4 hole injection.

6.2.Blowing ratio 0.9 with turbulence grid

Figure 6-3 and Figure 6-4 show measurements taken with a turbulence grid. Comparing the results presented below to those without a turbulence grid, it is immediately evident that the behaviour/structure of the coolant jet in the mainstream flow is nominally the same. This tells us that the physical mechanisms that determine the flow behaviour downstream in the case ‘without a turbulence grid’ are still dominant in the case ‘with a turbulence grid’ (the turbulence grid had little effect on the behaviour).

It is seen in Figure 6-3 that the geometries with less expansion areas (cylindrical, case 1 and case 3 hole) have more height, when compared to the geometries with larger expansion areas (laidback fan-shaped, case 2 and case 4 hole). The geometries with larger lateral expansions show better spread of the coolant downstream of the hole exit. The mechanisms that determine the behaviours observed have been discussed in detail in Chapter 5.

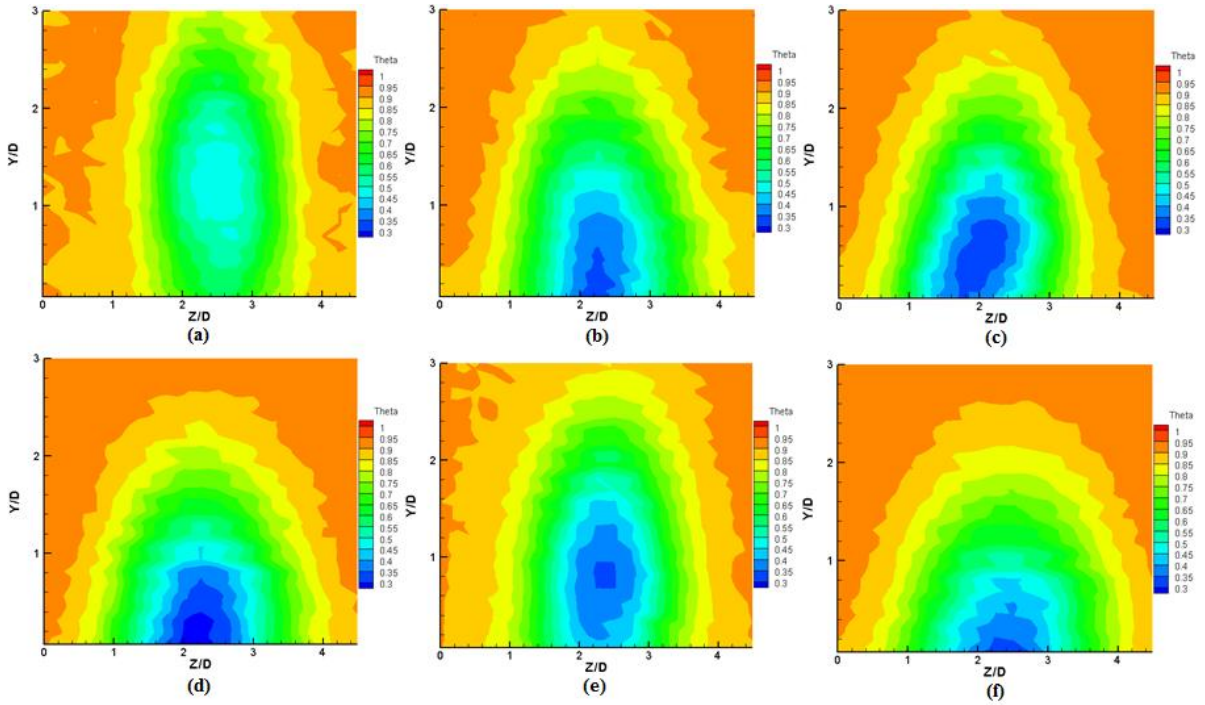

Figure 6-3: Temperature field measurements six (6) diameters downstream of hole exit trailing edge at blowing ratio of 0.9 and compound angle of zero (0) degrees, with turbulence grid. a) cylindrical hole injection, b) laidback fan-shaped hole injection, c) case 1 hole injection, d) case 2 hole injection, e) case 3 hole injection, f) case 4 hole injection.

Comparing the cylindrical hole and the laidback fan-shaped hole, it is see that the difference in height is approximately 1.0 (38%). A better lateral spread of the coolant is observed for the cylindrical hole, the difference being approximately 0.2 (33%).

The difference in height between the cylindrical hole and the case 1 hole is approximately 0.4 (25%). The difference in lateral spread is approximately 0.2 (25%).

The difference in height between the cylindrical hole and the case 2 hole is approximately 1.2 (75%). A better lateral spread of the coolant is observed for the cylindrical hole, the difference being approximately 0.1 (17%).

The difference in height between the cylindrical hole and the case 3 hole is approximately 0.6 (40%). A better lateral spread of the coolant is observed for the cylindrical hole, the difference being approximately 0.4 (67%).

The difference in height between the cylindrical hole and the case 4 hole is approximately 1.4 (88%). A better lateral spread of the coolant is observed for the cylindrical hole, the difference being approximately 0.1 (17%).

Figure 6-4 shows that the coolant jet is slightly skewed to the right and arguably better lateral spread is achieved, as compared to the streamwise oriented (zero (0) degrees compound angle) film cooling holes.

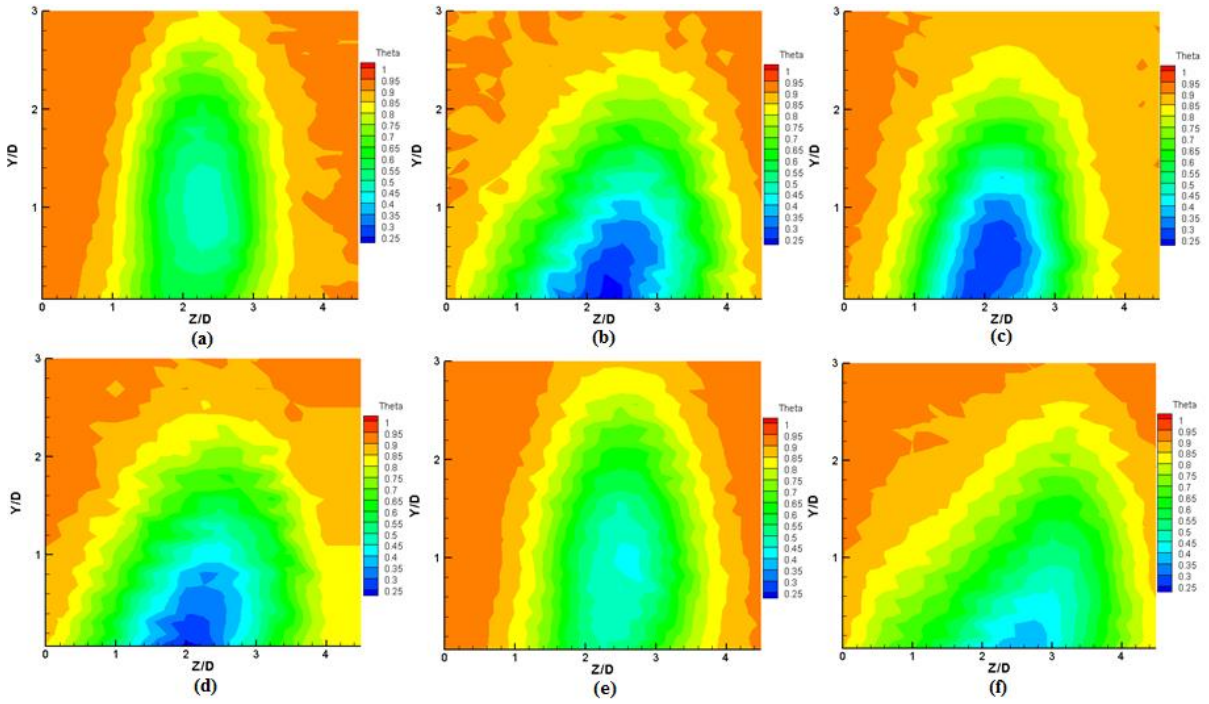

Figure 6-4: Temperature field measurements six (6) diameters downstream of hole exit trailing edge at blowing ratio of 0.9 and compound angle of 20 degrees, with turbulence grid. a) cylindrical hole injection, b) laidback fan-shaped hole injection, c) case 1 hole injection, d) case 2 hole injection, e) case 3 hole injection, f) case 4 hole injection.

6.3.Conclusion

Above, temperature field results were presented for six (6) film cooling hole geometries, with measurements taken on (1) plane, six (6) diameters downstream of hole exit trailing edge, at one (1) blowing ratios of 0.9, two (2) compound angles, 0 and 20 degrees, and with and without the presence of a turbulence grid.

It was found that the coolant jet core was lifted from the surface for the cylindrical hole. For the laidback fan-shaped hole the coolant jet core was much closer to the surface and showed better lateral spread closer to the surface as compared to the cylindrical hole. Additionally, It was seen that the coolant from the cylindrical hole had more height and the coolant jet core had a lower non-dimensionalized temperature.

In comparing cases 1 to 4 to the cylindrical hole, it was found that the new shapes had better lateral spread and the cylindrical hole had more height.

In comparing cases 1 and 3 to the laidback fan-shaped hole it was seen that the lateral spread of the laidback fan-shaped hole was superior, and the case 1 and 3 holes had higher height. It was also seen that the coolant jet core of the case 3 hole had a lower non-dimensional temperature.

In comparing case 2 and 4 to the laidback fan-shaped hole it was seen that better lateral spread of the coolant jet core is observed for cases 2 and 4; case 4 spreading even better than case 2. It was also seen that the coolant jet core of the case 4 hole has a lower non-dimensional temperature.

In comparing the new shapes against each other, it was seen that the coolant jet core of cases 2 and 4 has better lateral spread and cases 1 and 3 have better height.

In comparing the results at 20 degrees to those at zero (0) degrees compound angle, it was found that the coolant was slightly skewed to the right. Increased lateral spread was also observed. The effects of shape on the flow structure were found to be similar to those at a compound angle of zero (0) degrees.

Incorporation of a turbulence grid in the mainstream flow had a negligible effect on the temperature field downstream.

Based on the results presented above the case 2 hole geometry is recommended for further investigation. The case 2 hole geometry resulted in low jet height when in the mainstream, which means that it was closer to the surface that requires cooling. It resulted in a relatively good lateral spread of the coolant on the surface. And it resulted in a lower non-dimensional temperature of the coolant core, which means that the was less mixing/transfer of temperature (energy) between the mainstream and the coolant.

7.Adiabatic wall effectiveness results and discussion

Distributions of lateral and axial film cooling adiabatic effectiveness, and laterally averaged adiabatic effectiveness results along the end-wall are presented. The effectiveness parameter is used to quantify the cooling ability of the different film cooling hole geometries. The effectiveness results also allow us to get a better understanding of the coolant coverage distributions along the end-wall for the different configurations. The measurements are taken at three (3) blowing ratios; 0.6, 0.9 and 1.1, three (3) compound angles, 0, 20 and 40 degrees, with and without the turbulence grid. Results at blowing ratio equals to 0.6 and 1.1 are presented in the main thesis, chapter 7. They are classified as low and high blowing ratios in the discussions below. Results at compound angle equals to 0 and 20 degrees are presented in the main thesis, chapter 7. The other results are presented in Appendix H.

For the local effectiveness distribution results, It should be noted that the effectiveness is high when coolant remains adjacent to the end-wall and is low when the coolant lifts off the end-wall.

It is immediately noticeable from inspection of all the local effectiveness distribution results that the top hole, in the pair of holes, has less coolant coverage along the end-wall than that of the bottom hole. It is determined that the top hole has lower mass flux because of coolant at a lower temperature settling at the bottom of the plenum and coolant at a higher temperature rising to the top.

7.1.Effects of manufacturing method, 3D print build orientation and turbulence intensity

The student initially investigates the effects of manufacturing method, 3D print build orientation and the turbulence grid using the baseline geometries; the cylindrical and laidback fan-shaped hole. This was done because testing and comparisons with the new shapes, cases 1 to 4 hole geometries, were only done with the turbulence grid present and on only the 3D printed holes.

7.1.1.Local distributions of adiabatic effectiveness along end-wall

Comparing Figure 7-1 (a) and Figure 7-1 (b), it is seen that there is increased lateral spread (along Y/D) of effectiveness, closer to the hole exit for the cylindrical 3D printed hole as compared to the machined cylindrical hole. As we move further downstream (along X/D), we see that the effectiveness reaches further for the machined cylindrical hole as compared to the cylindrical 3D printed hole.

Comparing Figure 7-1(c), Figure 7-1(d) and Figure 7-1(e), it is seen that there is increased lateral spread of effectiveness closer to the hole exit for the laidback fan-shaped 3D zero (0) degrees printed hole, as compared to the machined laidback fan-shaped and laidback fan-shaped 3D 67 degrees printed hole. As we move further downstream, we see increased coolant coverage for the laidback fan-shaped 3D zero (0) degrees printed hole as compared to the machined laidback fan-shaped and laidback fan-shaped 3D 67 degrees printed hole. It is additionally seen that the behaviours of the machined laidback fan-shaped and laidback fan-shaped 3D 67 degrees printed hole are more comparable.

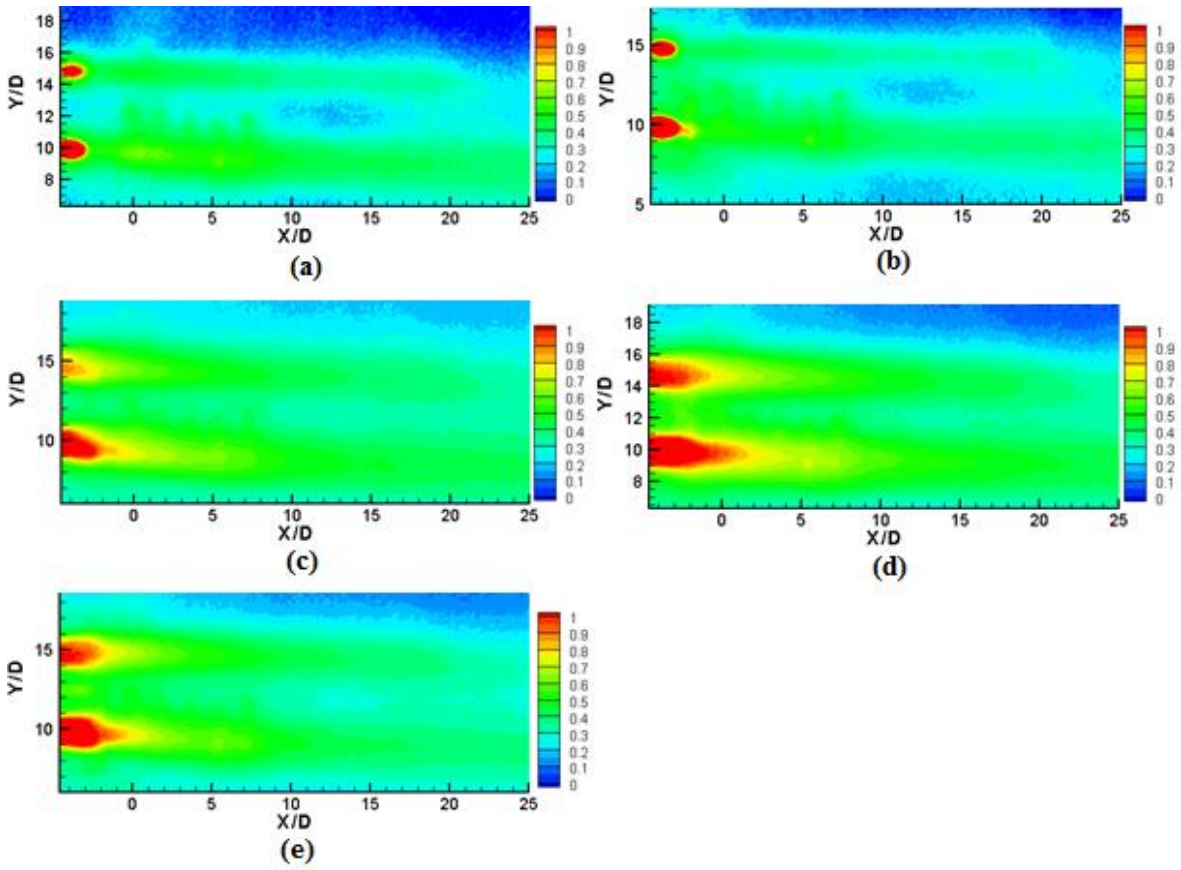

Figure 7-1: Local distributions of adiabatic effectiveness along end-wall at a blowing ratio of 0.6 and compound angle of zero (0) degrees, without turbulence grid. a) cylindrical machined hole, b) cylindrical 3D 60 degrees printed hole, c) laidback fan-shaped machined hole, d) laidback fan-shaped 3D zero (0) degrees printed hole, e) laidback fan-shaped 3D 67 degrees printed hole.

Comparing Figure 7-1 and Figure 7-2 to determine effect of the turbulence grid (increasing the turbulence intensity), it is seen for the cylindrical holes that inclusion of the turbulence grid decreases the lateral spread of the effectiveness.

For the laidback fan-shaped holes, it is seen that for the machined laidback fan-shaped hole and laidback fan-shaped 3D zero (0) degrees printed hole the is increased lateral spread and coolant coverage as we move further downstream for the flow conditions without a turbulence grid, as compared to the flow conditions with a turbulence grid. For the laidback fan-shaped 3D 67 degrees printed hole the inverse is observed; increased lateral spread and coolant coverage as we move further downstream is observed for the flow conditions with a turbulence.

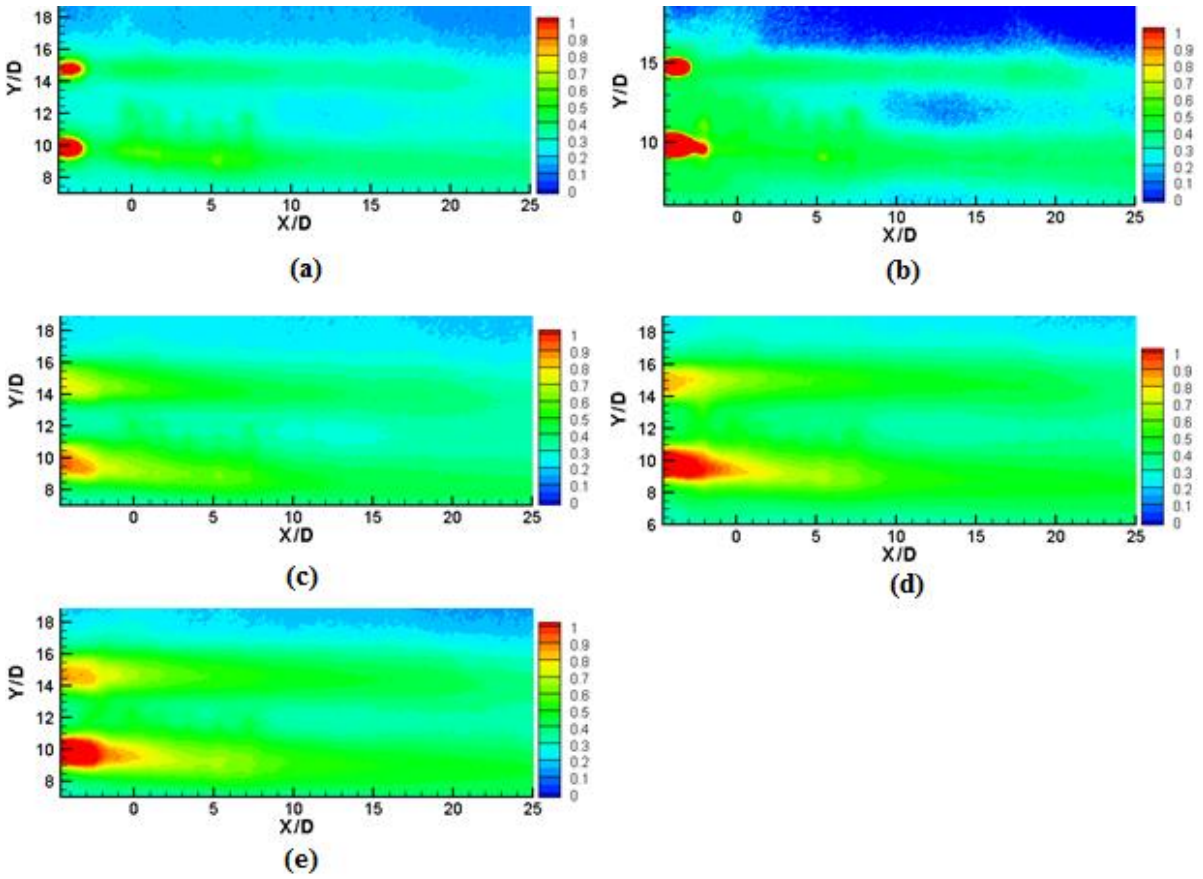

Figure 7-2: Local distributions of adiabatic effectiveness along end-wall at a blowing ratio of 0.6 and compound angle of zero (0) degrees, with turbulence grid. a) cylindrical machined hole, b) cylindrical 3D 60 degrees printed hole, c) laidback fan-shaped machined hole, d) laidback fan-shaped 3D zero (0) degrees printed hole, e) laidback fan-shaped 3D 67 degrees printed hole.

Shown in Figure 7-3 and Figure 7-4 are the local distributions of adiabatic effectiveness along end-wall at a blowing ratio of 1.1. Comparing these figures to those above it is seen that the behaviours observed are nominally the same at a blowing ratio of 1.1.

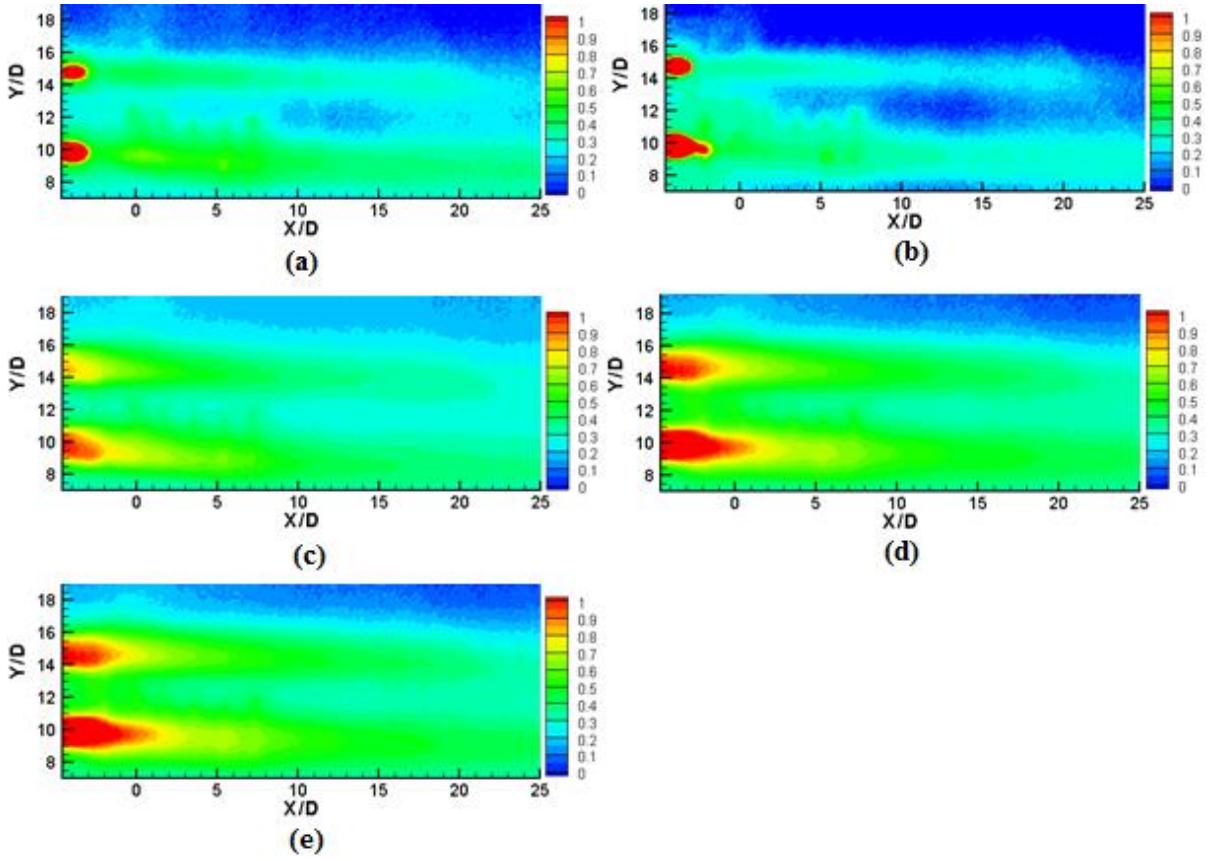

Figure 7-3: Local distributions of adiabatic effectiveness along end-wall at a blowing ratio of 1.1 and compound angle of zero (0) degrees, without turbulence grid. a) cylindrical machined hole, b) cylindrical 3D 60 degrees printed hole, c) laidback fan-shaped machined hole, d) laidback fan-shaped 3D zero (0) degrees printed hole, e) laidback fan-shaped 3D 67 degrees printed hole.

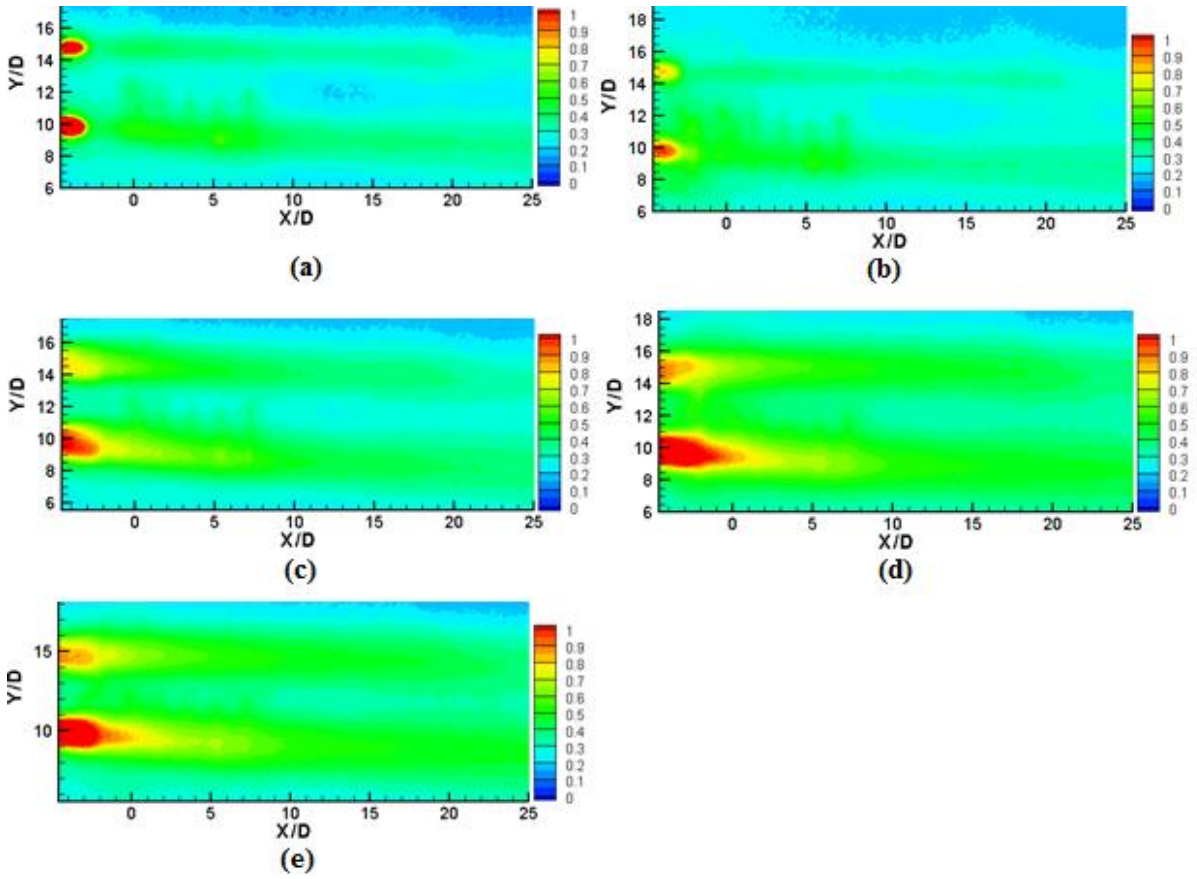

Figure 7-4: Local distributions of adiabatic effectiveness along end-wall at a blowing ratio of 1.1 and compound angle of zero (0) degrees, with turbulence grid. a) cylindrical machined hole, b) cylindrical 3D 60 degrees printed hole, c) laidback fan-shaped machined hole, d) laidback fan-shaped 3D zero (0) degrees printed hole, e) laidback fan-shaped 3D 67 degrees printed hole.

7.1.2. Laterally averaged adiabatic effectiveness

It is seen, for all configurations, that the effectiveness decreases as the coolant moves further downstream. This agrees with results by Hayms and Leylek (2000). The decrease in effectiveness may be due to mixing of the coolant jet with the crossflow as it moves further downstream.

It is seen that the turbulence grid, manufacturing method and 3D print build orientation affects the laterally averaged adiabatic film cooling effectiveness. It is seen that there is no pattern in the results which tells us that the behaviour is sensitive/dependent on the film cooling configuration and the testing conditions. This agrees with Brittingham and Leylek (2000) where it is reported that the film cooling behaviour does not follow the superposition principle.

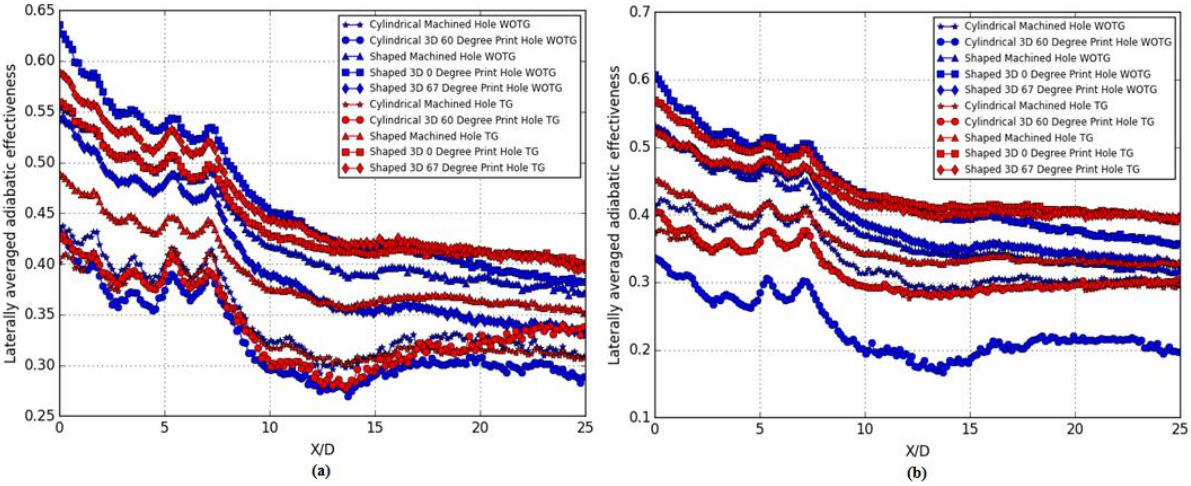

Figure 7-5: Effect of turbulence intensity (WOTG – without turbulence grid, TG – with turbulence grid), manufacturing method and 3D print build orientation on the laterally averaged adiabatic effectiveness. a) 0.6 blowing ratio, b) 1.1 blowing ratio.

7.2.Effect of hole geometry, compound angle and blowing ratio

7.2.1.Local distributions of adiabatic effectiveness along end-wall

The results in Figure 7-6 and Figure 7-7 suggest that the laidback fan-shaped hole, the case 2 hole and the case 4 hole result in a coolant better lateral spread, further reach downstream of the hole exit and, hence, superior coolant coverage on the end-wall as compared to the cylindrical hole, the case 1 hole and the case 3 hole. As discussed in chapter 5 and chapter 0 this is primarily due to the larger lateral expansions of the laidback fan-shaped hole, the case 2 hole and the case 4 hole geometries.

This agrees with the study by Hayms and Leylek (2000) where It was reported that the good thermal performance of the laterally diffused hole geometry is partly due to its low trajectory and wide breadth. The low trajectory results in the coolant being effectively injected into the mainstream flow boundary layer and remaining in the boundary layer until dissipated by diffusion mechanisms downstream. The wide breadth results in the vortex cores being spread apart in the lateral direction, which weakens induction lift.

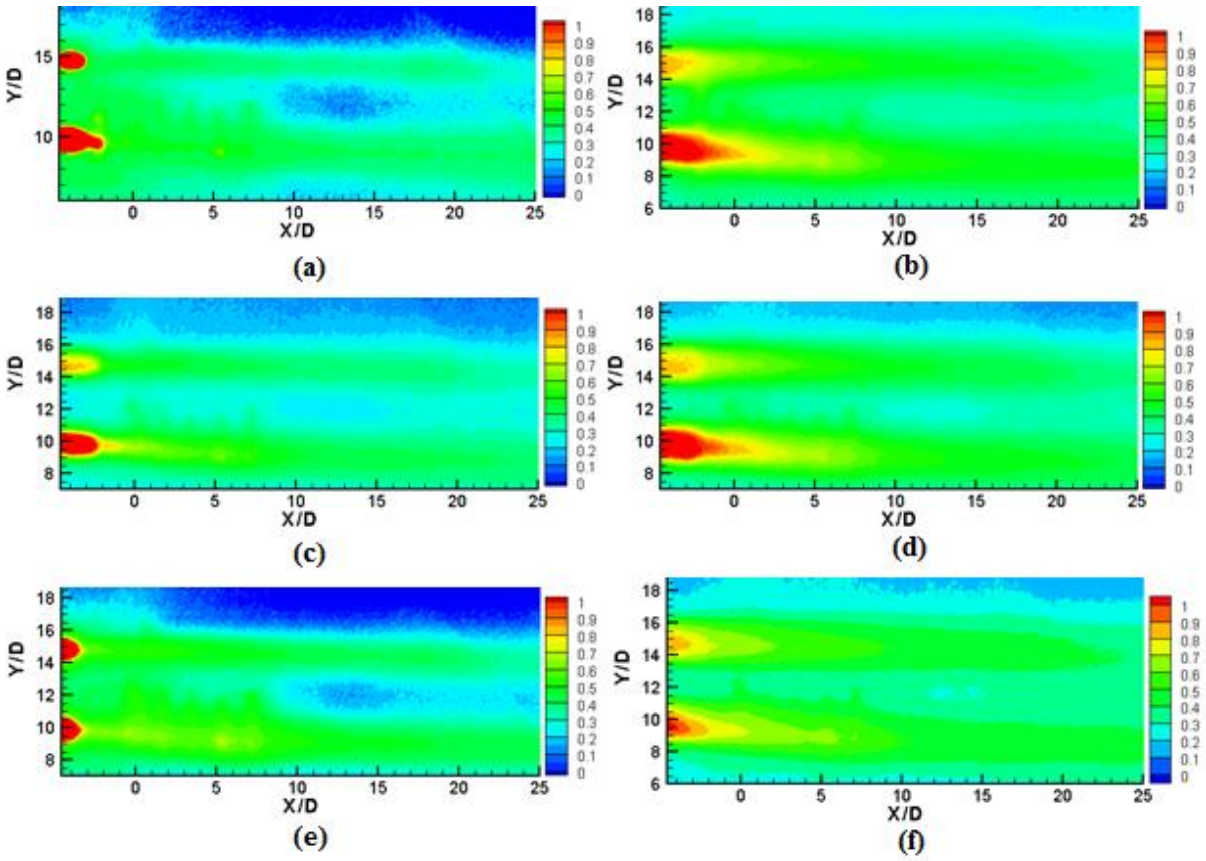

Figure 7-6: Local distributions of adiabatic effectiveness along end-wall at a blowing ratio of 0.6 and compound angle of zero (0) degrees, with turbulence grid. a) cylindrical 3D 60 degrees printed hole, b) laidback fan-shaped 3D zero (0) degrees printed hole, c) case 1 hole, d) case 2 hole, e) case 3 hole, f) case 4 hole.

Comparing Figure 7-6 to Figure 7-7, to determine the effects of the compound angle, it is seen that all the results suggest that increasing the compound angle slightly increases the lateral spread of the coolant jet but the effectiveness reach further downstream is slightly decreased.

As discussed in chapter 5, the increased lateral spread is due to the significant lateral motion caused by the asymmetric longitudinal vortices that eventually collapse into a single unidirectional vortex (McGovern & Leylek 2000).

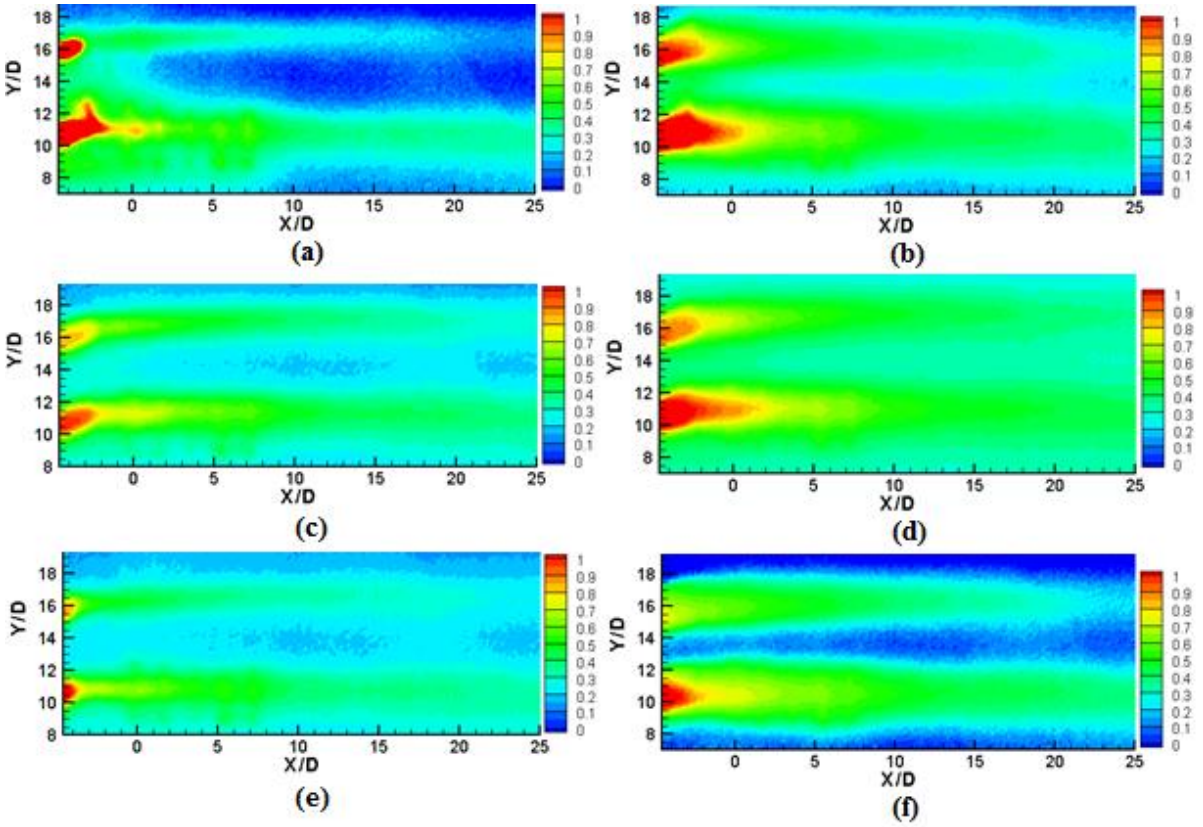

Figure 7-7: Local distributions of adiabatic effectiveness along end-wall at a blowing ratio of 0.6 and compound angle of 20 degrees, with turbulence grid. a) cylindrical 3D 60 degrees printed hole, b) laidback fan-shaped 3D zero (0) degrees printed hole, c) case 1 hole, d) case 2 hole, e) case 3 hole, f) case 4 hole.

Shown in Figure 7-8 and Figure 7-9 are the local distributions of adiabatic effectiveness along end-wall at a blowing ratio of 1.1, for compound angles zero (0) and 20 degrees, respectively.

At a compound angle of zero (0) degrees, it is seen that all the results suggest a slight decrease in the lateral spread as the blowing ratio is increased. As discussed in chapter 5, this is due to a strengthening of the mechanisms that result in poor film cooling performance (Walters & Leylek 1997).

This agrees with the flow structure and the temperature field results in chapter 5 and chapter 6. The physical mechanisms responsible for the observed behaviour have been discussed and reported in detail in chapter 5. The reader is encouraged to consult chapter 5 for a recap.

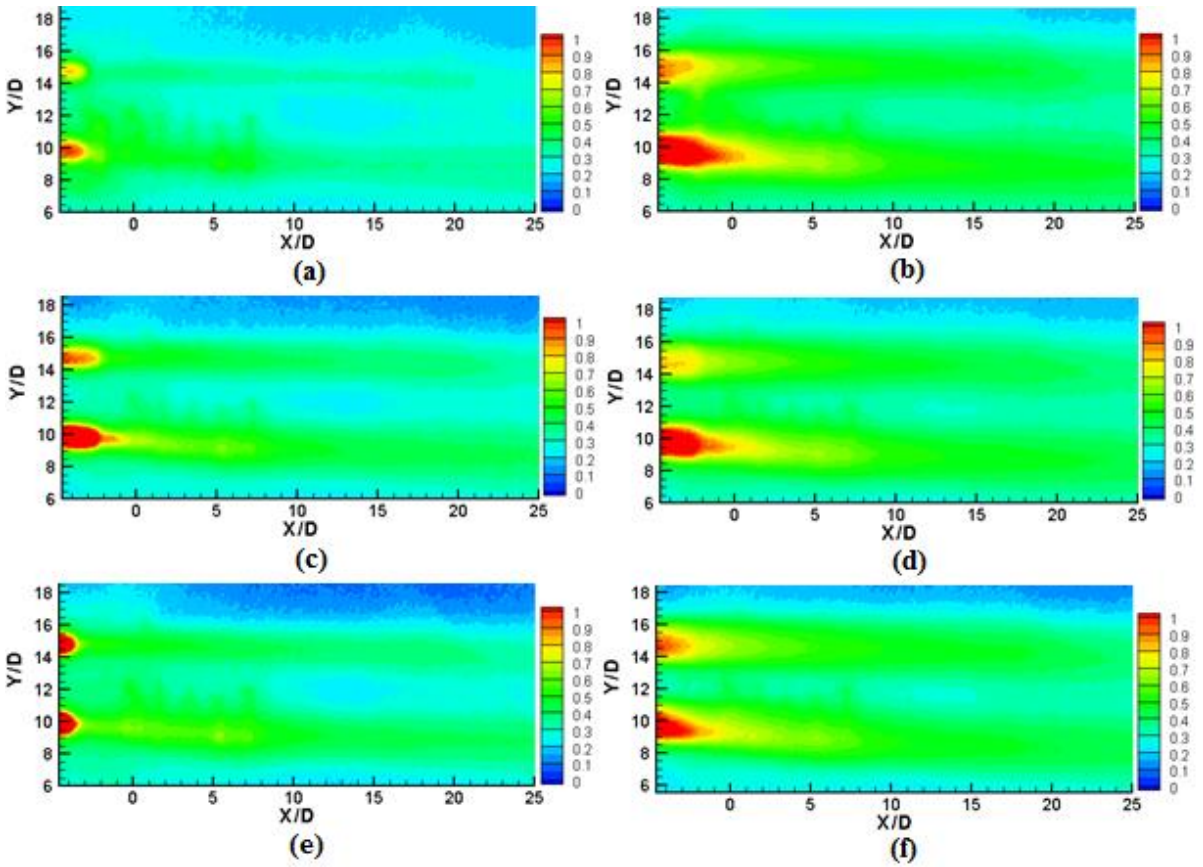

Figure 7-8: Local distributions of adiabatic effectiveness along end-wall at a blowing ratio of 1.1 and compound angle of zero (0) degrees, with turbulence grid. a) cylindrical 3D 60 degrees printed hole, b) laidback fan-shaped 3D zero (0) degrees printed hole, c) case 1 hole, d) case 2 hole, e) case 3 hole, f) case 4 hole.

At a compound angle of 20 degrees (see Figure 7-9), it is seen that the blowing ratio has a negligible effect on the effectiveness lateral spread, the reach of the effectiveness further downstream of hole exit and the coolant coverage.

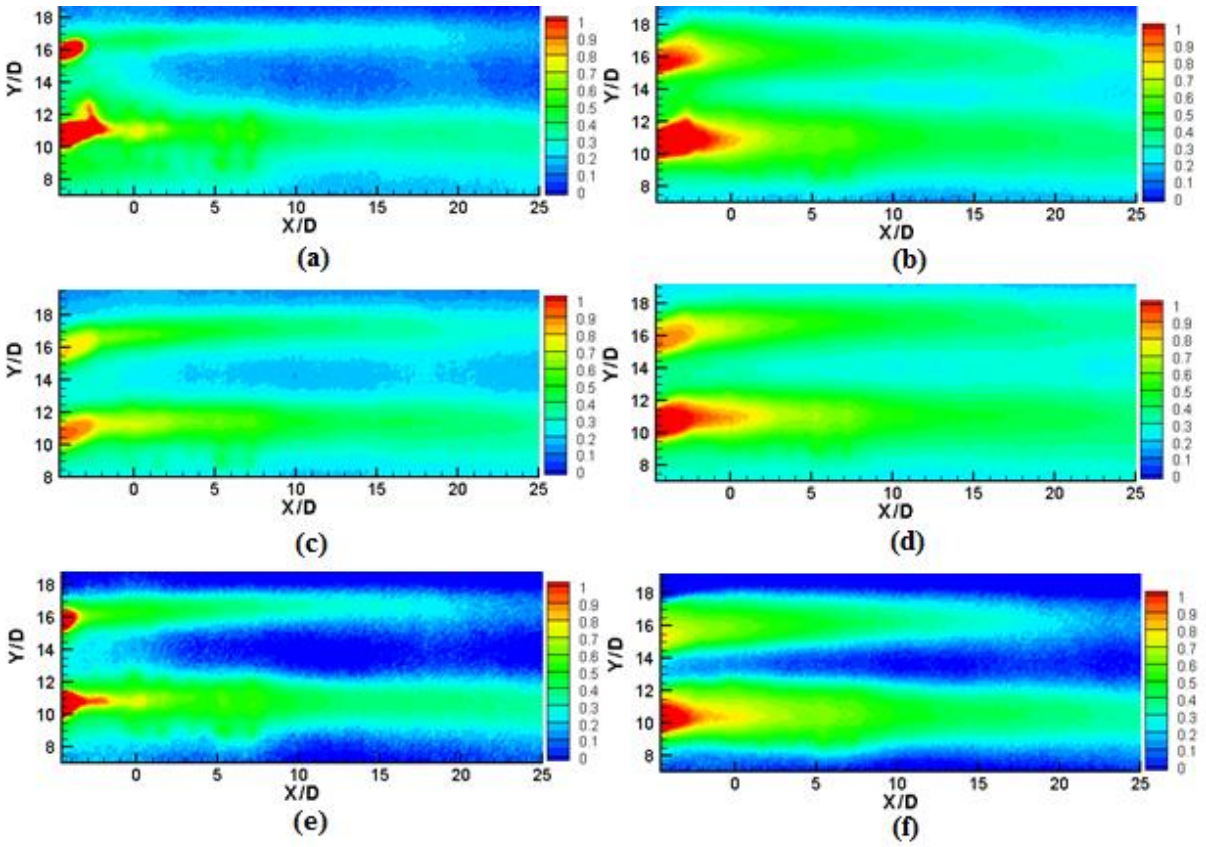

Figure 7-9: Local distributions of adiabatic effectiveness along end-wall at a blowing ratio of 1.1 and compound angle of 20 degrees, with turbulence grid. a) cylindrical 3D 60 degrees printed hole, b) laidback fan-shaped 3D zero (0) degrees printed hole, c) case 1 hole, d) case 2 hole, e) case 3 hole, f) case 4 hole.

7.2.2.Laterally averaged adiabatic effectiveness

It is seen, for all configurations, that the effectiveness decreases as the coolant moves further downstream. This agrees with results by Hayms and Leylek (2000). As stated above, the decrease in effectiveness may be due to mixing of the coolant jet with the crossflow as it moves further downstream.

7.2.2.1.Effect of compound angle

It is seen in Figure 7-10 that at X/D approximately less than 2.5 for the cylindrical hole the effectiveness is lower at zero (0) degrees compound angle than at the 20 degrees compound angle. As we move further downstream, the effectiveness is then higher for the zero (0) degrees compound angle. The difference in effectiveness then increases as the flow moves further downstream, with the maximum difference in effectiveness of approximately 0.1 (29.4%) being observed at X/D = 25.

Regarding the case 1 hole, at X/D approximately less than 7.5, the effectiveness is lower at zero (0) degrees compound angle than at the 20 degrees compound angle. As we move further downstream, the effectiveness is then higher for the zero (0) degrees compound angle. The difference in effectiveness nominally remains constant as the flow moves further downstream, with a difference in effectiveness of approximately 0.02 (5.9%) being observed.

Regarding the laidback fan-shaped hole, the case 2 hole, the case 3 hole and the case 4 hole, the highest effectiveness is observed at a compound angle of zero (0) degrees. It is significantly higher for the case 4 hole.

Regarding the laidback fan-shaped hole and the case 4 hole the difference in effectiveness , between the angles, increases as the flow moves further downstream. A maximum difference in effectiveness of approximately 0.12 (30%) is observed at X/D = 25. For the case 4 hole a maximum difference in effectiveness of approximately 0.11 (29.7%) is observed at X/D = 25.

Regarding the case 2 hole, it is observed that the difference in effectiveness between the angles is nominally constant as the flow moves further downstream, with a difference in effectiveness of approximately 0.025 (6.25%) being observed.

Regarding the case 3 hole, larger differences in effectiveness are observed at X/D < 10. The differences in effectiveness are smaller and relatively constant at X/D > 10. The largest effectiveness value of approximately 0.09 (19%) occurs at approximately X/D = 5.

The above reported behaviours contradict the findings of McGovern and Leylek (2000) where it was reported that increasing the compound angle resulted in an increase in the laterally averaged adiabatic effectiveness. It is reported that this is due to the coolant core being convected and diffused towards the surface more quickly as the compound angle is varied.

In the study by McGovern and Leylek (2000) higher blowing ratios, 1.25 and 1.88, were tested. Higher blowing ratios increase the strength of physical mechanisms that govern film cooling behaviour (Walters & Leylek 1997). So, it can be assumed that the convection to the surface is significantly stronger in the study by McGovern and Leylek (2000) because of the higher blowing ratios, as compared to this study.

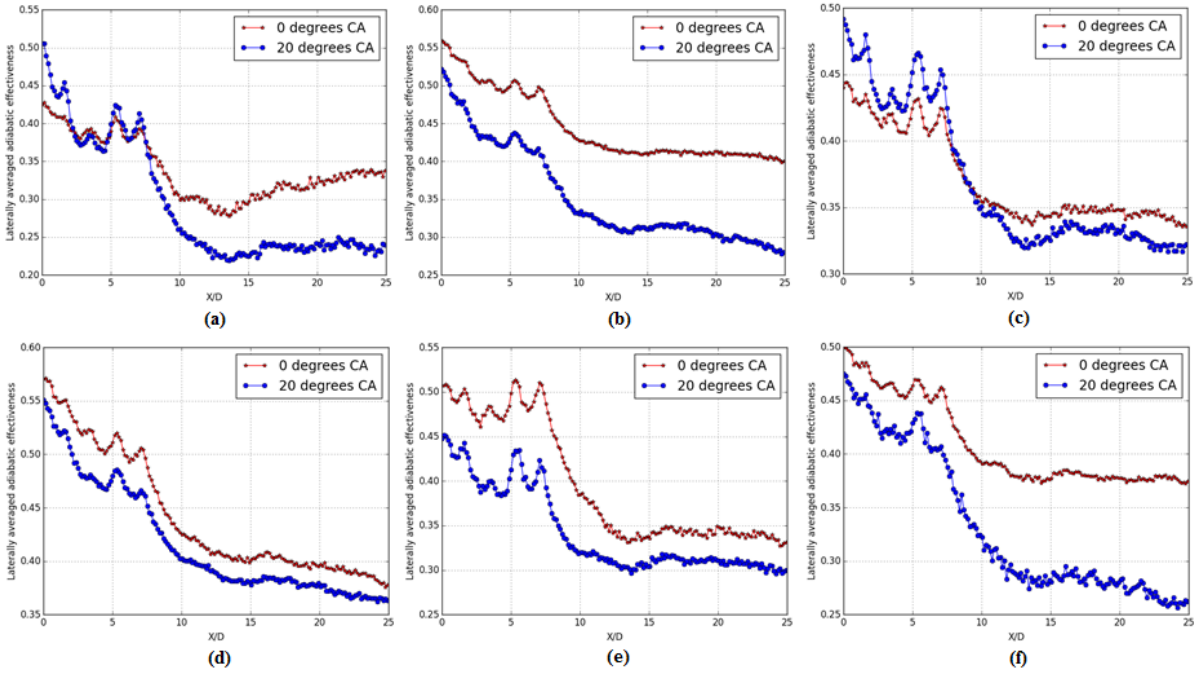

Figure 7-10: Effect of compound angle on the laterally averaged effectiveness at a blowing ratio equals to 0.6, with turbulence grid. a) cylindrical 3D 60 degrees printed hole, b) laidback fan-shaped 3D zero (0) degrees printed hole, c) case 1 hole, d) case 2 hole, e) case 3 hole, f) case 4 hole.

Nominally the same behaviour is observed at a blowing ratio of 1.1 (see Figure 7-11). The reasons, as above, are given for the observed behaviour.

Regarding the cylindrical hole, it is seen that significant differences between the laterally averaged effectiveness are observed at X/D > 7.5. It is seen that the difference increases as the flow moves further downstream. The largest effectiveness value of approximately 0.07 (23.3%) occurs at approximately X/D = 25.

Regarding the laidback fan-shaped hole, it is seen that the effectiveness is higher at compound angle zero (0) degrees in the whole range measured. It is seen that the difference increases as the flow moves further downstream. The largest effectiveness value of approximately 0.12 (30%) occurs at approximately X/D = 25.

Regarding the case 1 hole, it is seen that the effectiveness is higher for the 20 degrees compound angle at approximately X/D < 7.5. For X/D > 7.5, the effectiveness is higher at zero (0) degrees compound angle. The difference in effectiveness increases as the flow moves further downstream. The highest effectiveness is approximately 0.05 (14.7%) at X/D = 25.

Regarding the case 2 hole, it is seen that significant differences between the laterally averaged effectiveness are observed at X/D > 5. It is seen that the difference increases as the flow moves further downstream. The largest effectiveness value of approximately 0.04 (10.5%) occurs at approximately X/D = 25.

Regarding the case 3 hole, it is seen that the effectiveness is higher at compound angle zero (0) degrees in the whole range measured. It is seen that the difference increases as the flow moves further downstream. The largest effectiveness value of approximately 0.125 (38.5%) occurs at approximately X/D = 25.

Regarding the case 4 hole, it is seen that the effectiveness is higher at compound angle zero (0) degrees in the whole range measured. It is seen that the difference increases as the flow moves further downstream. The largest effectiveness value of approximately 0.16 (44.4%) occurs at approximately X/D = 25.

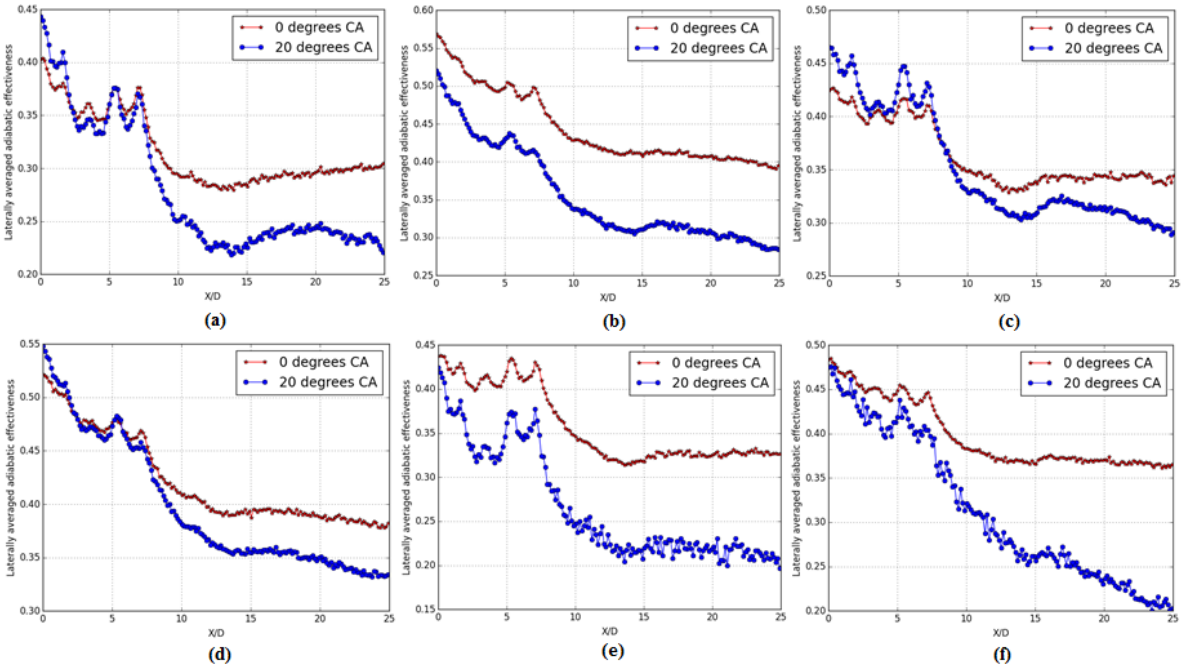

Figure 7-11: Effect of compound angle on the laterally averaged effectiveness at a blowing ratio equals to 1.1, with turbulence grid. a) cylindrical 3D 60 degrees printed hole, b) laidback fan-shaped 3D zero (0) degrees printed hole, c) case 1 hole, d) case 2 hole, e) case 3 hole, f) case 4 hole.

7.2.2.2. Effect of blowing ratio

It is seen in Figure 7-12 that for the cylindrical hole, the case 1 hole, the case 2 hole, the case 3 hole and the case 4 hole, on average the highest effectiveness is observed at a blowing ratio of 0.6. For the laidback fan-shaped hole the effectiveness is nominally the same at both blowing ratios.

Regarding the cylindrical hole, it is seen that relatively larger differences in effectiveness are observed at X/D < 7.5 and X/D > 15. The largest difference of approximately 0.03 (9.09%) is observed at approximately X = 25.

Regarding the case 1 hole, larger differences in effectiveness between the two (2) blowing ratios are observed closer to the film cooling holes. It is noted that as the flow moves further downstream the difference decreases. The largest difference in effectiveness of approximately 0.015 (3.66%) is observed at X/D = 2.5.

Similar behaviours as with the case 1 hole are observed for the case 2 hole, case 3 hole and the case 4 hole. Regarding the case 2 hole, the largest difference in effectiveness of approximately 0.055 (9.57%) is observed at X/D = 0. Regarding the case 3 hole, the largest difference in effectiveness of approximately 0.055 (9.57%) is observed at X/D = 0. Regarding the case 4 hole, the largest difference in effectiveness of approximately 0.02 (4.4%) is observed at approximately X/D = 2.5.

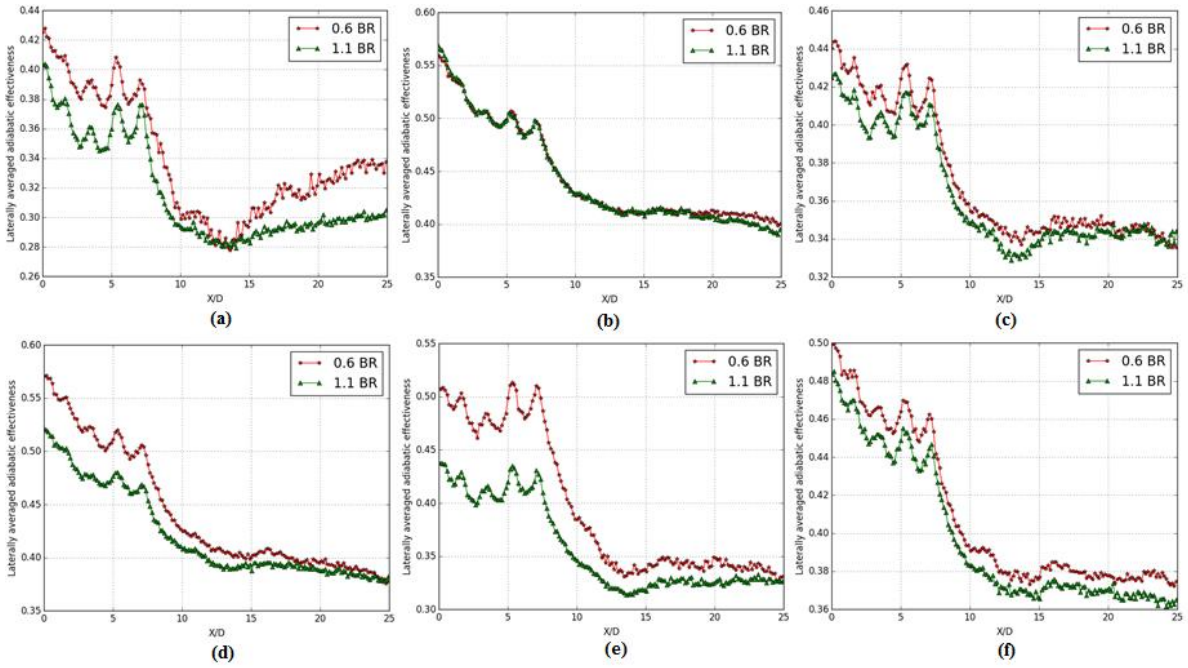

Figure 7-12: Effect of blowing ratio on the laterally averaged effectiveness at a compound angle equals to zero (0) degrees, with turbulence grid. a) cylindrical 3D 60 degrees printed hole, b) laidback fan-shaped 3D zero (0) degrees printed hole, c) case 1 hole, d) case 2 hole, e) case 3 hole, f) case 4 hole.

It is seen in Figure 7-13 that for the case 1 hole and the case 3 hole the highest effectiveness is observed at a blowing ratio of 0.6. For the case 1 hole, the largest difference in laterally averaged effectiveness of approximately 0.03 (9.4%) is observed at X/D = 25. For the case 3 hole, the largest difference in effectiveness of approximately 0.1 (33.33%) is observed at approximately X/D = 25.

Regarding the laidback fan-shaped hole, the effectiveness is nominally the same at both blowing ratios.

Regarding the cylindrical hole, the effectiveness is higher at a blowing ratio of 0.6 in the range of X/D less than ten (10). This may be due to the coolant jet being lifted off the surface closer to the hole, and then reattaching to the surface further downstream. The largest difference in effectiveness is observed of approximately 0.03 (8.1%) is observed at approximately X/D = 2.5.

Regarding the case 2 hole and the case 4 hole, the effectiveness, at both blowing ratios, is nominally the same closer to hole exit. A higher effectiveness is observed further downstream for a blowing ratio of 0.6. The difference in effectiveness increases as the flow moves further downstream. For the case 2 hole, the largest difference in effectiveness of approximately 0.035 (9.6%) is observed at approximately X/D = 25. For the case 4 hole, the largest difference in effectiveness of approximately 0.06 (23.1%) is observed at approximately X/D = 25.

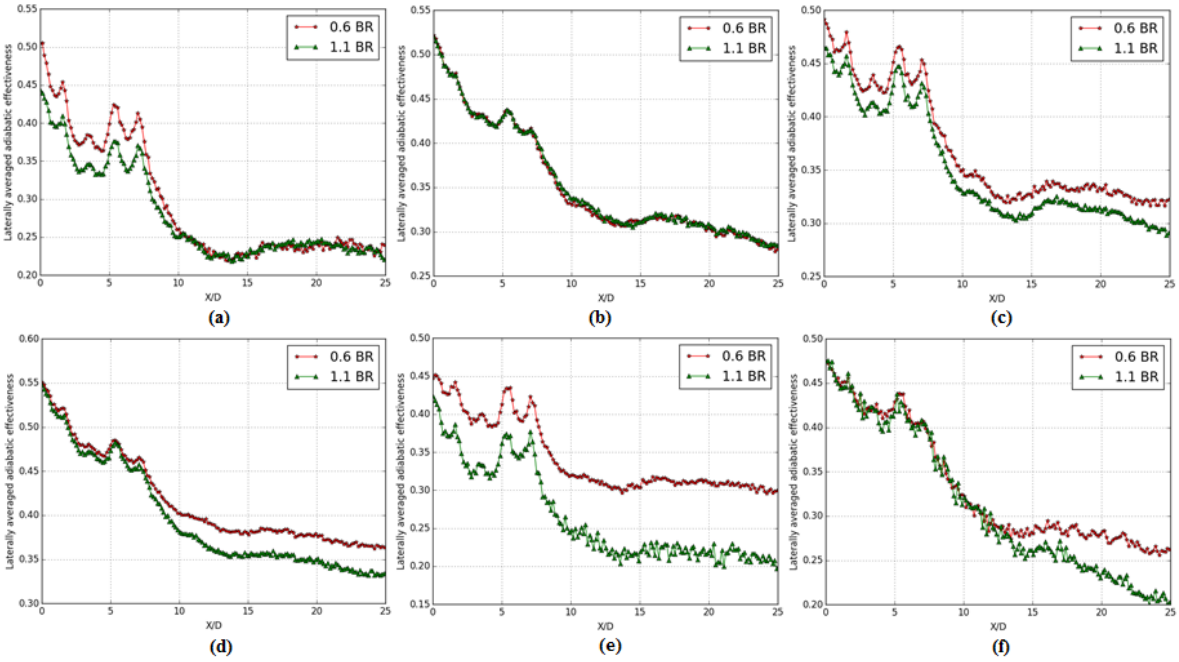

Figure 7-13: Effect of blowing ratio on the laterally averaged effectiveness at a compound angle equals to 20 degrees, with turbulence grid. a) cylindrical 3D 60 degrees printed hole, b) laidback fan-shaped 3D zero (0) degrees printed hole, c) case 1 hole, d) case 2 hole, e) case 3 hole, f) case 4 hole.

7.2.2.3. Effect of hole geometry

The behaviour of the baseline shapes, the cylindrical hole and the laidback fan-shaped hole, is first investigated. It is seen in Figure 7-14 that the effectiveness of the laidback fan-shaped hole is higher than that of the cylindrical hole. This behaviour is observed in the whole distance downstream of the hole, 0 < X/D < 25, for all blowing ratios and compound angles tested.

This agrees with the study by Hayms and Leylek (2000) where it was reported that the good thermal performance of the laterally diffused hole geometry is partly due to its low trajectory and wide breadth. The low trajectory results in the coolant being effectively injected into the mainstream flow boundary layer and remaining in the boundary layer until dissipated by diffusion mechanisms downstream. The wide breadth results in the vortex cores being spread apart in the lateral direction, which weakens induction lift.

It is seen from the results below that the case 2 hole shows the highest effectiveness and the cylindrical hole shows the lowest effectiveness. This behaviour is nominally the same for all blowing ratios and at all compound angles. No general pattern is observed for the other geometries as the blowing ratio and compound angle is varied.

Comparing the case 2 hole and the cylindrical hole, at all the blowing ratios and compound angles tested, it is seen that the largest difference in the laterally averaged effectiveness is observed at approximately X/D = 12.5. From Figure 7-14(a), it is seen that the largest difference in effectiveness is approximately 0.12 (30%). From Figure 7-14(b), it is seen that

the largest difference in effectiveness is approximately 0.15 (39.5%). From Figure 7-14(c), it is seen that the largest difference in effectiveness is approximately 0.12 (30.8%). From Figure 7-14(d), it is seen that the largest difference in effectiveness is approximately 0.12 (34.3%).

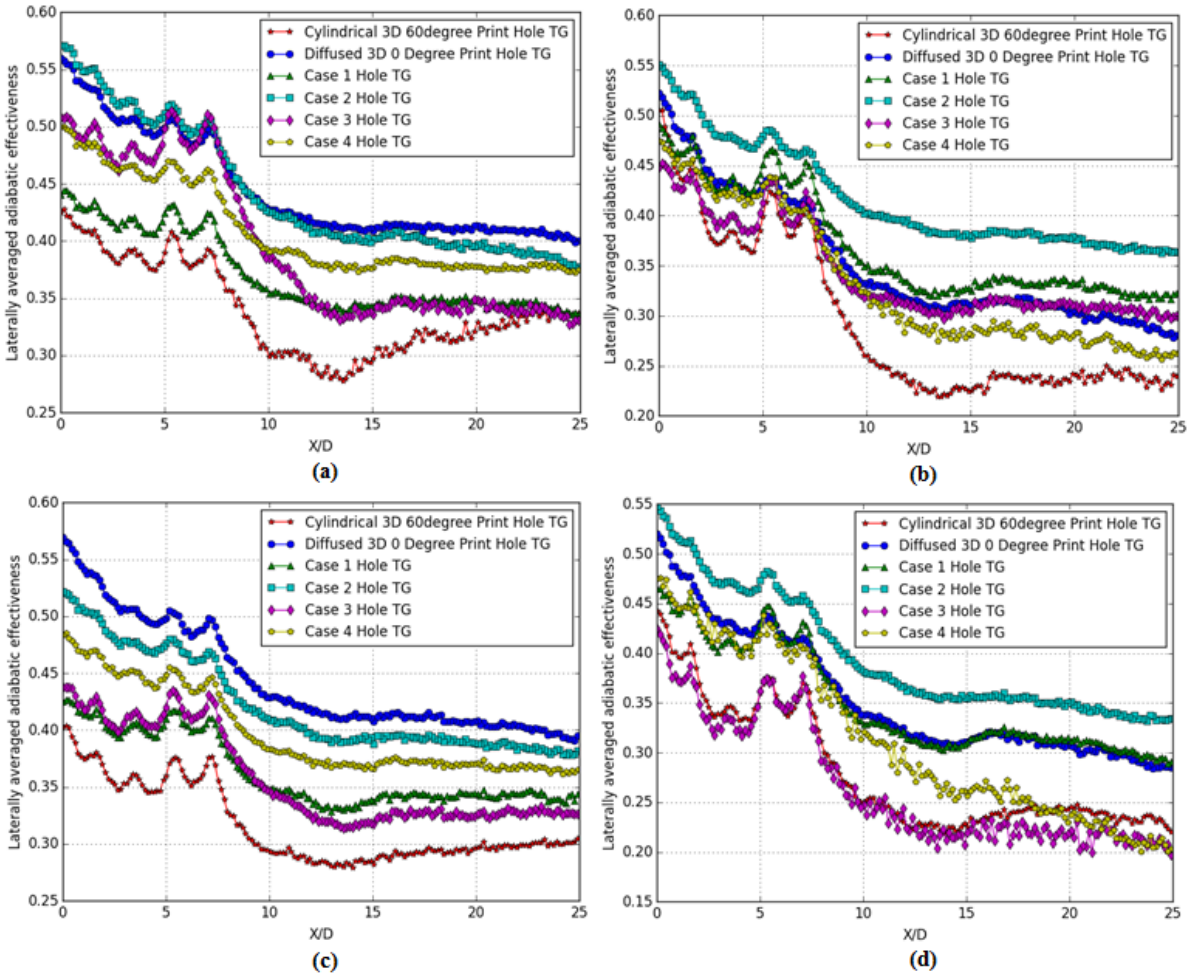

Figure 7-14: Effect of shape on the laterally averaged effectiveness. a) blowing ratio 0.6 compound angle zero (0) degrees, b) blowing ratio 0.6 compound angle 20 degrees, c) blowing ratio 1.1 compound angle zero (0) degrees, d) blowing ratio 1.1 compound angle 20 degrees.

7.3.Conclusion

Above, adiabatic effectiveness results were presented for nine (9) film cooling hole geometries, at two (2) blowing ratios of 0.6 and 1.1, two (2) compound angles, 0 and 20 degrees, and with and without the presence of a turbulence grid.

No general pattern was observed for the effects of turbulence intensity, manufacturing method and 3D print build orientation, on the adiabatic film cooling effectiveness. It was is concluded that the effects are strongly dependent on the hole geometry and test conditions.

It was found that the laidback fan-shaped hole, the case 2 hole and the case 4 hole have better lateral spread as compared to the cylindrical hole, the case 1 hole and the case 3 hole. It was also found that increasing the compound angle decreases the lateral averaged effectiveness. And a decrease in the lateral averaged effectiveness was observed as the blowing ratio was increased.

The highest laterally averaged effectiveness was observed at a compound angle of zero (0) degrees, a blowing ratio of 0.6 for most of the configurations tested. The case 2 film cooling

geometry resulted in the highest averaged effectiveness at most of the compound angles and blowing ratios tested.

8.Summary, Conclusion & Recommendations

8.1.Summary

Film cooling has, over the years, allowed for the operation of modern gas turbines at temperatures far exceeding the limits of the material properties of the turbine components. This has resulted in increased power output and efficiency of the gas turbines. But over 40+ years of research has not culminated in the goal of achieving ideal cooling films, such as from two-dimensional (2D) continuous slots.

This study employed a curvature in the forward diffuser section of the film cooling hole. This was expected to improve the performance of the hole. The performance parameters investigated and reported were the discharge coefficient of the holes, the flowfield downstream of the hole exit trailing edge, the temperature field downstream of the hole exit trailing edge and the heat transfer characteristics.

The effects of pressure ratio, mainstream crossflow, compound angle, hole geometry, manufacturing method, 3D print build orientation, and inclination angle, on the discharge coefficient were investigated.

On the flowfield, temperature field and adiabatic wall effectiveness, the effects of blowing ratio, hole geometry, compound angle, turbulence intensity and downstream distance from hole exit trailing edge, were also investigated.

8.2.Conclusion

8.2.1.Discharge Coefficient

Based on the results and discussion in chapter 4, it is concluded that:

- at low pressure ratios the discharge coefficient is a strong function of the pressure ratio, increasing with it, for all film cooling holes investigated;
- in the pressure ratio range tested, the mainstream crossflow only had a significant effect on the cylindrical and laidback fan-shaped holes. The effect of the mainstream crossflow was negligible for the cases where an arc was employed as the forward diffusion. This was due to the development of the flow inside the hole and the resulting exit coolant jet velocity profile and its interaction with the mainstream crossflow;
- the effect of the compound angle was found to be negligible for all film cooling hole geometries. This was a result of the development of the flow inside the hole and the resulting exit coolant jet velocity profile and its interaction with the mainstream crossflow;
- higher discharge coefficient values are observed for the holes with expanded exits as compared to those of the cylindrical holes. The reason being pressure recovery in the expanded sections of the diffused holes;
- cases 1 to 4 showed higher discharge coefficient values as compared to the laidback fan-shaped holes. This was a result of the development of the flow inside the hole and the resulting exit coolant jet velocity profile and its interaction with the mainstream crossflow;
- the manufacturing method and 3D print orientation, regardless of the hole geometry, has a negligible effect on the discharge coefficient. This is due to the small relative roughness of the holes. This is more evident at low pressure ratios; and
- the inclination angle has a negligible effect on the discharge coefficient.

8.2.2.Flow structure far downstream of hole exit

In chapter 5, flowfield results were presented for six (6) film cooling hole geometries, with measurements taken on two (2) planes, six (6) and twelve (12) diameters downstream of hole exit trailing edge, for two (2) blowing ratios, 0.9 and 1.3, and two (2) compound angles, zero (0) and 20 degrees.

It was found that at a blowing ratio of 0.9 and compound angle equals to zero (0) degrees, for all geometries, the coolant jet was close to the surface. This is because of the small vertical momentum of the coolant jet at the exit. Additionally, because the jet is close to wall, the counterrotating vortices responsible for upward lift are rapidly degraded.

It was also found that the geometries with less expansion areas (cylindrical, case 1 and case 3 hole) have more height, as compared to the geometries with larger expansion areas (laidback fan-shaped, case 2 and case 4 hole). The geometries with larger lateral expansions showed better spread of the coolant downstream of the hole exit.

The higher height is due to the area expansion, which decreases the effective velocity and the vertical momentum content of the coolant jet on exit and decreases the penetration into the boundary layer of the crossflow. Additionally, the area expansion relaxes the velocity gradients on the side walls which decreases the strength of the streamwise film hole boundary layer vortices emanating from the hole. This decreases the strength of the counterrotating vortices. The better lateral spread is due to the lateral diffusion of the hole which locates the longitudinal vortices farther apart from each other such that the convective strength of the secondary flow at the centreline is reduced.

At a blowing ratio of 1.3 and compound angle equals to zero (0) degrees it was determined that for the cylindrical hole, case 1 and case 3 holes, the coolant jet is lifted from the wall. For the laidback fanshaped hole, case 2 and case 4 holes, the coolant is still close to the surface. It was determined that differences in behaviour were significantly due to the differences in lateral expansion between the geometries.

The coolant jet significantly lifting-off for the cylindrical hole, the case 1 hole and the case 3 hole, is due to the initial positioning, in the near-field, of the coolant jet as it exits the hole coupled with the increased strength of the counterrotating vortices as the coolant jet moves downstream. The strength of the counterrotating vortices, which is related to the upward lift (induction lift) generated by the counterrotating vortices downstream of the hole exit, is strongly dependent on the blowing ratio.

The increased vertical momentum of the jet positions it farther from the wall as it exits the film cooling hole. The coolant jet exiting the hole further from the wall results in further increased strength of the longitudinal vortices. As the coolant jet moves downstream, it is lifted away from the surface by the counter-rotating vortices. Since the location of maximum vorticity is farther from the wall the streamwise counter-rotating vorticity is dissipated less rapidly and is apparent farther downstream.

For the case 2 hole, case 4 hole and the laidback fan-shaped hole it was determined that the increased blowing ratio did not significantly strengthen the mechanisms that result in poor film cooling performance in other geometries. These mechanisms include the strengthening of the longitudinal vortices which results in, 1) coolant upwards lift from the surface and 2) the inability of the coolant to properly laterally spread because of the strengthened coolant convection towards the centreline.

At a blowing ratio of 0.9 and compound angle equals to 20 degrees it was determined, for all hole geometries, that the coolant is close to the wall and the coolant jet is skewed to the right

and arguably better lateral spread is achieved. The skewness to the right of the coolant jet downstream is primarily due to the significant lateral motion imposed by the asymmetric vortex structure.

At a blowing ratio of 1.3 and compound angle equals to 20 degrees it was determined that for the cylindrical hole, case 1 and case 3, the coolant jet was significantly lifted from the surface and the motion of the coolant jet is skewed to the right.

For the laidback fan-shaped hole, case 2 and case 4 hole, comparing the velocity results, with those at a compound angle of 20 degrees and a blowing ratio of 0.9, it is seen that the coolant is still close to the wall and the motion of the coolant jet is skewed to the right. But the coolant jet is slightly more pronounced in the mainstream flow. This was expected because an increased amount of coolant was being injected into the flow.

It was additionally determined that employing the curvature decreases the height and trajectory of the jet on exit. The decreased height is due to the decreased vertical momentum content of the coolant jet. The decreased trajectory positions the longitudinal vortices closer to the wall which results in better lateral spread of the coolant. This could not be concluded with certainty because of the variation in the lateral expansion of the film cooling geometries, case 1 to 4 and also because the five hole probe could not get close enough to the wall.

With a turbulence grid included in the flow it was determined that the behaviour of the coolant jet in the mainstream flow is nominally the same. From this it was concluded that the physical mechanisms that determine the flow behaviour downstream in the case ‘without a turbulence grid’ are still dominant in the case ‘with a turbulence grid’; the turbulence grid had little effect on the behaviour. The added turbulence intensity of approximately 4.9%, by the turbulence grid, was not significant enough to result in an appreciable effect on the flow structure downstream of the hole exit. The wanted effect being to aid in spreading the coolant jet on the surface.

Further downstream of the hole exit trailing edge, twelve (12) diameters downstream, the coolant jet is barely noticeable in the mainstream flow. The effects of the secondary flow are negligible, and the coolant jet diffuses and takes on the shape of the boundary layer.

The case 2 hole geometry is recommended for further investigation. The case 2 hole geometry resulted in low jet height when in the mainstream, which means that it was closer to the surface that requires cooling. It also resulted in a relatively good lateral spread of the coolant on the surface.

8.2.3. Temperature field far downstream of hole exit

In chapter 6, temperature field results were presented for six (6) film cooling hole geometries, with measurements taken on (1) plane, six (6) diameters downstream of hole exit trailing edge, at one (1) blowing ratios of 0.9, two (2) compound angles, 0 and 20 degrees, and with and without the presence of a turbulence grid.

It was found that the coolant jet core was lifted from the surface for the cylindrical hole. For the laidback fan-shaped hole the coolant jet core was much closer to the surface and showed better lateral spread closer to the surface as compared to the cylindrical hole. Additionally, It was seen that the coolant from the cylindrical hole had more height and the coolant jet core had a lower non-dimensionalized temperature.

In comparing cases 1 to 4 to the cylindrical hole, it was found that the new shapes had better lateral spread and the cylindrical hole had more height.

In comparing cases 1 and 3 to the laidback fan-shaped hole it was seen that the lateral spread of the laidback fan-shaped hole was superior, and the case 1 and 3 holes had higher height. It was also seen that the coolant jet core of the case 3 hole had a lower non-dimensional temperature.

In comparing case 2 and 4 to the laidback fan-shaped hole it was seen that better lateral spread of the coolant jet core is observed for cases 2 and 4; case 4 spreading even better than case 2. It was also seen that the coolant jet core of the case 4 hole has a lower non-dimensional temperature.

In comparing the new shapes against each other, it was seen that the coolant jet core of cases 2 and 4 has better lateral spread and cases 1 and 3 have better height.

In comparing the results at 20 degrees to those at zero (0) degrees compound angle, it was found that the coolant was slightly skewed to the right. Increased lateral spread was also observed. The effects of shape on the flow structure were found to be similar to those at a compound angle of zero (0) degrees.

Incorporation of a turbulence grid in the mainstream flow had a negligible effect on the temperature field downstream.

The case 2 hole geometry is recommended for further investigation. The case 2 hole geometry resulted in low jet height when in the mainstream, which means that it was closer to the surface that requires cooling. It resulted in a relatively good lateral spread of the coolant on the surface. And it resulted in a lower non-dimensional temperature of the coolant core, which means that the was less mixing/transfer of temperature (energy) between the mainstream and the coolant.

8.2.4. Adiabatic wall effectiveness downstream of hole exit

In chapter 7, adiabatic effectiveness results were presented for nine (9) film cooling hole geometries, at two (2) blowing ratios of 0.6 and 1.1, two (2) compound angles, 0 and 20 degrees, and with and without the presence of a turbulence grid.

No general pattern was observed for the effects of turbulence intensity, manufacturing method and 3D print build orientation, on the adiabatic film cooling effectiveness. It was is concluded that the effects are strongly dependent on the hole geometry and test conditions.

It was found that the laidback fan-shaped hole, the case 2 hole and the case 4 hole have better lateral spread as compared to the cylindrical hole, the case 1 hole and the case 3 hole. It was also found that increasing the compound angle decreases the lateral averaged effectiveness. And a decrease in the lateral averaged effectiveness was observed as the blowing ratio was increased.

The highest laterally averaged effectiveness was observed at a compound angle of zero (0) degrees, a blowing ratio of 0.6 for most of the configurations tested. The case 2 film cooling geometry is recommended for further investigation as it resulted in the highest laterally averaged effectiveness at most of the compound angles and blowing ratios tested.

8.3. Recommendations

Based on the above results and discussion the following recommendations are made:

- The measurement uncertainty of the discharge coefficient, blowing ratio and momentum flux ratio is relatively large. This is more prevalent at low pressure ratios; Figure 3-9. This is mainly due to the measurements from the compressor. These measurements are the volume flowrate and the density of the coolant, which are used to calculate the actual mass flow rate through the holes. This large uncertainty makes

it difficult to investigate the effects of small changes, such as the 10 degrees increments of the compound angle that was investigated in this study. It is recommended that the accuracy of measuring be improved. Possibly the addition of another flow meter downstream of the location where the flow is expanded into the plenum box.

- With a large uncertainty interval, the tests should be repeated several times, in order to gain more clarity and confidence on the observed behaviour.
- Flow structure measurements, velocity and turbulence intensity, at the hole exit plane would prove the assumptions made by the student about the flow structure and its effect on the discharge coefficient. A properly done CFD model, as was done in the study by, Leylek and Zerkle (1993) or Li *el al.* (2017), would also allow for determination of the flow structure.
- Testing at higher pressure ratios, in the ranges commonly reported in literature, so that proper comparisons can be made.
- The hole geometries of case 1 to 4 have different lateral spread angles. Keeping this angle fixed at seven (7) degrees, for all the hole geometries, would isolate the effect of employing arcs at the diffusion sections of the hole.
- The full range of momentum flux ratio, for the different hole geometries, be tested to verify that the behaviour observed at this constant pressure ratio range persists.
- For the flow structure measurements, use a miniature probe, that will allow for measurements to be taken closer to the wall. Alternatively, optical velocity measurement techniques, such as PIV, could be used.
- For the flow structure measurements, decrease the traversing increments so that mechanisms/effects at, and around the coolant jet, can be captured adequately.
- The case 2 hole geometry is recommended for further investigation. The case 2 hole geometry resulted in low jet height when in the mainstream, which means that it was closer to the surface that requires cooling. It also resulted in a relatively good lateral spread of the coolant on the surface. And it resulted in the highest laterally averaged effectiveness at most of the compound angles and blowing ratios tested.

9.Conference Paper

The conference paper, titled '*Experimental Study of Diffused Cylindrical Holes For Film-Cooling Performance*', is currently being prepared for publication.

10. References

- Aghasi, P, Gutmark, E & Munday, D 2017, ' Dependence of film cooling effectiveness on three-dimensional printed cooling holes', *Journal of Heat Transfer*, vol. 139, pp. 102003-1 : 102003-15.Anderson, JB, Boyd, EJ & Bogard, DG 2015, 'Experimental Investigation of Coolant-to-Mainstream Scaling Parameters with Cylindrical and Shaped Film Cooling Holes', ASME Paper No. GT2015-43072.
- Andreopoulus, J & Rodi, W 1983, 'Experimental Investigation of Jets in a Crossflow', *Journal of Fluid Mechanics*, vol. 138, pp. 93-127.
- Andrews, GE & Mkpadi, MC 1984, 'Full-Coverage Discrete Hole Wall Cooling: Discharge Coefficients', *Journal of Engineering for Gas Turbines and Power*, vol. 106, pp. 183-192.
- Armfield 2016, Centrifugal compressor demonstration unit: Instruction manual, England, UK: Author.
- Beckwith, TG, Maragoni, RD & Lienhard V, JH 2009, *Mechanical Measurements*, Prentice Hall, New Jersey.
- Benmansour, S 1981, 'Discharge Coefficients of Film Cooling Holes', MPhil Thesis, University of Nottingham, UK.
- Bernsdorf, S, Rose, MG & Abhari, RS 2006, 'Modeling of Film Cooling—Part I: Experimental Study of Flow Structure', *Journal of Turbomachinery*, 128(1), pp. 141–149.
- Brittingham, RA & Leylek, JH 2000, 'A detailed analysis of film cooling physics: Part 4 – Compound angle injection with shaped holes', *Journal of Turbomachinery*, vol. 122, pp. 133-145.
- Bromley, SJ 1994, 'Flow in Flares', BEng Thesis, Department of Mechanical Engineering, University of Nottingham, UK.
- Bunker, RS 2005, 'A Review of Shaped Hole Turbine Film Cooling Technology', *Journal of Heat Transfer*, vol. 127, pp. 441-453.
- Bunker, RS 2010, 'Film Cooling: Breaking the Limits of Diffusion Shaped Holes', *Heat Transfer Research*, 41(6), pp. 627–650.
- Burd, SW & Simon, TW 1999, 'Measurements of Discharge Coefficients in Film Cooling', *Journal of Turbomachinery*, vol. 121, pp. 243-248.
- Ekkad, S & Han, JC 2013, 'A Review of Hole Geometry and Coolant Density Effect on Film Cooling', ASME Paper No. HT2013-17250.
- Frenkiel, FN 1948, 'The decay of isotropic turbulence', *Journal of Applied mechanics*, pp. 311-321.
- Gritsch, M, Schulz, A & Wittig, S 1998, 'Discharge Coefficients Measurements of Film-Cooling Holes With Expanded Exits', *Journal of Turbomachinery*, vol. 120, pp. 557-563.
- Gritsch, M, Schulz, A & Wittig, S 1998b, 'Adiabatic Wall Effectiveness Measurements for Film Cooling Holes With Expanded Exits', *Journal of Turbomachinery*, vol 120, pp. 549-556.
- Gritsch, M, Schulz, A & Wittig, S 2001, 'Effect of Crossflows on the Discharge Coefficient of Film Cooling Holes With Varying Angles of Inclination and Orientation', *Journal of Turbomachinery*, vol 123, pp. 781-787.
- Hay, N, Henshall, SE & Manning, A 1994, 'Discharge Coefficient of Holes Angled to the Flow Direction', *Journal of Turbomachinery*, vol. 115, pp. 92-96.
- Hay, N, Lampard, D & Benmansour, S 1983, 'Effect of Crossflows on the Discharge Coefficient of Film Cooling Holes', *Journal of Engineering for Power*, vol. 105, pp. 243-248.

- Hay, N, Lampard, D & Khaldi, A 1994, The Coefficient of Discharge of 30° Inclined Film Cooling Holes With Rounded Entries or Exits, ASME Paper No. 94-GT-180.
- Hay, N & Lampard, D 1995, 'The Discharge Coefficient of Flared Film Cooling Holes', ASME Paper No. 95-GT-15.
- Hay, N & Lampard, D 1998, 'Discharge Coefficient of Turbine Cooling Holes: A Review', *Journal of Turbomachinery*, vol. 120, pp. 314-319.
- Hayms, DG & Leylek, JH 2000, 'A detailed analysis of film cooling physics: Part 3 - Streamwise injection with shaped holes', *Journal of Turbomachinery*, vol. 122, pp. 122-132.
- Japan Society of Mechanical Engineers 1988, 'Visualized Flow', Pergamon Press.
- Khaldi, A 1987, 'Discharge Coefficients of Film Cooling Holes With Rounded Entries or Exits', PhD Thesis, University of Nottingham, UK.
- Klein, A 1981, 'Effects of Inlet conditions on conical-diffuser performance', *ASME Journal of Fluid Engineering*, vol. 103, pp. 250-257.
- Leylek, JH & Zerkle, RD 1993, 'Discrete-Jet Film Cooling: A comparison of Computational Results with Experiments', ASME Paper No. 93-GT-207.
- Lichtarowicz, A, Duggins, RK & Markland, E 1965, 'Discharge Coefficients for Incompressible Non-Cavitating Flow through Long Orifices', *Journal Mechanical Engineering Science*, vol. 7, no. 2, pp. 210-219.
- Li, Y, Zhang, Y, Su, X & Yuan, X 2017, 'Experimental and numerical investigations of shaped hole film cooling with the influence of endwall cross flow', *International Journal of Heat and Mass Transfer*, vol. 120, pp. 42-55.
- Ligrani, PM, Singer, BA & Baun, LR 1989, 'Miniature five-hole pressure probe for measurement of three mean velocity components in low-speed flows', *Journal of Physics E: Scientific Instruments*, vol: 22, pp. 868-876.
- Ligrani, PM, Singer, BA & Baun, LR 1989b, 'Spatial resolution and downwash velocity corrections for multiple-hole pressure probes in complex flows', *Experiments in Fluids*, pp. 424-426.
- Mahmood, GI, Shote, AS & Huyssen, BS, n.d.,'Performance of Film-cooling Flow from Upstream Endwall Holes in a Vane Cascade', University of Pretoria, South Africa.
- McGovern, KT & Leylek, JH 2000, 'A detailed analysis of film cooling physics: Part 2 – Compound angle injection with cylindrical holes', *Journal of Turbomachinery*, vol. 122, pp. 113-121.
- Panton, RL 2013, *Incompressible Flow*, John Wiley & Sons Inc., Massachusetts.
- Persh, J and Bailey, BM 1954, 'Effect of Surface Roughness Over the Downstream Region of a 23 Degree Conical Diffuser', Langley Field, Hampton, VA, Report No. NACA-TN-3066.
- Pietrzyk, JR, Bogard, DG & Crawford, ME 1989, 'Hydrodynamic Measurements of Jets in Crossflow for Gas Turbine Film Cooling Applications', *Journal of Turbomachinery*, vol. 111, pp. 139-145.
- Rogers, T & Hersh, AS 1975, 'The Effect of Grazing Flow on the Steady State Resistance of Square-Edged Orifices', AIAA Paper No. 75-493.
- Rowbury, DA, Oldfield, MLG, & Lock, GD 1997, 'Engine Representative Discharge Coefficients Measured in an Annular Nozzle Guide Vane Cascade', ASME Paper No. 97-GT-99.
- Rowbury, DA, Oldfield, MLG, & Lock, GD 2001, 'A Method for Correlating the Influence of External Crossflow on the Discharge Coefficients of Film Cooling Holes', *ASME Journal of Turbomachinery*, vol. 123, pp. 258–265.
- Roach, PE 1987, 'The generation of nearly isotropic turbulence by means of grids', *Heat and Fluid flow*, vol. 8, no. 2, pp. 82–92.
- Ryan, A 2013, 'Jet Engine Design: Turbine Cooling', *Aerospace Engineering Blog*, viewed 05 November 2019, https://aerospaceengineeringblog.com/turbine-cooling/

- Sargent, SR, Hedlund, CR & Ligrani, PM 1998, 'An infrared thermography imaging system for convective heat transfer measurements in complex flows', *Measurements Science and Technology*, vol. 9, pp. 1974-1981.
- Sasaki, M, Takahara, K, Sakata, K & Kumagai, T 1975, 'Study on Film Cooling of Turbine Blades (1st Report, Experiments on Film Cooling with Injection through Holes near leading Edge)', *Bulletin of the JSME*, vol. 19, no. 137, pp. 1344-1352.
- Saumweber, C & Schulz, A 2012, 'Free-Stream Effects on the Cooling Performance of Cylindrical Fan-Shaped Cooling Holes', *Journal of Turbomachinery*, vol. 134, pp. 061007-061018.
- Schroeder, RP & Thole, KA 2014, 'Adiabatic Effectiveness Measurements for a Baseline Shaped Film Cooling Hole', ASME Paper No. GT2014-25992.
- Shote, AS, 2020, 'Aerodynamic losses and endwall heat transfer in a linear vane cascade with endwall film-cooling and endwall leading-edge contouring', PhD thesis, University of Pretoria, South Africa.
- Shote, AS, Mahmood, GI & Meyer, JP 2020, 'Influences of large fillets on endwall flows in vane cascade with upstream slot flim-cooling', *Experimental Thermal and Fluid Science*, 112.
- Shote, AS, Huyssen, BB & Mahmood, GI, n.d.,'Heat Transfer and Slot Film-Cooling Effectiveness on Endwall in a Filleted Vane Cascade', University of Pretoria, South Africa.
- Sinha, AK, Bogard, DG, & Crawford, ME 1991, 'Film-Cooling Effectiveness Downstream of a Single Row of Holes With Variable Density Ratio', *Journal of Turbomachinery*, 113(3), pp. 442–449.
- Stern, F, Muste, M, Beninati, M & Eichinger, WE 1999, 'Summary of Experimental Uncertainty Assessment Methodology With Example', IIHR Technical Report No. 406, The University of Iowa.
- Stimpson, CK, Snyder, JC, Thole, KA & Mongillo, D 2017, 'Scaling Roughness Effects on Pressure Loss and Heat Transfer of Additively Manufactured Channels', *Journal of Turbomachinery*, vol. 139, no. 2, p. 021003.
- Stimpson, CK, Snyder, JC, Thole, KA & Mongillo, D 2018, 'Effects of Coolant Feed Direction on Additively Manufactured Film Cooling Holes', *Journal of Turbomachinery*, vol. 140, pp. 111001-1 – 111001-10.
- Thole, KA, Gritsch, M, Schulz, A & Wittig, S 1997, 'Effect of a Crossflow at the Entrance to a Film Cooling-Cooling Hole', *Journal of Fluids Engineering*, vol. 119, pp. 533-540.
- Thole, KA, Gritsch, M, Schulz, A & Wittig, S 1998, 'Flowfield Measurements for Film Cooling Holes With Expanded Exits', *Journal of Turbomachinery*, vol. 120, pp. 327-336.
- Timko, LP 1984, 'Energy Efficient Engine High Pressure Turbine Component Test Performance Report', viewed 03 February 2021, https://ntrs.nasa.gov/citations/19900019237.
- Walters, DK & Leylek, JH 1997, 'A detailed analysis of film cooling physics: Part 1 - Streamwise injection with cylindrical holes', ASME Paper No. 97-GT-269.
- Xue, S & Ng, WF 2018, 'Turbine Blade Tip External Cooling Technologies', *Aerospace*, vol. 5, no. 3, p. 90.

List of Amendments as recommended by Professor Dirker & Professor Sundén

Page	Paragraph No.	Amendment
7	N/A	Bullets used with headings.
11	N/A	Figure 2-5 has been re-sketched.
34	14	Dimensions of test set-up related to actual turbine dimensions.
37	N/A	Figure 3-6 moved to section where it is described in more detail. Origin of velocity/temperature has been indicated on the figure.
39	N/A	Origin of velocity/temperature has been indicated on the figure 3-7.
46	N/A	Words that were too long were fit to column width.
47	N/A	Sub figures in that were missing in Figure 3-9 are included.
48	N/A	Vertical axis title on Figure 3-10 has been changed to indicate no unit.
49	N/A	Multiple conclusions in chapter 4 sections have been combined into a single conclusion presented at the end of the chapter
72	4	Quantitative analysis of 'effect of shape data' is included.
76	N/A	Figure 5-1 amended.
76	N/A	Figures in chapter 5 were moved closer to paragraphs where they are discussed.
77	2 & 3	An explanation of the velocity vectors normal to the flow is provided.
98	4	Recommendation of most proper hole geometry based on flow field results has been included.
99	N/A	Quantitative analysis of data is included in chapter 6.
105	3	Recommendation of most proper hole geometry based on temperature field results has been included.
115	N/A	Quantitative analysis of data been included for the line plots.
126	N/A	Reference to the conference paper being prepared has been included.

Appendices

A. Derivation of the ideal mass flow rate expression

The velocity measured at the exit of a contraction is less than the maximum value because of losses. Therefore, the velocity value measured at the exit of the contraction is proportional to the actual mass flow rate through the contraction:

$$\dot{m}_{actual} \propto V_{measured}$$

where:

$\dot{m}_{actual}$: actual mass flow rate through hole

$V_{measured}$: measured velocity

The pressure drop across the contraction does not capture the losses due to the conversion from static pressure energy to kinetic energy. Therefore, the pressure difference across the contraction corresponds to an ideal flow of the coolant. This means that the pressure difference is proportional to the ideal mass flow rate, m_i, through the contraction.

$$\dot{m}_{ideal} \propto \Delta P_{across\_contraction}$$

where:

$\dot{m}_{ideal}$: ideal mass flow rate through hole

$\Delta P_{across\_contraction}$: pressure drop across contraction

The ideal flow is based upon an isentropic, one dimensional expansion of the coolant from supply plenum total pressure, P_{tc}, to the mainstream static pressure, P_{sm}. Euler's equation describes how the velocity, pressure and density in a moving fluid are related; equation below:

$$\frac{dP}{(\rho)} + (V)dV + (g)dz = 0$$

Taking the integral of equation (1), we obtain Bernoulli's equation; equations below:

$$\int \frac{dP}{(\rho)} + \int (V)dV + \int (g)dz = \text{constant}$$

$$\int \frac{dP}{\rho} + \frac{V^2}{2} + gz = \text{constant}$$

The first term in the equation above is the pressure head energy term and its significance is that it describes the relation between pressure and density in fluid flow. It is the term that distinguishes whether a flow is compressible or incompressible. In the present study the variation of density during flow will be very small, $\frac{dP}{\rho} \cong 0$; this is elaborated in Appendix B where it is shown that compressibility effects can be ignored in the pressure ratio range tested in this study. Therefore, the flow can be approximated as incompressible and the assumption

is made that the density remains nearly constant throughout; $\rho \cong \text{constant}$. Therefore, Bernoulli's equation simplifies to:

$$\frac{P}{\rho} + \frac{V^2}{2} + gz = \text{constant}$$

Applying the above equation between two (2) points and neglecting potential head energy the form below of the Bernoulli equation is obtained; equation below. The potential head energy is insignificant because there is no appreciable change in height in the flow.

$$\rho = \rho_1 = \rho_2$$

$$P_1 + \frac{1}{2}\rho {V_1}^2 = P_2 + \frac{1}{2}\rho {V_2}^2$$

'Isentropic expansion' is loss free flow through a contraction. Isentropic means that the process is loss free (no entropy is generated). Expansion of the fluid implies that as the fluid moves from state 1 to state 2 the static pressure of the coolant, at state 2, must be equal to that of the mainstream.

The process is characterized by an increase in kinetic energy coupled with a decrease in static pressure energy as the fluid flows through the contraction. The isentropic expansion process of the coolant from plenum total pressure to mainstream static pressure is described by the equation below:

$$P_{tc} + \frac{1}{2}\rho_{c1} {V_1}^2 = P_{sm} + \frac{1}{2}\rho_{c2} {V_2}^2$$

where:

P_{tc} : total coolant pressure

V_1 : coolant velocity inside plenum box

P_{sm} : static mainstream pressure

V_2 : coolant ideal velocity at hole exit

$\rho_c = \frac{P_{tc}}{R \times T_{tc}}$: density of coolant

R : ideal gas constant

T_{tc} : total temperature of coolant

The coolant flows from a large plenum. The velocity of the coolant, sufficiently far from the hole inlet (inside the plenum box), is very small. Therefore, the kinetic energy quantity at the inlet is insignificant when compared to the other terms in equation; $\frac{1}{2}\rho_{c1} {V_1}^2 \cong 0$. This leads to the equation below, after re-arranging to make the velocity the subject of the formula:

$$V_2 = \sqrt{\frac{2 \times (P_{tc} - P_{sm})}{\rho_{c2}}}$$

The ideal mass flow rate can then be determined, with V_2 being the ideal average velocity of the coolant, by substituting the equations above:

$$\dot{m}_2 = \rho_{c2} \times A_{hole} \times V_2$$

$$\dot{m}_2 = \dot{m}_{ideal} = A_{hole}\sqrt{2 \times \rho_{c2} \times (P_{tc} - P_{sm})}$$

where:

$A_{hole} = \frac{\pi}{4}(D_{hole})^2$: Cross − sectional area of cylindrical portion of hole

D_{hole} : diameter of cylindrical portion of hole

B. Pressure ratio testing range

The flow will be kept in the incompressible flow region. For compressibility effects to be negligible in flow the Mach number should be less than 0.3 (Panton 2013):

$$\text{Mach number} = \frac{V}{c} < 0.3$$

where:

$V = \sqrt{\frac{2\times(P_{tc}-P_{sm})}{\rho_c}}$: velocity of the coolant

$c = \sqrt{\gamma R T_{tc}}$: speed of sound in fluid

P_{tc} : total coolant pressure

P_{sm} : static mainstream pressure

$\rho_c = \frac{P_{tc}}{R\times T_{tc}}$: density of coolant through film cooling hole

T_{tc} : total temperature inside plenum

R : ideal gas constant

γ : ratio of specific heats of air

Substituting the equations of the definitions of the velocity and the speed of sound, the equation below is obtained:

$$\frac{\sqrt{\frac{2\times(P_{tc}-P_{sm})}{\rho_c}}}{\sqrt{\gamma R T_{tc}}} < 0.3$$

With some manipulation and re-arranging the pressure ratio upper limit is determined as:

$$\frac{P_{t,c}}{P_{s,m}} < \frac{1}{0.937} = 1.0672$$

Therefore, the pressure ratio testing range is:

$$1 < \frac{P_{t,c}}{P_{s,m}} < 1.0672$$

C. Turbulence grid design

Square-mesh arrays of round rods (SMR), as shown in Figure C-1, are used to generate turbulence in the mainflow tunnel for this study.

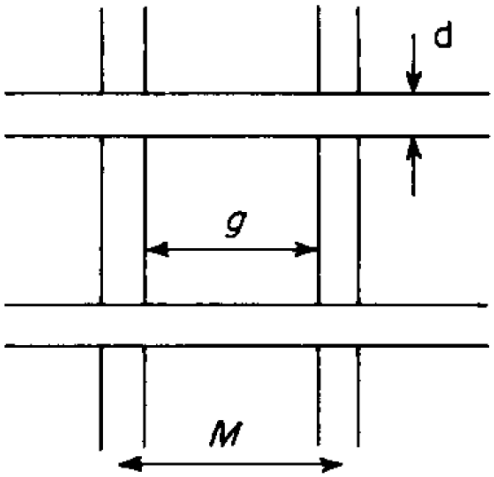

Figure C-1: Schematic of square mesh array turbulence grid (Roach 1987).

To design the grid for turbulence generation the study by Roach (1987) is used. In the study by Roach (1987), it is stated that the method by Frenkiel (1948) appears to give the best agreement with experimental results for high Reynolds number flows (i.e. above those where viscous effects are significant),

$$\mathrm{Tu} = \mathrm{C}\left(\frac{\mathrm{x}}{\mathrm{d}}\right)^{-5/7}$$

where *Tu* is the streamwise component of the turbulence intensity, *x* is the distance downstream of the grid, and *d* is the representative grid dimension (Frenkiel (1948) suggests the rod/wire diameter is the appropriate dimension). The 'constant' C is a function of grid geometry and possibly Reynolds number, and also reflects the drag force experienced by the individual (isolated) elements of the grid. The method by Frenkiel (1948) has the added attraction that it is not necessary to estimate the grid pressure loss in order to compute the downstream turbulence energy.

Only the streamwise component is considered because it was shown in the study by Roach (1987) that turbulence generated by grid gives a 'more nearly' isotropic turbulence field.

Results from a number of studies in literature, including the study by Roach (1987), suggest that the constant C is independent of Reynolds number in the range $10^2 < \mathrm{Re_d} < 10^4$. It was found that C = 0.80.

Parameters to be considered in design

1) According to Roach (1987), complications arise if grid dimensions are large relative to the duct geometry. The formation and growth of the turbulence eddies will be strongly inhibited by the duct walls if the ratio of the grid duct dimensions is significant. Designing such that the grid mesh is much less than 10% of the minimum side length (W = 375mm in this study) of the duct is recommended.

$$\frac{\mathrm{M}}{\mathrm{W}} < 10\%$$

$$M < 0.1 \times 375 = 37.5 \text{ mm}$$

where M is the mesh length (M = g + d) and W is the tunnel width. ‘g’ is the gap between rods.

2) There is an initial distance in the immediate wake region downstream of a grid where the flow is strongly inhomogeneous. This ‘set-up’ phase is a result of the initially isolated bar wakes growing in size and eventually coalescing into a truly homogeneous turbulent flow. According to Roach (1987), the flow may be considered homogeneous by ten mesh lengths downstream of the grid.

$$x > 10 \times M$$

The diameter of the rods used is 12mm. The rods are placed 600 mm upstream of the film cooling holes. Therefore, based on the above correlation the expected freestream turbulence intensity is:

$$Tu = 0.80\left(\frac{600}{12}\right)^{-5/7} = 0.049 = 4.89\%$$

The parameters are summarized in the table below:

Tu(%)	d(mm)	x(mm)	M(mm)	g(mm)	β^*
4.89	12	600	37.5	25.5	0.46

$* \beta = \left(1 - \frac{d}{M}\right)^2$

Shown in Figure C-2 is the turbulence grid design.

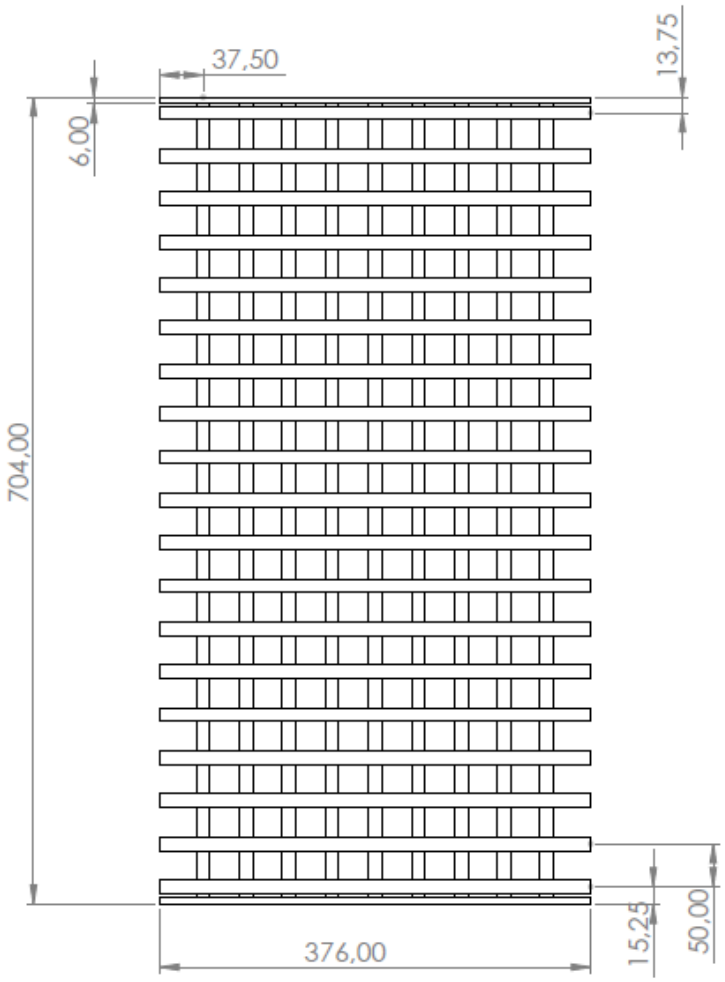

Figure C-2: Turbulence grid design.

D. Data reduction

Discharge coefficient

The discharge coefficient, C_d, is defined as shown in the equation below:

$$C_d = \frac{\dot{m}_{actual}}{\dot{m}_{ideal}}$$

The actual mass flow rate is calculated as shown in the equation below:

$$\dot{m}_{actual} = \frac{Q_v}{2} \times \rho_{air\_inlet}$$

where:

C_d : discharge coefficient of film cooling hole

Q_v : volume flow rate from compressor

ρ_{air_inlet} : density of air at the inlet of compressor

The volume flow rate and the density of air at the inlet are acquired from the compressor software. The volume flow rate is divided by two (2) because the compressor supplies two (2) film cooling holes. The student takes a sample of 10 data points for each calculation. The average of this sample is used in the calculation of the mass flow rate.

The ideal mass flow is defined as shown in the equation below:

$$\dot{m}_{ideal} = A_{hole}\sqrt{2 \times \rho_c \times (P_{tc} - P_{sm})}$$

where:

P_{tc} : total coolant pressure

P_{sm} : static mainstream pressure

ρ_c : density of coolant through film cooling hole

A_{hole} : cross − sectional area of cylindrical portion of hole

Substitution of the equations above leads to the equation below:

$$C_d = \frac{Q_v \times \rho_{air\_inlet}}{A_{hole}\sqrt{2 \times \rho_c \times (P_{tc} - P_{sm})}}$$

From the calibration of the pressure transducers it was determined that the equations below are used to calculate the total coolant pressure and the static mainstream pressure:

$$P_{tc} = 124.39 \times (V_{tc} - V_{offset,tc}) - 0.6237$$

$$P_{sm} = 24.57 \times (V_{sm} - V_{offset,sm}) - 0.0426$$

where:

V_{tc} : plenum transducer voltage response

$V_{offset,tc}$: plenum transducer offset voltage response

V_{sm} : mainstream static transducer voltage response

$V_{offset,sm}$: mainstream static transducer offset voltage response

The offset voltages are recorded when the is no flow. They introduce bias errors into the measured responses. Hence, they are subtracted from the measurements when experiments are done.

The coolant density is calculated using the ideal gas law, using state conditions inside the plenum box; equation below:

$$\rho_c = \frac{P_{tc}}{R \times T_{tc}}$$

where:

T_{tc} : total temperature inside plenum

R : ideal gas constant

The total temperature inside the plenum is taken as the average of the temperature of the two (2) thermocouples inside the plenum box. From the calibration of the thermocouples it was determined that the equations below are used to calculate the total temperatures:

$$T_{actual,1} = 1.0024 \times T_{thermocouple,1} + 0.9941$$

$$T_{actual,2} = 1.002 \times T_{thermocouple,2} + 0.9643$$

$$T_{tc} = \frac{T_{actual,1} + T_{actual,2}}{2}$$

where:

$T_{thermocouple}$: thermocouple temperature measurement inside plenum

T_{actual} : actual temperature inside plenum

The cross-sectional area of the cylindrical portion is calculated as shown in the equation below:

$$A_{hole} = \frac{\pi}{4} \times D^2$$

where:

D : diameter of the cylindrical portion of hole

Outlet Additive Losses Coefficient

The outlet additive losses coefficient is defined by Sasaki *et al.* (1975) as shown in the equation below:

$$\delta_{out} = \frac{1}{(C_d)^2} - \frac{1}{(C_{d,o})^2}$$

where:

C_d : film cooling hole discharge coefficient with mainstream crossflow (WC)

$C_{d,o}$: film cooling hole discharge coefficient without mainstream crossflow (WOC)

The outlet losses are calculated at data points where the velocities between both cases, with and without mainstream crossflow, match. The student manually matches the velocities. This isolates the losses to those caused by the presence of the mainstream crossflow. Shown in the tables below is a sample of the process of manually matching velocities.

Shown in the table below are the discharge coefficient results, for the case of with and without mainstream crossflow, as the flow rate through the hole is increased. A sample of three (3) velocities that were matched are coloured coded in the table.

Cylindrical Machined 0 degrees compound angle				
With Mainstream Crossflow			**Without Mainstream Crossflow**	
Momentum Flux Ratio	**Average coolant velocity**	**Discharge Coefficient**	**Average coolant velocity**	**Discharge Coefficient**
0.362516	9.87457	0.391435	8.113918	0.425712
0.488314	11.44324	0.44171	9.069842	0.453715
0.532549	11.95652	0.448383	11.28011	0.542074
0.63736	13.08204	0.476767	12.78213	0.589911
0.63713	13.04275	0.463563	13.6913	0.606241
0.79259	14.57561	0.503195	14.98145	0.639968
0.876112	15.28882	0.514045	15.63299	0.642507
1.019752	16.43474	0.539628	16.86247	0.669914
1.003559	16.31935	0.522057	17.79551	0.683562
1.081708	16.94801	0.529732	19.20304	0.713606
1.342043	18.89766	0.57529	20.02766	0.722057
1.385657	19.22791	0.571185	21.10693	0.736625
1.536508	20.2644	0.586372	22.52495	0.763579
1.568298	20.36984	0.577342	23.354	0.769748
1.80647	21.82611	0.604153	24.53871	0.785837
1.971728	22.90836	0.620227	25.96314	0.808919
2.078621	23.53703	0.622552	26.8753	0.815691
2.426579	25.22606	0.653998	28.25895	0.835774
2.423453	25.2937	0.642614	29.09452	0.840472
2.678578	26.66442	0.661627	30.44734	0.85774
2.901662	27.72479	0.674932	31.23615	0.858684
3.140621	28.88861	0.688577	32.24579	0.866088
			34.05617	0.894235
			35.77903	0.920047

Shown in the table below are the all discharge coefficient results where the velocities matched. The outlet additive losses coefficient at each point was then calculated from these results that matched.

Cylindrical Machined 0 degrees compound angle				
With Mainstream Crossflow			Without Mainstream Crossflow	
Momentum Flux Ratio	Average coolant velocity	Discharge Coefficient	Average coolant velocity	Discharge Coefficient
0.362516	9.87457	0.391435	9.069842	0.453715
0.488314	11.44324	0.44171	11.28011	0.542074
0.63736	13.08204	0.476767	13.6913	0.606241
0.79259	14.57561	0.503195	14.98145	0.639968
0.876112	15.28882	0.514045	15.63299	0.642507
1.081708	16.94801	0.529732	16.86247	0.669914
1.385657	19.22791	0.571185	19.20304	0.713606
1.536508	20.2644	0.586372	20.02766	0.722057
1.80647	21.82611	0.604153	21.10693	0.736625
1.971728	22.90836	0.620227	22.52495	0.763579
2.078621	23.53703	0.622552	23.354	0.769748
2.423453	25.2937	0.642614	25.96314	0.808919
2.678578	26.66442	0.661627	26.8753	0.815691
3.140621	28.88861	0.688577	28.25895	0.835774

Looking at the matched velocities it is seen that the is an error associated with matching the velocities. Selecting the case of with mainstream crossflow as the 'true value', a percentage error can be defined as shown in the equation below:

$$\%\text{error} = \frac{|\bar{U}_{WC} - \bar{U}_{WOC}|}{\bar{U}_{WC}} \times 100$$

where:

$\bar{U}_{WC}$: average coolant velocity with mainstream crossflow

$\bar{U}_{WOC}$: average coolant velocity without mainstream crossflow

Shown in the table below are the outlet additive losses coefficient results where the velocities matched.

Cylindrical Machined 0 degrees compound angle	
Momentum Flux Ratio	Outlet Additive Losses Coefficient
0.362516226	1.668761627
0.488313804	1.722216235
0.63736004	1.678466777
0.792590405	1.507717246
0.876112112	1.362009665

1.081708263	1.335344162
1.385656989	1.101372818
1.536507608	0.990358578
1.80646953	0.896800998
1.971728011	0.8844434
2.078620647	0.892444829
2.423453373	0.893348304
2.678577571	0.781447129
3.140621183	0.677485345

Pressure Ratio

The pressure ratio (PR) is defined as shown in the equation below:

$$PR = \frac{P_{tc}}{P_{sm}}$$

In the equation above the absolute pressures of the total and static pressures must be used. The reference pressure for all the transducers was atmospheric conditions. The conversion is shown in the equations below:

$$P_{tc} = P_{atm} + \Delta P_{tc}$$

$$P_{sm} = P_{atm} - \Delta P_{sm}$$

where:

P_{tc} : total coolant pressure

P_{sm} : static mainstream pressure

P_{atm} : atmospheric pressure

ΔP : gauge pressure reading from transducers

Blowing Ratio

The blowing ratio (BR) is defined as shown in the equation below:

$$BR = \frac{\rho_c \times U_c}{\rho_m \times U_m}$$

where:

U_c : average coolant velocity

U_m : freestream velocity

ρ_c : coolant density

ρ_m : freestream density

The product $\rho_c \times U_c$ is determined using the equation below:

$$\rho_c \times U_c = \frac{\dot{m}_{actual}}{A_{hole}}$$

The freestream velocity is calculated using the equation below:

$$U_m = \sqrt{\frac{2(P_{tm} - P_{sm})}{\rho_m}}$$

where:

P_{tm} : total mainstream pressure

P_{sm} : static mainstream pressure

The freestream density is calculated using the equation below:

$$\rho_m = \frac{P_{tm}}{R \times T_{tm}}$$

where:

T_{tm} : total mainstream temperature

Momentum Flux Ratio

The momentum flux ratio (MFR) is calculated using the equation below:

$$MFR = \frac{\rho_c \times {U_c}^2}{\rho_m \times {U_m}^2}$$

The momentum flux of the coolant flow is calculated using the equation below:

$$\rho_c {U_c}^2 = \frac{\left(\frac{\dot{m}_{actual}}{A_{hole}}\right)^2}{\rho_c}$$

Flow structure

The method by Ligrani, Singer and Baun (1989) was used to calibrate the five hole probe and then decompose the three mean velocity components (Ux, Uy and Uz) and the streamwise vorticity. Below the student presents a brief outline of the procedure.

First, the probe is calibrated in the uniform freestream of the wind tunnel. This position corresponds to the centre of the wind tunnel. The probe is calibrated to determine/measure/quantify the pressure response of the five ports when they are subjected to different loads. The load is varied by incrementally rotating the probe about the yaw and pitch.

Using the pressure responses at each port pressure coefficients are calculated at each position. Calibration curves are then plotted. The calibration curves are used in the data reduction process. The calibration procedure of the five hole probe is outlined in Appendix F.

Data reduction procedure at each position

- Measured pressures from each port are corrected to account for the fact that they are not measured at the same physical location. This is done by fitting a cubic spline, that is a function of the distance, between the data from each port. Using the cubic spline, the pressure readings from the ports that are not at port 1 are mapped to the location of port 1.

- A line of least error is fit in the pitch angle calibration curve data. The linear equation is used to calculate a preliminary pitch angle.
- Using the yaw angle calibration curve data, a preliminary yaw angle is then determined by interpolation using the calculated preliminary pitch angle and the yaw pressure coefficient.
- Using the pitch angle calibration curve data, the final pitch angle is then determined using the measured pitch pressure coefficient and the preliminary yaw angle, and again interpolating.
- Using the yaw angle calibration curve data, the final yaw angle is determined from the yaw pressure coefficient and the final pitch angle, by interpolating.
- Using the total minus static calibration curve data, the final yaw angle and the final pitch angle, the total minus static pressure coefficient is computed using a double interpolation procedure. This coefficient is then used to determine the total velocity magnitude:

$$V = \left[2C_{pts}(P_1 - \bar{P})/\rho\right]^{1/2}$$

where:

V : total velocity magnitude

ρ : fluid density

- The three velocity components are then determined using the equations below:

$$\mathrm{U_x} = \mathrm{V}\cos(\mathrm{y})\cos(\mathrm{p})$$
$$\mathrm{U_y} = \mathrm{V}\sin(\mathrm{y})$$
$$\mathrm{U_z} = \mathrm{V}\cos(\mathrm{y})\sin(\mathrm{p})$$

where:

$\mathrm{U_x}$: velocity in the $\mathrm{x}-$direction (mainstream direction)

$\mathrm{U_y}$: velocity in the $\mathrm{y}-$direction

$\mathrm{U_z}$: velocity in the $\mathrm{z}-$direction

y : yaw angle

p : pitch angle

- The streamwise vorticity is determined using the equation below:

$$\mathrm{W_x} = \frac{\partial \mathrm{U_y}}{\partial \mathrm{z}} - \frac{\partial \mathrm{U_z}}{\partial \mathrm{y}}$$

where:

$\mathrm{W_x}$: vorticity in the $\mathrm{x}-$direction

The partial derivatives above are approximated by taking the differences between successive locations.

- Corrections are then made to account for streamline deflection from the probe tip in the presence of transverse gradients of the streamwise velocity (downwash velocity). This process is outlined in the study by Ligrani, Singer and Baun (1989b).

Temperature field

A non-dimensionalized temperature parameter was used to present the results. It is calculated as shown below:

$$\theta = \frac{T_{probe} - T_c}{T_{tm} - T_c}$$

where:

θ : non − dimensionalized temperature

T_{probe} : probe temperature

T_c : total coolant temperature in the plenum box

T_{tm} : total mainstream temperature

E. Test piece manufacturing method

According to Aghasi, P, Gutmark, E and Munday, D (2017) the build layer thickness is the parameter with the largest influence on the geometric fidelity and surface roughness. An increase in build layer thickness generally leads to an increase in surface roughness which:

1) showed a decrease in discharge coefficient.
2) showed higher span-averaged film cooling effectiveness at BR = 3.5 likely due to the film diffusion on the rough surface that prevents it from penetrating into the mainstream.
3) showed lower effectiveness values at lower BR's due to increased turbulent mixing at the boundary layer.

The build orientation should be such that the diffuser sections of the holes are built vertically to prevent the stair stepping effect on the diffuser section of the hole interior. This is an attempt to decrease the surface roughness in the diffuser section of the hole. This implies that the cylindrical section of the hole is expected to be slightly rougher (due to stair stepping effect) as compared to the diffuser section. According to Persh and Bailey (1954) surface roughness slightly upstream of the diffuser throat stabilizes the resulting flow downstream. It was also shown that in cases where the flow separated from part of the diffuser wall producing an asymmetrical profile, increasing the surface roughness near the diffuser throat reduced separation producing a more uniform (symmetrical) profile. In short, increasing surface roughness near the diffuser throat improved diffuser performance.

Cylindrical Hole manufacturing

The build orientation should be such that the cylindrical hole is perpendicular to the build floor; Figure E-1. This will minimize the effect of the stair stepping effect inside hole interior. This is an attempt to decrease the surface roughness of the hole.

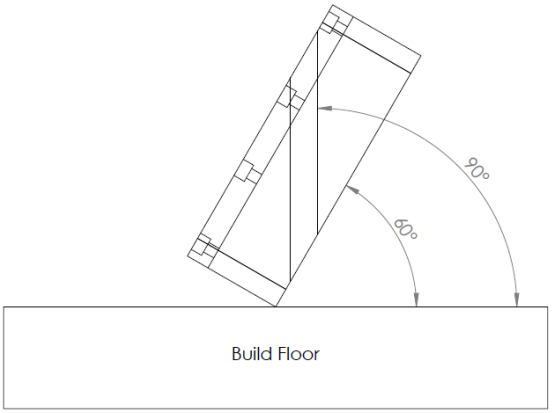

Figure E-1: Cylindrical hole manufacturing orientation.

Shaped Hole Manufacturing

The build orientation should be such that the diffuser section of the holes are built vertically to prevent the stair stepping effect on the diffuser section of the hole interior; please see attached drawing (the diffuser section is the section that is 90 degrees to the build floor). This is an attempt to decrease the surface roughness in the diffuser section of the hole. This implies that the cylindrical section of the hole is expected to be slightly rougher (due to stair stepping effect) as compared to the diffuser section (the cylindrical section is the section that is 97 degrees to the build floor; Figure E-2).

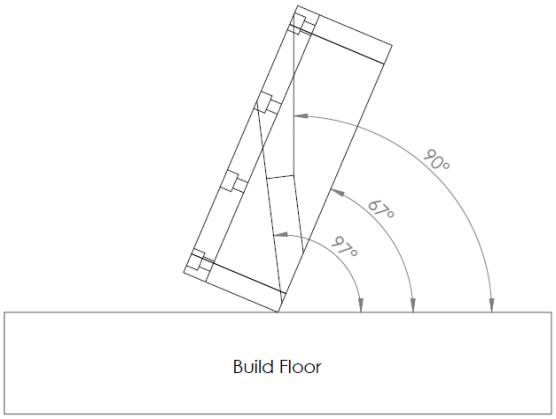

Figure E-2: Laidback fan-shaped manufacturing orientation.

F. Instruments calibration

Below the student discusses the process and presents the results from the calibration of the pressure transducers, the thermocouples and the five hole probe that were used for measurement.

The purpose of calibration is to determine the response of the instrument when a known load is applied. The NI Signal express data logging software was used to record the data.

Pressure Transducers

The pressure transducers were calibrated using a Setra Micro-Cal model 869 calibrator.

The calibration process involved, firstly, noting the zero-offset voltage. This is the voltage reading observed at zero pressure. This voltage reading is 'noise' generated by the equipment. This value propagates in all the results. Therefore, it is a bias/systematic error.

Secondly, incrementally increasing the pressure from zero (0) to the maximum pressure of the transducer and then incrementally decreasing the pressure from the maximum pressure to zero (0), whilst recording the voltage response of the pressure transducer. A line of Best-fit is then placed in the data to find the relationship of the calibration curve to a specified straight line. This helps determine the non-linearity error. The above also helps determine if there is a difference in output values depending on the direction of approach; Hysteresis error.

Shown below are the pressure transducer calibration curves.

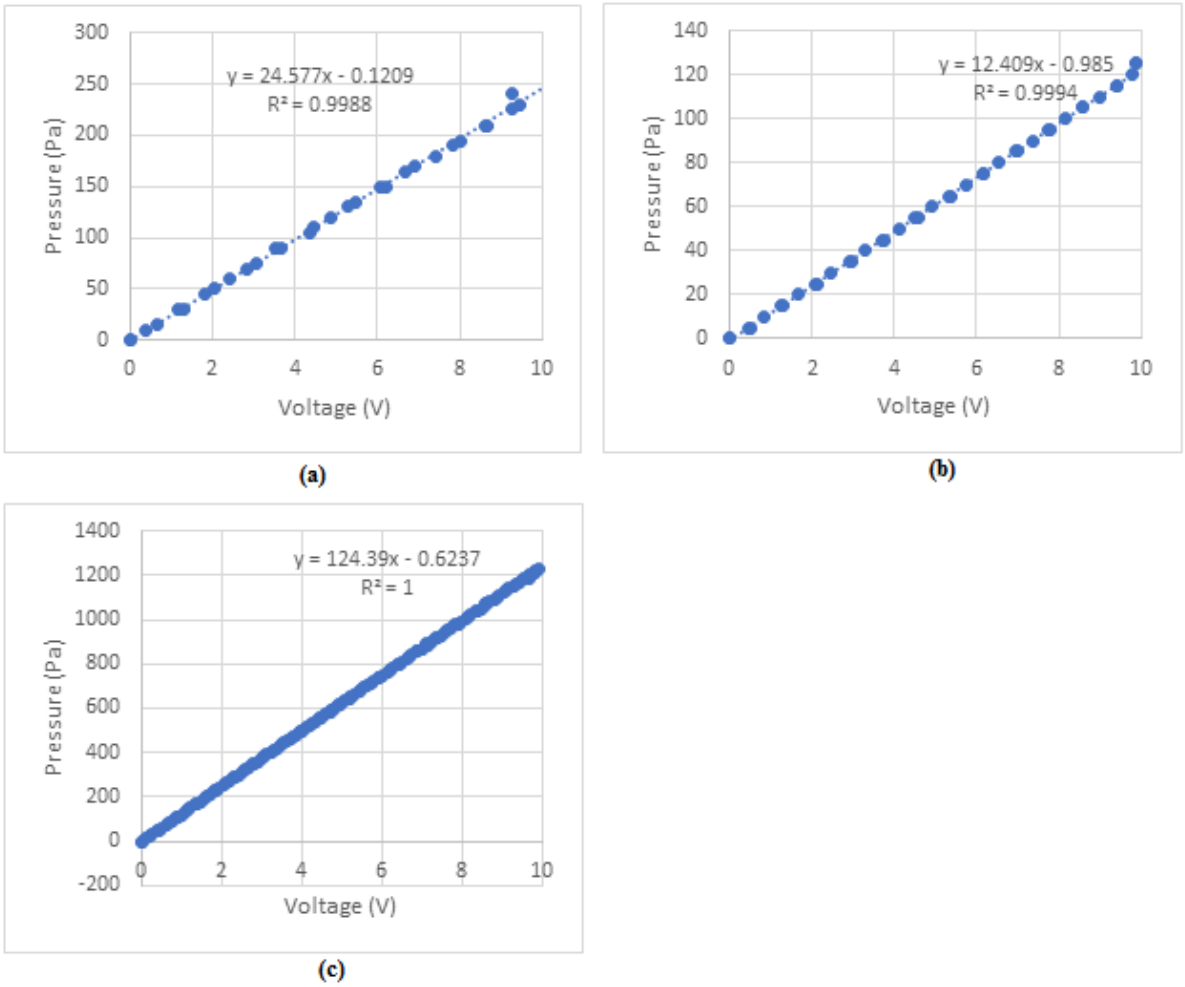

Figure F-1: Pressure transducer calibration curves. a) static mainstream pressure, b) total mainstream pressure, c) plenum total pressure.

Shown in Figure F-2 is a schematic of the five hole probe convention used in the study by Ligrani, Singer and Baun (1989) and also in this study. Shown in Figure F-3 are the five hole probe pressure transducer calibration curves.

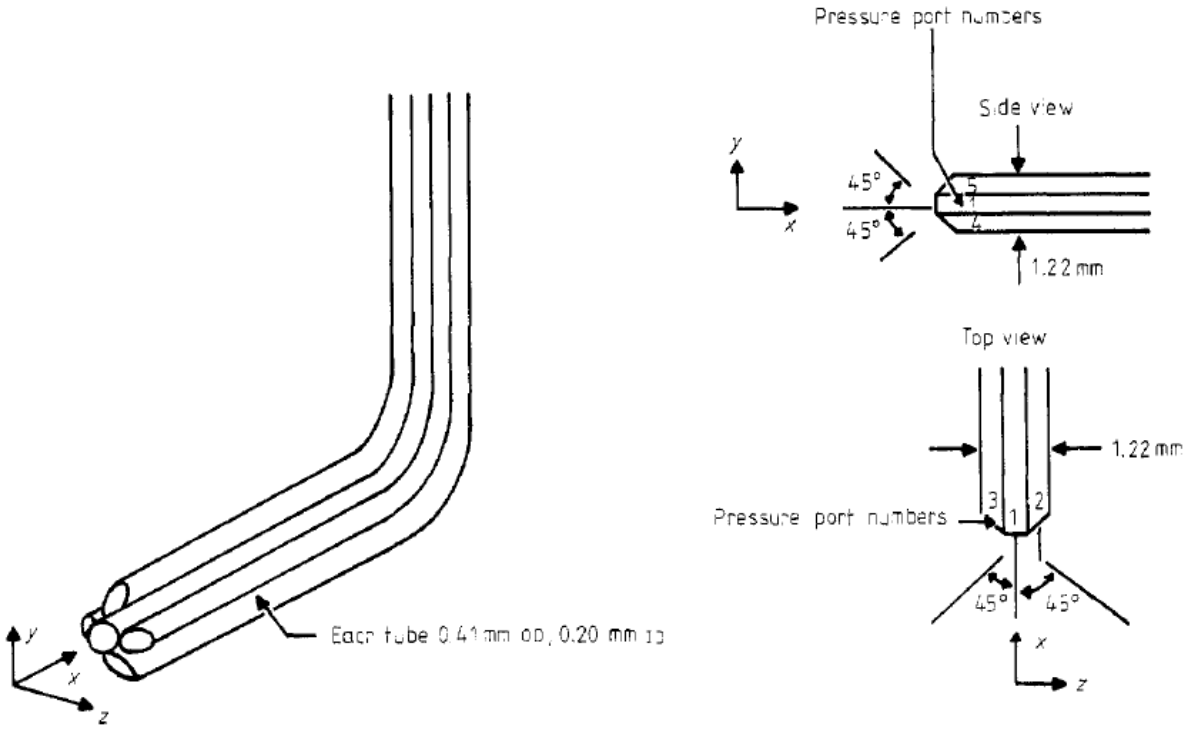

Figure F-2: Five hole probe schematic and convention (Ligrani, Singer & Baun 1989).

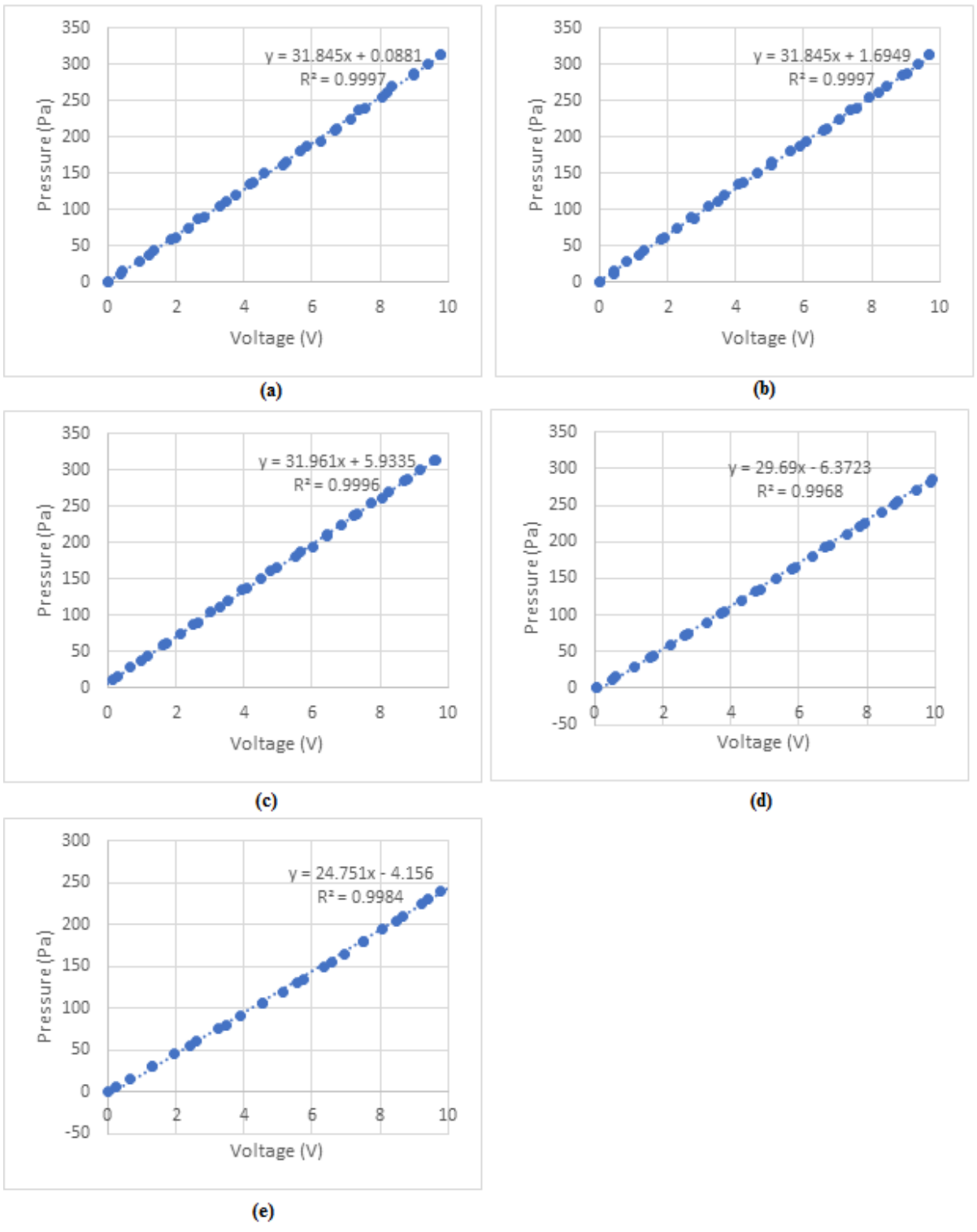

Figure F-3: Five hole probe pressure transducer calibration curves. a) port 1, b) port 2, c) port 3, d) port 4, e) port 5.

Thermocouples

The thermocouples were calibrated using Lauda Alpha RA 8 water bath. A mixture of water and glycol was used so that temperatures less than zero (0) degrees Celsius could be obtained without the fluid changing phase.

The water bath temperature was incrementally increased and then decreased incrementally, whilst recording the temperature response of the thermocouples. A line of best-fit is then placed in the data to find the relationship of the calibration curve to a specified straight line. This helps determine the non-linearity error. The above also helps determine if there is a difference in output values depending on the direction of approach; Hysteresis error.

Shown in figures below are the thermocouple calibration curves.

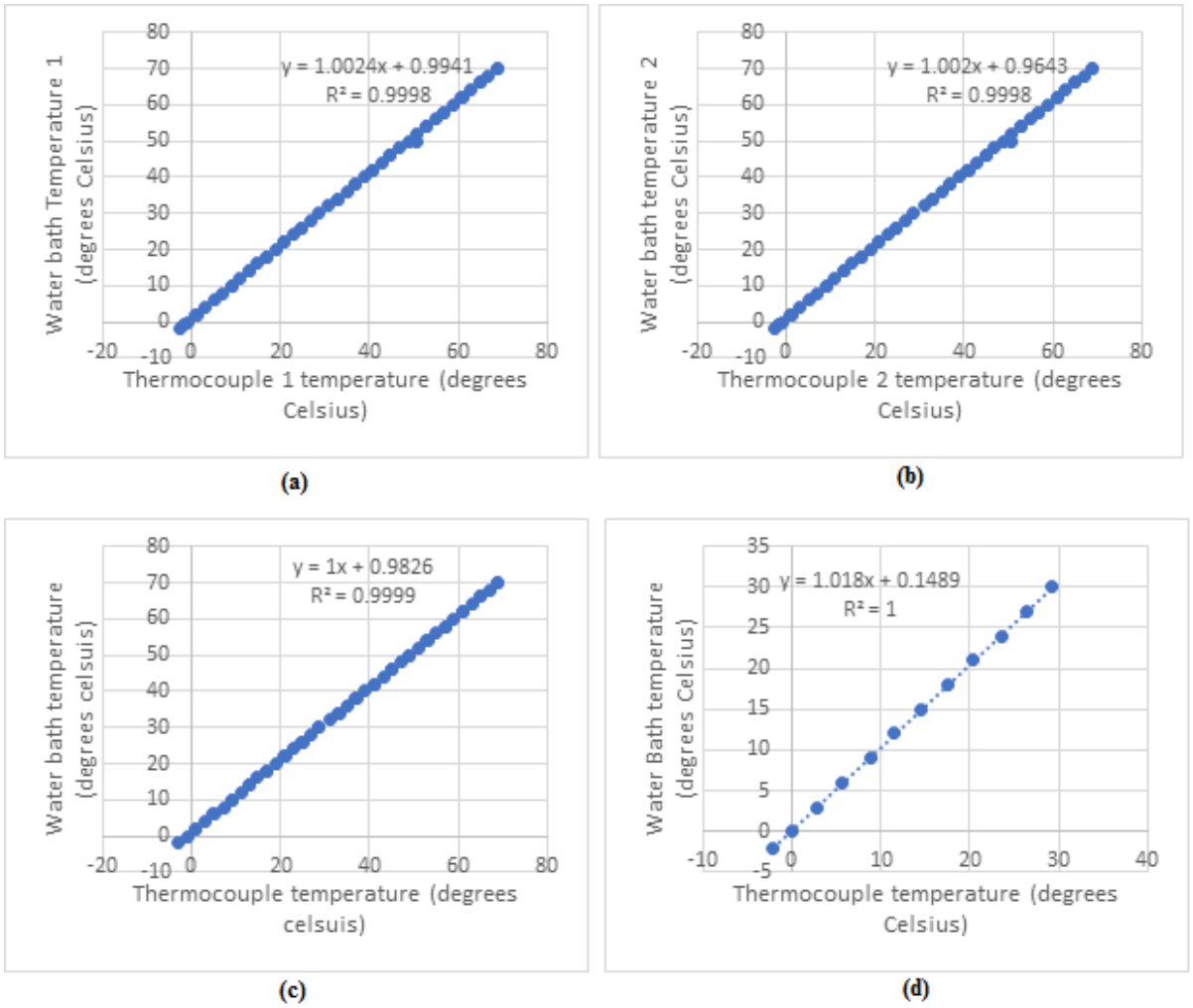

Figure F-4: a) plenum thermocouple 1 calibration curve, b) plenum thermocouple 2 calibration curve, c) freestream thermocouple calibration curve, d) temperature probe calibration curve.

Shown in *Figure F-5* are the calibration curves of the thermocouples at different locations on the wall. The hole numbering starts from the bottom left, increasing, as shown in Figure 3-7.

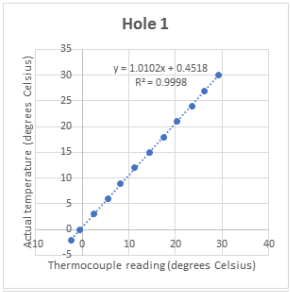

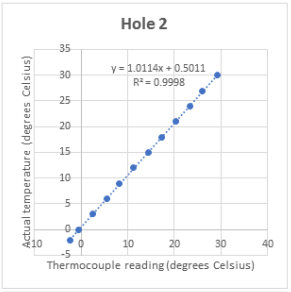

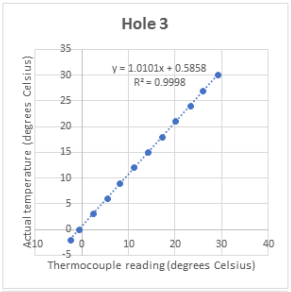

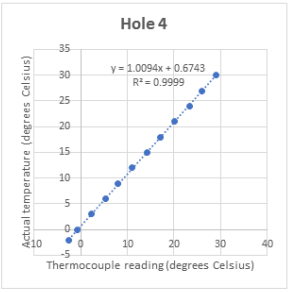

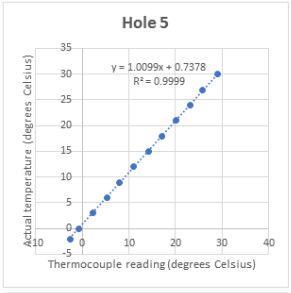

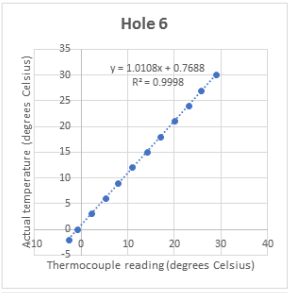

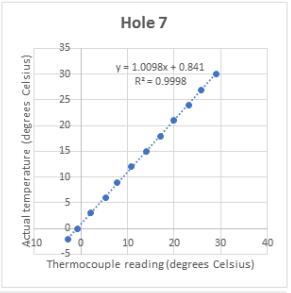

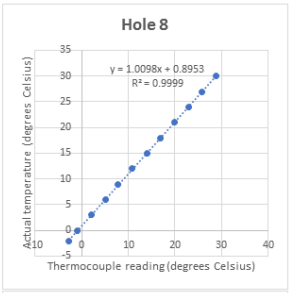

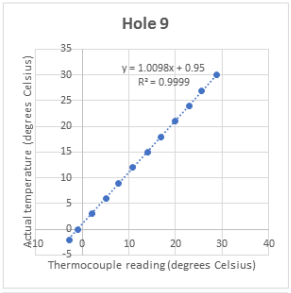

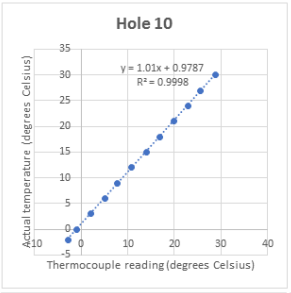

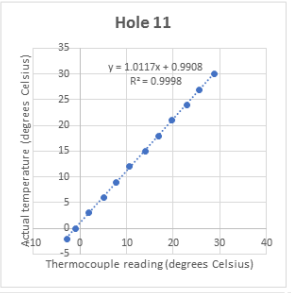

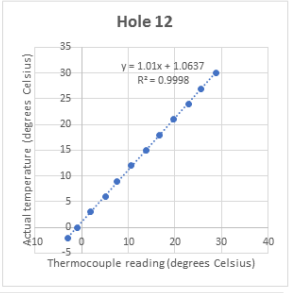

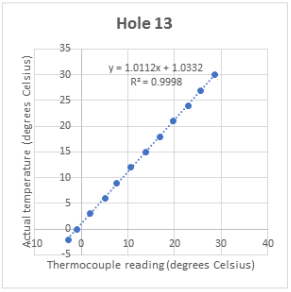

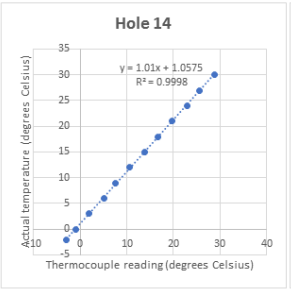

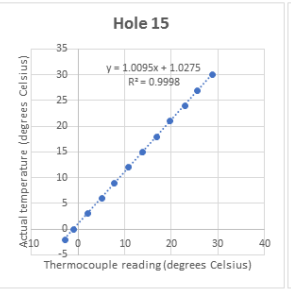

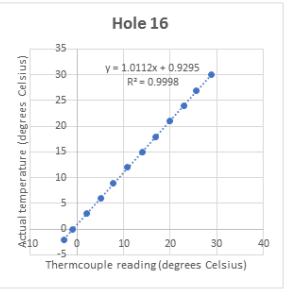

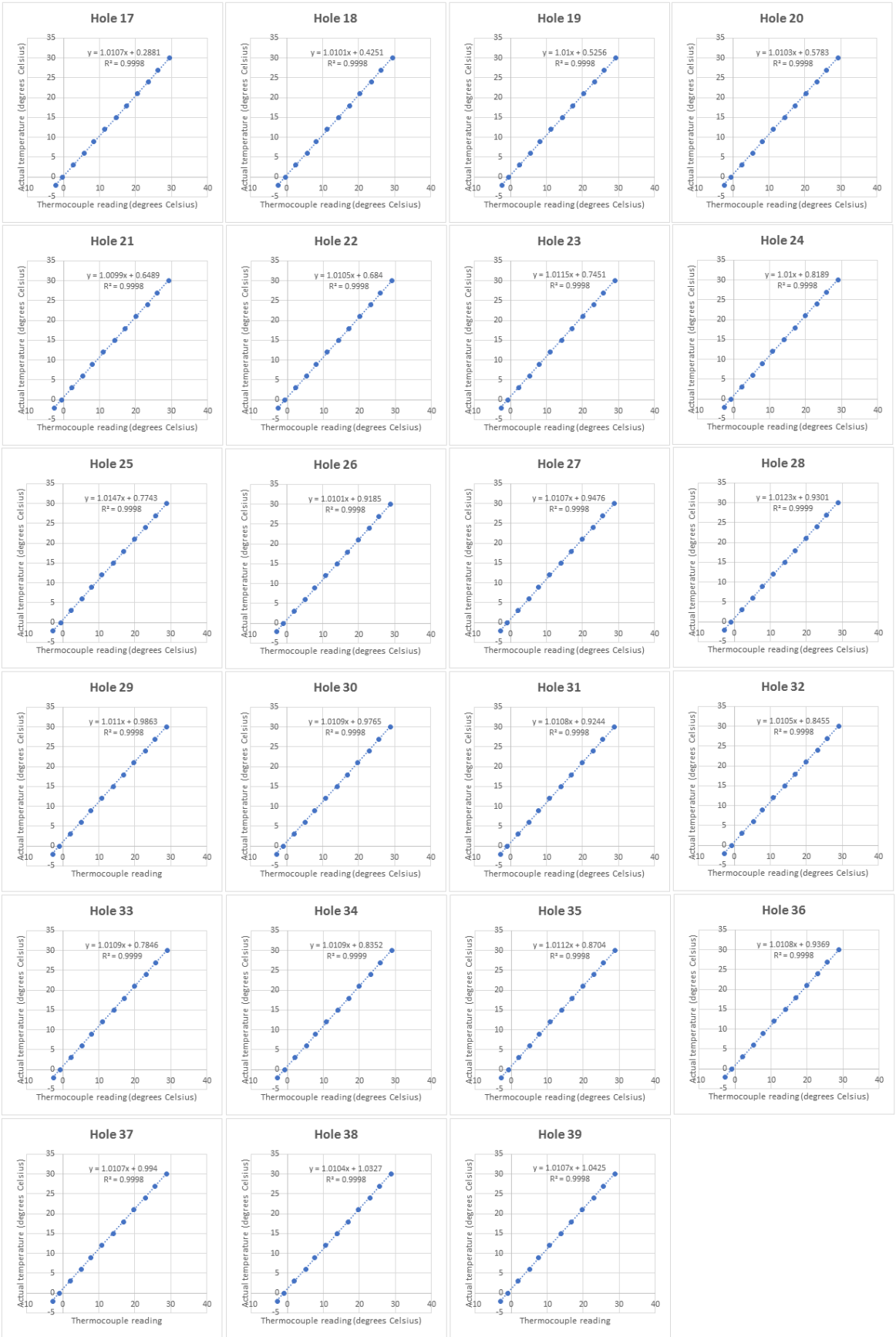

Figure F-5: Wall/surface thermocouple calibration curves.

Five hole probe calibration

The procedure in the study Ligrani, Singer and Baun (1989) was used to calibrate the five hole probe used in this study.

The probe tip was positioned in the freestream of the wind tunnel with a velocity of approximately 7 m/s. It was rotated in the range -35 degrees to 35 degrees in the yaw and pitch, in increments of 5 degrees. This was done to determine the pressure coefficients at each position. The pressure coefficients are calculated as shown below:

$$C_{py} = \frac{(P_2 - P_3)}{(P_1 - \overline{P})}$$

$$C_{pp} = \frac{(P_4 - P_5)}{(P_1 - \overline{P})}$$

$$C_{pt} = \frac{(P_t - \overline{P})}{(P_1 - \overline{P})}$$

$$C_{pts} = \frac{(P_t - P_s)}{(P_1 - \overline{P})}$$

$$C_{ps} = \frac{(P_1 - P_s)}{(P_1 - \overline{P})}$$

where:

C_{py} : yaw pressure coefficient

C_{pp} : pitch pressure coefficient

C_{pt} : total pressure coefficient

C_{pts} : total minus static pressure coefficient

C_{ps} : static pressure coefficient

P_t : total pressure

P_s : static pressure

P_1 : central port pressure

$P_{2\,\&\,3}$: pressure ports on the yaw plane

$P_{4\,\&\,5}$: pressure ports on the pitch plane

$\overline{P} = \frac{P_2+P_3+P_4+P_5}{4}$: average pressure of the yaw and pitch

Using the calculated pressure coefficients, at each position, calibration curves are plotted. The procedure outlined below is used to plot the calibration curves:

- The yaw angle calibration graph is obtained by plotting the yaw pressure coefficient data as a function of the yaw angle, for the different pitch angles.
- The pitch angle calibration graph is obtained by plotting the pitch pressure coefficient data as a function of the pitch angle, for the different yaw angles.
- The total minus static calibration graph is obtained by plotting the total minus static pressure coefficient data as a function of the pitch angle, for the different yaw angles.

- The total pressure calibration graph is obtained by plotting the total pressure coefficient as a function of the pitch angle, for the different yaw angles.
- The static pressure calibration graph is obtained by plotting the static pressure coefficient as a function of the pitch angle, for the different yaw angles.

The calibration curves are shown in *Figure F-6*.The calibration curves are used in the data reduction process; the data reduction process, using the calibration curves, is discussed in Appendix D.

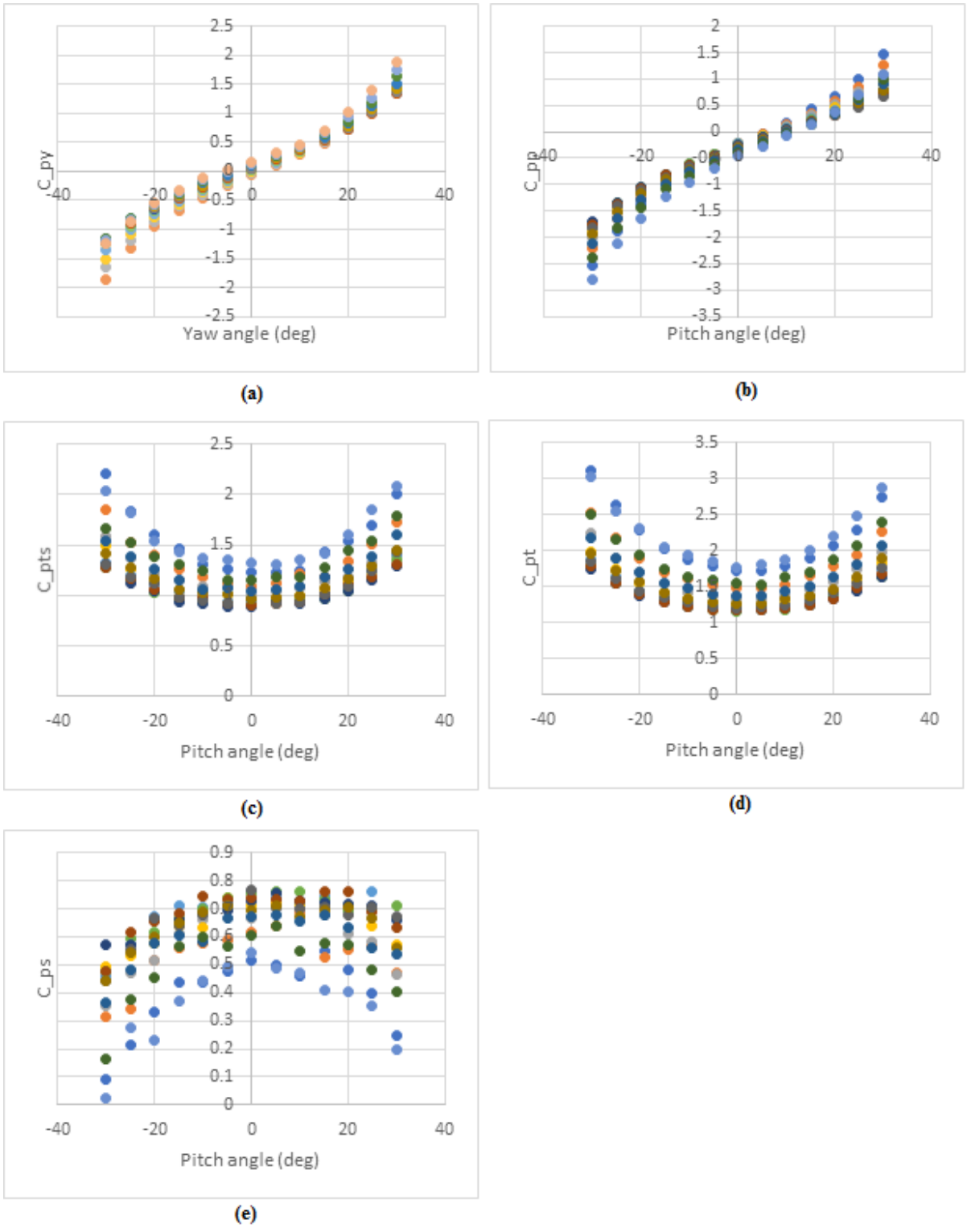

Figure F-6: Five hole probe calibration data. a) yaw angle calibration graph, b) pitch angle calibration graph, c) total minus static pressure calibration graph, d) total pressure calibration graph, e) static pressure calibration graph.

IR Camera calibration

The in situ method by Sargent, Hedlund and Ligrani (1998) was used for the heat transfer measurements. Using this in situ procedure the infrared images from the IR camera are calibrated at the same time as measurements are taken by using thermocouples positioned at discrete locations on the surface, which measure the surface temperature. A second or third

order polynomial where surface temperature is a function of grey scale value is then determined for every infrared image. The calibration curves are shown below. The calibration curves are used to spatially resolve the surface temperature over the entire test surface.

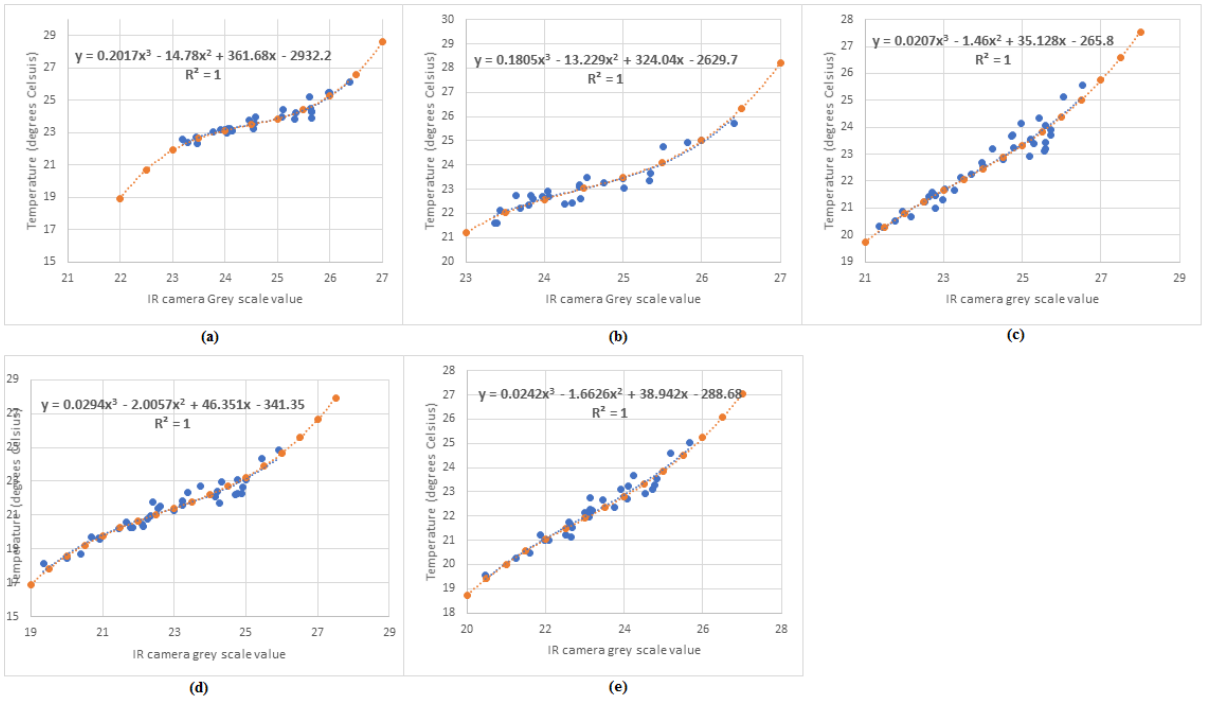

Figure F-7: IR camera calibration curves at a blowing ratio of 0.6 and compound angle of zero (0) degrees, without turbulence grid. a) cylindrical machined hole, b) cylindrical 3D 60 degrees printed hole, c) laidback fan-shaped machined hole, d) laidback fan-shaped 3D zero (0) degrees printed hole, e) laidback fan-shaped 3D 67 degrees printed hole.

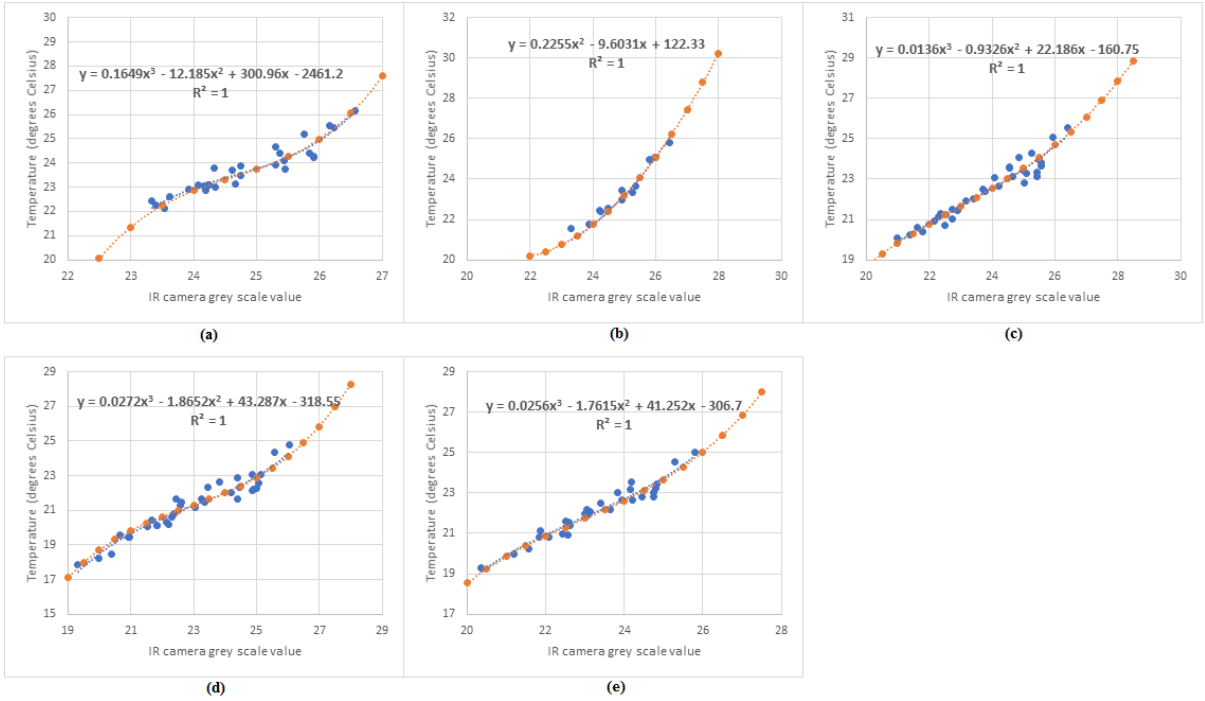

Figure F-8: IR camera calibration curves at a blowing ratio of 0.9 and compound angle of zero (0) degrees, without turbulence grid. a) cylindrical machined hole, b) cylindrical 3D 60 degrees printed hole, c) laidback fan-shaped

machined hole, d) laidback fan-shaped 3D zero (0) degrees printed hole, e) laidback fan-shaped 3D 67 degrees printed hole.

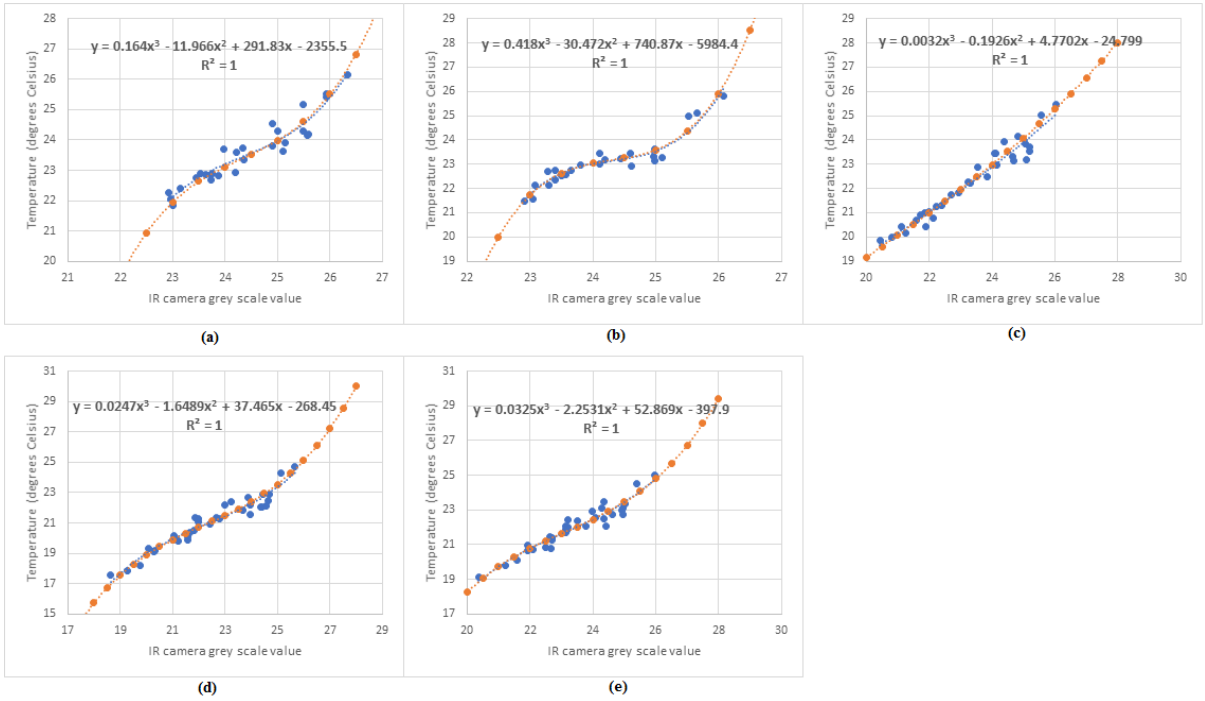

Figure F-9: IR camera calibration curves at a blowing ratio of 1.1 and compound angle of zero (0) degrees, without turbulence grid. a) cylindrical machined hole, b) cylindrical 3D 60 degrees printed hole, c) laidback fan-shaped machined hole, d) laidback fan-shaped 3D zero (0) degrees printed hole, e) laidback fan-shaped 3D 67 degrees printed hole.

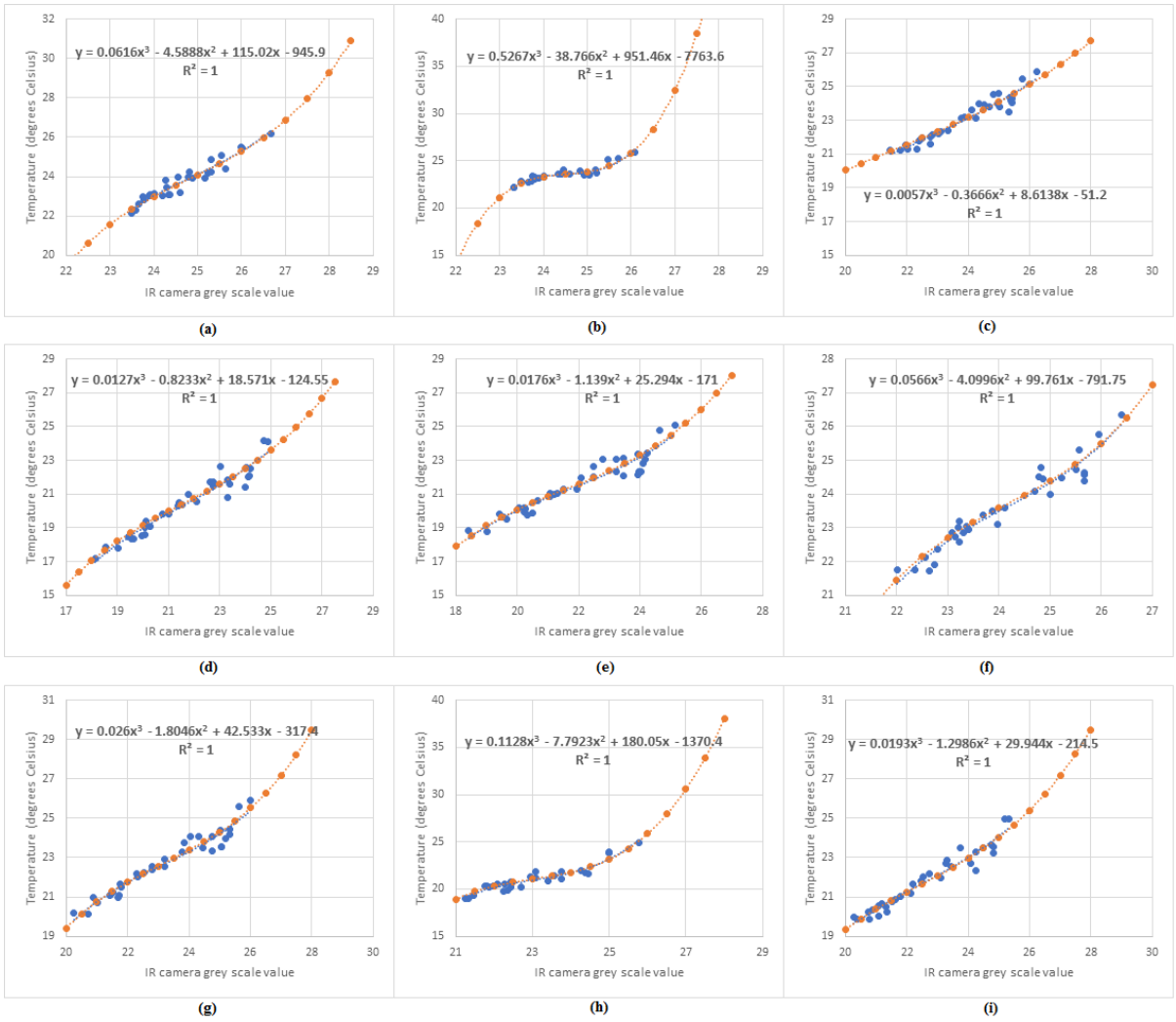

Figure F-10: IR camera calibration curves at a blowing ratio of 0.6 and compound angle of zero (0) degrees, with turbulence grid. a) cylindrical machined hole, b) cylindrical 3D 60 degrees printed hole, c) laidback fan-shaped machined hole, d) laidback fan-shaped 3D zero (0) degrees printed hole, e) laidback fan-shaped 3D 67 degrees printed hole, f) case 1 hole, g) case 2 hole, h) case 3 hole, i) case 4 hole.

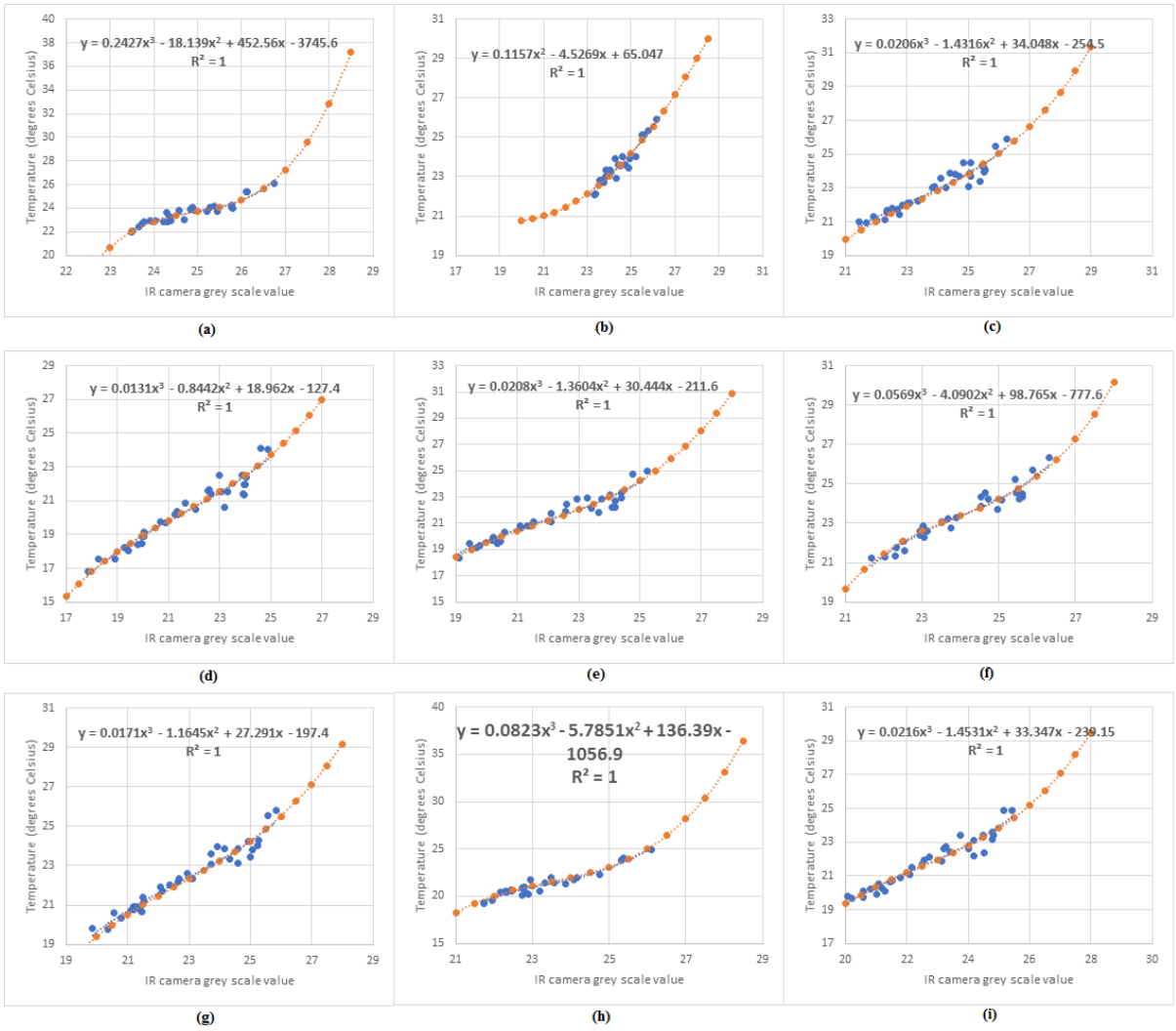

Figure F-11: IR camera calibration curves at a blowing ratio of 0.9 and compound angle of zero (0) degrees, with turbulence grid. a) cylindrical machined hole, b) cylindrical 3D 60 degrees printed hole, c) laidback fan-shaped machined hole, d) laidback fan-shaped 3D zero (0) degrees printed hole, e) laidback fan-shaped 3D 67 degrees printed hole, f) case 1 hole, g) case 2 hole, h) case 3 hole, i) case 4 hole.

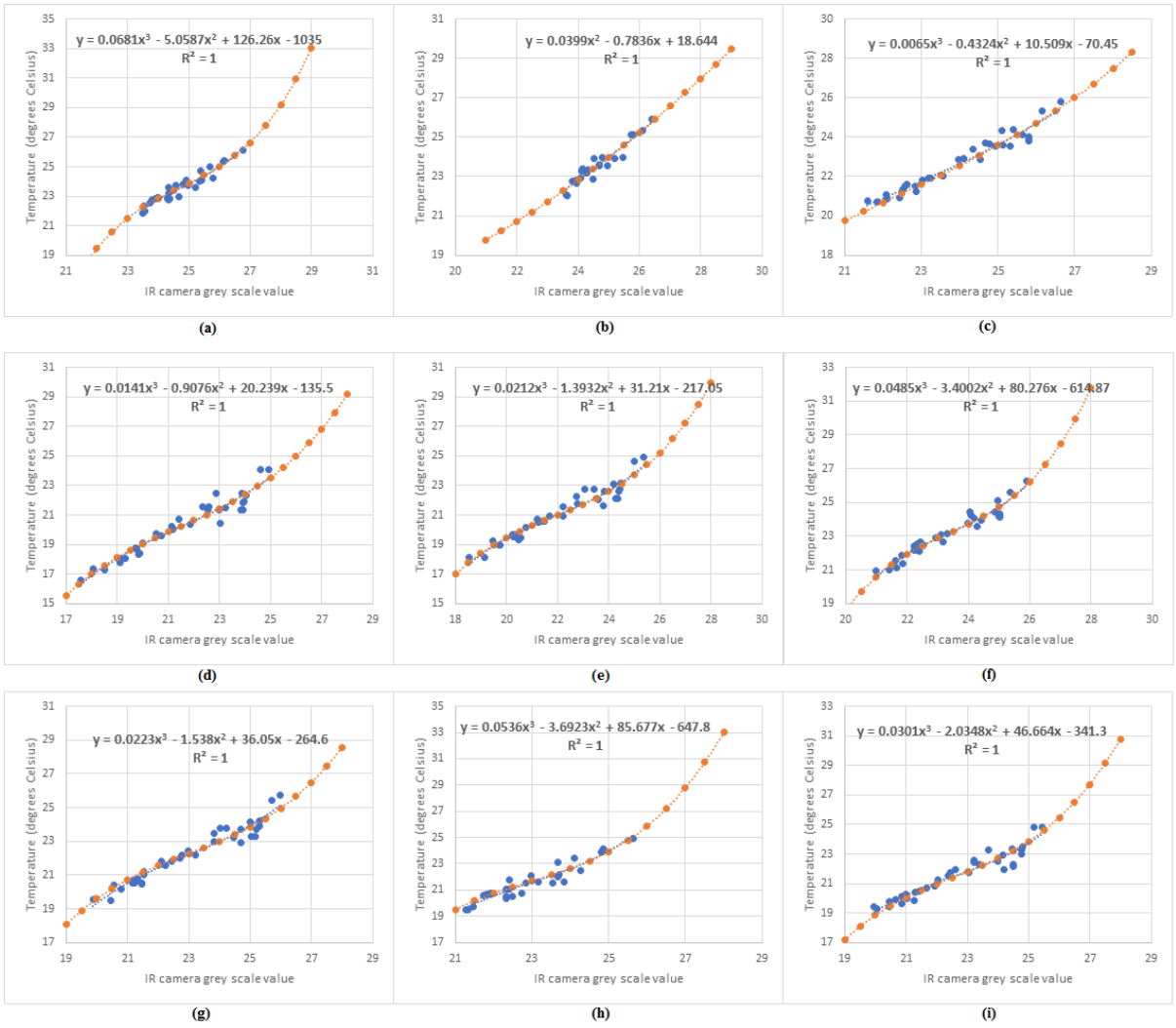

Figure F-12: IR camera calibration curves at a blowing ratio of 1.1 and compound angle of zero (0) degrees, with turbulence grid. a) cylindrical machined hole, b) cylindrical 3D 60 degrees printed hole, c) laidback fan-shaped machined hole, d) laidback fan-shaped 3D zero (0) degrees printed hole, e) laidback fan-shaped 3D 67 degrees printed hole, f) case 1 hole, g) case 2 hole, h) case 3 hole, i) case 4 hole.

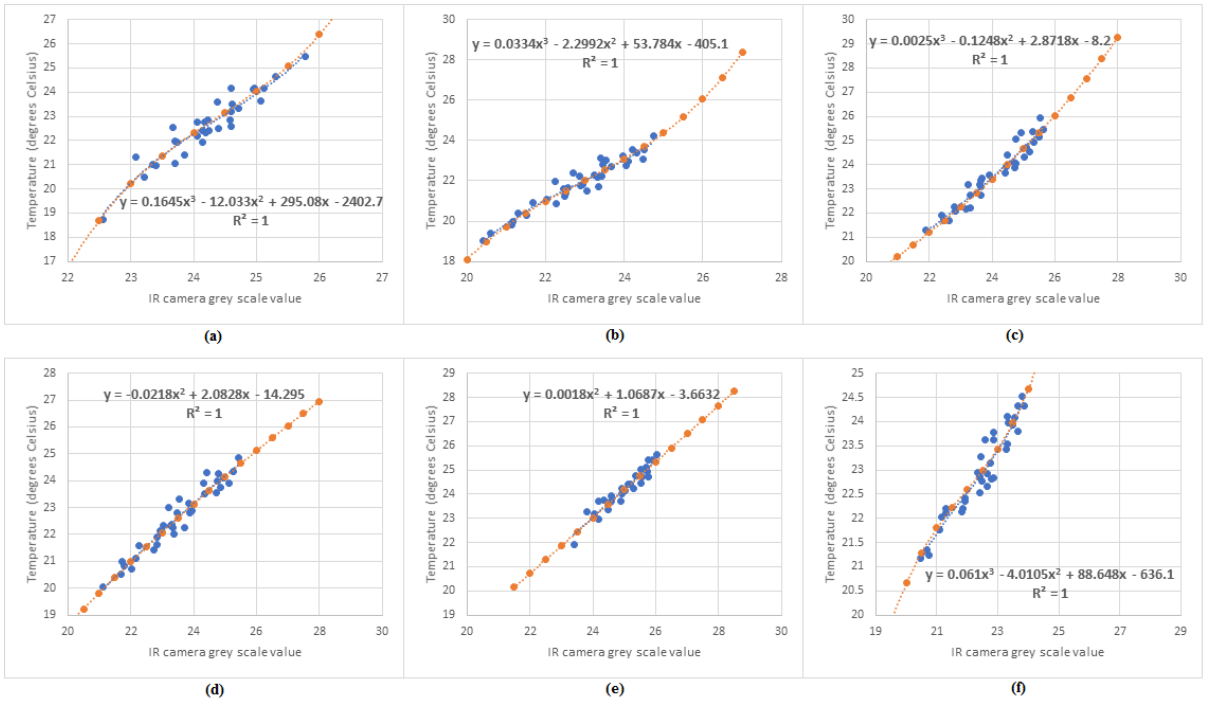

Figure F-13: IR camera calibration curves at a blowing ratio of 0.6 and compound angle of 20 degrees, with turbulence grid. a) cylindrical 3D 60 degrees printed hole, b) laidback fan-shaped 3D zero (0) degrees printed hole, c) case 1 hole, d) case 2 hole, e) case 3 hole, f) case 4 hole.

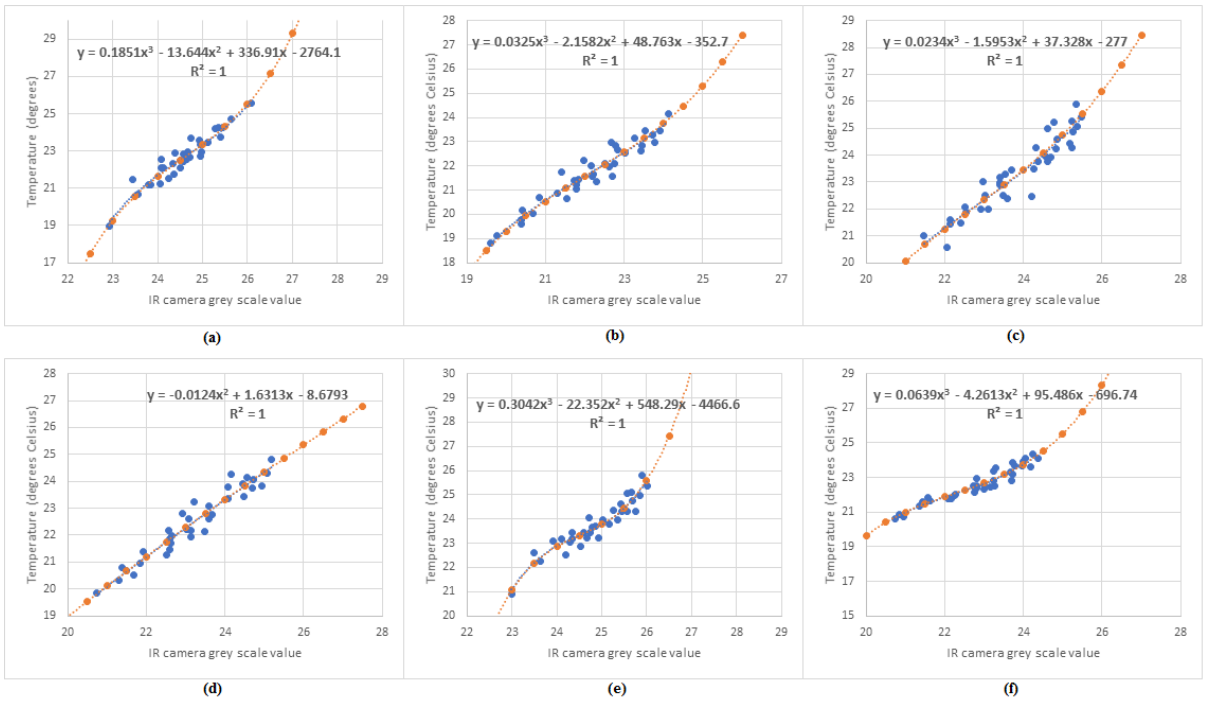

Figure F-14: IR camera calibration curves at a blowing ratio of 0.9 and compound angle of 20 degrees, with turbulence grid. a) cylindrical 3D 60 degrees printed hole, b) laidback fan-shaped 3D zero (0) degrees printed hole, c) case 1 hole, d) case 2 hole, e) case 3 hole, f) case 4 hole.

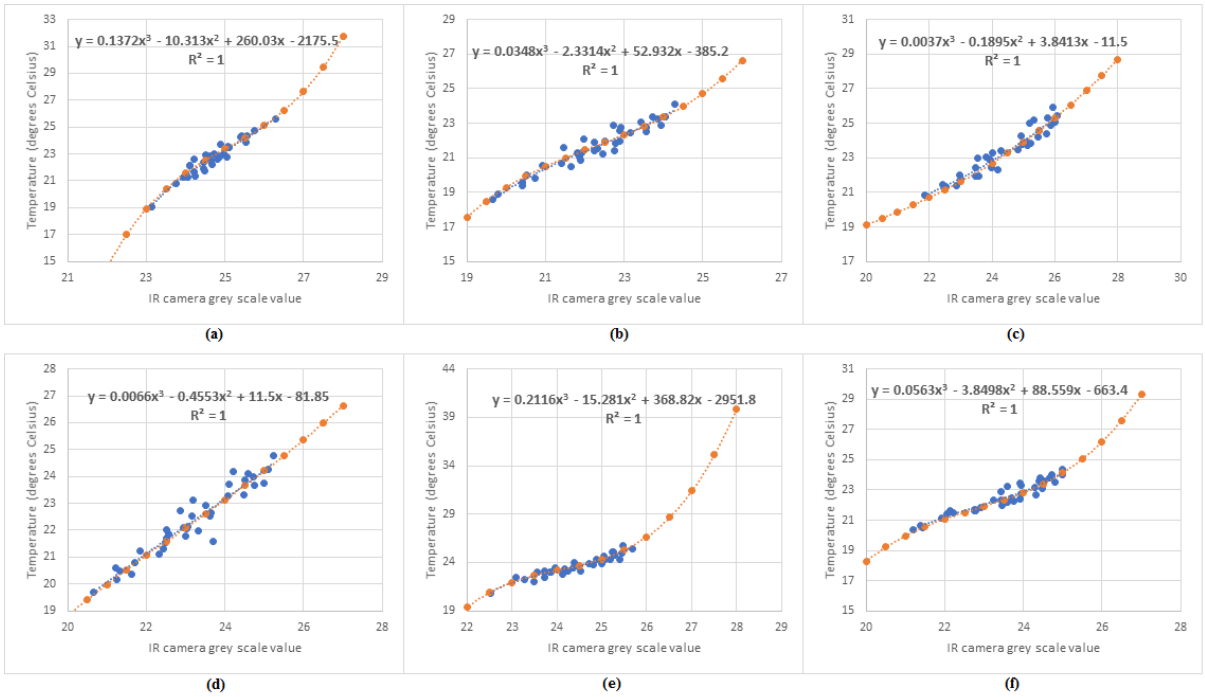

Figure F-15: IR camera calibration curves at a blowing ratio of 1.1 and compound angle of 20 degrees, with turbulence grid. a) cylindrical 3D 60 degrees printed hole, b) laidback fan-shaped 3D zero (0) degrees printed hole, c) case 1 hole, d) case 2 hole, e) case 3 hole, f) case 4 hole.

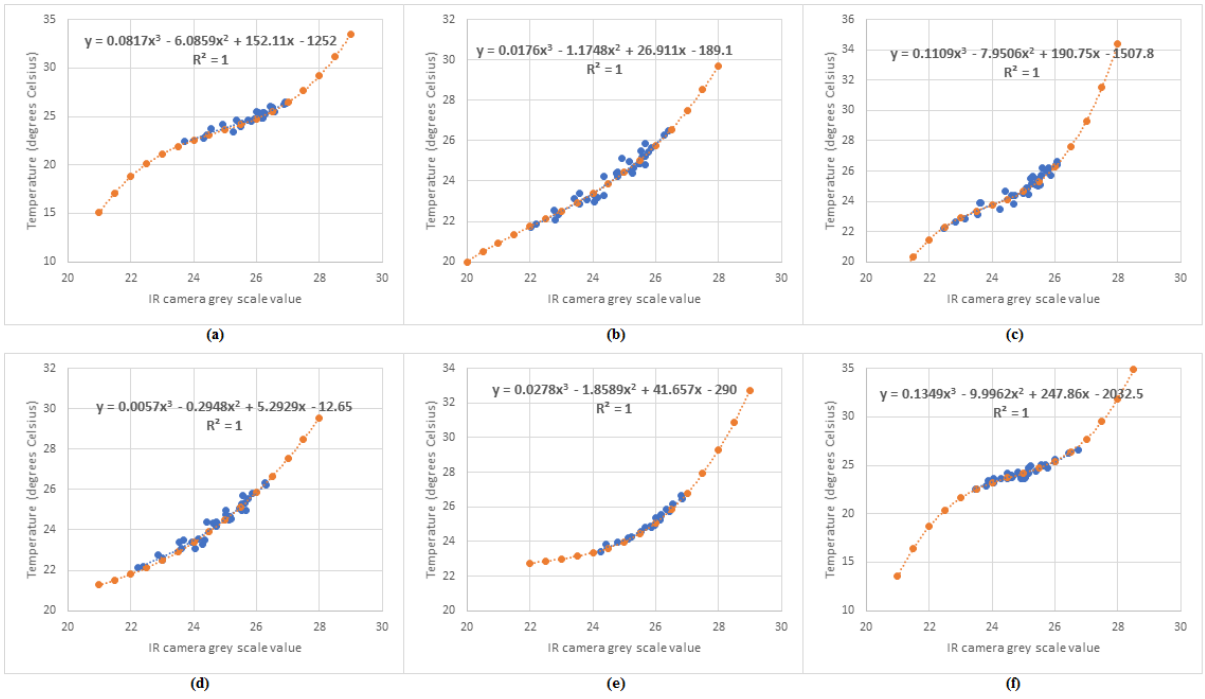

Figure F-16: IR camera calibration curves at a blowing ratio of 0.6 and compound angle of 40 degrees, with turbulence grid. a) cylindrical 3D 60 degrees printed hole, b) laidback fan-shaped 3D zero (0) degrees printed hole, c) case 1 hole, d) case 2 hole, e) case 3 hole, f) case 4 hole.

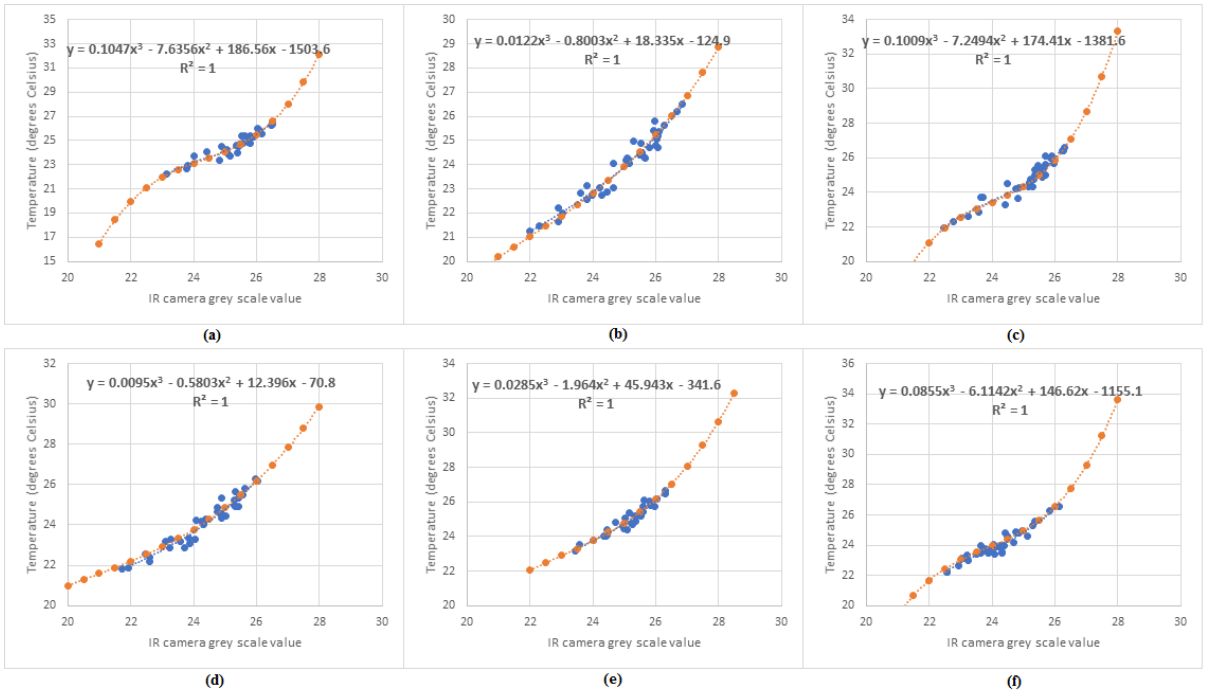

Figure F-17: IR camera calibration curves at a blowing ratio of 0.9 and compound angle of 40 degrees, with turbulence grid. a) cylindrical 3D 60 degrees printed hole, b) laidback fan-shaped 3D zero (0) degrees printed hole, c) case 1 hole, d) case 2 hole, e) case 3 hole, f) case 4 hole.

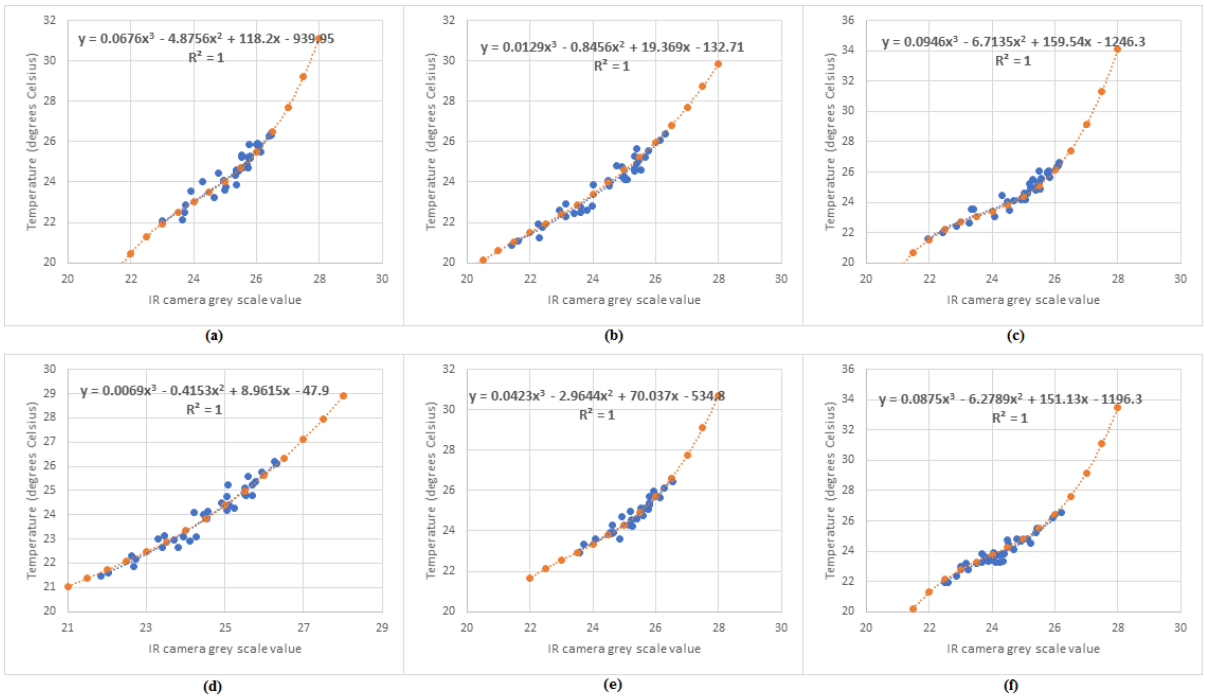

Figure F-18: IR camera calibration curves at a blowing ratio of 1.1 and compound angle of 40 degrees, with turbulence grid. a) cylindrical 3D 60 degrees printed hole, b) laidback fan-shaped 3D zero (0) degrees printed hole, c) case 1 hole, d) case 2 hole, e) case 3 hole, f) case 4 hole.

G. Uncertainty analysis

An uncertainty/error analysis is performed because the true values of measured variables is seldom known, and experiments inherently have errors. These errors are due to instrumentation, data acquisition and reduction limitations, and facility and environmental effects (Stern *et al.* 1999).

The uncertainty analysis was performed on the cylindrical machined holes at a compound angle of zero (0) degrees. The analysis is performed on the discharge coefficient, pressure ratio, blowing ratio and momentum flux ratio.

The method followed is by Stern *et al.* (1999) and accounts for the propagation of errors in the data reduction equations. The uncertainty estimate is made at a 95 percent confidence level. The total error is an estimate of the range in which the possible true value of the measured quantity may lie relative to the average of the measured quantity. It is composed of the bias and precision error components; equation below.

$$U = \pm\sqrt{B^2 + P^2}$$

where:

U : total uncertainty

B : bias uncertainty

P : precision uncertainty

The bias limit is obtained by multiplying the biases of the individual variables with their respective sensitivity coefficients and then summing the products of the individual variables; equation below.

$$B^2 = \sum_{i=1}^{J} {\theta_i}^2 {B_i}^2$$

where:

$\theta_i = \frac{\partial R}{\partial X_i}$: sensitivity coefficient of individual variable

B_i : bias error of individual variable

R : data reduction equation

X_i : individual variable

The bias errors of the individual variables were obtained from manufacturers specifications or taken as the scale resolution, where possible; table below. The bias error of the volume rate from the compressor and the inlet air density could not be obtained and have been excluded in the uncertainty calculation. It should also be noted that correlated biases were neglected in the uncertainty analysis.

Instruments	Bias error
Pressure transducers	0.1 V
Thermocouples	1 °C
Dimensions of film cooling holes	0.02 mm
Mercury manometer to read of atmospheric pressure	0.05 mmHg

Five (5) samples were taken at each pressure ratio, in the pressure ratio range tested. The precision error was obtained by multiplying the standard deviation of the samples with student's t-variable and dividing by the square root of the number of samples; equation below.

$$P^2 = \frac{tS_i}{\sqrt{M}}$$

where:

t : student's t − variable

S_i : standard deviation of individual variable

M : number of samples

Below the student shows an error analysis sample calculation on the discharge coefficient at a 22% compressor speed. The same procedure is followed in calculating the error of the other variables used in this study. An error analysis of the non-dimensional temperature parameter is also shown.

Discharge Coefficient

The discharge coefficient is defined as shown in the equation below:

$$C_d = \frac{\left(\frac{Q_v}{2} \times 0.001\right) \times \rho_{air\_inlet}}{A_{hole}\sqrt{2 \times \rho_c \times (P_{tc} - P_{sm})}}$$

where:

C_d : discharge coefficient of film cooling hole

Q_v : volume flow rate from compressor

ρ_{air_inlet} : density of air at the inlet of compressor

P_{tc} : total coolant pressure

P_{sm} : static mainstream pressure

$\rho_c = \frac{P_{tc}}{R \times T_{tc}}$: density of coolant through film cooling hole

$A_{hole} = \frac{\pi}{4} \times D^2$: cross − sectional area of cylindrical portion of hole

D : diameter of the cylindrical portion of hole

T_{tc} : total temperature inside plenum

R : ideal gas constant

From the calibration of the pressure transducers it was determined that the equations below are used to calculate the total coolant pressure and the static mainstream pressure:

$$P_{tc} = [13593 \times 9.81 \times (P_{atm} \times 10^{-3})] + [124.39 \times (V_{tc} - V_{offset,tc}) - 0.6237]$$

$$P_{sm} = [13593 \times 9.81 \times (P_{atm} \times 10^{-3})] - [24.57 \times (V_{sm} - V_{offset,sm}) - 0.0426]$$

where:

V_{tc} : plenum transducer voltage response

$V_{offset,tc}$: plenum transducer offset voltage response

V_{sm} : mainstream static transducer voltage response

$V_{offset,sm}$: mainstream static transducer offset voltage response

P_{atm} : atmospheric pressure in mm of mercury

The total temperature inside the plenum is taken as the average of the temperature of the two (2) thermocouples inside the plenum box. From the calibration, Appendix F, of the thermocouples it was determined that the equations below are used to calculate the total temperatures:

$$T_{actual,1} = 273.15 + [1.0024 \times T_{thermocouple,1} + 0.9941]$$

$$T_{actual,2} = 273.15 + [1.002 \times T_{thermocouple,2} + 0.9643]$$

$$T_{tc} = \frac{T_{actual,1} + T_{actual,2}}{2}$$

where:

$T_{thermocouple}$: thermocouple temperature measurement inside plenum

T_{actual} : actual temperature inside plenum

Substitution of the above equations into the discharge coefficient equation, the discharge coefficient data reduction equation is obtained; shown below:

$$C_d = \frac{\left(\frac{Q_V}{2} \times 0.001\right) \times \rho_{air\_inlet}}{\left(\frac{\pi}{4} \times D^2\right)\sqrt{2 \times \left(\frac{[13593 \times 9.81 \times (P_{atm} \times 10^{-3})] + [124.39 \times (V_{tc} - V_{offset,tc}) - 0.6237]}{R \times \left(273.15 + \frac{[1.0024 \times T_{thermocouple,1} + 0.9941] + [1.002 \times T_{thermocouple,2} + 0.9643]}{2}\right)}\right) \times ([13593 \times 9.81 \times (P_{atm} \times 10^{-3})] + [124.39 \times (V_{tc} - V_{offset,tc}) - 0.6237] - [13593 \times 9.81 \times (P_{atm} \times 10^{-3})] - [24.57 \times (V_{sm} - V_{offset,sm}) - 0.0426])}}$$

The bias error calculation of the discharge coefficient is shown below:

$$B_{C_d}{}^2 = (\theta_D)^2 (B_D)^2 + (\theta_{P_{atm}})^2 (B_{P_{atm}})^2 + (\theta_{V_{tc}})^2 (B_{V_{tc}})^2 + (\theta_{V_{sm}})^2 (B_{V_{sm}})^2 + (\theta_{T_1})^2 (B_{T_1})^2 + (\theta_{T_2})^2 (B_{T_2})^2$$

$$B_{C_d}{}^2 = \left(\frac{\partial C_d}{\partial D}\right)^2 B_D{}^2 + \left(\frac{\partial C_d}{\partial P_{atm}}\right)^2 B_{P_{atm}}{}^2 + \left(\frac{\partial C_d}{\partial V_{tc}}\right)^2 B_{V_{tc}}{}^2 + \left(\frac{\partial C_d}{\partial V_{sm}}\right)^2 B_{V_{sm}}{}^2 + \left(\frac{\partial C_d}{\partial T_1}\right)^2 B_{T_1}{}^2 + \left(\frac{\partial C_d}{\partial T_2}\right)^2 B_{T_2}{}^2$$

$$\begin{aligned} B_{C_d}{}^2 &= (-0.076168765)^2\left(0.002(10^{-3})\right)^2 + (-0.000230507)^2(13593 \times 9.81 \times 0.05)^2 \\ &\quad + (-0.049394525)^2(0.1)^2 + (-0.009716895)^2(0.1)^2 \\ &\quad + (0.000256874)^2(273.15+1)^2 + (0.000256772)^2(273.15+1)^2 \\ &= 0.009942268 \end{aligned}$$

The precision error calculation of the discharge coefficient is shown below:

$$P^2 = \frac{tS_i}{\sqrt{M}}$$

$$P_{C_d}{}^2 = \frac{2.776445 \times 0.051338659}{\sqrt{5}} = 0.004063471$$

The total uncertainty error calculation of the discharge coefficient is shown below:

$$U_{C_d} = \pm\sqrt{B_{C_d}{}^2 + P_{C_d}{}^2}$$

$$U_{C_d} = \pm\sqrt{0.009942268 + 0.004063471} = 0.118345844$$

The total uncertainty error percentage of the average calculation of the discharge coefficient is shown below:

$$\%U = \frac{U_{C_d}}{\overline{C_d}} \times 100$$

$$\%U_{C_d} = \frac{0.118345844}{0.270314776} \times 100 = 43.78\%$$

where:

$\%U_{C_d}$: discharge coefficient percentage total uncertainty

U_{C_d} : discharge coefficient total uncertainty

$\overline{C_d}$: discharge coefficient average

Shown in Figure G-1 are the uncertainty results for the other parameters used in this study.

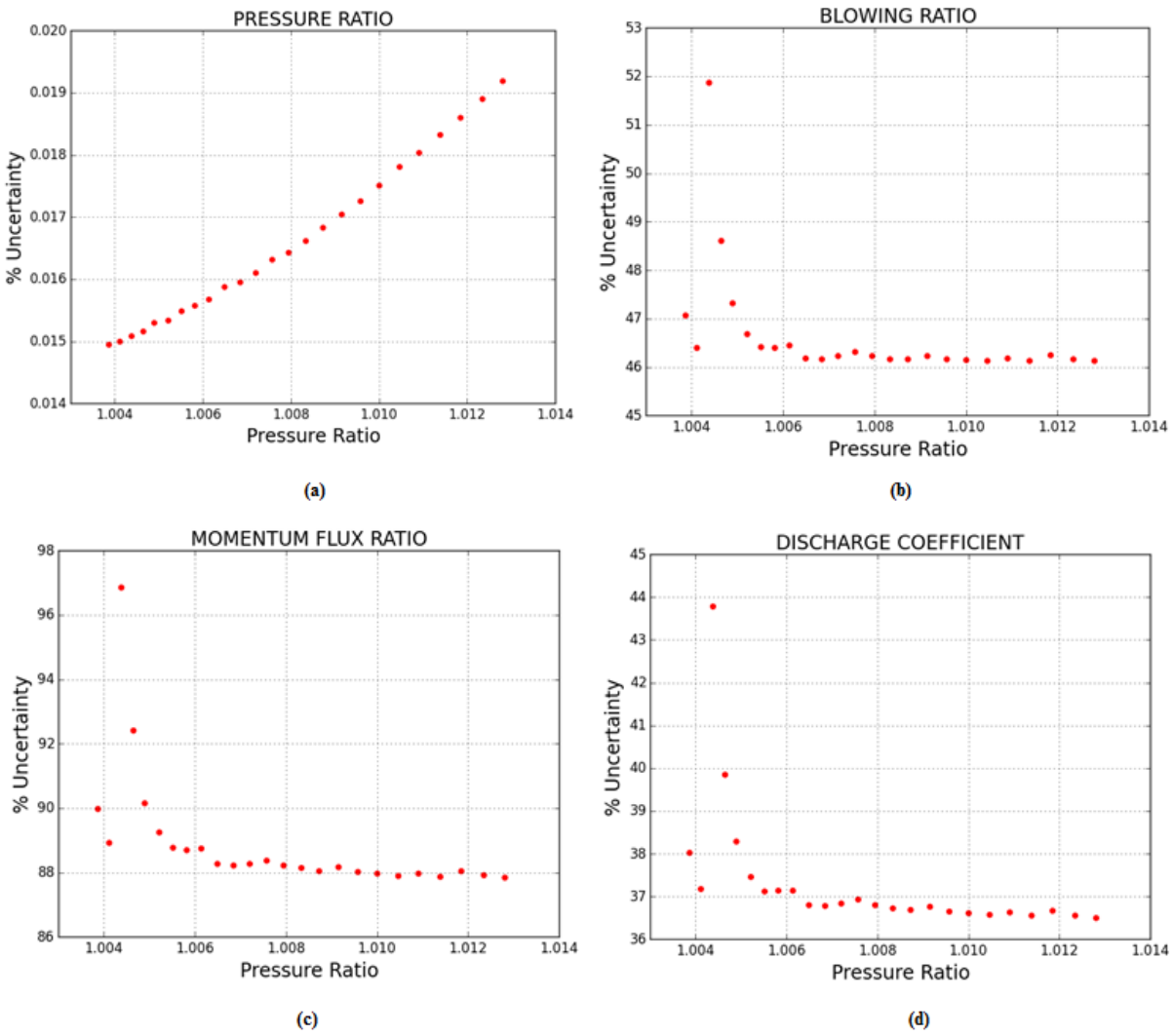

Figure G-1: Percentage total uncertainty of a) Pressure ratio, b) Blowing ratio, c) Momentum flux ratio, d) Discharge coefficient

Non-dimensional temperature

The non-dimensional temperature parameter is defined as shown below:

$$\theta = \frac{T_{probe} - T_c}{T_{tm} - T_c}$$

where:

θ : non − dimensionalized temperature

T_{probe} : probe temperature

T_c : total coolant temperature in the plenum box

T_{tm} : total mainstream temperature

From the calibration of the thermocouples, Appendix F, it was determined that the equations below are used to calculate the total temperatures:

$$T_{actual,probe} = 1.018 \times T_{thermocouple,probe} + 0.1489$$
$$T_{actual,coolant} = 1.008 \times T_{thermocouple,coolant} + 0.3515$$

$$T_{actual,mainstream} = 1 \times T_{thermocouple,mainstream} + 0.9826$$

where:

$T_{thermocouple}$: thermocouple temperature measurement

T_{actual} : actual temperature measurement

Substitution of the above equations into the definition of the non-dimensional temperature parameter, the non-dimensionalized temperature data reduction equation below is obtained:

$$\theta = \frac{[1.018 \times T_{thermocouple,probe} + 0.1489] - [1.008 \times T_{thermocouple,coolant} + 0.3515]}{[1 \times T_{thermocouple,mainstream} + 0.9826] - [1.008 \times T_{thermocouple,coolant} + 0.3515]}$$

The bias error calculation is shown below:

$$B_\theta{}^2 = \left(\theta_{T_{probe}}\right)^2 \left(B_{T_{probe}}\right)^2 + \left(\theta_{T_c}\right)^2 \left(B_{T_c}\right)^2 + \left(\theta_{T_{tm}}\right)^2 \left(B_{T_{tm}}\right)^2$$

$$B_\theta{}^2 = \left(\frac{\partial\theta}{\partial T_{probe}}\right)^2 \left(B_{T_{probe}}\right)^2 + \left(\frac{\partial\theta}{\partial T_c}\right)^2 \left(B_{T_c}\right)^2 + \left(\frac{\partial\theta}{\partial T_{tm}}\right)^2 \left(B_{T_{tm}}\right)^2$$

$$B_\theta{}^2 = (0.1089991)^2(1)^2 + (-0.07227)^2(1)^2 + (-0.03537)^2(1)^2 = 0.018355535$$

The precision error calculation is shown below:

$$P^2 = \frac{tS_i}{\sqrt{M}}$$

$$P_{C_d}{}^2 = \frac{2.776445 \times 0.012339}{\sqrt{5}} = 0.00023473$$

The total uncertainty error calculation of the non-dimensional temperature parameter is shown below:

$$U_\theta = \pm\sqrt{B_\theta{}^2 + P_\theta{}^2}$$

$$U_\theta = \pm\sqrt{0.018355535 + 0.00023473} = 0.136346123$$

The total uncertainty error percentage of the average calculation of the discharge coefficient is shown below:

$$\%U = \frac{U_\theta}{\bar{\theta}} \times 100$$

$$\%U_\theta = \frac{0.136346123}{0.369053} \times 100 = 36.94488\%$$

where:

$\%U_\theta$: non − dimensionalized temperature percentage total uncertainty

U_θ : non − dimensionalized temperature total uncertainty

$\bar{\theta}$: non − dimensionalized temperature average

H. Additional results and tests done in this study

Shown in the figures below are additional results presented and additional tests that were done in this study. The additional results presented are zoomed out plots of the results presented in chapter 5. As mentioned in chapter 5, it is easier to locate the coolant jet using the Uy and Uz from the zoomed-out results. The additional results presented are also the longitudinal vortices with the inclusion of the turbulence grid in the flow.

Additional tests were done whose results are not included in the main thesis. The results of the additional tests are presented below.

H.1. Flow structure results

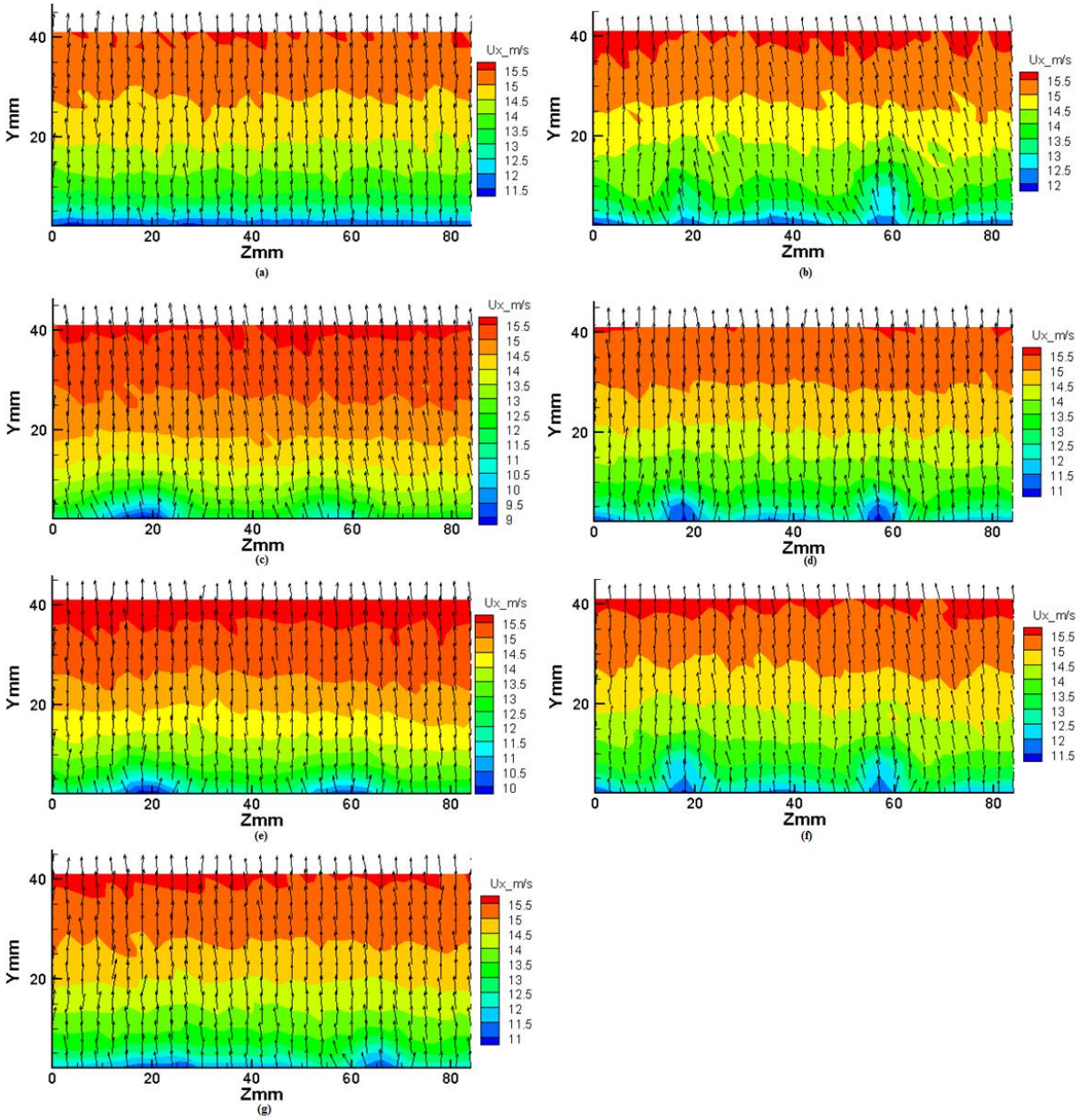

Figure H-1: Flowfield measurements 48 mm downstream of hole exit trailing edge at blowing ratio of 0.9 and compound angle of zero (0) degrees. a) No coolant injection, b) cylindrical hole injection, c) laidback fan-shaped hole injection, d) case 1 hole injection, e) case 2 hole injection, f) case 3 hole injection, g) case 4 hole injection.

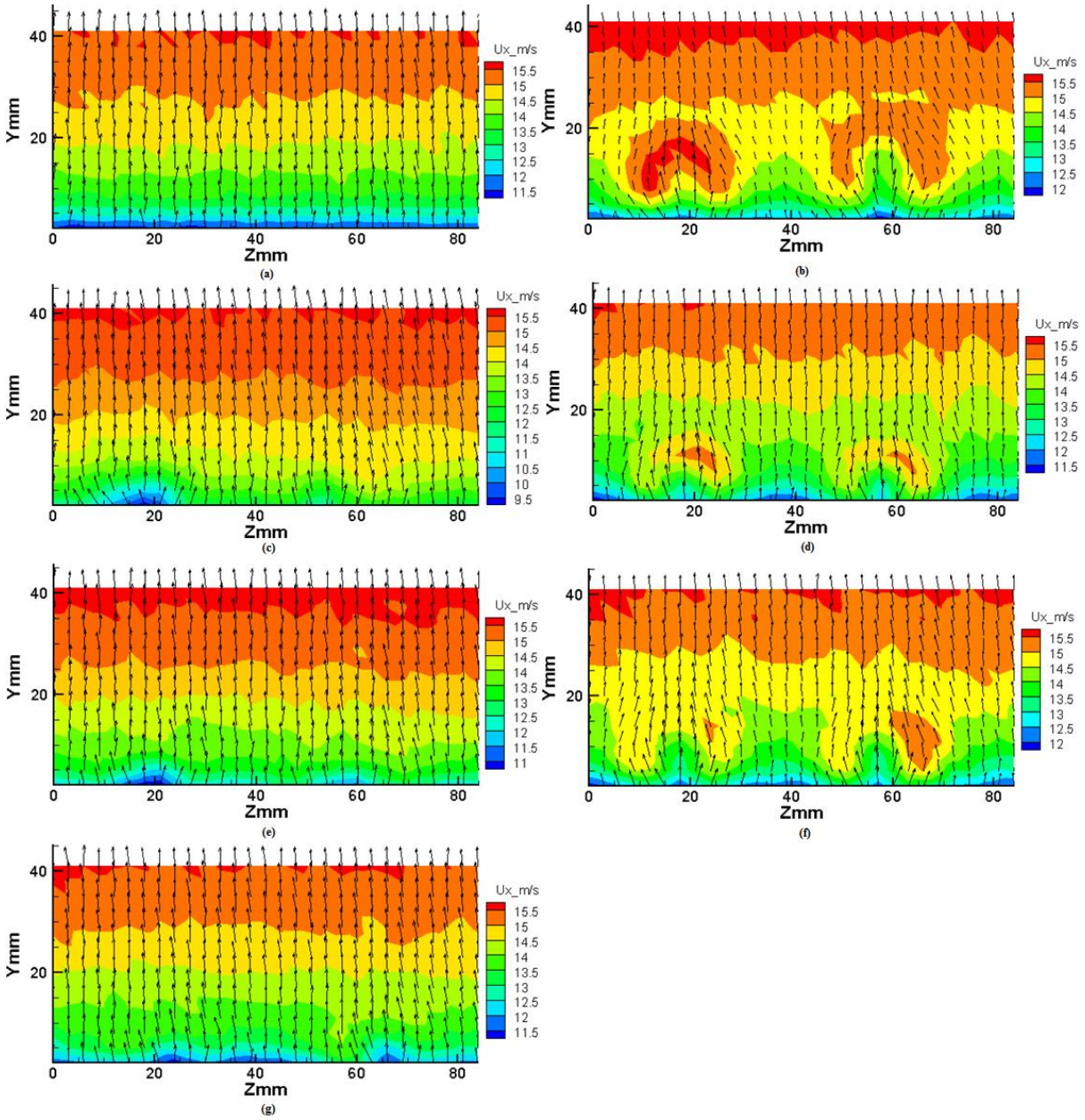

Figure H-2: Flowfield measurements 48 mm downstream of hole exit trailing edge at blowing ratio of 1.3 and compound angle of zero (0) degrees. a) No coolant injection, b) cylindrical hole injection, c) laidback fan-shaped hole injection, d) case 1 hole injection, e) case 2 hole injection, f) case 3 hole injection, g) case 4 hole injection.

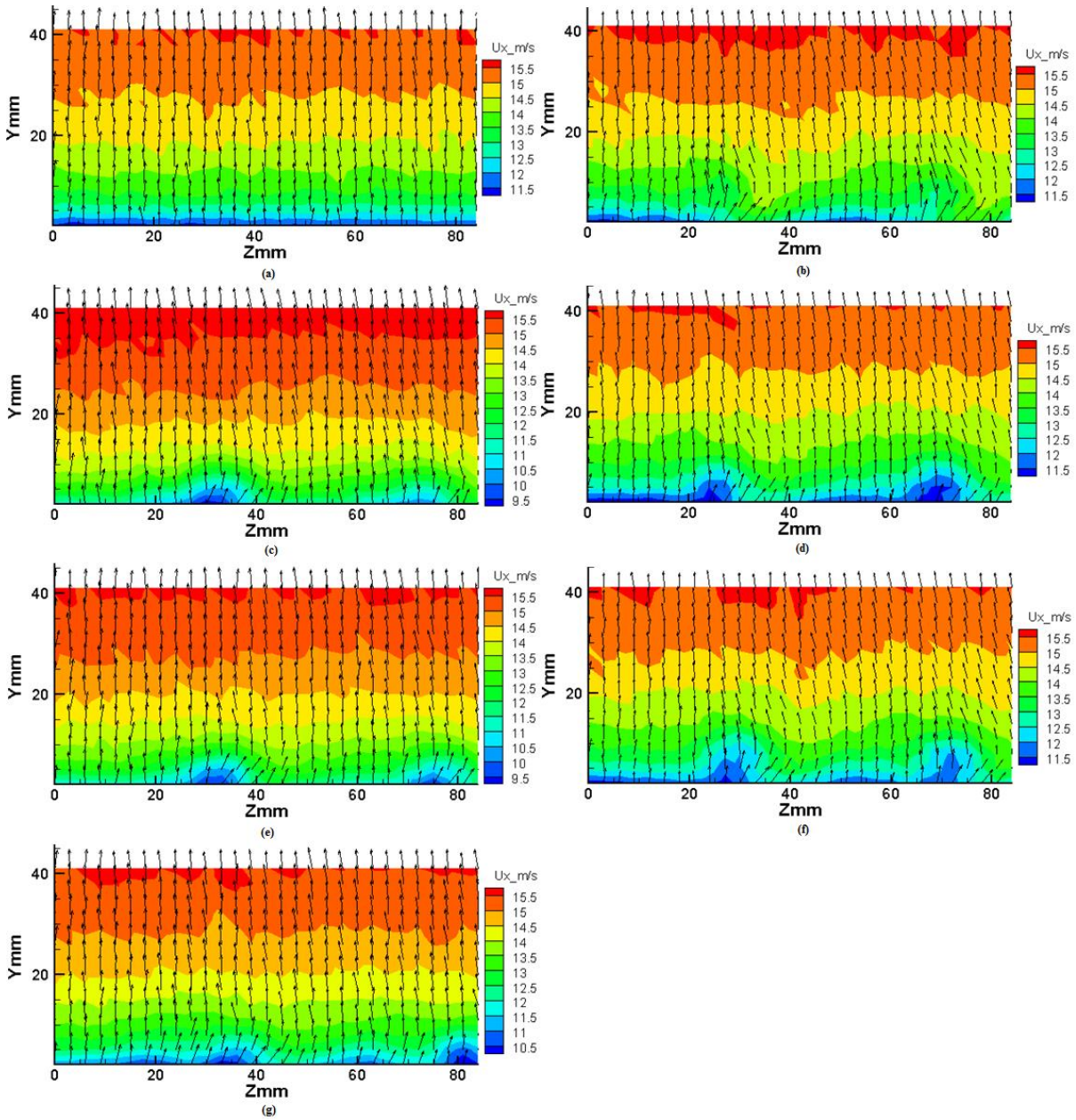

Figure H-3: Flowfield measurements 48 mm downstream of hole exit trailing edge at blowing ratio of 0.9 and compound angle of 20 degrees. a) No coolant injection, b) cylindrical hole injection, c) laidback fan-shaped hole injection, d) case 1 hole injection, e) case 2 hole injection, f) case 3 hole injection, g) case 4 hole injection.

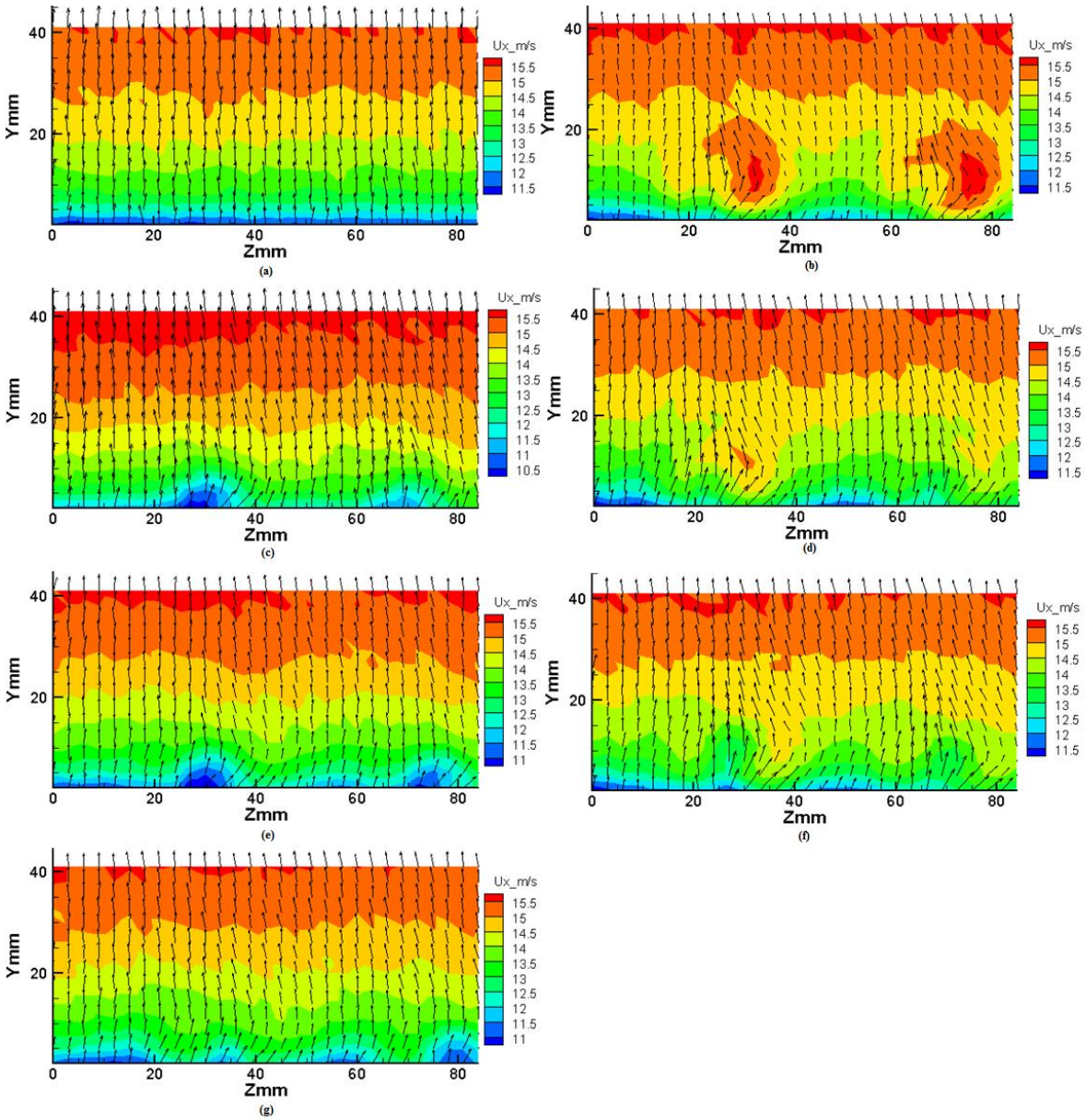

Figure H-4: Flowfield measurements 48 mm downstream of hole exit trailing edge at blowing ratio of 1.3 and compound angle of 20 degrees. a) No coolant injection, b) cylindrical hole injection, c) laidback fan-shaped hole injection, d) case 1 hole injection, e) case 2 hole injection, f) case 3 hole injection, g) case 4 hole injection.

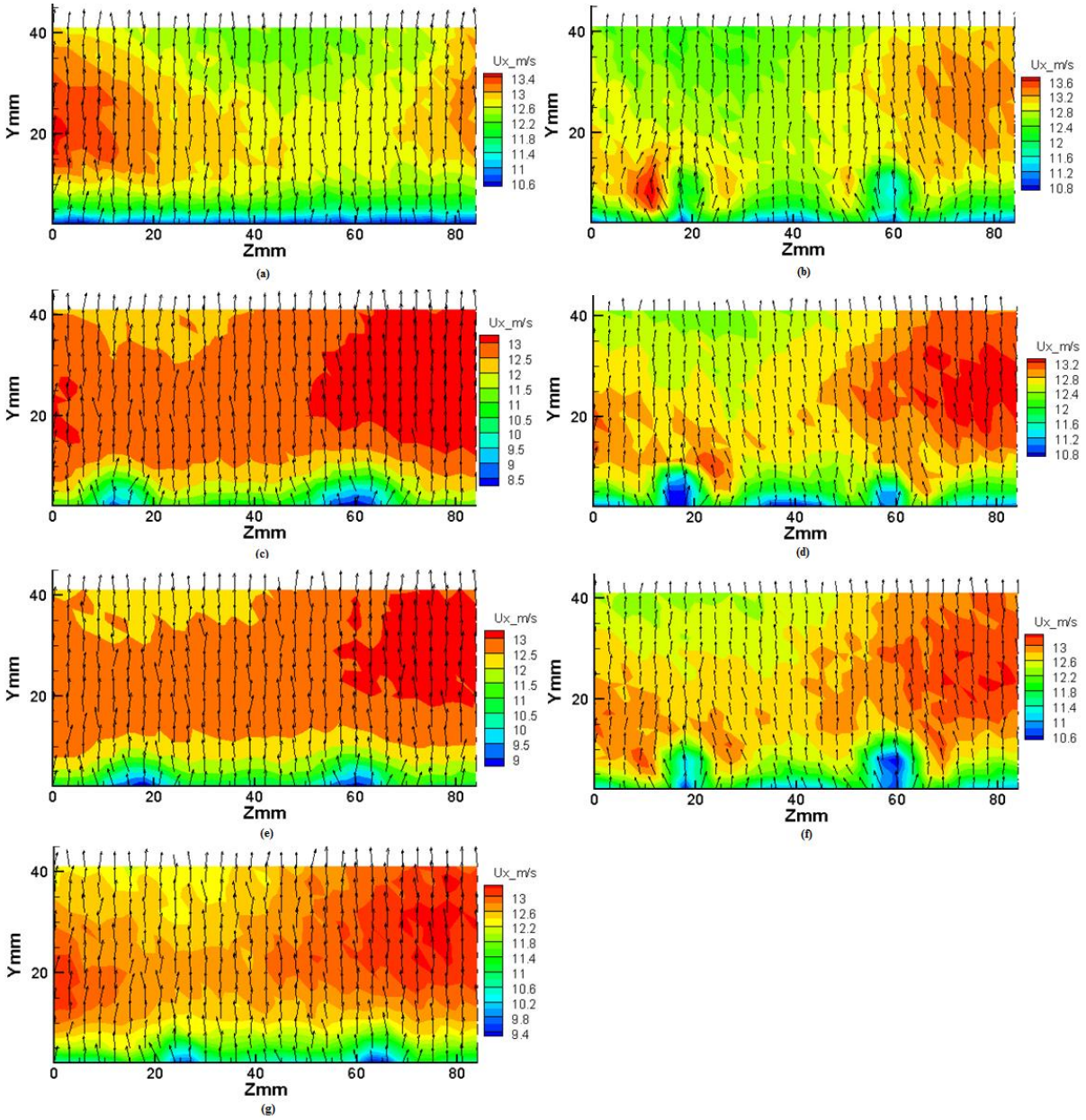

Figure H-5: With turbulence grid flowfield measurements 48 mm downstream of hole exit trailing edge at blowing ratio of 0.9 and compound angle of zero (0) degrees. a) No coolant injection, b) cylindrical hole injection, c) laidback fan-shaped hole injection, d) case 1 hole injection, e) case 2 hole injection, f) case 3 hole injection, g) case 4 hole injection.

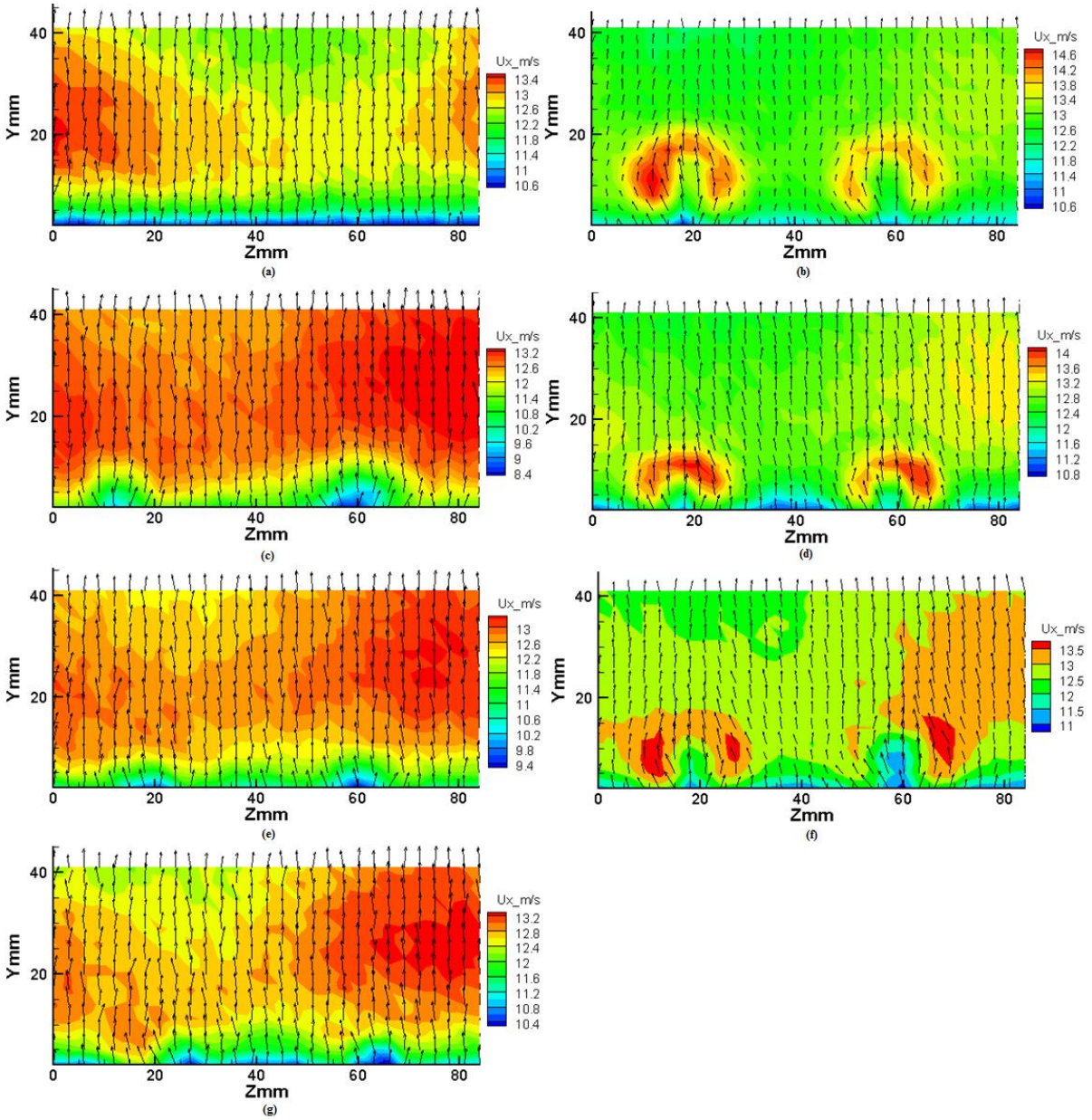

Figure H-6: With turbulence grid flowfield measurements 48 mm downstream of hole exit trailing edge at blowing ratio of 1.3 and compound angle of zero (0) degrees. a) No coolant injection, b) cylindrical hole injection, c) laidback fan-shaped hole injection, d) case 1 hole injection, e) case 2 hole injection, f) case 3 hole injection, g) case 4 hole injection.

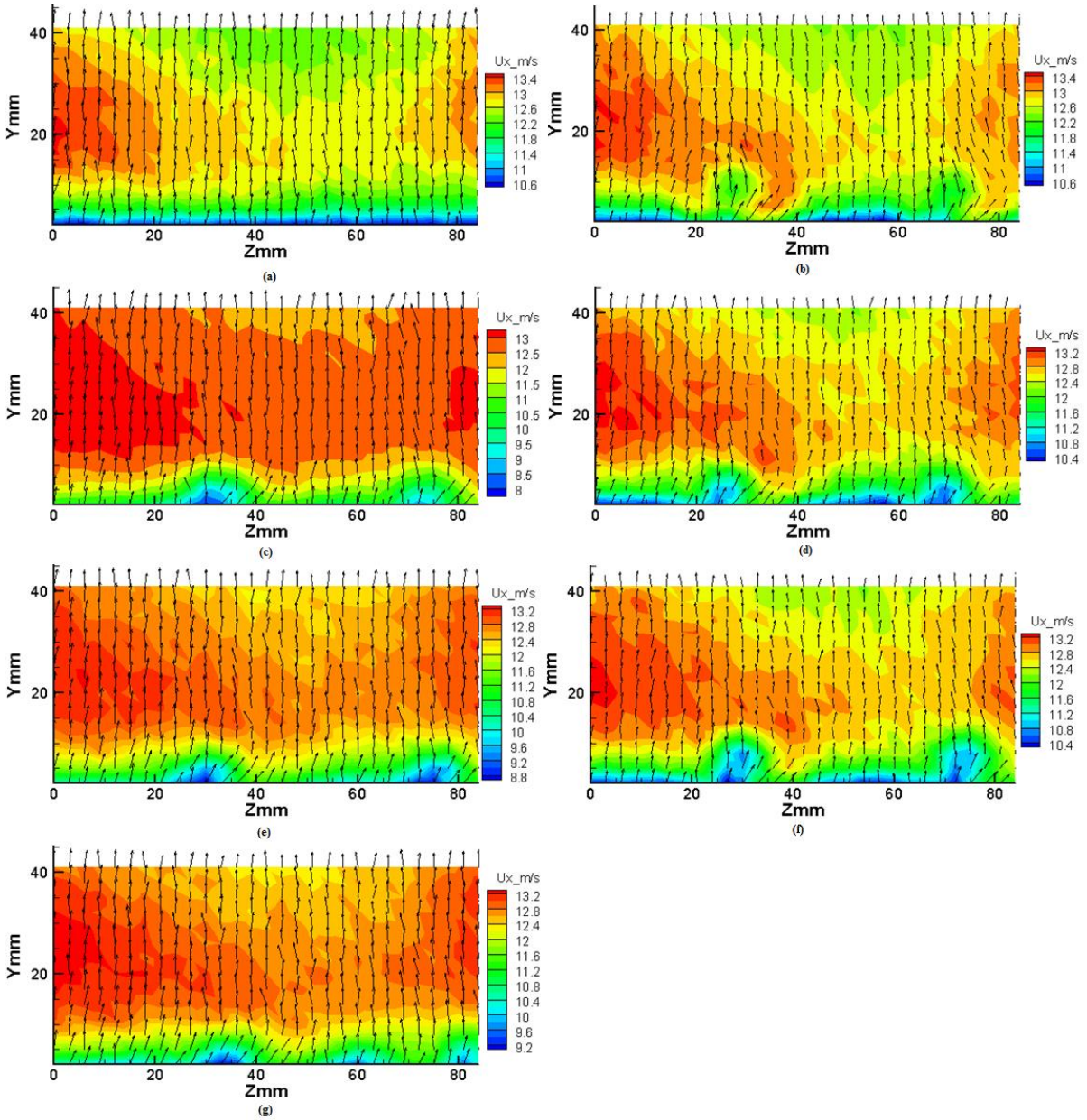

Figure H-7: With turbulence grid flowfield measurements 48 mm downstream of hole exit trailing edge at blowing ratio of 0.9 and compound angle of 20 degrees. a) No coolant injection, b) cylindrical hole injection, c) laidback fan-shaped hole injection, d) case 1 hole injection, e) case 2 hole injection, f) case 3 hole injection, g) case 4 hole injection.

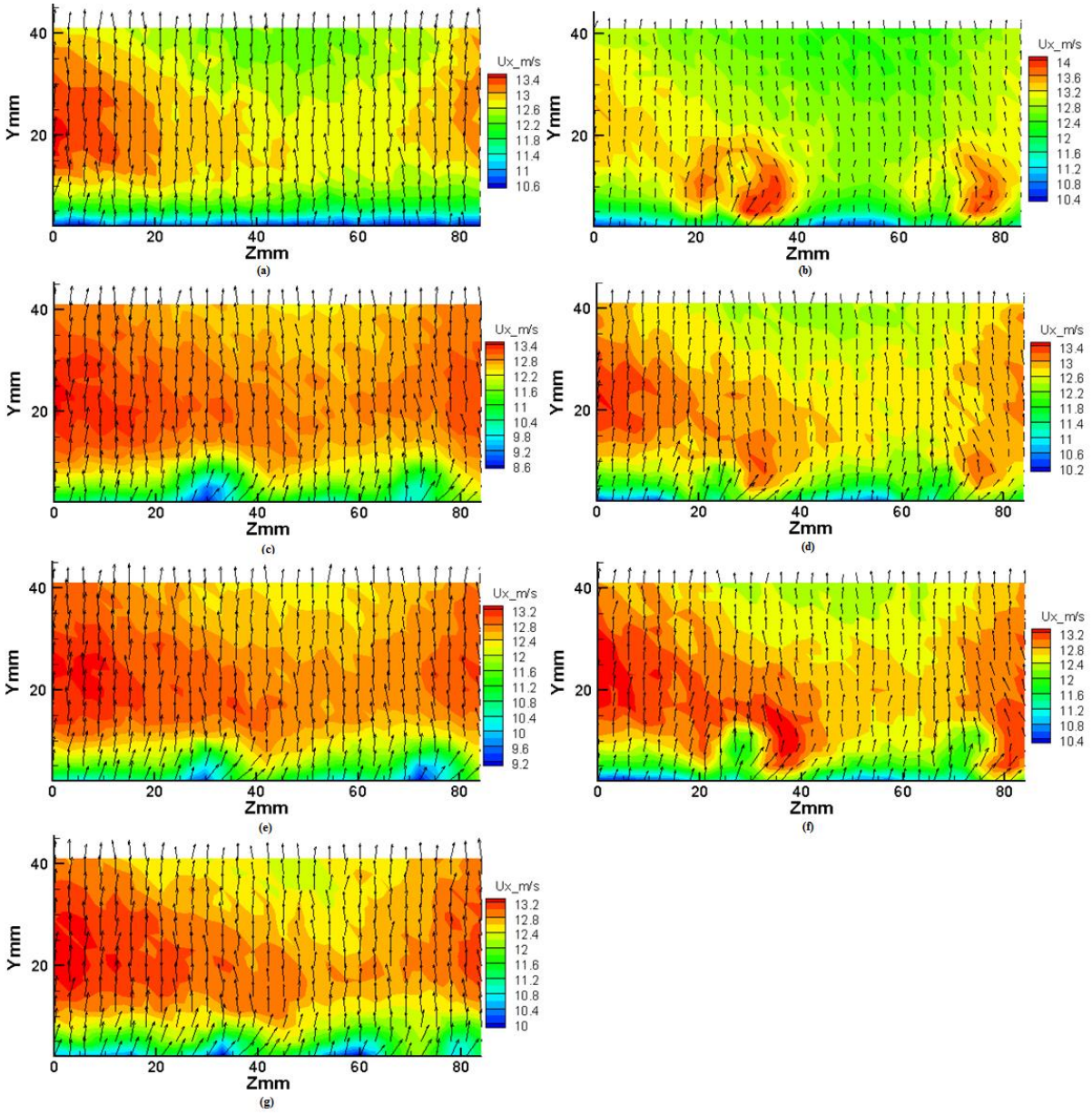

Figure H-8: With turbulence grid flowfield measurements 48 mm downstream of hole exit trailing edge at blowing ratio of 1.3 and compound angle of zero (0) degrees. a) No coolant injection, b) cylindrical hole injection, c) laidback fan-shaped hole injection, d) case 1 hole injection, e) case 2 hole injection, f) case 3 hole injection, g) case 4 hole injection.

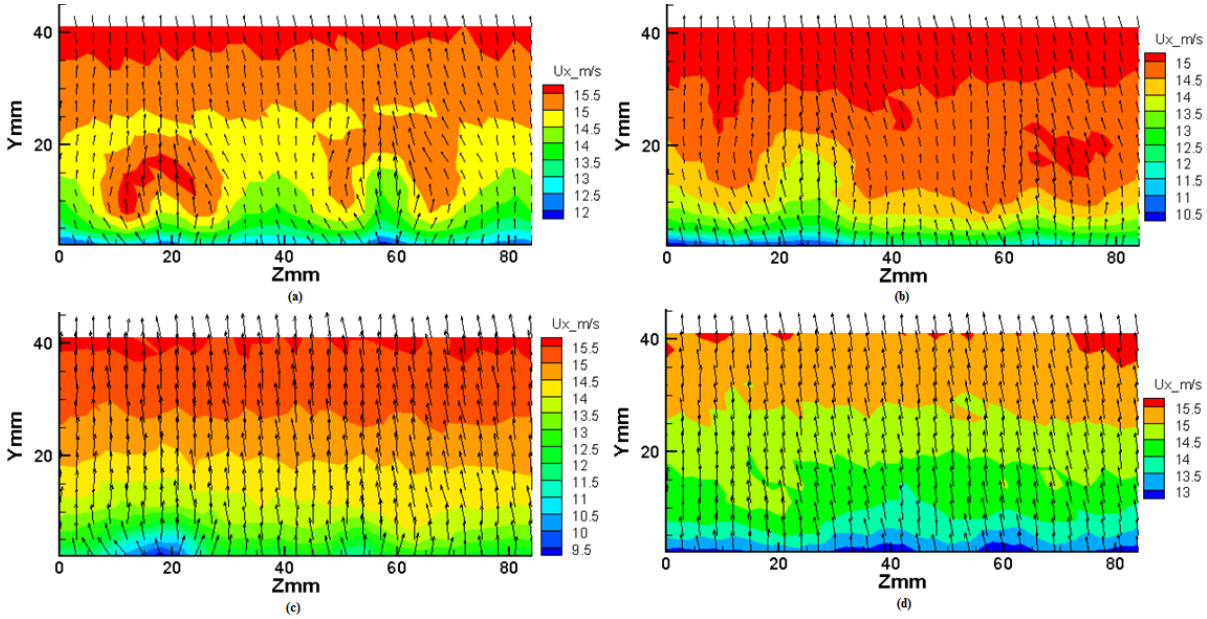

Figure H-9: Flowfield measurements downstream of hole exit edge. a) cylindrical hole injection 48 mm downstream, b) cylindrical hole 96 mm downstream, c) laidback fan-shaped hole 48 mm downstream, d) laidback fan-shaped hole 96 mm downstream.

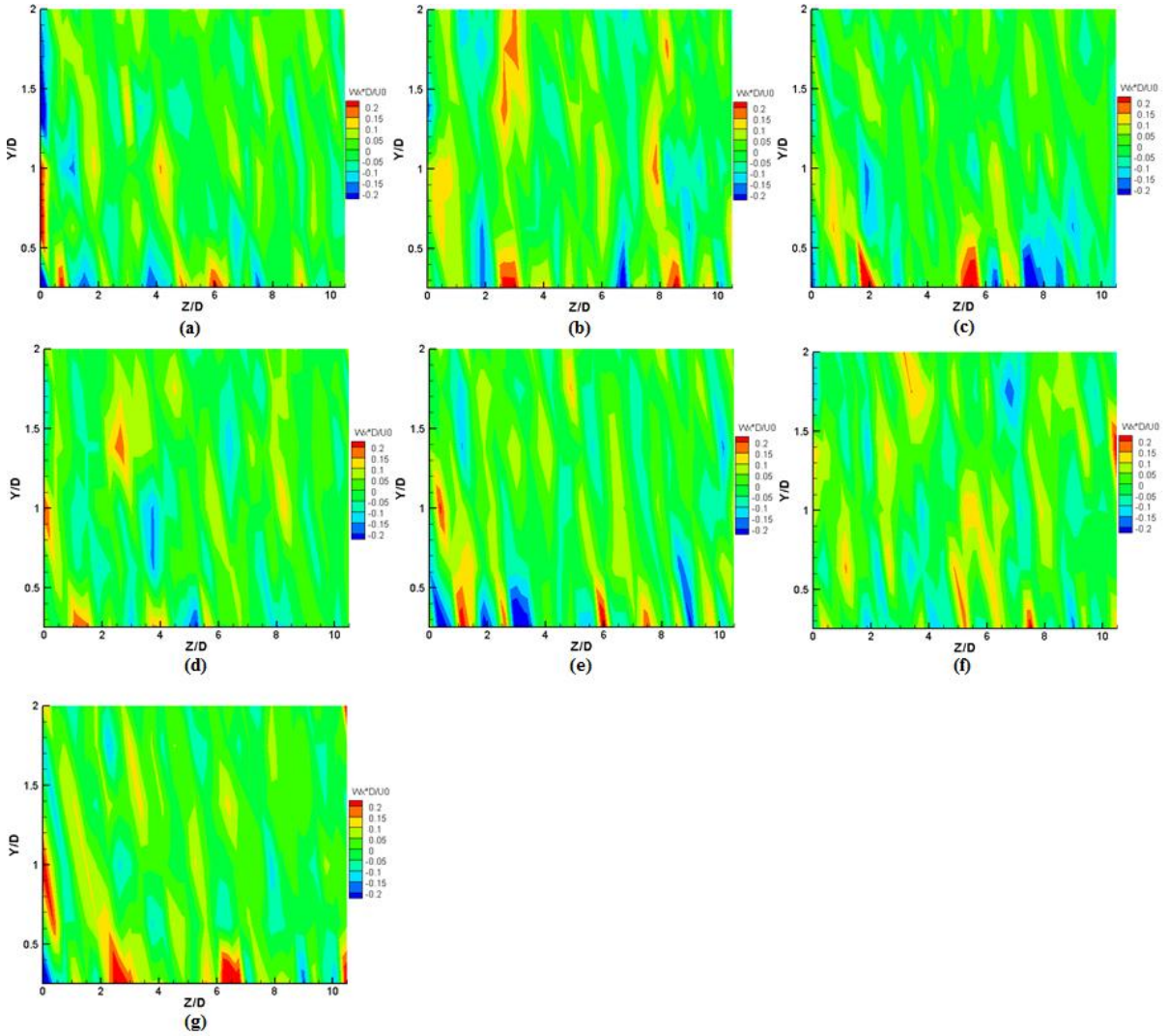

Figure H-10: With turbulence grid streamwise vorticity measurements 48 mm downstream of hole exit trailing edge at blowing ratio of 0.9 and compound angle of zero (0) degrees. a) no coolant injection, b) cylindrical hole injection, c) laidback fan-shaped hole injection, d) case 1 hole injection, e) case 2 hole injection, f) case 3 hole injection, g) case 4 hole injection.

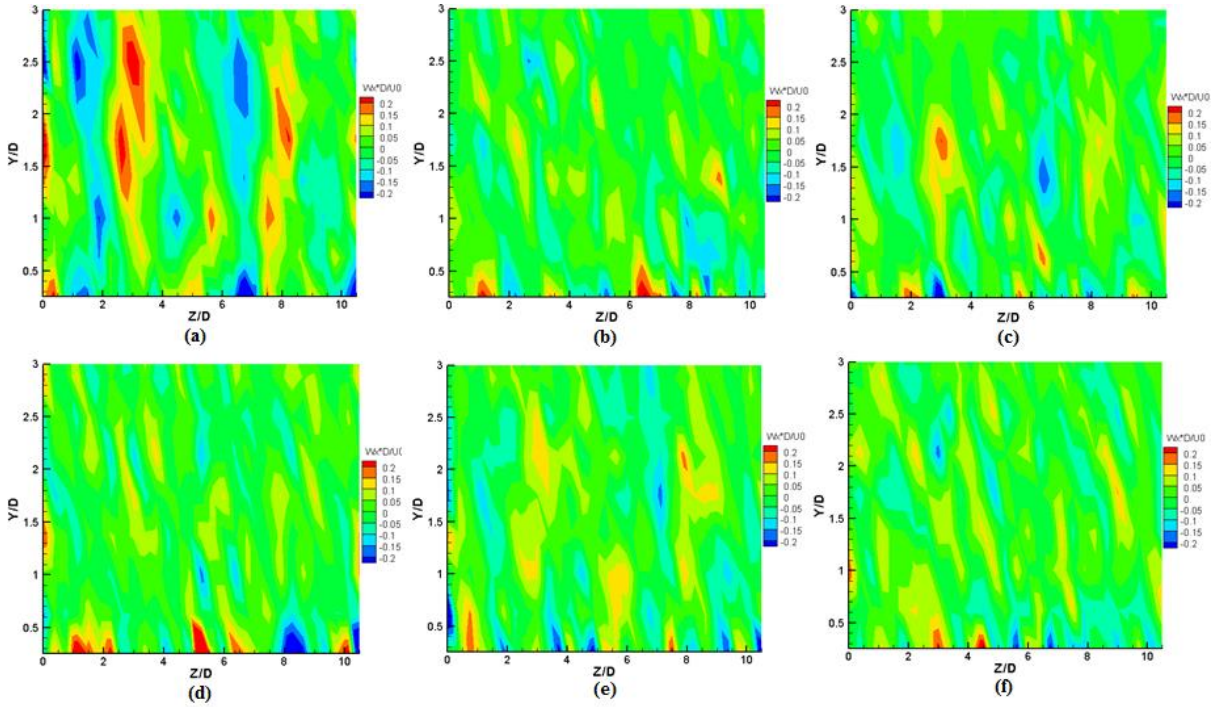

Figure H-11: With turbulence grid streamwise vorticity measurements 48 mm downstream of hole exit trailing edge at blowing ratio of 1.3 and compound angle of zero (0) degrees. a) cylindrical hole injection, b) laidback fan-shaped hole injection, c) case 1 hole injection, d) case 2 hole injection, e) case 3 hole injection, f) case 4 hole injection.

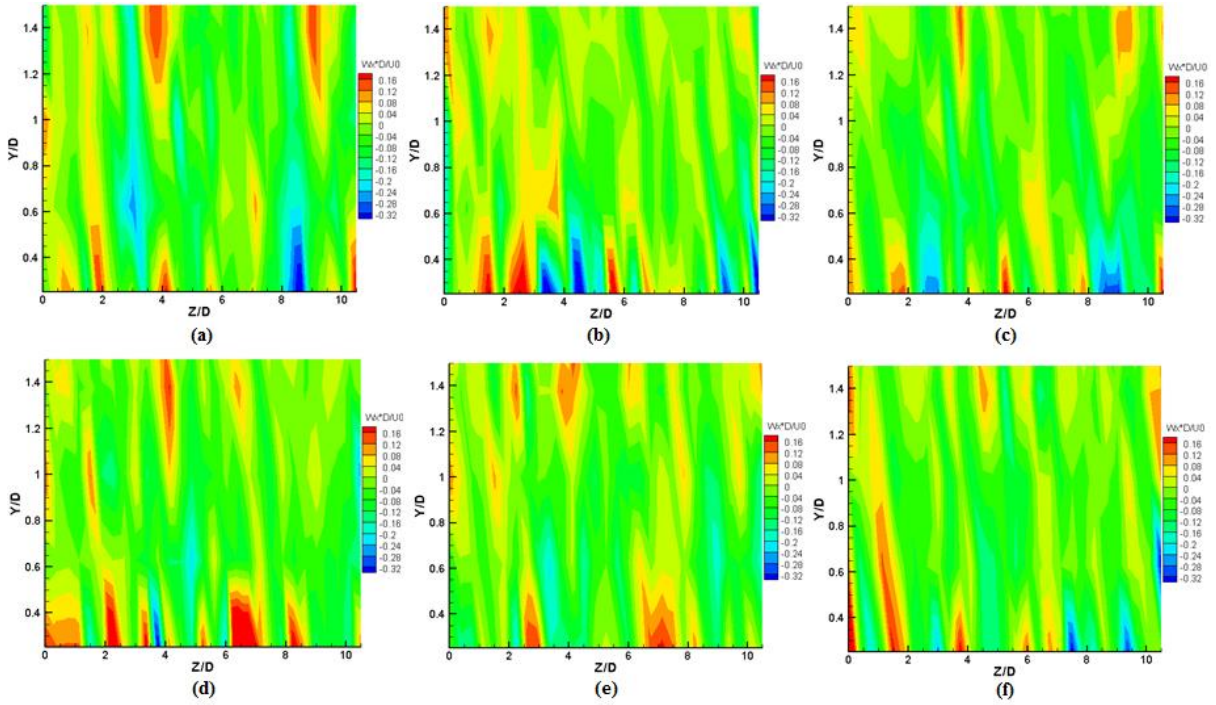

Figure H-12: With turbulence grid streamwise vorticity measurements 48 mm downstream of hole exit trailing edge at blowing ratio of 0.9 and compound angle of twenty (20) degrees. a) cylindrical hole injection, b) laidback fan-shaped hole injection, c) case 1 hole injection, d) case 2 hole injection, e) case 3 hole injection, f) case 4 hole injection.

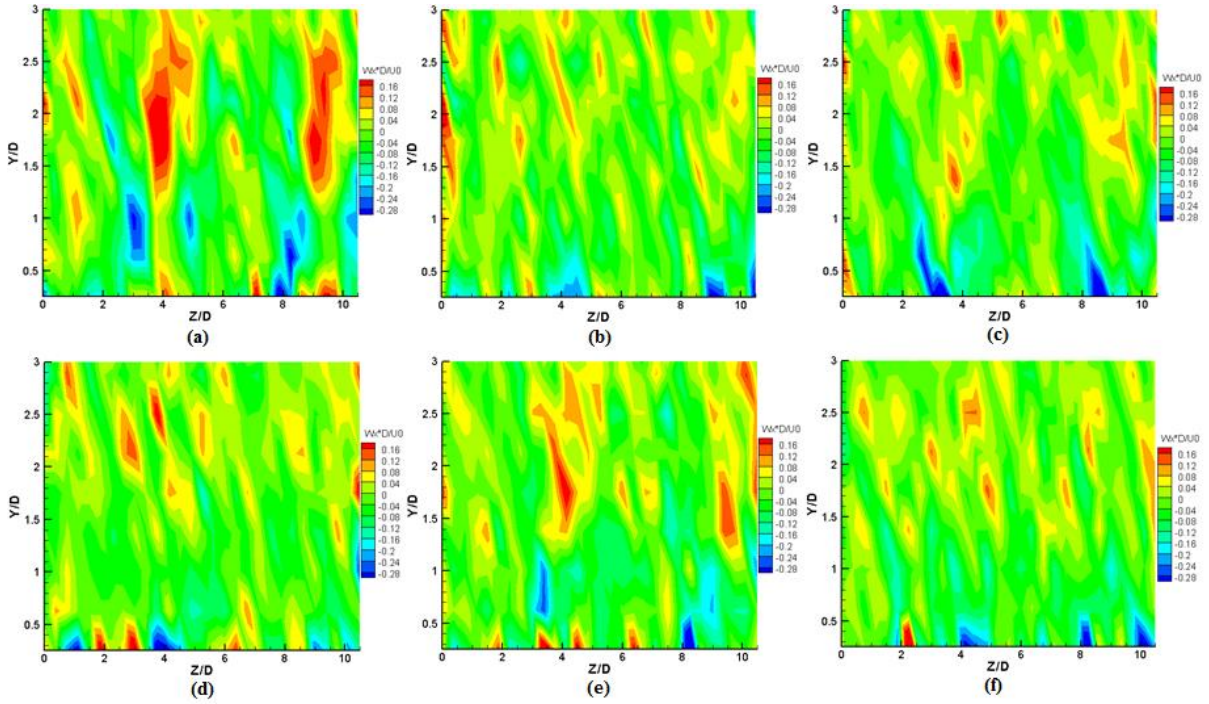

Figure H-13: With turbulence grid streamwise vorticity measurements 48 mm downstream of hole exit trailing edge at blowing ratio of 1.3 and compound angle of twenty (20) degrees. a) cylindrical hole injection, b) laidback fan-shaped hole injection, c) case 1 hole injection, d) case 2 hole injection, e) case 3 hole injection, f) case 4 hole injection.

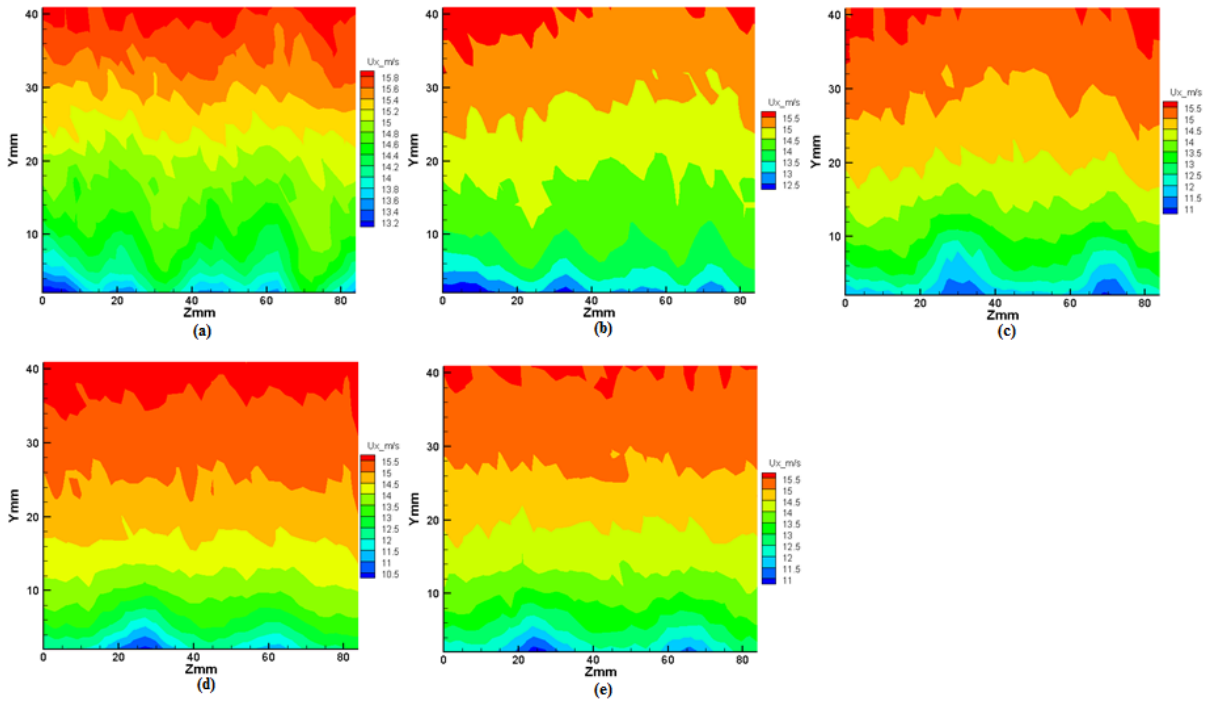

Figure H-14: Flow structure 96 mm downstream of hole exit trailing edge at blowing ratio equals to 0.7 and compound angle of zero (0) degrees. a) cylindrical machined hole, b) cylindrical 3D zero (0) degree Print orientation hole, c) diffused machined hole, d) diffused 3D zero (0) degree print orientation hole, e) diffused 3D 67 degree print orientation hole.

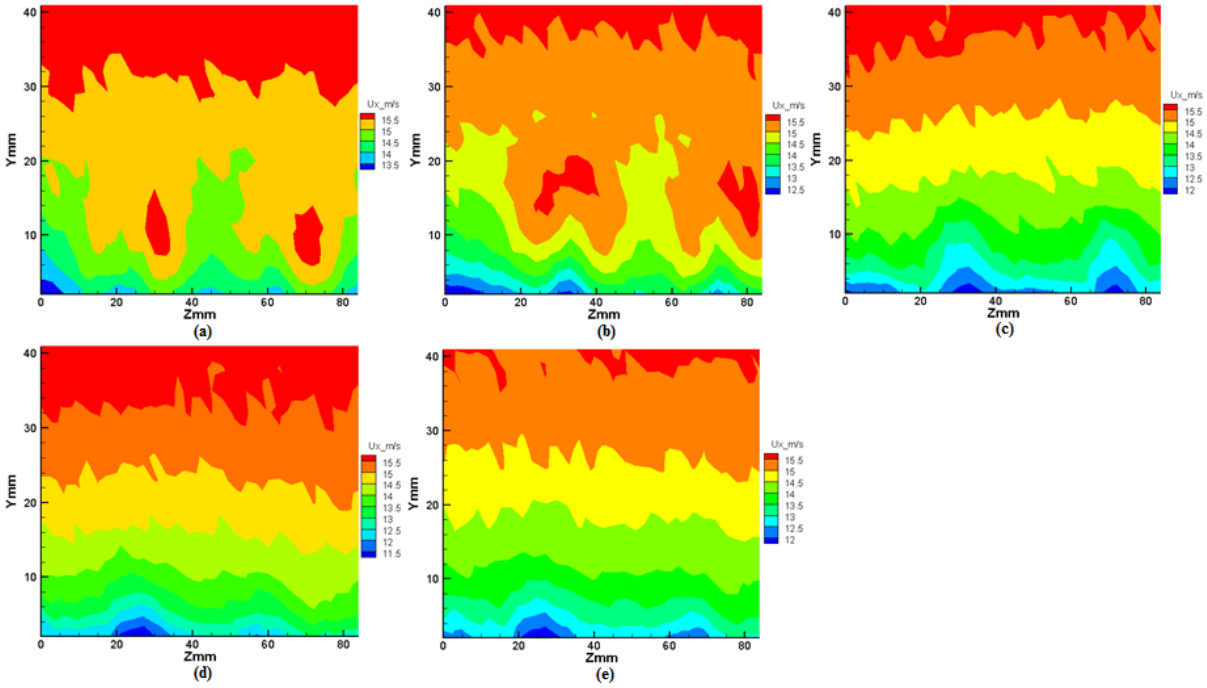

Figure H-15: Flow structure 96 mm downstream of hole exit trailing edge at blowing ratio equals to one (1) and compound angle of zero (0) degrees. a) cylindrical machined hole, b) cylindrical 3D zero (0) degree Print orientation hole, c) diffused machined hole, d) diffused 3D zero (0) degree print orientation hole, e) diffused 3D 67 degree print orientation hole.

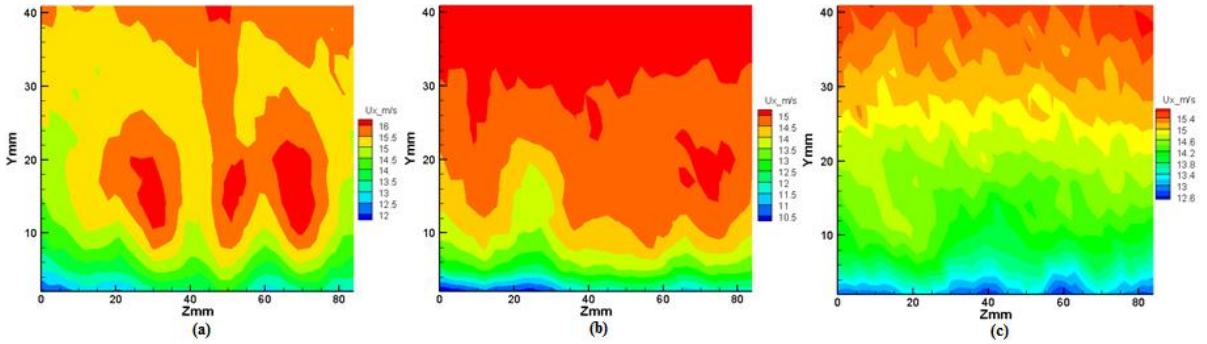

Figure H-16: Flow structure 96 mm downstream of hole exit trailing edge at blowing ratio equals to 1.3 and compound angle of zero (0) degrees. a) cylindrical machined hole, b) cylindrical 3D zero (0) degree Print orientation hole, c) diffused 3D 67 degree print orientation hole.

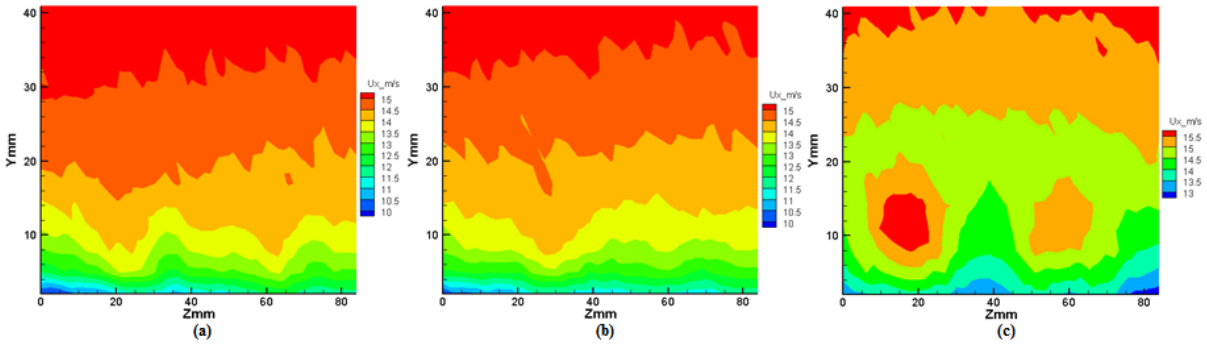

Figure H-17: Flow structure 96 mm downstream of hole exit trailing edge at blowing ratio equals to 1.8 and compound angle of zero (0) degrees. a) diffused machined hole, b) diffused 3D zero (0) degree Print orientation hole, c) diffused 3D 67 degree print orientation hole.

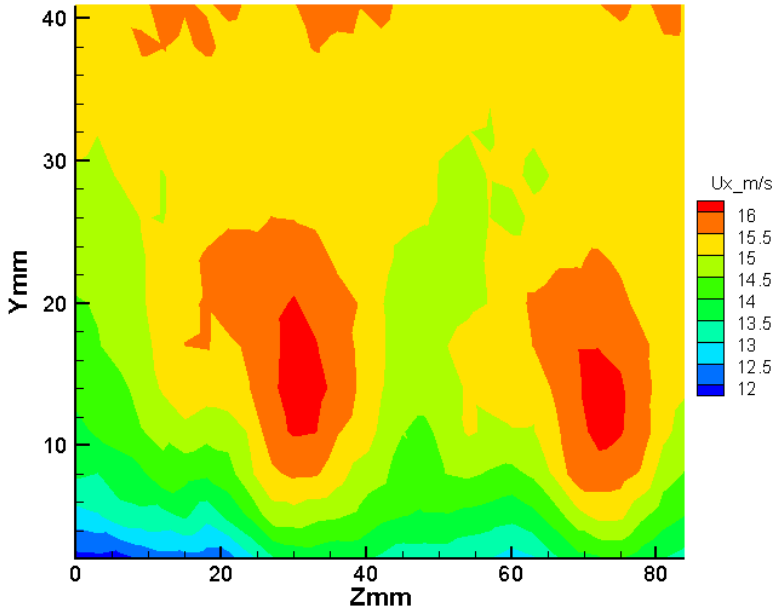

Figure H-18: Flow structure 96 mm downstream of hole exit trailing edge at blowing ratio equals to 1.3 and compound angle of 20 degrees for the cylindrical 3D zero 60 degree Print orientation hole.

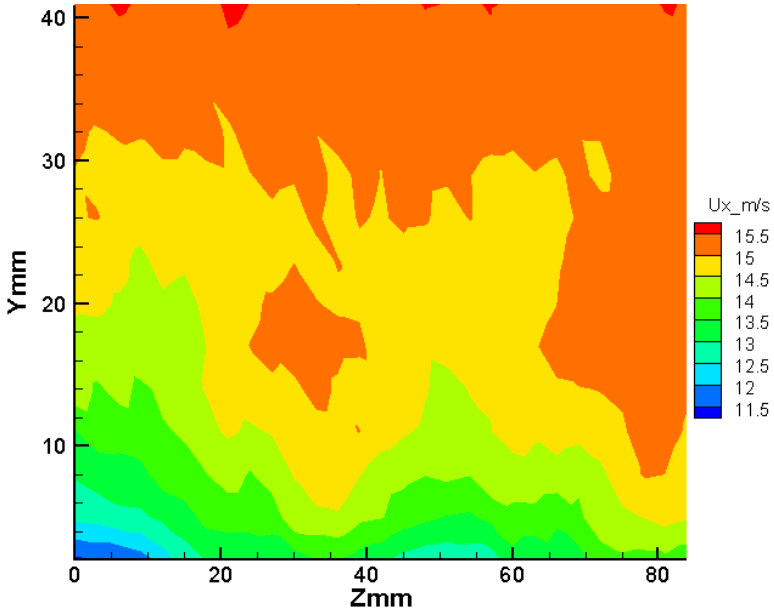

Figure H-19: Flow structure 96 mm downstream of hole exit trailing edge at blowing ratio equals to 1.8 and compound angle of 20 degrees for the diffused machined hole.

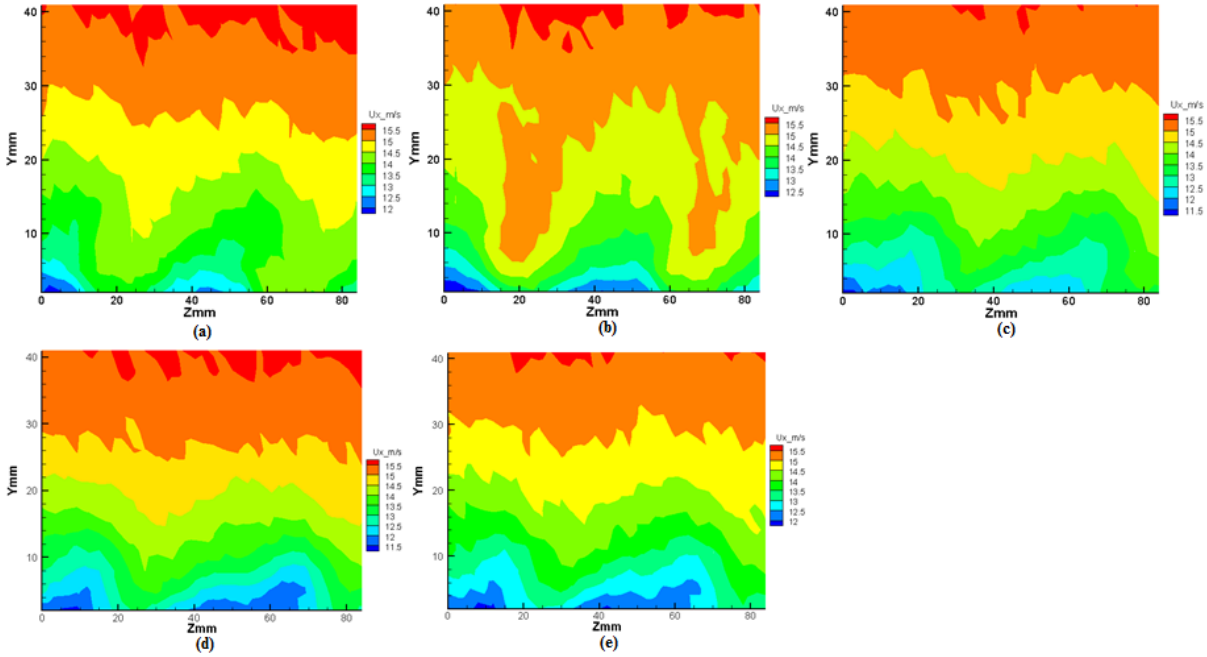

Figure H-20: Flow structure 96 mm downstream of hole exit trailing edge at blowing ratio equals to one (1) and compound angle of 30 degrees. a) cylindrical machined hole, b) cylindrical 3D zero (0) degree Print orientation hole, c) diffused machined hole, d) diffused 3D zero (0) degree print orientation hole, e) diffused 3D 67 degree print orientation hole.

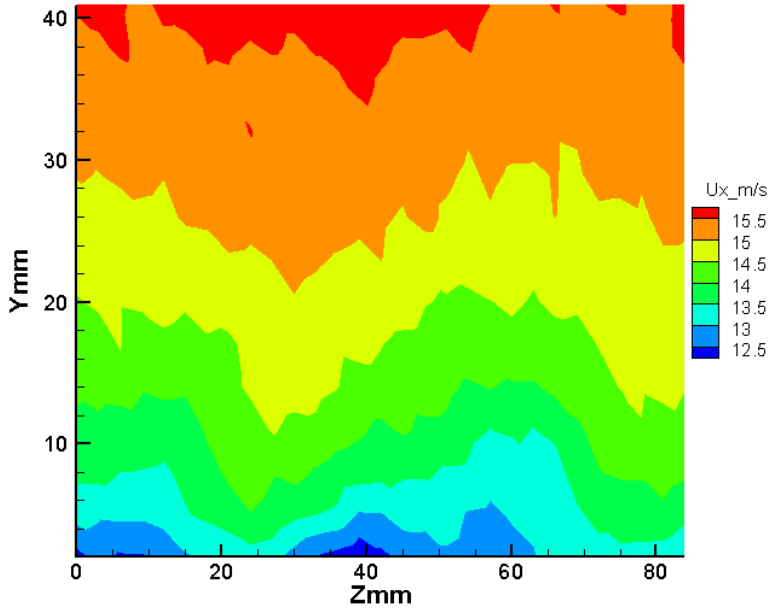

Figure H-21: Flow structure 96 mm downstream of hole exit trailing edge at blowing ratio equals to 1.8 and compound angle of 30 degrees for the diffused 3D 67 degree print orientation hole.

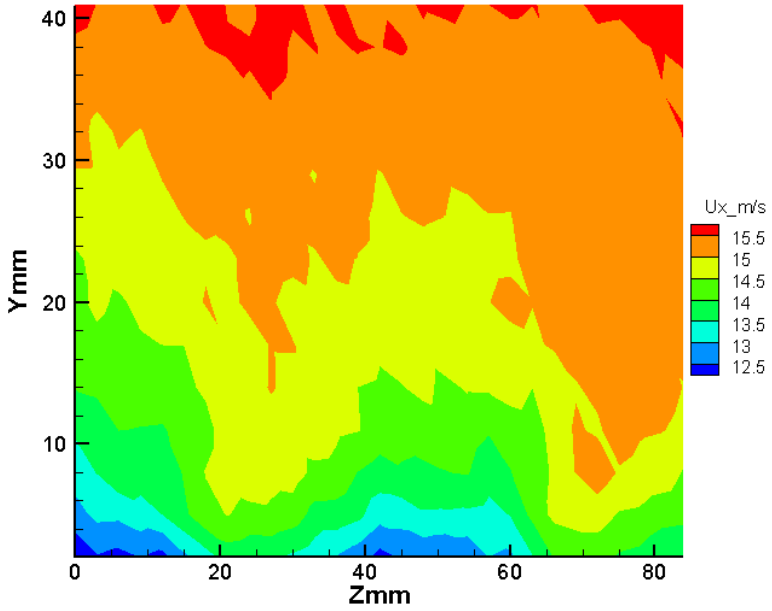

Figure H-22: Flow structure 96 mm downstream of hole exit trailing edge at blowing ratio equals to 1.8 and compound angle of 30 degrees for the diffused machined hole.

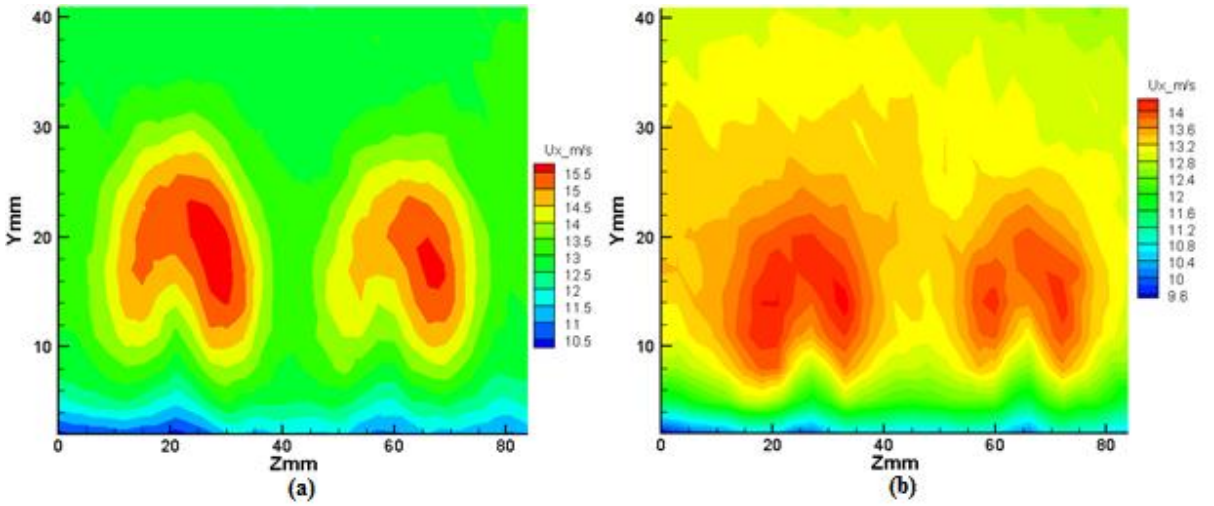

Figure H-23: Flow structure 96 mm downstream of hole exit trailing edge at blowing ratio equals to 1.3, compound angle of zero (0) degrees and with turbulence grid. a) cylindrical machined hole, b) cylindrical 3D zero (0) degree Print orientation hole.

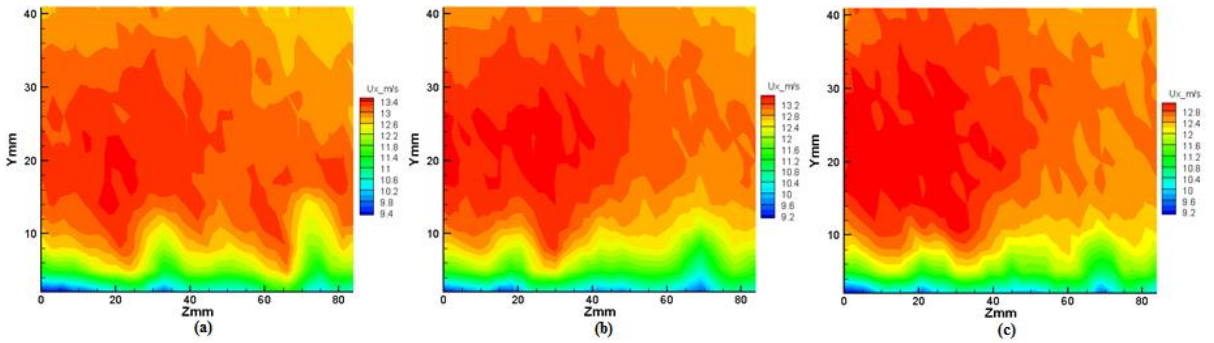

Figure H-24: Flow structure 96 mm downstream of hole exit trailing edge at blowing ratio equals to one (1) and compound angle of 30 degrees. a) diffused machined hole, b) diffused 3D zero (0) degree print orientation hole, c) diffused 3D 67 degree print orientation hole.

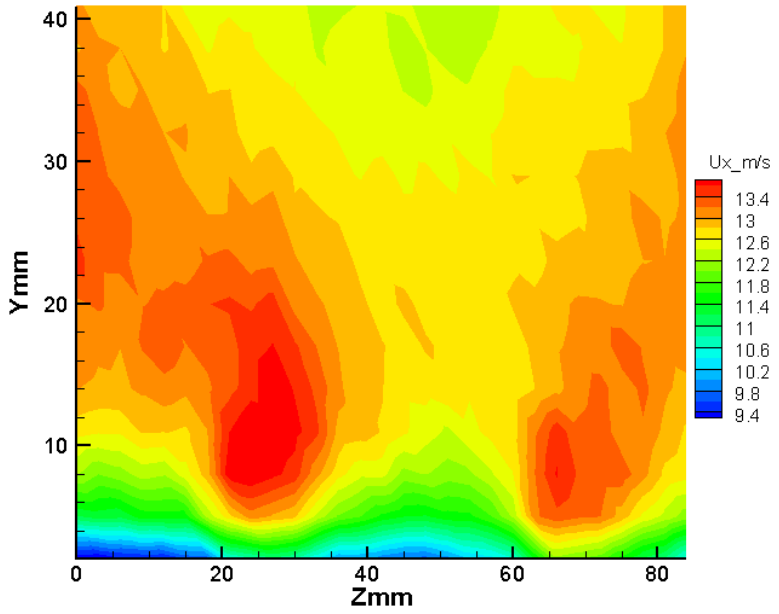

Figure H-25: Flow structure 96 mm downstream of hole exit trailing edge at blowing ratio equals to 1.3, compound angle of 20 degrees and with turbulence grid for the cylindrical machined hole.

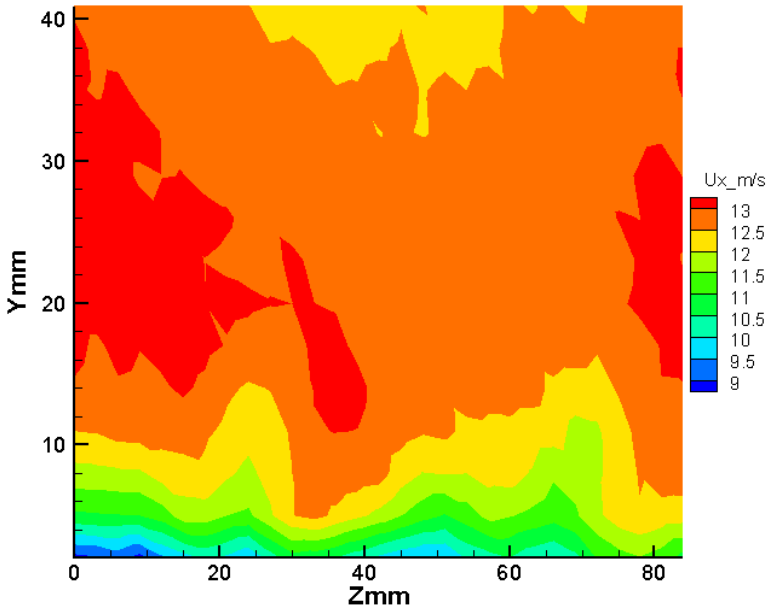

Figure H-26: Flow structure 96 mm downstream of hole exit trailing edge at blowing ratio equals to 1.8, compound angle of 20 degrees and with turbulence grid for the diffused machined hole.

H.2.Temperature field results

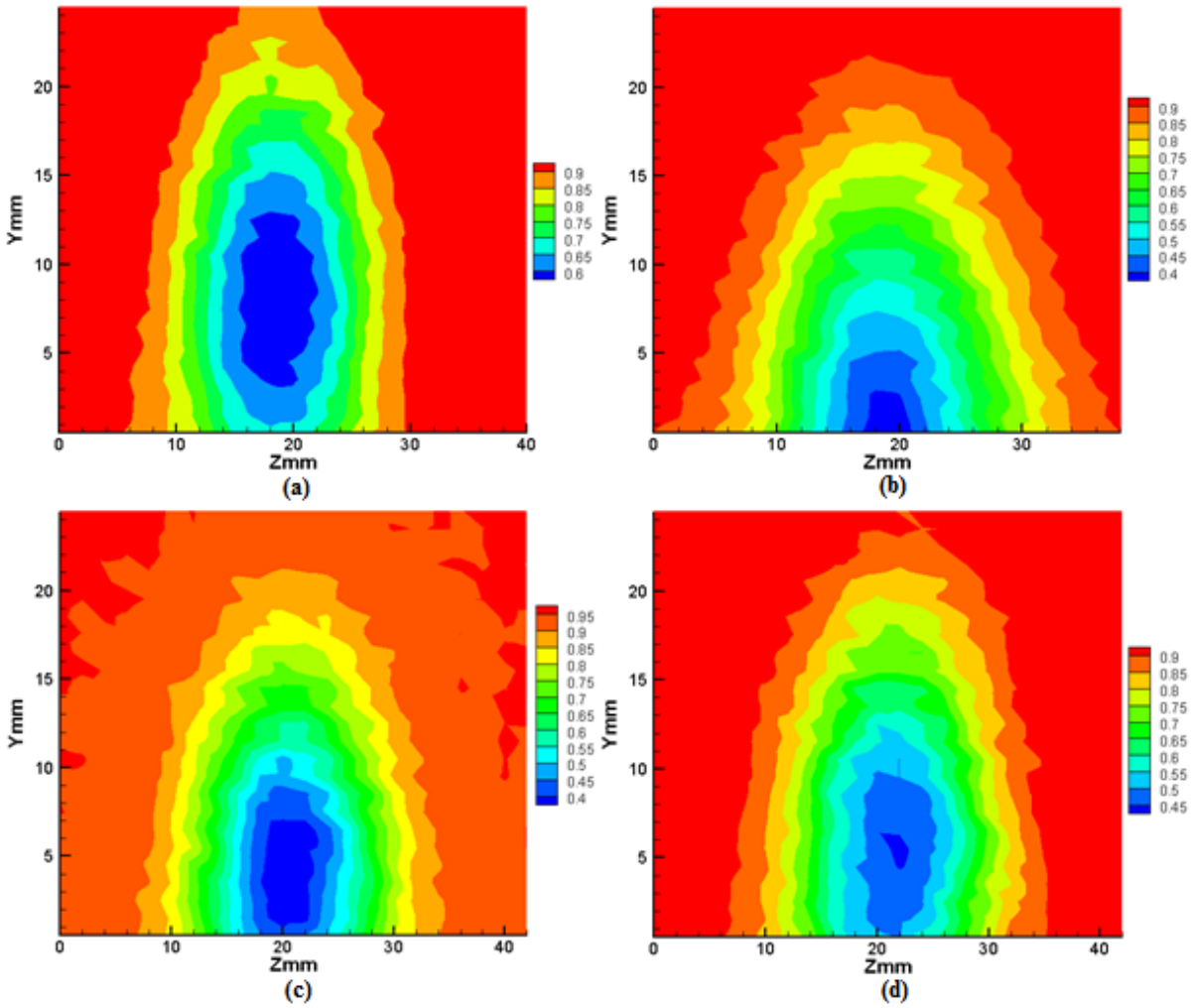

Figure H-27: Temperature field measurements 48 mm downstream of hole exit trailing edge at blowing ratio of 1.1 and compound angle of 0 degrees, without a turbulence grid. a) cylindrical hole injection, b) laidback fan-shaped hole injection, c) case 1 hole injection, d) case 3 hole injection.

H.3.Adiabatic effectiveness results

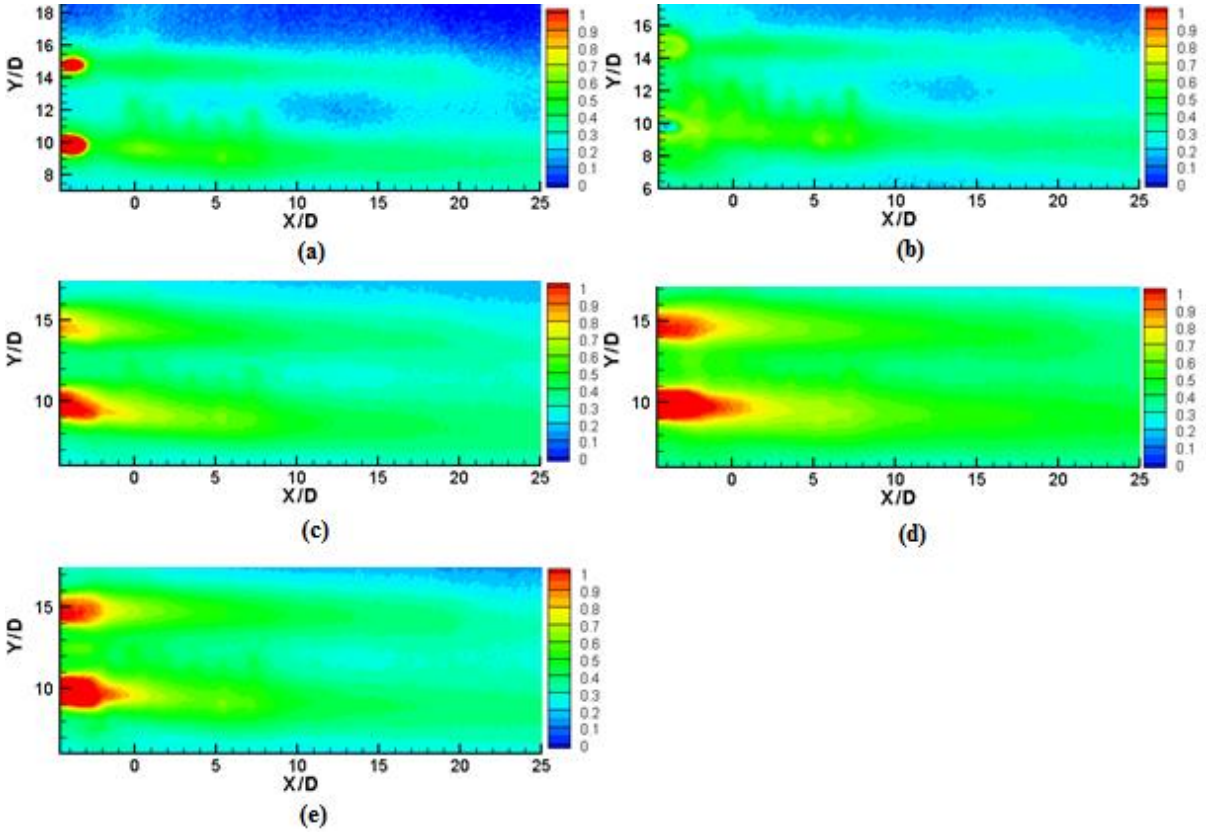

Figure H-28: Local distributions of adiabatic effectiveness along end-wall at a blowing ratio of 0.9 and compound angle of zero (0) degrees, without turbulence grid. a) cylindrical machined hole, b) cylindrical 3D 60 degrees printed hole, c) laidback fan-shaped machined hole, d) laidback fan-shaped 3D zero (0) degrees printed hole, e) laidback fan-shaped 3D 67 degrees printed hole.

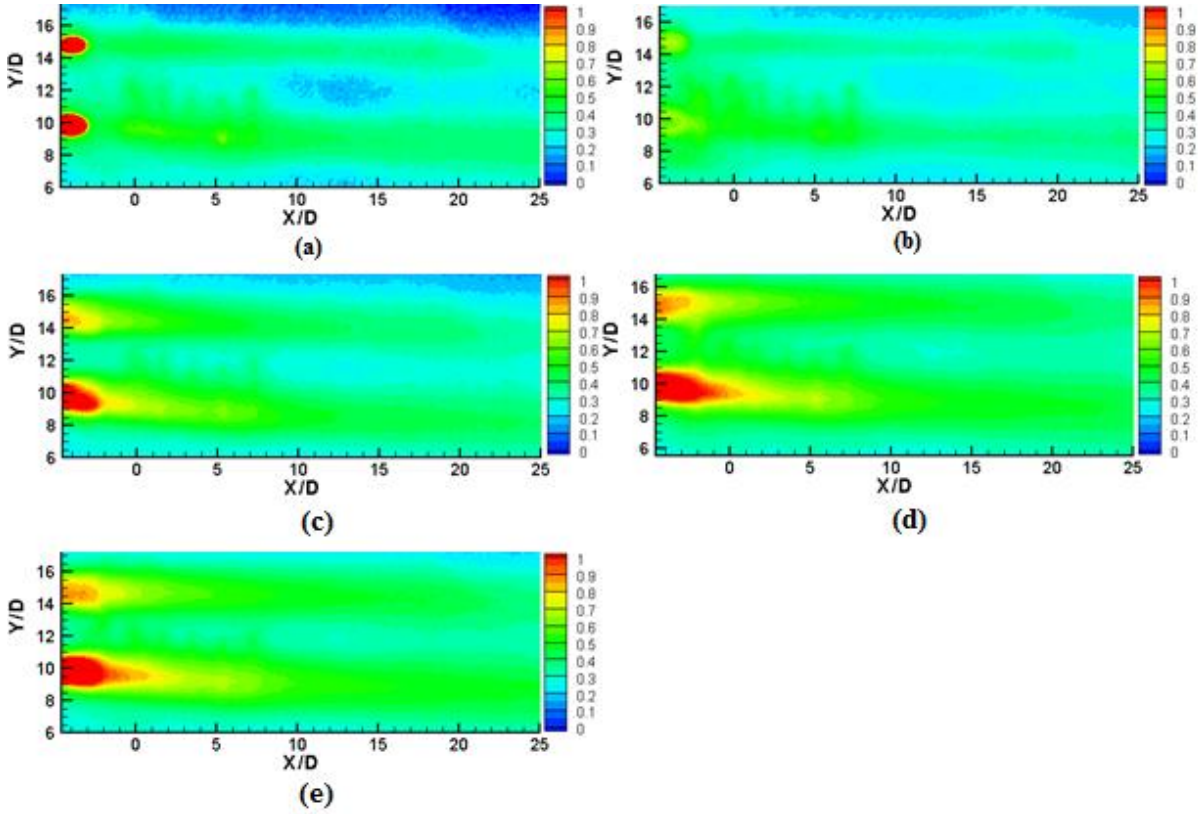

Figure H-29: Local distributions of adiabatic effectiveness along end-wall at a blowing ratio of 0.9 and compound angle of zero (0) degrees, with turbulence grid. a) cylindrical machined hole, b) cylindrical 3D 60 degrees printed hole, c) laidback fan-shaped machined hole, d) laidback fan-shaped 3D zero (0) degrees printed hole, e) laidback fan-shaped 3D 67 degrees printed hole.

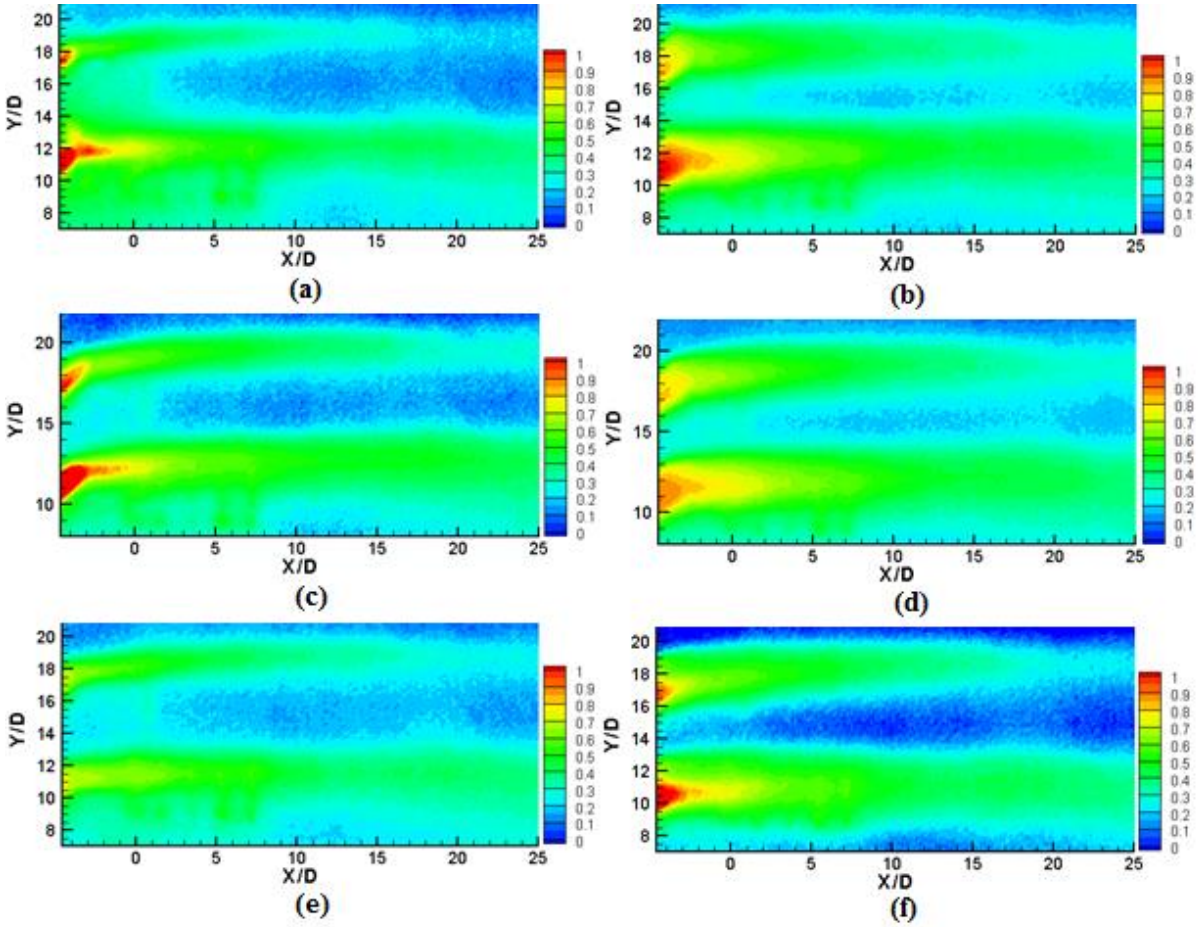

Figure H-30: Local distributions of adiabatic effectiveness along end-wall at a blowing ratio of 0.6 and compound angle of 40 degrees, with turbulence grid. a) cylindrical 3D 60 degrees printed hole, b) laidback fan-shaped 3D zero (0) degrees printed hole, c) case 1 hole, d) case 2 hole, e) case 3 hole, f) case 4 hole.

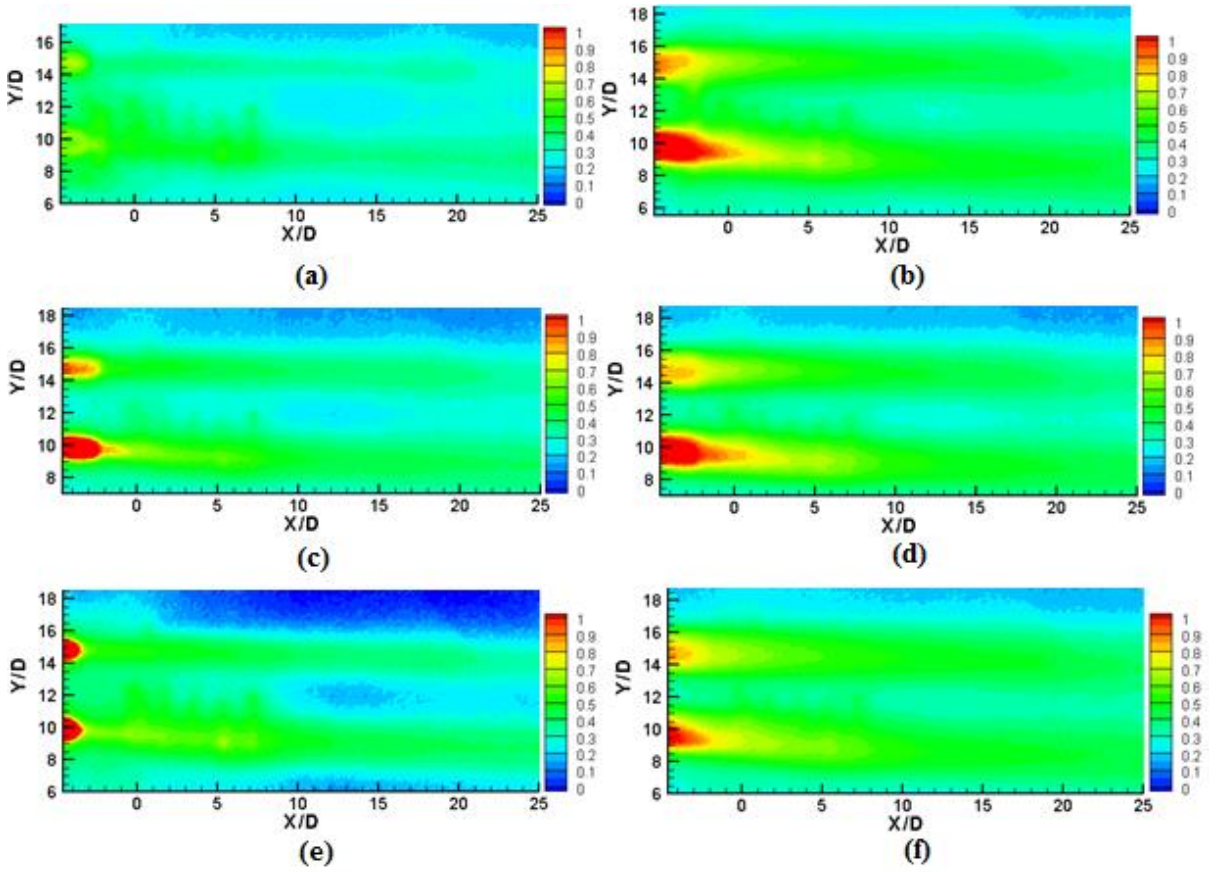

Figure H-31: Local distributions of adiabatic effectiveness along endwall at a blowing ratio of 0.9 and compound angle of 0 degrees, with turbulence grid. a) cylindrical 3D 60 degrees printed hole, b) laidback fan-shaped 3D zero (0) degrees printed hole, c) case 1 hole, d) case 2 hole, e) case 3 hole, f) case 4 hole.

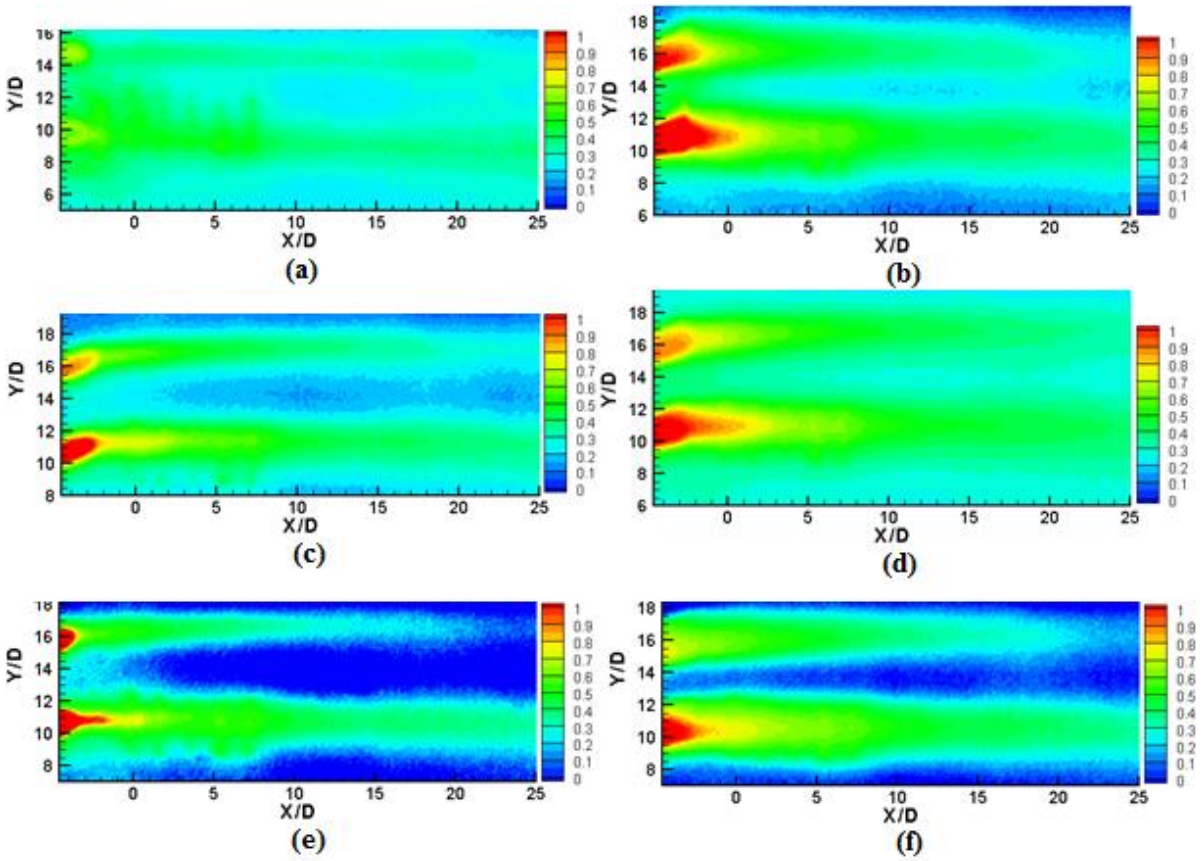

Figure H-32: Local distributions of adiabatic effectiveness along endwall at a blowing ratio of 0.9 and compound angle of 20 degrees, with turbulence grid. a) cylindrical 3D 60 degrees printed hole, b) laidback fan-shaped 3D zero (0) degrees printed hole, c) case 1 hole, d) case 2 hole, e) case 3 hole, f) case 4 hole.

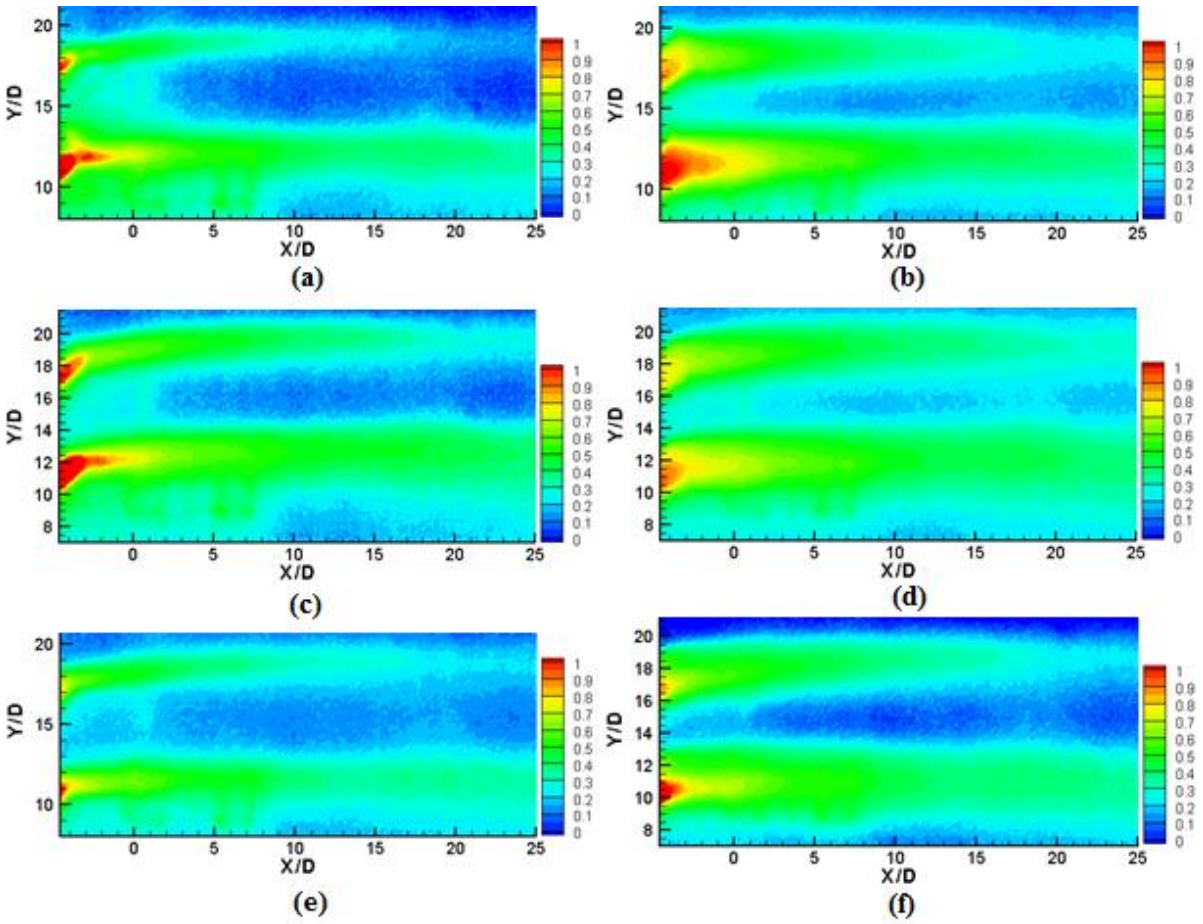

Figure H-33: Local distributions of adiabatic effectiveness along end-wall at a blowing ratio of 0.9 and compound angle of 40 degrees, with turbulence grid. a) cylindrical 3D 60 degrees printed hole, b) laidback fan-shaped 3D zero (0) degrees printed hole, c) case 1 hole, d) case 2 hole, e) case 3 hole, f) case 4 hole.

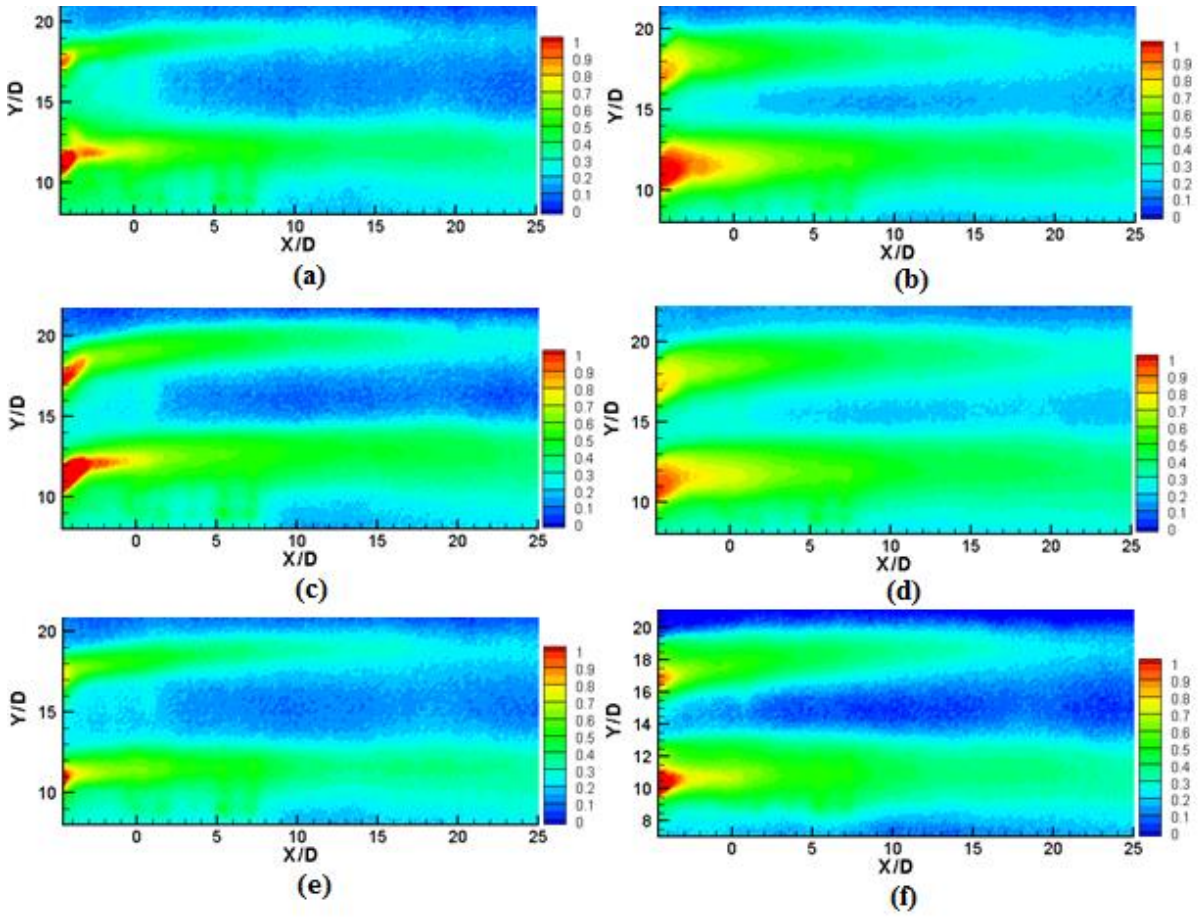

Figure H-34: Local distributions of adiabatic effectiveness along end-wall at a blowing ratio of 1.1 and compound angle of 40 degrees, with turbulence grid. a) cylindrical 3D 60 degrees printed hole, b) laidback fan-shaped 3D zero (0) degrees printed hole, c) case 1 hole, d) case 2 hole, e) case 3 hole, f) case 4 hole.

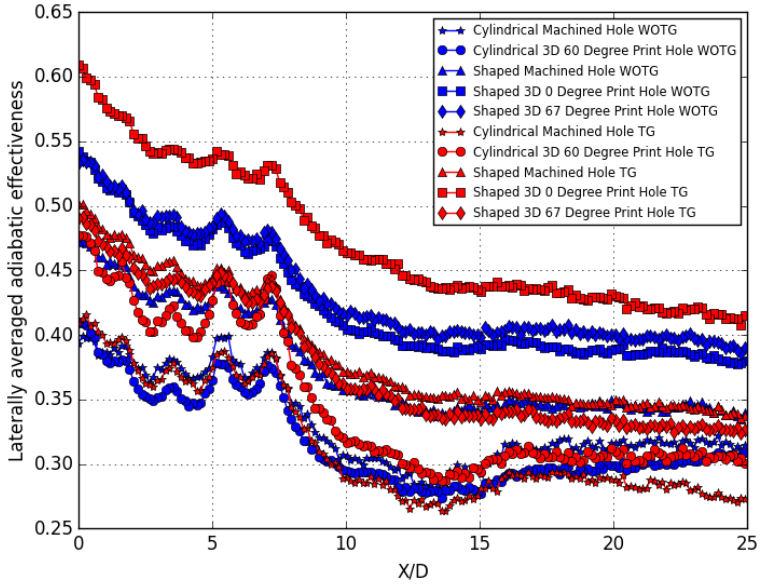

Figure H-35: Effect of turbulence intensity (WOTG – without turbulence grid, TG – with turbulence grid), manufacturing method and 3D print build orientation on the laterally averaged adiabatic effectiveness at blowing ratio equals to 0.9.

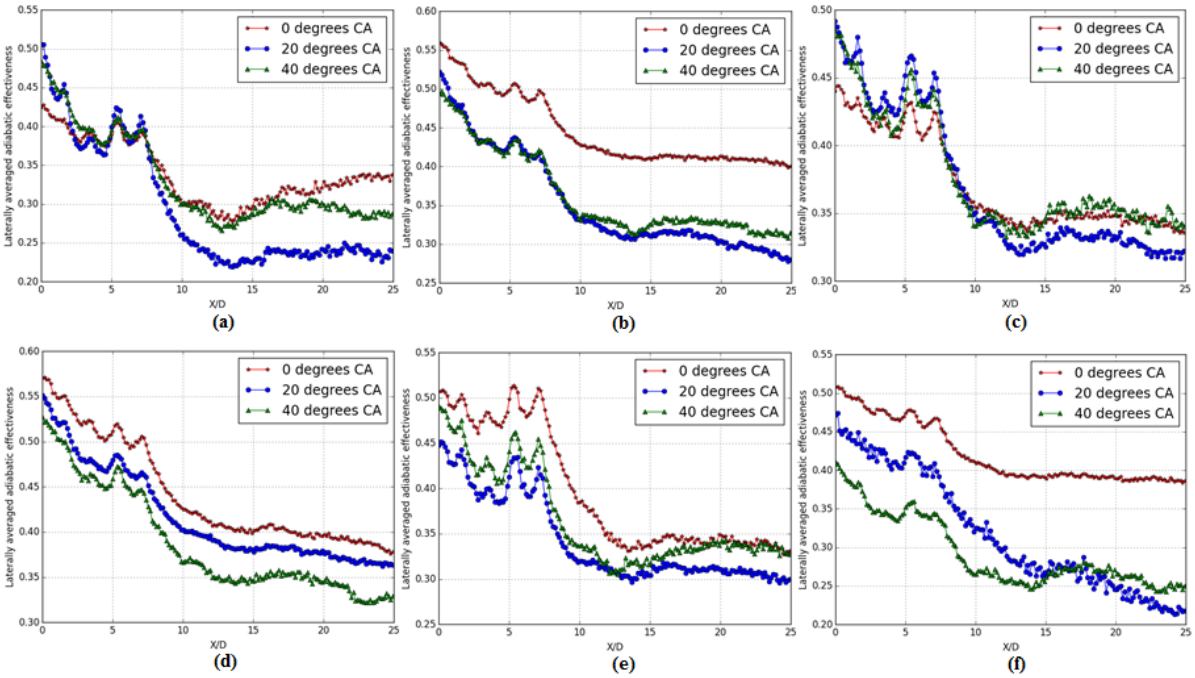

Figure H-36: Effect of compound angle on the laterally averaged effectiveness at a blowing ratio equals to 0.6, with turbulence grid. a) cylindrical 3D 60 degrees printed hole, b) laidback fan-shaped 3D zero (0) degrees printed hole, c) case 1 hole, d) case 2 hole, e) case 3 hole, f) case 4 hole.

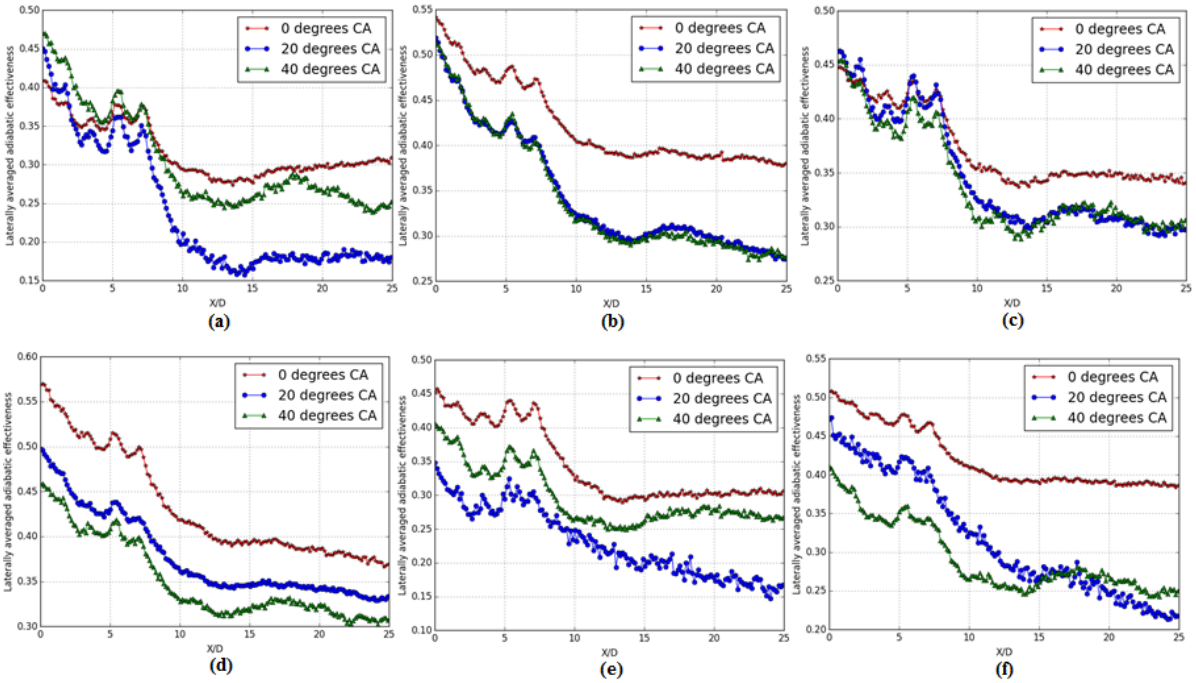

Figure H-37: Effect of compound angle on the laterally averaged effectiveness at a blowing ratio equals to 0.9, with turbulence grid. a) cylindrical 3D 60 degrees printed hole, b) laidback fan-shaped 3D zero (0) degrees printed hole, c) case 1 hole, d) case 2 hole, e) case 3 hole, f) case 4 hole.

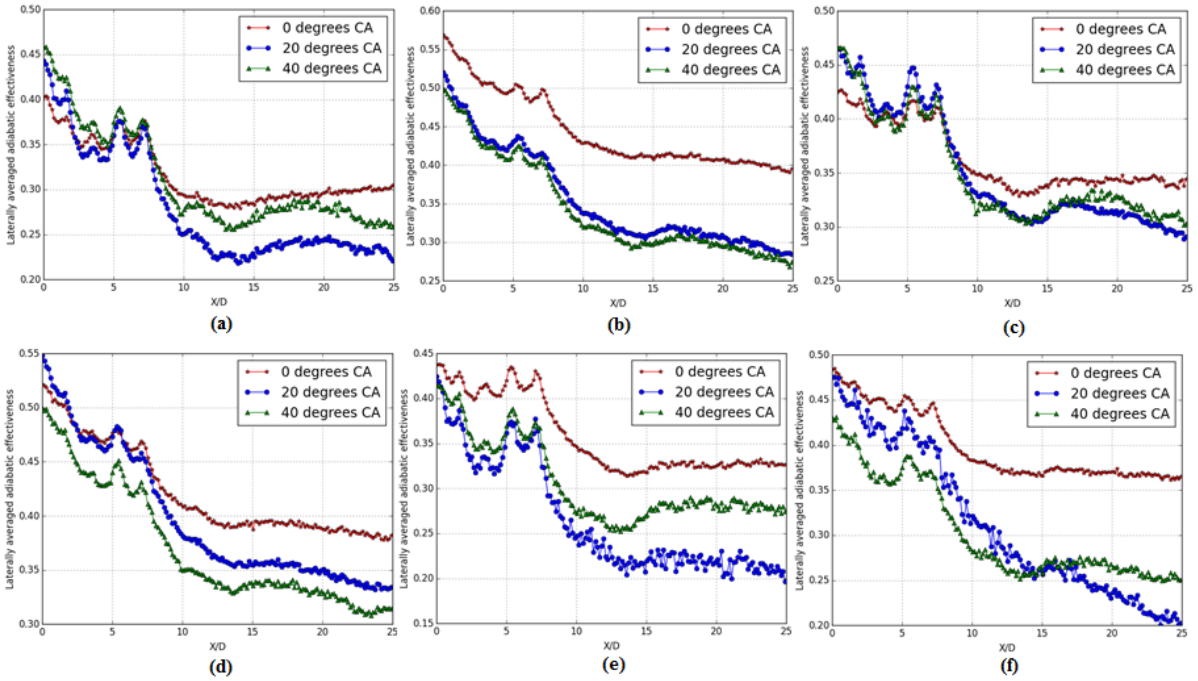

Figure H-38: Effect of compound angle on the laterally averaged effectiveness at a blowing ratio equals to 1.1, with turbulence grid. a) cylindrical 3D 60 degrees printed hole, b) laidback fan-shaped 3D zero (0) degrees printed hole, c) case 1 hole, d) case 2 hole, e) case 3 hole, f) case 4 hole.

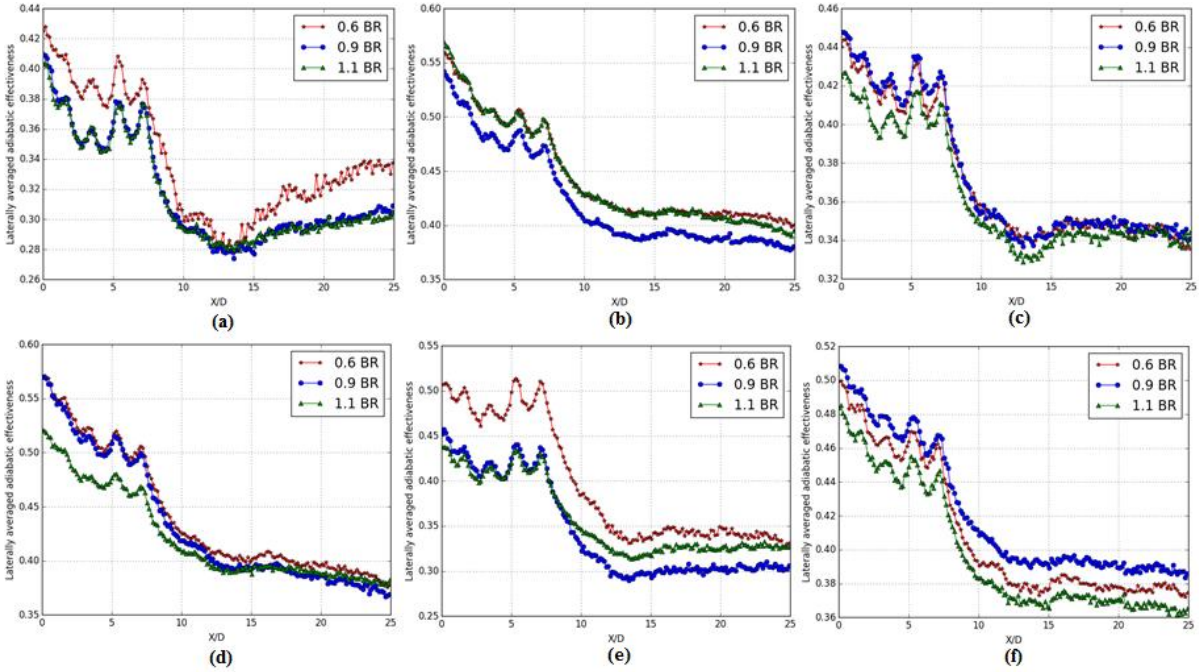

Figure H-39: Effect of blowing ratio on the laterally averaged effectiveness at a compound angle equals to zero (0) degrees, with turbulence grid. a) cylindrical 3D 60 degrees printed hole, b) laidback fan-shaped 3D zero (0) degrees printed hole, c) case 1 hole, d) case 2 hole, e) case 3 hole, f) case 4 hole.

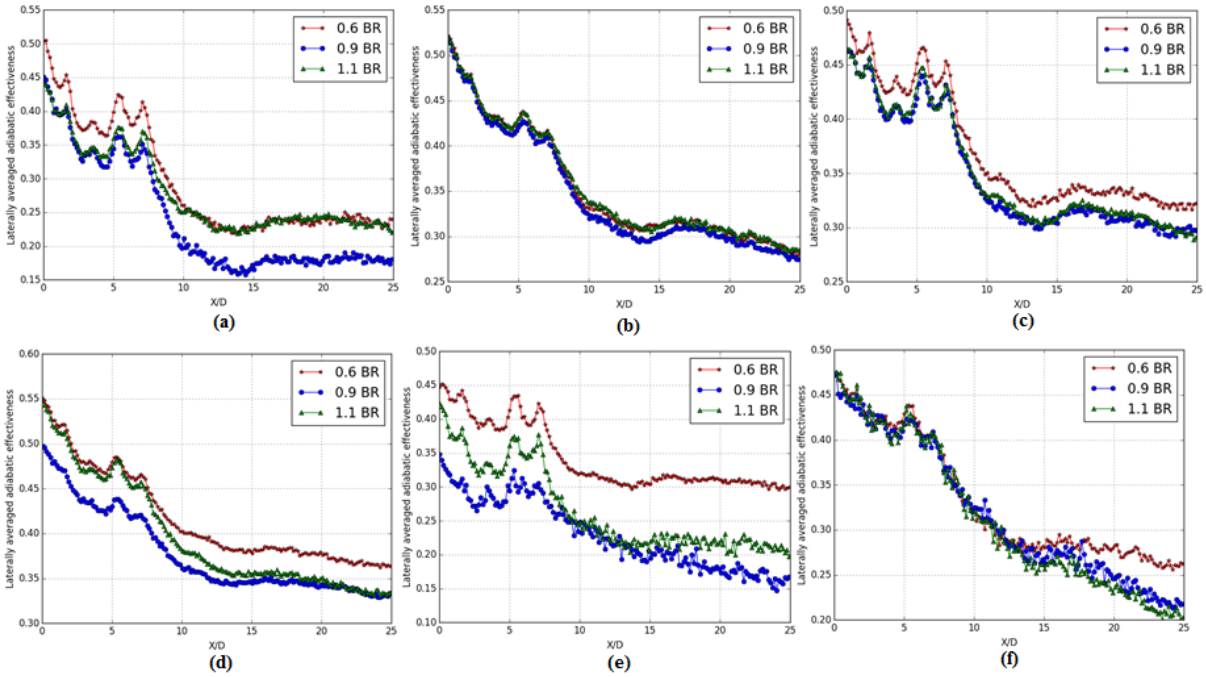

Figure H-40: Effect of blowing ratio on the laterally averaged effectiveness at a compound angle equals to 20 degrees, with turbulence grid. a) cylindrical 3D 60 degrees printed hole, b) laidback fan-shaped 3D zero (0) degrees printed hole, c) case 1 hole, d) case 2 hole, e) case 3 hole, f) case 4 hole.

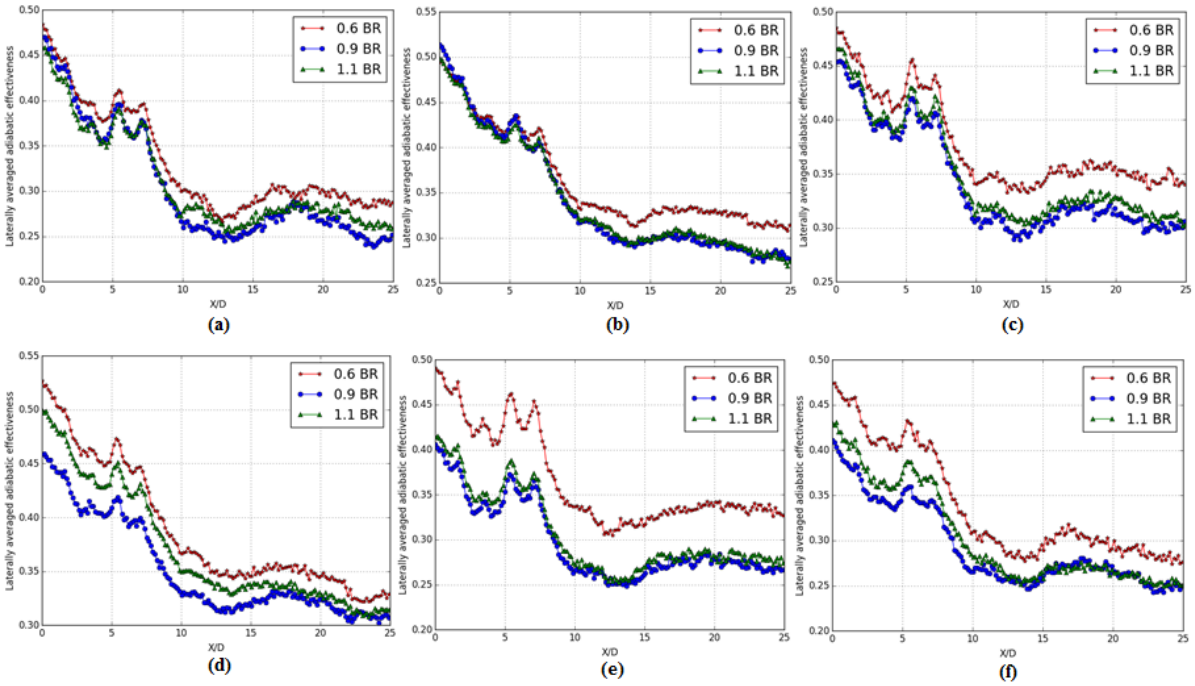

Figure H-41: Effect of blowing ratio on the laterally averaged effectiveness at a compound angle equals to 40 degrees, with turbulence grid. a) cylindrical 3D 60 degrees printed hole, b) laidback fan-shaped 3D zero (0) degrees printed hole, c) case 1 hole, d) case 2 hole, e) case 3 hole, f) case 4 hole.

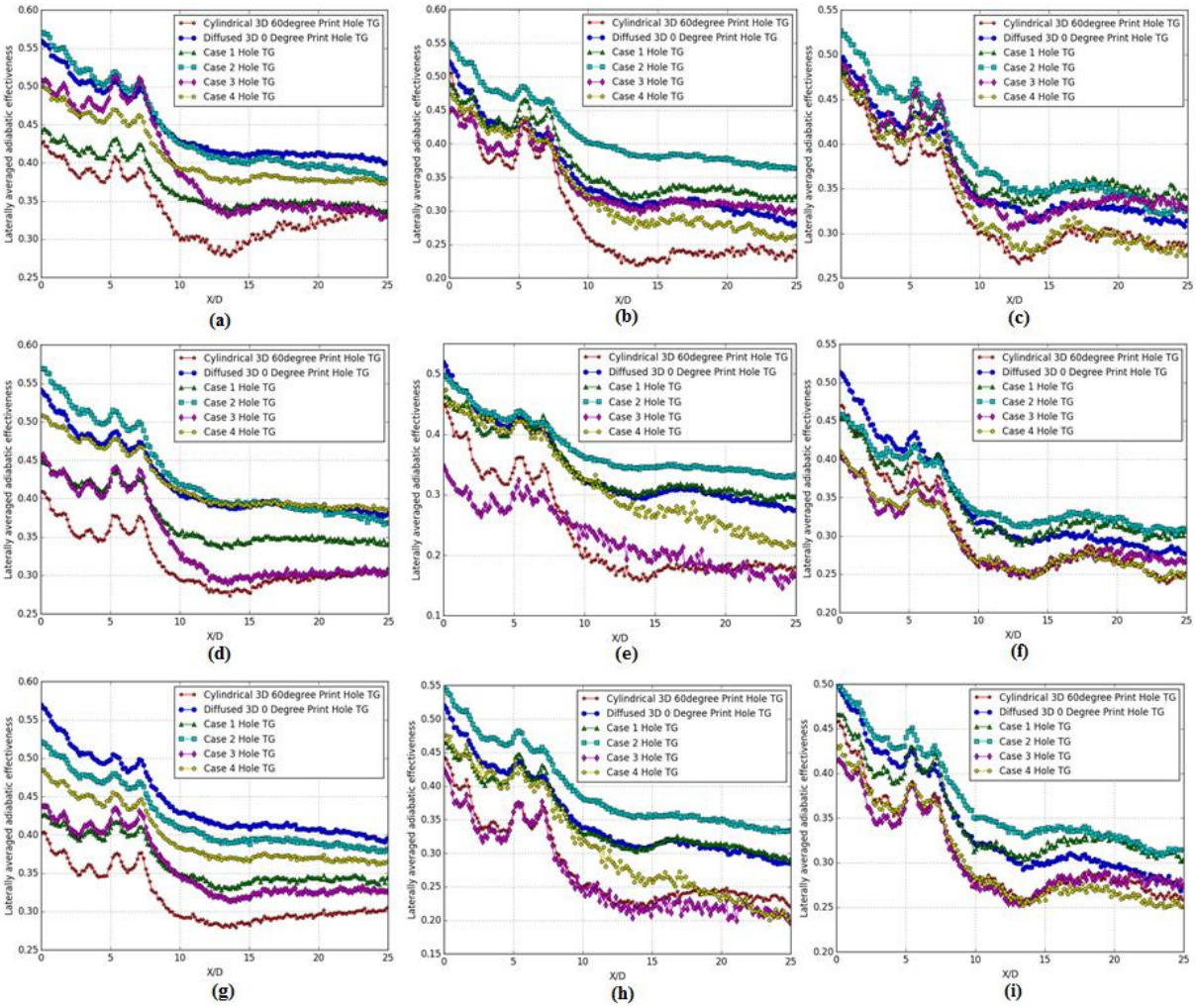

Figure H-42: Effect of shape on the laterally averaged effectiveness. a) blowing ratio 0.6 compound angle zero (0) degrees, b) blowing ratio 0.6 compound angle 20 degrees, c) blowing ratio 0.6 compound angle 40 degrees, d) blowing ratio 0.9 compound angle zero (0) degrees, e) blowing ratio 0.9 compound angle 20 degrees, f) blowing ratio 0.9 compound angle 40 degrees, g) blowing ratio 1.1 compound angle zero (0) degrees, h) blowing ratio 1.1 compound angle 20 degrees, i) blowing ratio 1.1 compound angle 40 degrees.

I. Film cooling configurations

Figure I-1: 3D printed film cooling geometries.

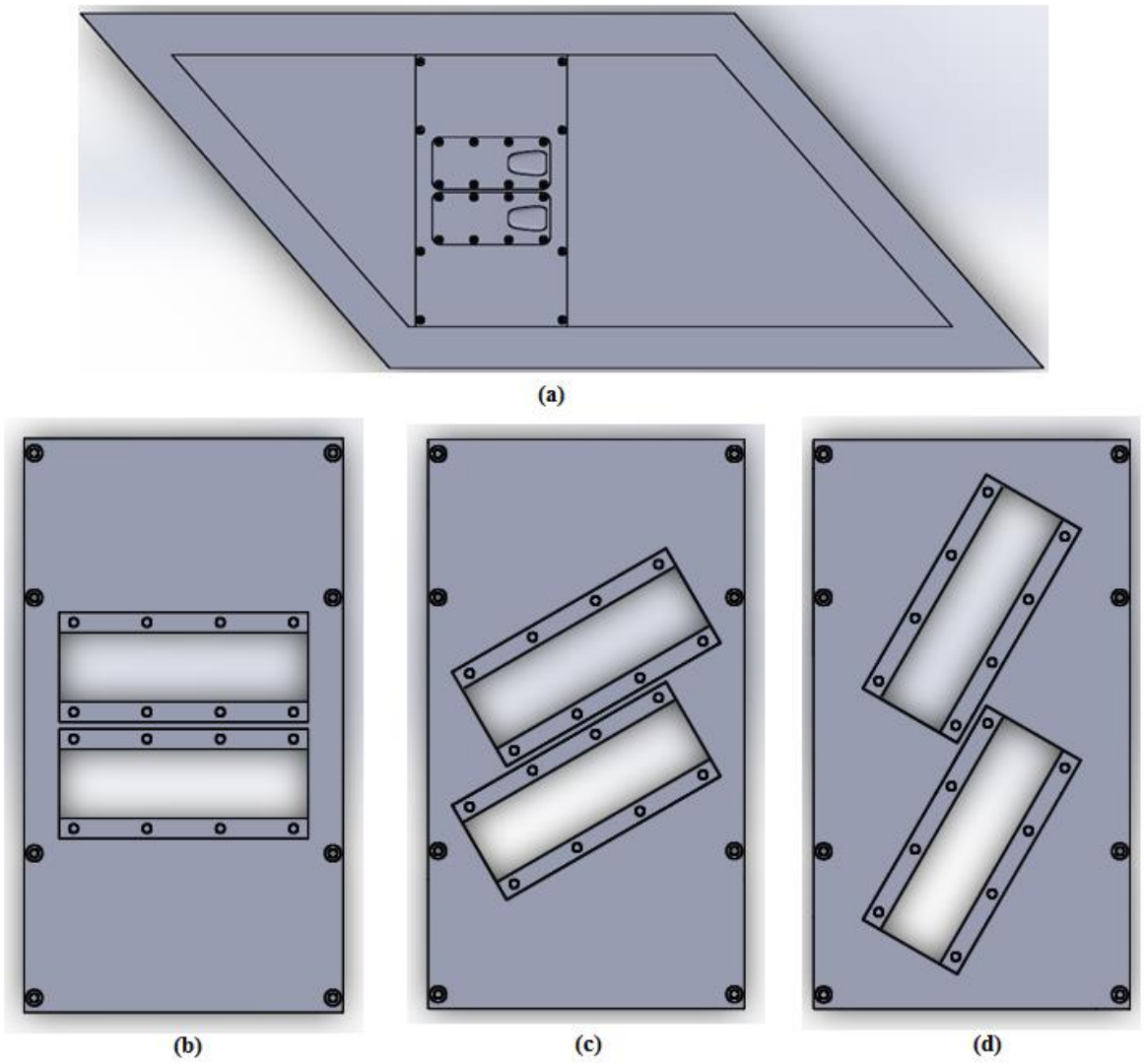

Figure I-2: Test piece facilitation, b) zero (0) degrees compound angle orientation, c) 30 degrees compound angle orientation, d) 60 degrees compound angle orientation.